DISS. ETH NO. 22902

Creation of Squeezed Schrödinger's Cat States in a Mixed-Species Ion Trap

A thesis submitted to attain the degree of

DOCTOR OF SCIENCE of ETH ZÜRICH

(Dr. sc. ETH ZÜRICH)

presented by

HSIANG-YU LO

M.S., National Chiao Tung University, 2007

born on 22.12.1983

citizen of
Taiwan

Accepted on the recommendation of

Prof. Dr. J. P. Home
Dr. C. F. Roos

2015

Abstract

This thesis reports on novel experiments in the field of quantum state engineering and preparation using a single trapped $^{40}Ca^{+}$ ion. It also covers the laser system, optical setups, experimental characterizations and theoretical study for the $^{9}Be^{+}$ ions. In addition, a newly set-up mixed-species ion trap and imaging system are described.

We demonstrate the generation of squeezed Schrödinger's cat states by applying a state-dependent force (SDF) to a single trapped ion initialized in a squeezed vacuum state. Using SDF technique allows us to directly measure the phase coherence and quadratures of the initial squeezed wavepacket by monitoring the spin-motion entanglement. The evolution of the number states of the oscillator is measured as a function of the duration of the force. In both experiments, we observe clear differences between displacements aligned with the squeezed and anti-squeezed axes. Coherent revivals of the squeezed Schrödinger's cat state are observed after separating the wavepackets by more than 19 times the ground state root-mean-square extent, which corresponds to 56 times the r.m.s. extent of the squeezed wavepacket along the displacement direction. To our knowledge, this is the largest cat state created in any technology so far.

The beryllium laser system built as part of this thesis is designed to perform a high-fidelity control of beryllium qubits. The new 235 nm laser source is first described and used for loading beryllium ions. For quantum control of the ion, we generated 1.9 Watts of continuous-wave ultraviolet light at 313 nm, which may help towards fault-tolerant quantum computation. Using these sources, the control of beryllium is described, including the ground state cooling and a long-lived quantum memory. The coherence time of the $^{9}Be^{+}$ qubit with a first-order magnetic-field-independent hyperfine transition is measured to be ≈ 1.5 seconds.

This work provides basic techniques for quantum control of both ion species in the same experimental setup as well as developing new tools for quantum state engineering, quantum metrology and quantum information processing.

This is the first edition of the thesis, released on Monday 27$^{\text{th}}$ July, 2015. This is the second edition of the thesis with corrections according to examiners' comments, released on Monday 1$^{\text{st}}$ February, 2016.

Zusammenfassung

Diese Dissertation dokumentiert neuartige Experimente mit einzelnen gefangenen $^{40}Ca^{+}$ Ionen im Forschungsfeld der Quantenzustandspräparation. Sie behandelt ausserdem ein Lasersystem, den optischen Aufbau, die experimentelle Charakterisierung, sowie theoretische Studien für $^{9}Be^{+}$ Ionen. Zusätzlich werden eine neu aufgebaute Ionenfalle und ein Abbildungssystem für Ionenkristalle verschiedener Spezies beschrieben.

Wir demonstrieren die Erzeugung gequetschter Schrödingers-Katzen Zustände durch die Anwendung einer zustandsabhängigen Kraft auf ein in einem gequetschten Grundzustand initialisierten, gefangenen Ion. Die Verwendung der Methode der zustandsabhängigen Kraft erlaubt es uns, durch die Beobachtung der Verschränkung zwischen Spin- und Bewegungszustand direkt die Phasenkohärenz und Quadraturen des gequetschten Wellenpakets zu messen. Die Entwicklung der Fock-Zustände des Oszillators wird als Funktion der Dauer der zustandsabhängigen Kraft gemessen. In beiden Experimenten beobachten wir deutliche Unterschiede für den Versatz entlang der gequetschten und der anti-gequetschten Achse. Kohärente Wiederkehr der gequetschten Schrödinger-Katzen-Zustände nach einer Separation der Wellenpakete von mehr als 19 mal der Ausdehnung des Grundzustandswellenfunktion wird beobachtet (quadratischer Mittelwert). Dies entspricht einer Separation von 56 mal der Ausdehnung des gequetschten Wellenpakets (quadratischer Mittelwert) entlang der Richtung des Versatzes. Nach unserem Wissen ist dies der grösste Katzen-Zustand der bisher, unabhängig von der angewandten Technologie, erzeugt wurde.

Das Lasersystem für Beryllium, gebaut als Teil dieser Arbeit, wurde entworfen, um Kontrolle hoher Güte von Beryllium-Ionen auszuüben. Die neue 235 nm Laserquelle wird zuerst beschrieben und verwendet um Beryllium-Ionen zu laden. Für Quantenkontrolle erzeugen wir 1.9 W an Dauerstrich-Ultraviolett-Licht bei 313 nm, was hilfreich für fehlertolerantes Quanten-Rechnen sein könnte. Die Kontrolle von Beryllium mit Verwendung dieser Quellen wird beschrieben, inklusive Grundzustandskühlen und eines langlebigen Quantenspeichers. Die Kohärenzzeit eines $^{9}Be^{+}$ Qubits mit einem in erster Ordnung magnetfeldunabhängigen Übergang in der Hyperfeinstruktur wurde zu ≈ 1.5 Sekunden gemessen.

Diese Arbeit beschreibt grundlegende Techniken zur Quantenkontrolle von beiden Ionenspezies im selben experimentellen Aufbau sowie die Entwicklung neuer Techniken zum Erzeugen von Quantenzuständen, der Quantenmeteorologie und der Quanteninformationsverarbeitung.

Acknowledgements

It has been a great privilege to work in Trapped Ion Quantum Information Group at ETH Zürich. I had wonderful time in the past five years during my PhD. I gained a lot of knowledge and experience about trapped-ion physics, experimental design, experimental techniques, and the data processing and analysis. All of these provide me an insightful perspective on different kinds of problems, which we encounter in the day-to-day operations. I still remember when I joined the group in November 2010, we only had four members plus one group secretary, and we didn't have a proper laboratory. Starting from zero until now, the group has been grown quite fast. I have been working with many brilliant people. First, I really thank my supervisor, Jonathan Home, for giving me this opportunity to work in the group. I appreciate that he recognized my ability in the Skype interview and let me design and set up the key apparatus in the laboratory when the group started. Jonathan, with his massive knowledge, is always helpful when I have questions. He always has many ideas and can just point out the key for solving the problem I have. He also gives his students support as much as he can.

I thank all my colleagues I have ever worked with. Specially I would like to thank Daniel Kienzler. Basically we joined the group at the same period as a PhD student and worked closely. He not only built the first ion trap in the group but also set up a lot of experimental apparatus. He is an important member in the group and always self-motivated with an attitude of "just do/try it". It's my pleasure that I did many beautiful experiments with him.

I want to thank Ben Keitch for putting a lot of effort on the computer control system I used. Additionally, he is always generously sharing his technical knowledge with everyone and willing to help. Although my project did not overlap with his too much, I still learnt tricks from him when I worked on electronics or mechanical design. I also thank Ludwig de Clercq for designing and constructing the amazing laser locking box used everywhere in the lab and for taking the final data presented in this thesis with me over the night.

We always have very fun discussions about physics, travel, food, photography and hiking. He is a great colleague and friend. I would like to thank Joseba Alonso who contributed his talent to the frequency doubling cavity design and helped me for the data analysis in the paper. He likes to listen, discuss everything, and provide suggestions to everyone.

I think I'm very lucky to be able to meet these people, and I appreciate their helps and the great time we together: Vlad Negnevitsky for contributing his fruitful knowledge to every electronics device we have built and to our new computer control system. Matteo Marinelli for the achievements on the simulation of quantum harmonic oscillator state generation and the computer control system. Frieder Lindenfelser, Florian Leupold, Martin Sepiol, Karin Fisher, and Christa Flühmann for their great work on the calcium laser systems. Alexander Hungenberg, David Nadlinger, Robin Oswald, Roland Habluetzel, Dominik Wild, Martin Paesold, Mario Rusev, Mathieu Chanson, Peter Strassmann, Manuel Zeyen, Lukas Gerster, Ursin Solèr, Matteo Fadel, Felix Krauthand, Robert Davies, Christoph Fischer, Chi Zhang, Nelson Oppong, and Chiara Decaroli for their contributions to a variety of lab equipments. Besides, I would like to say thank you to our group secretaries, Lisa Artel and Mirjam Bruttin. They helped me a lot for the permit issue, German translation, shipment of the broken devices, and many other administrative stuffs.

Outside the group, I would like to thank Dietrich Leibfried and Andrew Wilson from NIST for useful discussions and guidance when I started setting up the beryllium laser system. I also thank Christian Rahlff from Covesion for providing useful information about the nonlinear crystal used in our laser system.

I have to thank my previous supervisors: The first one is my master thesis advisor, Hsueh-Yung Chao. He applied for a fellowship for me, gave me a lot of freedom doing my project and taught me a lot of numerical computation and analysis skills. The other advisor I would like to thank is Yong-Fan Chen at National Cheng Kung University, Taiwan. During the time of doing the research assistant in his group, I learnt plenty of experimental skills and knowledge of quantum physics and quantum optics from him. He also encouraged me to pursue my PhD abroad, to see a different world. All the experience and skills I learnt in his lab are very useful for my PhD work.

Finally, I need to thank my family, especially my parents, for their encouragement and support. Special thanks to my wife, Amber, who resigned a good job in Taiwan, married me, and came to a place where we have never thought of. During my PhD period, she devotes her time to the family, taking care of the baby as well as working quite hard in order to make our life better. All in all, it has been like an adventure in the past five years. Both Amber and I had great and unforgettable time living, working, and travelling in Switzerland.

Contents

Chapter 1

Introduction

Quantum mechanics provides an accurate description of the behavior of objects typically at atomic length scales. The physical phenomena predicted by quantum mechanics have also been verified in the experiment to an extremely high accuracy. Experimental control of quantum systems is very difficult to pursue because the quantum systems can easily lose their quantum properties as soon as they interact with the environment. The work on studies of the fundamental interaction between light and matter was considerably grown up since the mid-1980s. There were many advances and techniques being made and developed in this research field over the past 30 years. Particularly there was a field of research recognized by the Nobel Prize to Serge Haroche and David J. Wineland "for ground-breaking experimental methods that enable measuring and manipulation of individual quantum systems". Both experimental pioneers independently invented and developed a variety of experimental techniques for measuring and controlling individual particles. Their works provide this field of research a foundation towards building a new type of computer based on quantum physics. Besides the atomic systems that Haroche and Wineland use, control of the quantum states for realizing quantum computing or quantum simulation is also widely pursued in many different kinds of physical systems, for example, photons, atoms in optical lattices, quantum dots, superconducting circuits, and nuclear magnetic resonance [Ladd 10, Buluta 09, Georgescu 14]. Among all the possible candidates for implementing a practical quantum computing, trapped ions are still one of the most promising technologies [Häffner 08]. The ions are well isolated from the environment, so quantum states can be stored robustly in the internal and motional states (with a long coherence time). These ions can be precisely and rapidly controlled using near resonant optical or microwave fields. The stored quantum information can be transferred between ions using collective quantized motion of the ions which interact strongly through Coulomb forces [Cirac 95, Wineland 98], or alternatively one can also transfer quantum information using photons in a trapped ion based quantum network

[Duan 10, Northup 14]. In the following, three main subjects that we would like to address using trapped atomic ions will be introduced.

1.1 Quantum Computation

The basic element in classical computer is the bit, which can be either 0 or 1. In quantum computer, this term is called the quantum bit or qubit. The qubit is a two-level quantum system, which are labeled with 0 and 1. However, a qubit also allows to exist in a coherent superposition state, both 0 and 1 at the same time [Schrödinger 35, Nielsen 00]. An operation on such a qubit acts on both values simultaneously. As a result, increasing the number of qubits exponentially increases the "quantum parallelism" that we obtain from the system.

A number of key advances have been developed in the theory of quantum computation, the first was that a controllable quantum system could simulate the properties of another quantum system much faster than classical computers, by Richard Feynman in 1982 [Feynman 82]. Perhaps, the most important discovery was made by David Deutsch in 1985 [Deutsch 85], where he formulated a description for a quantum Turing machine and presented a fully quantum model for computation, the universal quantum computer. In 1994 Peter Shor discovered a quantum algorithm for prime factorization in polynomial time [Shor 94]. The same problem running on a classical computer would scale exponentially with the size of the problem. In 1995, Barenco *et al.* showed that a set of gates consisting of all single-qubit gates and the two-qubit entangling gate (controlled NOT gate) is universal [Barenco 95]. That means all unitary operations on arbitrarily n qubits can be decomposed with these gates. They carefully analyzed the number of the above gates required to implement other quantum gates like generalized Deutsch-Toffoli gates [Deutsch 89], which plays an important role in many proposals of quantum computation.

In the same year (1995), Cirac and Zoller proposed a scheme of implementing a two-qubit controlled-NOT gate with trapped ions [Cirac 95]. The first experimental demonstration was realized by Schmidt-Kaler *et al.* [Schmidt-Kaler 03]. However, an alternative method for realizing a two-qubit entangling gate is to apply a spin-state-dependent force on two or more ions simultaneously which was proposed in 1999 [Mølmer 99, Sørensen 99, Solano 99, Milburn 00] and then implemented by several groups [Sackett 00, Haljan 05b, Benhelm 08a, Home 06a, Leibfried 03b]. This type of gate has some useful features namely that it does not require individual addressing of the ions and it can work without cooling the ions to the motional ground state, both of which are the technical requirements for the Cirac-Zoller gate operation. Many trapped-ion groups throughout the world are still trying to push the gate fidelity to meet the fault-tolerant threshold (10^{-4}) for realization of quantum computation

[Benhelm 08a, Brown 11, Harty 14].

1.2 Quantum Simulation

Quantum simulation is one of the branches in quantum information science. It is very similar to the idea that Richard Feynman pointed out in 1982 [Feynman 82]. Simulating certain quantum systems, for instance quantum many-body systems, is intractable with classical computers. The best algorithms for their exact simulation require computational resources that grow exponentially with the number of particles. This kind of problem not only appears in solid-state physics, but also in chemistry, material science and even biology [Zeng 12]. One promising approach to overcome this problem is the quantum simulation in which one could catch more insight into complex quantum dynamics by using precise control of a controllable quantum system to simulate the behavior of another quantum system. Quantum simulations would not only provide new results that cannot be obtained from classical computers, but also allow us to test and simulate physical models.

Many theoretical proposals have shown that the trapped-ion quantum simulator could help tackle difficult problems in condensed-matter physics, for instance Hubbard models [Deng 08], spin models [Jané 03, Porras 04, Deng 05, Bermudez 09, Edwards 10, Kim 11], quantum phase transitions [Retzker 08, Ivanov 09, Giorgi 10], and disordered systems [Bermudez 10]. It would also have applications in understanding other fields like Dirac particles [Lamata 07, Casanova 10, Casanova 11], cosmological models [Alsing 05, Menicucci 10], as well as nonlinear interferometry [Leibfried 02, Hu 12, Lau 12].

There have been several experimental realizations of quantum simulation with trapped ions [Blatt 12, Schneider 12]. For example, in 2008 simulation of a quantum magnet with trapped ions was demonstrated [Friedenauer 08]. In 2010 a quantum simulation of the 1-D Dirac equation using a single trapped ion was performed [Gerritsma 10], and then another counter-intuitive prediction of the Dirac equation, the Klein paradox, was observed [Gerritsma 11]. In 2011, Lanyon *et al.* demonstrated quantum simulation in a digital way with trapped ions [Lanyon 11]. A number of quantum simulations for quantum phase transitions and spin models have also been realized [Kim 09, Kim 10, Islam 11, Britton 12, Islam 13]. Recently, quasiparticle dynamics was observed in a quantum many-body system of trapped atomic ions [Jurcevic 14, Richerme 14], and the trapped ions have been used to engineer an effective system of interacting spin-1 particles [Senko 15]. These research works suggest that trapped-ion systems are powerful for quantum simulations.

Those quantum simulation schemes demonstrated have primarily been considered in closed quantum systems [Berry 07], i.e. isolated systems that cannot exchange energy with their surroundings and do not interact with other quan-

tum systems. However, in real-life situations, if we are interested in the physical properties of a quantum system, we need to deal with this system as an open quantum system which does exchange energy with its surroundings. For example, in experiments with quantum dots an open quantum system exists because a single electron spin interacts with a nuclear spin bath due to the material of the quantum dot. While quantum simulation experiments have been demonstrated with coherently controlling the dynamics of a quantum system, how to perform quantum simulation for an open-quantum system by engineering the coupling to an environment becomes an attractive research topic [Blatt 12].

For the trapped-ion system a toolbox for simulating an open quantum system has been reported in [Barreiro 11]. Usually the dynamics of an open quantum system in the Markovian regime is described by a master equation in which the dissipative dynamics of the system coupled to an environment is involved. As shown in [Barreiro 11], the trapped ion systems allow the realization of such master equations. The idea is to divide the trapped ions into "system" and "environment" ions. The ancilla ion is coupled to the vacuum modes of the radiation field through the optical pumping. Using the combination of single qubit and entangling gate operations for the ions, this provides a powerful toolbox to build a given dissipative dynamics of a master equation.

1.3 Quantum State Engineering

The preparation of nonclassical states of quantum systems is of interest because these nonclassical states cannot be described by classical physics, and their properties reveal some of the intriguing features of quantum mechanics. In the field of quantum optics, nonclassical states are usually quoted in the context of nonclassical states of light. Here we are interested in the generation and measurement of nonclassical states of ion's motion in a quantum harmonic oscillator as well as their possible applications.

The most common nonclassical states of the harmonic oscillator are probably the Fock (or called number) states, the coherent states, the squeezed states, and the Schrödinger's cat states. Their properties are widely discussed in many textbooks and literature [Gerry 05]. Especially the squeezed states and the Schrödinger's cat (SC) states expose important non-intuitive elements of quantum mechanics. The squeezed states are at the limit of the Heisenberg uncertainty principle, with one part of the state compressed to below its natural limit while the other expands to compensate. The SC states and their decay provide the closest realization to date of Schrödinger's well known thought experiment [Monroe 96, Hempel 13]. The other key quantum state is the entangled states, which are useful resources in quantum physics, quantum cryptography and quantum computation [Nielsen 00].

Experimental realizations of generation of these nonclassical states are typically done with coherently control of the system [Meekhof 96]. However, the decoherence of these states may occur, arising from the coupling between the system and the environment and imperfect control of the experiments. A dissipative way of quantum state preparation is another approach in which controlled couplings to an environment can be used to engineer the dynamics of the system to reach the steady state of the dissipative process. Theoretical work has shown the potential for using such engineered dissipation for quantum harmonic oscillator state synthesis [Cirac 93b, Poyatos 96, Carvalho 01] and for universal quantum computation [Verstraete 09]. Experimentally, these techniques have been implemented to generate entangled superposition states of qubits in atomic ensembles [Krauter 11], trapped ions [Barreiro 11, Lin 13], and superconducting circuits [Shankar 13]. Our group also experimentally demonstrated the generation of quantum harmonic oscillator states by reservoir engineering [Kienzler 15a].

1.4 Our Work

Motivated by those advantages of the trapped ion systems and the interesting problems in quantum physics mentioned above, we seek to a new possibility for experimental realization of high-fidelity quantum control of a quantum system. In our group, we plan to investigate quantum simulations of open quantum systems and perform quantum information processing using a new approach which involves two species of ion (beryllium and calcium). The advantage of using mixed-species ions is that these can be perfectly individually addressed due to the large wavelength difference between the transitions in each ion. While optical transitions in beryllium ions are at wavelengths around 313 nm, the transition wavelengths in calcium are all above 393 nm. This means that we can individually manipulate each ion species with a wide range of light fields without disturbing the internal states of the other. This has been shown to have significant advantages in quantum information processing [Jost 09, Home 09, Hanneke 09] and frequency metrology [Chou 10].

The information is encoded in the internal (electronic) states of the ion. Beryllium ($^9Be^+$) and calcium ($^{40}Ca^+$) ions are different types of qubit. The $^9Be^+$ ion is called "hyperfine qubit" where two sublevels of a ground state within the hyperfine structure are used to encode the information and the spacing of such two sublevels is in the range of gigahertz. For $^{40}Ca^+$ ions the information is stored in one of the ground and metastable states of the fine structure, where the qubit transition frequency is in the optical range. This is called an "optical qubit".

Each type of qubit has their own advantages and weakness. For the $^9Be^+$ qubit, we can find a pair of states that is insensitive to the first-order magnetic field

fluctuations, which is one of the dominant sources inducing the decoherence, so the quantum information can be preserved for a long time. If such a qubit is manipulated using two-photon Raman transitions, the coupling to the ion's motion can be varied by changing the laser beam configurations, but the fundamental limit is the spontaneous photon scattering from the excited state that the two Raman beams are coupled to. Alternatively this qubit can be controlled with microwaves [Ospelkaus 11] to avoid the use of lasers. For the $^{40}Ca^{+}$ qubit, the lifetime of the metastable state is around one second (natural linewidth in a hundred of millihertz level), which means very good laser frequency stability is needed for controlling such a qubit. Since the time scale of the gate operations and the qubit readout is much shorter than the lifetime of the the metastable state, the spontaneous emission from the metastable state can be negligible, resulting in an excellent gate and readout fidelity. However there is no magnetic-field-independent states that can be chosen so active magnetic field stabilization is helpful. Designing and building the experiments for the aforementioned research topics are extremely challenging but most of the basic techniques required have been developed in the past few years.

1.5 Thesis Layout

This thesis describes the work that has been carried out at ETH Zürich in order to perform flexible and high-fidelity control of mixed-species ion chains for quantum information science. In this thesis, quantum control of calcium and beryllium ions are described. Apart from the experimental side, theoretical studies of some properties of both ion species are also presented. We used our system to realize quantum harmonic oscillator state synthesis and create superpositions of distinct squeezed oscillator wavepackets that are entangled with a pseudo-spin encoded in the electronic states of a single calcium ion. The squeezed wavepacket entangled states are analogous to the well known Schrödinger's cat states. This is the first time that these squeezed Schrödinger's cat states are created.

Chapter 2 is a theoretical study of beryllium ions. Calculations of the energy levels of hyperfine structures, finding the first-order magnetic-field-independent qubits and derivations of the coherent quantum control via stimulated Raman transitions are shown. Qubit initialization and readout error are analyzed in detail. A brief introduction to the two-qubit quantum gates and the discussions of their error sources are given in this chapter for the long-term plan.

Chapter 3 focuses on some specific subjects of calcium ions. Most of the calcium setups and characterizations are covered in the thesis of Daniel Kienzler [Kienzler 15b]. First, generation of $^{40}Ca^{+}$ ions using the two-photon photoionization scheme is described. Due to a relatively high magnetic field we use, it makes the energy level splittings larger than the linewidth of the excited

states and thus more laser beams to control the ion efficiently are required. The simulation solving the optical Bloch equations for a multi-level atomic system is given for finding suitable laser parameters, such as the intensity and the detuning.

The ion trap and the imaging system used for mixed-species ion chains are given in Chapter 4. An overview of ion trapping principles and the segmented ion trap which is used for the work covered in the thesis are described. Designing an imaging system with near-diffraction-limit resolution is challenging for two different wavelengths. The design procedure and features of the imaging system for two species of ions are described in detail.

Chapter 5 describes the laser systems and optical setups for ionization, cooling and quantum state manipulation of beryllium ions. The wavelengths required for the lowest-energy transitions for excitation from the ground state of both the beryllium ion and the beryllium atom are in the ultraviolet region, at 313 and 235 nm respectively. The nonlinear frequency conversion techniques are employed to produce these UV wavelengths of light. The beam lines for delivering the light to the ions as well as the laser frequency stabilizations are also presented in this chapter.

Since the experimental systems are newly set up, many basic experimental techniques are used to characterize the system and the qubit. Chapter 6 shows the experimental methods and the measurement results mainly for beryllium ions in order to understand the system better. The procedure of calibration and optimization of experimental parameters is described. One of the major concerns of working with a mixed-species ion chain is that the equilibrium positions of the ions in the crystal change in the presence of additional stray fields. The influence of the stray fields on the ion in our trap must be understood well. A detailed study of compensating the stray fields is discussed using a single ion.

Although many works presented here are related to beryllium ions, several techniques are developed for calcium ions too. Chapter 7 describes the main achievement that we experimentally demonstrate spin–motion entanglement and state diagnosis with squeezed oscillator wavepackets [Lo 15]. By applying an internal-state-dependent force to a single trapped ion initialized in a squeezed vacuum state, we are able to observe the squeezed nature directly and then generate squeezed Schrödinger's cat states. The squeezed wavepacket entangled states are verified to be coherent by reversing the effect of the state-dependent force, resulting in recombination of the squeezed wavepackets, which we measure through the revival of the spin coherence. To prepare squeezed states of motion we use a newly developed technique called reservoir engineering. These methods allow us to synthesize various quantum harmonic oscillator states [Kienzler 15a].

The last chapter summaries the work and briefly describes a couple of probable experiments that can be performed using the system constructed.

Chapter 2

The $^9Be^+$ Qubit

The ion species we use in our experiments are beryllium and calcium. The discussions of the calcium ion will be given in Chapter 3. Beryllium ions have previously been using for experiments of quantum computation [Leibfried 03b], quantum state engineering [Meekhof 96], robust quantum memory [Langer 05], quantum logic spectroscopy [Schmidt 05], precise spectroscopy [Wineland 83], and quantum simulations [Britton 12]. In this chapter, I first describe the relevant atomic structure of $^9Be^+$. Since we use two hyperfine ground states to store and manipulate quantum states, I show how to theoretically obtain a pair of levels whose frequency separation has zero first-order dependence on the magnetic field for which the fluctuation is one of the principal problems in the laboratory. I then describe how we initialize the system to a well defined state and how we read out the final state after the quantum manipulations. A detailed analysis of measurement error is given. I explain the stimulated Raman transitions which we use to do the coherent control of the beryllium ion, and the basics of quantum gate operations. Finally, I discuss the errors in quantum gates due to off-resonant spontaneous photon scattering.

2.1 Atomic Structure

Beryllium ions have similar electrical structures to alkali neutral atoms, with a single valence electron. The $^9Be^+$ ion is the lightest ion species which is commonly trapped with an advantage of strong confinement in the trap, resulting in high oscillation frequencies. The energy level diagram is shown in Fig. 2.1. The fine structure is a result of the coupling between the orbital angular momentum $\mathbf{L}$ of the outer electron and its spin angular momentum $\mathbf{S}$. The total electron angular momentum is then given by $\mathbf{J} = \mathbf{L} + \mathbf{S}$, and the magnitude of $\mathbf{J}$ must lie in the range $|L - S| \leq J \leq L + S$. For the ground state, $L = 0$ and $S = 1/2$, so $J = 1/2$ and it has no fine structure. For the first excited state (P state), $L = 1$ and $S = 1/2$, so $J = 1/2$ or $J = 3/2$. Since the

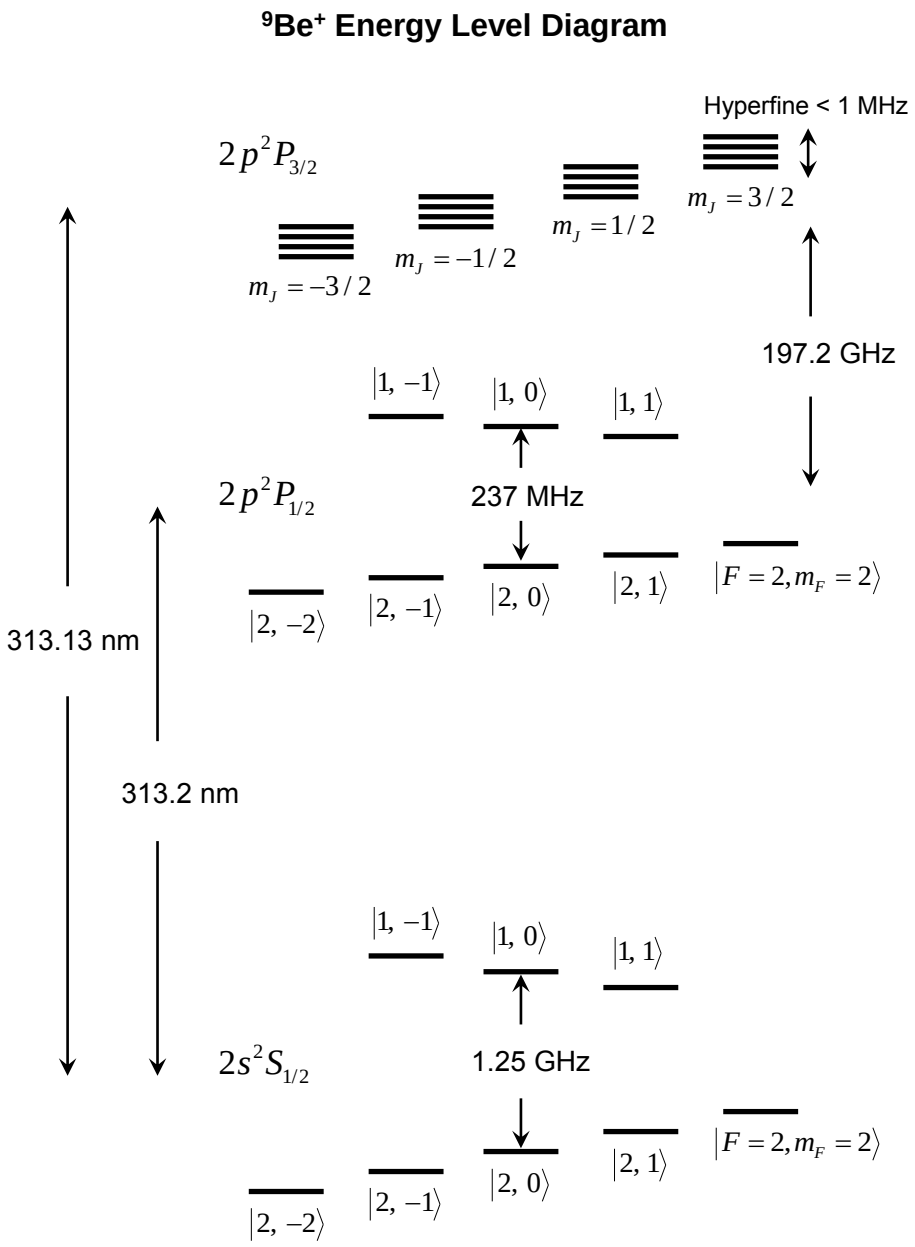

Figure 2.1: The energy level diagram of $^9Be^+$ ions. The frequency splitting between $P_{1/2}$ and $P_{3/2}$ states is 197.2 GHz. The hyperfine splittings in $S_{1/2}$, $P_{1/2}$ and $P_{3/2}$ are 1.25 GHz, 237 and < 1 MHz respectively. The wavelengths required to drive $S \leftrightarrow P$ transitions are all in the vicinity of 313 nm. In the later chapter we will describe how to generate these ultra-violet wavelengths by using nonlinear optics techniques.

energy of any particular level is shifted according to the value of J, the excited P state is split into two components, $2p\ ^2P_{1/2}$ and $2p\ ^2P_{3/2}$, with a splitting of 197.2 GHz [Bollinger 85]. The $2s\ ^2S_{1/2} \leftrightarrow 2p\ ^2P_{1/2}$ and $2s\ ^2S_{1/2} \leftrightarrow 2p\ ^2P_{3/2}$ transitions are the components of a fine-structure doublet, and can be driven via electric dipole radiation in the vicinity of 313 nm. The excited state has a lifetime of 8.2 ns, corresponding to a natural linewidth $\gamma = 2\pi \times 19.4$ MHz. In spectroscopic notation, these states ($2s\ ^2S_{1/2}$, $2p\ ^2P_{1/2}$ and $2p\ ^2P_{3/2}$) will be labeled as $S_{1/2}$, $P_{1/2}$ and $P_{3/2}$ for simplicity.

The nuclear spin of the $^9Be^+$ ion is $I = 3/2$ and thus it possesses hyperfine structure, which is a result of the coupling of $\mathbf{J}$ with the nuclear angular momentum $\mathbf{I}$. This interaction leads to a splitting of the levels into states with a total angular momentum given by $\mathbf{F} = \mathbf{J} + \mathbf{I}$. In the $S_{1/2}$ state, the hyperfine splitting is 1.25 GHz [Wineland 83]; the hyperfine splittings in the excited $P_{1/2}$ state and $P_{3/2}$ state are 237 MHz [Bollinger 85] and less than 1 MHz respectively [Poulsen 75]. Each hyperfine manifold, for example $F = 1$ manifold in $S_{1/2}$ state, is degenerate at zero magnetic field. In the presence of magnetic fields, this degeneracy is broken by the Zeeman effect. For quantum control, we use two Zeeman states in the $S_{1/2}$ state as the quantum bit (qubit). In principle, we can choose any pair of levels for the qubit, but certain pairs are better for the quantum information processing than others since they have much longer coherence time. These will be discussed in Chapter 2.2.

2.2 Hyperfine Structure and Field-Independent Qubits

The hyperfine structure is a result of the coupling of $\mathbf{J}$ with the total nuclear angular momentum $\mathbf{I}$. The Hamiltonian that describes the total system, including hyperfine interaction and the atomic interaction with the magnetic field, is

$$\begin{aligned} H_{\text{tot}} &= H_{\text{hfs}} + H_B \\ H_{\text{hfs}} &= hA_{\text{hfs}}\mathbf{I}\cdot\mathbf{J} \\ H_B &= \mu_B(g_S\mathbf{S} + g_L\mathbf{L} + g_I\mathbf{I})\cdot\mathbf{B}. \end{aligned} \tag{2.1}$$

For H_{hfs}, h is the Planck's constant, and A_{hfs} is called the hyperfine constant and has an unit of frequency. The operators $\mathbf{I}$ and $\mathbf{J}$ are dimensionless. In our discussions if we take the magnetic field to be along the z-direction, which is considered to be along the atomic quantization axis, H_B can be written as

$$H_B = \mu_B(g_S S_z + g_L L_z + g_I I_z)B_z \tag{2.2}$$

where μ_B is the Bohr magneton, and the quantities g_S, g_L, and g_I are the electron spin, electron orbital and nuclear g-factors, respectively. If the energy shift due to the magnetic field is small compared to the fine-structure splitting,

then J is a good quantum number and Eq. (2.2) becomes

$$H_B = \mu_B(g_J J_z + g_I I_z)B_z$$

Here, the Landé factor g_J is given by

$$g_J = g_L \frac{J(J+1) - S(S+1) + L(L+1)}{2J(J+1)} + g_S \frac{J(J+1) + S(S+1) - L(L+1)}{2J(J+1)} \tag{2.3}$$

The H_{hfs} term described above only considers the interaction of the nuclear and electron magnetic dipoles. In general, the interaction between the nuclear and electron angular momenta can be expanded in a multipole series so the higher-order corrections become quite involved, for example, the electric quadrupole interaction, magnetic octupole interaction, etc [Woodgate 80]. These interactions cause a shift of the hyperfine structure levels. In our case, to more accurately determine the energy levels of $P_{3/2}$ state we take the electric-quadrupole term into account. We should notice that this electric-quadrupole interaction is only applicable for the states with $I, J > 1/2$. Combining two terms, the Hamiltonian for the hyperfine structure is

$$\begin{aligned} H_{\text{hfs}} &= hA_{\text{hfs}}\mathbf{I}\cdot\mathbf{J} \\ &\quad + hB_{\text{hfs}} \frac{3(\mathbf{I}\cdot\mathbf{J})^2 + \frac{3}{2}(\mathbf{I}\cdot\mathbf{J}) - I(I+1)J(J+1)}{2I(2I-1)J(2J-1)} \end{aligned} \tag{2.4}$$

where B_{hfs} is is the electric-quadrupole hyperfine constant.

Now we can compute the expectation values for the given total Hamiltonian $H_{\text{tot}} = H_{\text{hfs}} + H_B$ to obtain the energy levels as a function of applied magnetic fields. When the Zeeman interaction is small compared to the hyperfine interaction, the total angular momentum $F = I + J$ and m_F, which is the projection of F on z-axis, are good quantum numbers to use because the Zeeman interaction here is treated as a perturbation. In the opposite case where the magnetic field is very strong such that the Zeeman interaction dominates, the eigenstates are well described by the $|I, m_I; J, m_J\rangle$ basis (we will use $|m_I, m_J\rangle$ for simplicity). However, for intermediate fields, where the Zeeman interaction neither perturbs nor dominates the hyperfine interaction, the system is in general difficult to calculate analytically. In general one must numerically diagonalize the Hamiltonian H_{tot}. There is an exception coming about in hyperfine structure when $J = 1/2$ (e.g. $S_{1/2}$ and $P_{1/2}$ states). In this case, the hyperfine Hamiltonian (Eq. (2.4)) is given only by the magnetic-dipole term and the energy levels can be solved analytically, which is so-called the Breit-Rabi formula [Woodgate 80]. I will focus on how to calculate the energy levels by diagonalizing the Hamiltonian so here I skip the detailed derivations

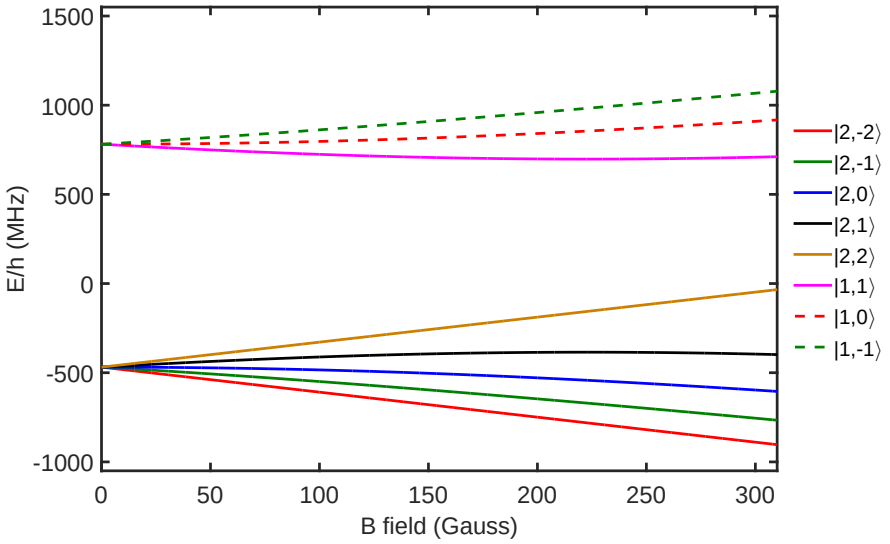

Figure 2.2: $^9Be^+$ $S_{1/2}$ (ground) state hyperfine structure in an external magnetic field. The parameters used in the calculation are $A_{\rm hfs} = -625.008837048$ MHz, $g_L = 1$, $g_S = 2.0023193043622$, g_J obtained from Eq. (2.3), $g_I = g_J \times 2.134779853 \times 10^{-4}$, $\mu_B = 9.27400968 \times 10^{-24}$ J/Tesla [Yerokhin 08, Puchalski 09].

of the Breit-Rabi formula and only show the result [Woodgate 80]:

$$\begin{aligned} E_{|F,m_F\rangle} &= -\frac{\Delta E_{\rm hfs}}{2(2I+1)} + g_I \mu_B m_F B \\ &\quad \pm \frac{\Delta E_{\rm hfs}}{2}\left(1 + \frac{4m_F x}{2I+1} + x^2\right)^{1/2} \end{aligned} \tag{2.5}$$

where $\Delta E_{\rm hfs} = A_{\rm hfs}\left(I + \frac{1}{2}\right)$ and $x = \frac{\mu_B(g_J - g_I)B}{\Delta E_{\rm hfs}}$. For the beryllium ions, the minus sign applies to the $F = 1$ manifold, the plus sign applied to $F = 2$ manifold, and $A_{\rm hfs}$ can be found in [Yerokhin 08, Puchalski 09]. To avoid the discontinuity in evaluating Eq. (2.5) the more direct formula

$$E_{|F,m_F\rangle} = -\frac{\Delta E_{\rm hfs}}{2(2I+1)} + g_I \mu_B m_F B + \frac{\Delta E_{\rm hfs}}{2}(1+x)$$

is used for the state $m_F = (I + 1/2)$. The physical picture behind the Breit-Rabi formula for quantum information processing is that it allows us to identify a pair of levels where the differential energy shift with respect to magnetic field vanishes to the first order. The main advantage of using such a transition as a qubit is that any small fluctuation in magnetic field does not influence the qubit frequency to the first order such that the qubit which stores the quantum information has a relatively long coherence time [Langer 05].

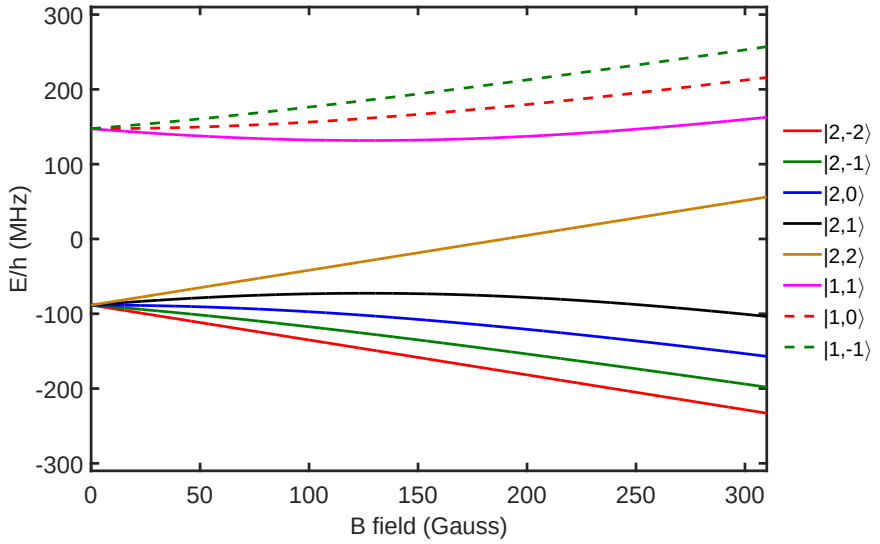

Figure 2.3: $^9Be^+$ $P_{1/2}$ (excited) state hyperfine structure in an external magnetic field. The hyperfine constant $A_{\rm hfs}$ used in the calculation is -117.919 MHz [Yerokhin 08, Puchalski 09] and the rest are the same as for Fig. 2.2.

As mentioned above, the general way of calculating the energy levels of hyperfine states is to numerically diagonalize the total Hamiltonian. In order to do that, one needs to calculate the matrix elements for given computational basis. For convenience, here we only show the matrix elements using the Hamiltonian in Eq. (2.1) for $S_{1/2}$ and $P_{1/2}$ states, and the matrix elements for the electric-quadrupole interaction for the $P_{3/2}$ state are given in Appendix A. Recalling the basic relations in quantum mechanics, we have

$$\begin{aligned}\mathbf{I}\cdot\mathbf{J} &= I_zJ_z + I_xJ_x + I_yJ_y \\ &= I_zJ_z + \frac{I_+J_- + I_-J_+}{2}\end{aligned}$$

If now we choose the strong-field basis, the diagonal matrix elements are

$$\langle m_I, m_J|H_{\rm tot}|m_I, m_J\rangle = hA_{\rm hfs}m_Im_J + \mu_B(g_Jm_J + g_Im_I)B$$

and also the off-diagonal matrix elements are

$$\begin{aligned}&\langle m_I+1, m_J-1|H_{\rm tot}|m_I, m_J\rangle = \\ &\frac{hA_{\rm hfs}}{2}\sqrt{(J-m_J+1)(J+m_J)(I+m_I+1)(I-m_I)} \\ &\langle m_I-1, m_J+1|H_{\rm tot}|m_I, m_J\rangle = \\ &\frac{hA_{\rm hfs}}{2}\sqrt{(J+m_J+1)(J-m_J)(I-m_I+1)(I+m_I)}\end{aligned}$$

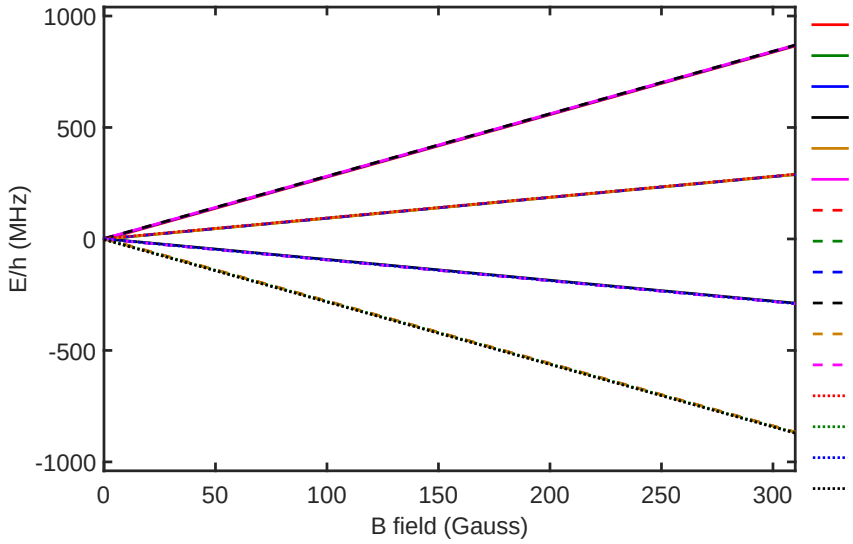

Figure 2.4: $^9Be^+$ $P_{3/2}$ (excited) state hyperfine structure in an external magnetic field. The hyperfine splitting is already small in the low-field regime so it is not obvious that the levels are grouped according to the value of F, but they are grouped according to m_J (from top to bottom: $m_J = 3/2$, $1/2$, -1/2 and -3/2) as the magnetic field increases. The parameters used in the calculation are $A_{\rm hfs} = -1.015$ MHz and $B_{\rm hfs} = -2.299$ MHz [Yerokhin 08, Puchalski 09].

Using the eigenvalue solver in numerical software, we can easily obtain the energy levels of hyperfine states in the presence of applied magnetic fields.

The energy levels for $S_{1/2}$, $P_{1/2}$ and $P_{3/2}$ states as a function of magnetic fields are shown in Figs. 2.2, 2.3, and 2.4 respectively, ranging from the weak-field (Zeeman) regime through the strong-field regime. Although these spectrum are numerically solved by diagonalizing the Hamiltonian, for the states with $J = 1/2$ the Breit-Rabi formula can be applied and produce the same results as well. However, it does not apply to the $P_{3/2}$ state in which the level structure is more complicated.

To determine which transition in $S_{1/2}$ state is more desirable to use to perform quantum information processing experiments, we differentiate each energy level in Fig. 2.2 with respect to the B-field. Figure 2.5 shows the results. The first crossing point (at non-zero field) occurs at 119.4428 Gauss (G) for the $|S_{1/2}, F = 2, m_F = 0\rangle \leftrightarrow |S_{1/2}, F = 1, m_F = 1\rangle$ transition and the second crossing is at 119.6390 G for the $|S_{1/2}, F = 2, m_F = 1\rangle \leftrightarrow |S_{1/2}, F = 1, m_F = 0\rangle$ transition, showing these transitions are field-independent to the first order. The Ion Storage Group at NIST has demonstrated the qubit coherence time up to 15 seconds [Langer 05] using a field-independent transition. The magnetic field we use in our group is around 119.45 G.

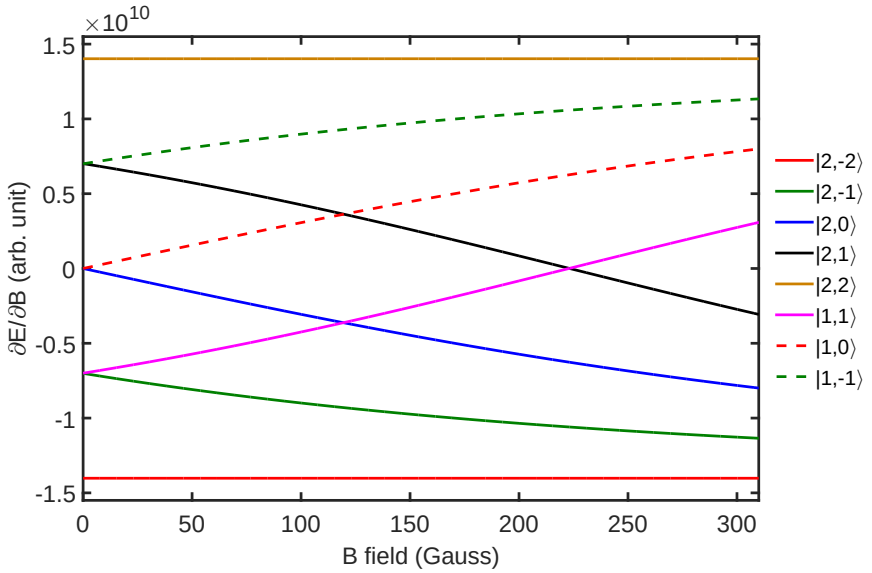

Figure 2.5: Differential of energy $\partial E/\partial B$ versus B for the $S_{1/2}$ ground state of $^9Be^+$ ions. Each crossing point is a first-order field-independent transition that occurs when $\partial E/\partial B$ is equal for both states. In our experiment, we can use the first and the second field-independent transitions as the qubit states.

Here we define the bright state as $|b\rangle \equiv \left|S_{1/2}, F = 2, m_F = 2\right\rangle$, which is coupled to the state $\left|P_{3/2}, F' = 3, m'_F = 3\right\rangle$ and used for the qubit readout (see Chapter 2.4), and encode the two-level field-independent qubit (FIQ) as $|\uparrow\rangle \equiv \left|S_{1/2}, F = 1, m_F = 1\right\rangle$ and $|\downarrow\rangle \equiv \left|S_{1/2}, F = 2, m_F = 0\right\rangle$. If we work with a standard field-dependent qubit (FDQ), those states are chosen as $|\uparrow\rangle \equiv \left|S_{1/2}, F = 1, m_F = 1\right\rangle$ and $|b\rangle = |\downarrow\rangle \equiv \left|S_{1/2}, F = 2, m_F = 2\right\rangle$ (see Fig. 2.6). More experimental characterizations will be discussed in Chapter 6.

2.3 Qubit Initialization

In 2000, David DiVincenzo summarized five requirements that any candidate quantum computer implementation must satisfy and two additional criteria for quantum communication [DiVincenzo 00]. These are called DiVincenzo criteria. From previous discussions about the $^9Be^+$ qubit transition, we have satisfied the first DiVincenzo criteria, a scalable physical system with well characterized qubits. I will introduce how we meet the second criteria, the ability to initialize the state of the qubits to a well-defined state. We carry out this via optical pumping process. In the experiment, we use circularly polarized $\hat{\sigma}^+$ laser light propagating along the direction of the magnetic field since this is the only way of producing a purely $\hat{\sigma}^+$ light. The $\hat{\sigma}^+$ laser light optically pumps the internal state of the ion into $|F = 2, m_F = 2\rangle$ state

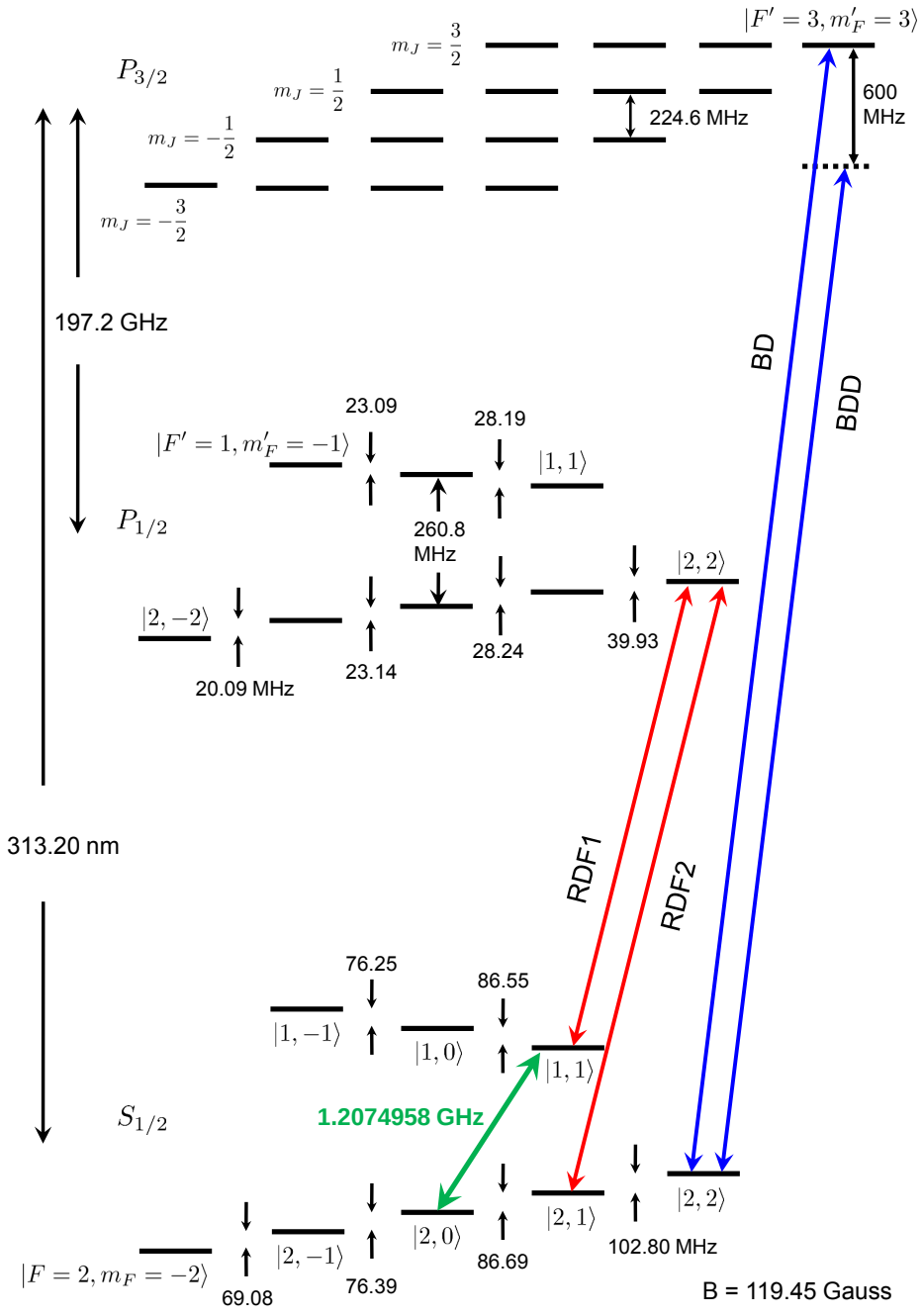

Figure 2.6: The energy splittings of $^9Be^+$ ions at $B = 119.45$ Gauss and the required laser beams for cooling, detection and repumping. The bright state used for qubit readout is $|S_{1/2}, F = 2, m_F = 2\rangle$. At this magnetic field the frequency splitting of the two-level field-independent qubit (FIQ) is 1.2074958 GHz.

in the $S_{1/2}$ ground state. The implementation consists of four laser beams overlapped in space with different frequencies at 313 nm. As shown in Fig. 2.6, they are 1) The near-resonant "Blue Doppler" (BD) beam red detuned $\gamma/2$ ($\gamma = 2\pi \times 19.4$ MHz, the natural linewidth of the excited state as mentioned in Chapter 2.1) from the $|S_{1/2}, F = 2, m_F = 2\rangle \leftrightarrow |P_{3/2}, F' = 3, m'_F = 3\rangle$ cycling transition. 2) The "BD Detuned" (BDD) beam tuned 600 MHz to the red of the cycling transition. 3) The "Red Doppler F1" (RDF1) beam tuned slightly red of $|S_{1/2}, F = 1, m_F = 1\rangle \leftrightarrow |P_{1/2}, F' = 2, m'_F = 2\rangle$, which pumps the population out of $F = 1$ manifold into $|S_{1/2}, F = 2, m_F = 2\rangle$ state. 4) The "Red Doppler F2" (RDF2) beam tuned slightly red or on resonance of $|S_{1/2}, F = 2, m_F = 1\rangle \leftrightarrow |P_{1/2}, F' = 2, m'_F = 2\rangle$, which serves as repumping for the population not in $|S_{1/2}, F = 2, m_F = 2\rangle$ state.

The BDD beam is responsible for pre-cooling very hot ions while loading or after collisions with thermal background gas. Because this beam is far detuned from resonance, it requires higher power than others in order to broaden the transition. The parameters used in our experiments are the laser power of approximately few hundreds μW in ≈ 60 μm beam waist and the pulse length of 3.5 ms. We found that if the laser power of this beam is too high, the line shape of the transition becomes too broad such that the cooling efficiency would be decreased and the ions can not be crystalized. The BD beam serves the Doppler cooling after the pre-cooling stage. Typically the time of Doppler cooling is around 700 μs in our case. The intensity of the Doppler beam is set to slightly below half of the saturation intensity (≈ 2.5 μW in 60 μm waist in our case). The saturation intensity is about 0.76 mW/mm^2 for $^9Be^+$ ion. The RDF1 and RDF2 beams assist optical pumping for $F = 1$ and $F = 2$ manifolds when performing the resolved sideband cooling (see Chapter 6.4). The duration used for the optical pumping is around 5 μs with a certain optical power (see Chapter 6.3). It is worth noting that the high power BDD beam is also sufficient for optically pumping the $F = 1$ manifold even though it is ≈ 400 MHz off-resonant from $|S_{1/2}, F = 1\rangle \leftrightarrow |P_{3/2}, m_J = 3/2\rangle$ transitions. During the loading process, we could only use BD and BDD beams without RDF1 and RDF2 beams.

After the ion has been prepared in $|S_{1/2}, F = 2, m_F = 2\rangle$ state, there are two ways of preparing the ion in $|S_{1/2}, F = 1, m_F = 1\rangle$ state for driving the field-independent transition. First, we can apply a π-pulse directly on the $|S_{1/2}, F = 2, m_F = 2\rangle \leftrightarrow |S_{1/2}, F = 1, m_F = 1\rangle$ transition. Or we could use a combination of RDF2 beam with a Raman pulse that drives $|S_{1/2}, F = 2, m_F = 2\rangle \leftrightarrow |S_{1/2}, F = 2, m_F = 1\rangle$ transition such that the ion can be dissipatively pumped in $|S_{1/2}, F = 1, m_F = 1\rangle$ state.

For some experiments in which the ion needs to be cooled close to the motional ground state for the qubit initialization [Cirac 95, Meekhof 96], Raman sideband cooling is used. It is performed on $|S_{1/2}, F = 2, m_F = 2\rangle \leftrightarrow |S_{1/2}, F =$

$1, m_F = 1\rangle$ transition at 1017.9946 MHz, followed by a final repumping process to prepare the ion in $|S_{1/2}, F = 2, m_F = 2\rangle$ state. Sideband cooling technique can provide the ion in the motional ground state with > 99 % fidelity [Wineland 98]. The experimental results are given in Chapter 6.4.

The infidelity of the ion's internal state initialization (here we are interested in $|S_{1/2}, F = 2, m_F = 2\rangle$ state preparation) arises from the impurity of polarization of the RDF1 and RDF2 beams because this optical pumping is the final stage prior to any quantum operation. It is worth studying the preparation error given some impurity in the polarization. We consider the optical pumping rate out of $|S_{1/2}, F = 2, m_F = 2\rangle$ state due to the impure polarization in RDF2. The frequency of this beam is closest to the resonance of $|S_{1/2}, F = 2, m_F = 2\rangle \leftrightarrow |P_{1/2}\rangle$ transition so it can easily pump the population away from $|S_{1/2}, F = 2, m_F = 2\rangle$ state with non-$\hat{\sigma}^+$ light.

In the following analysis we assume that RDF2 beam has a small amount of $\hat{\sigma}^-$ and $\hat{\pi}$ polarization components. The optical pumping rate from the initial state i to the final state f through a single excited state is

$$\Gamma_{i\to f} = \frac{\gamma}{2}\frac{s_0}{1 + s_0 + 4\delta^2/\gamma^2} c_{i\to f} \tag{2.6}$$

where γ is the natural linewidth, δ is the laser detuning from the excited state, and $c_{i\to j}$ is the coupling coefficient between states i and j, which can be calculated from the coefficients of eigenvector when solving the eigenvalue problem of Eq. (2.1). $s_0 = I/I_{\text{sat}}$ is the saturation parameter, where I is the intensity of the laser beam and $I_{\text{sat}} = \frac{\hbar\omega^3\gamma}{12\pi c^2}$ is the saturation intensity for which ω is 2π times the transition frequency and c is the speed of light. For an ion in $|S_{1/2}, F = 2, m_F = 2\rangle$, it can be excited to $|P_{1/2}, F' = 2, m'_F = 2\rangle$ state by absorbing $\hat{\pi}$ polarized light. Then it will emit $\hat{\sigma}^+$ photons and decay to either $|S_{1/2}, F = 2, m_F = 1\rangle$ or $|S_{1/2}, F = 1, m_F = 1\rangle$ state. The total coupling coefficient for this scattering event is $\sum_j c_{i\to j} = 2/9$, which is the sum over a product of the transition probabilities. The total coupling coefficient for the scattering through $|P_{1/2}, F' = 2, m'_F = 1\rangle$ state driven by $\hat{\sigma}^-$ polarized light is also 2/9. Both coupling coefficients are independent of the magnetic field. The optical pumping from $|S_{1/2}, F = 2, m_F = 1\rangle$ to $|S_{1/2}, F = 2, m_F = 2\rangle$ state has a coupling coefficient of $\sim 1/18$. Given an admixture of both $\hat{\pi}$ and $\hat{\sigma}^-$ polarizations in the RDF2 beam, denoted with ϵ_π and ϵ_{σ^-}, the optical pumping rates from Eq. (2.6) are

$$\begin{aligned}
\Gamma_{\sigma^-} &= \frac{\gamma}{2}\frac{\epsilon_{\sigma^-} s_0}{1 + s_0 + 4\delta^2_{\sigma^-}/\gamma^2}\frac{2}{9} \\
\Gamma_{\pi} &= \frac{\gamma}{2}\frac{\epsilon_{\pi} s_0}{1 + s_0 + 4\delta^2_{\pi}/\gamma^2}\frac{2}{9}
\end{aligned}$$

The optical pumping rate with an ideal RDF2 beam ($\delta = 0$) is

$$\Gamma_{\sigma^+} = \frac{\gamma}{2}\frac{s_0}{1 + s_0}\frac{1}{18}$$

Here we ignore the RDF2 beam acting on $|S_{1/2}, F = 1, m_F = 1\rangle \leftrightarrow |P_{1/2}\rangle$ transition due to far off-resonance. Therefore the error in initialization (steady state) can be evaluated as follows:

$$\begin{aligned} e_{\text{init}} &= \frac{\Gamma_\pi}{\Gamma_{\sigma^+}} + \frac{\Gamma_{\sigma^-}}{\Gamma_{\sigma^+}} \\ &= \frac{4(1+s_0)\epsilon_\pi}{1+s_0+4\delta_\pi^2/\gamma^2} + \frac{4(1+s_0)\epsilon_{\sigma^-}}{1+s_0+4\delta_{\sigma^-}^2/\gamma^2} \end{aligned}$$

For the $^9Be^+$ ion working on the field-independent qubit at $B = 119.45$ G, $\delta_\pi = 2\pi \times 102.8$ MHz and $\delta_{\sigma^-} = 2\pi \times 142.7$ MHz. Assuming $\epsilon_{\sigma^-} = \epsilon_\pi = 0.1\%$ and the saturation parameter $s_0 = 1$, the error in initialization is $e_{\text{init}} \approx 7.6 \times 10^{-5}$. The more general method to determine the initialization error is to solve the rate equation for all allowed transitions.

2.4 Qubit Readout

For trapped-ion experiments qubit read-out is performed by state-dependent fluorescence, which measures the projection of the state vector along a given axis. This technique was proposed by Dehmelt *et al.* [Dehmelt 75] and first demonstrated by Wineland *et al.* [Wineland 80]. It utilizes a closed transition or so-called a cycling transition in the internal states of the ion. When exciting a cycling transition, the ion behaves like a two-level system. Performing this kind of projective measurement collapses the ion's wavefunction in either one of its computational basis states. If one of the computational basis states is involved in the cycling transition, many photons can scatter without leaving the transition and the fluorescence can be collected. In the opposite situation, if the ion's wavefunction collapses to the basis state that does not participate in the cycling transition, only the background photons will be measured. For the $^9Be^+$ ion, we use the BD beam, which has been mentioned in Chapter 2.3, as the detection beam, but its frequency is tuned to be on resonance of the $|S_{1/2}, F = 2, m_F = 2\rangle \leftrightarrow |P_{3/2}, F' = 3, m'_F = 3\rangle$ or alternatively $|P_{3/2}, m_I = 3/2, m_J = 3/2\rangle$ cycling transition.

2.4.1 Readout Error - Dark to Bright State Leakage

The main source of the read-out error is the leakage of the qubits initially in the dark state into the closed transition by off-resonantly coupling to other excited states (other than the one in the closed transition) during measurement. When this happens, the ion in dark state has a possibility entering the closed transition and then starts scattering at a high rate. For a multi-level atomic system like $^9Be^+$ ions, the general treatment is to solve a rate equation for all allowed scattering paths such that the time evolution of the probability of the ion to be in any state can be calculated. The other advantage of the rate-equation treatment is that we are able to investigate how to improve dark to

bright state leakage by transferring the dark ion to the other hyperfine state which is even "darker".

The population in each hyperfine ground state is represented by a vector $\mathbf{v}$. For the $^9Be^+$ ion, its length is 8. We define the rate matrix $\mathbf{\Gamma}^{\sigma^+}$ in which the matrix elements $\Gamma^{\sigma^+}_{i,j}$ are the photon scattering rates from state $|j\rangle$ to state $|i\rangle$ and σ^+ in the superscript means that we assume the polarization of the detection beam is purely σ^+. These non-zero matrix elements $\Gamma^{\sigma^+}_{i,j}$ can be calculated using the Kramers-Heisenberg formula [Ozeri 05, Loudon 95]:

$$\Gamma^{\sigma^+}_{i,j} = \frac{g^2}{4}\gamma\left|\sum_m \frac{a^{(m)}_{i,j}}{\Delta_m}\right|^2 \tag{2.7}$$

where $g = \frac{E\mu}{\hbar} = \gamma\sqrt{\frac{s_0}{2}}$ is the single-photon Rabi frequency (E is the electric field amplitude of the laser beam, and $\mu = |\langle P_{3/2}, F' = 3, m'_F = 3|\mathbf{d}\cdot\hat{\sigma}^+ |S_{1/2}, F = 2, m_F = 2\rangle|$ is the magnitude of the cycling transition electric-dipole moment.), the coefficient $a^{(m)}_{i,j} = \sum_q \langle i|\mathbf{d}\cdot\hat{\sigma}^q|e_m\rangle\langle e_m|\mathbf{d}\cdot\hat{\sigma}^+|j\rangle/\mu^2$ is the normalized transition strength from state $|j\rangle$ to state $|i\rangle$ through an intermediate state $|e_m\rangle$ and here we sum over different polarizations q of the emitted light, Δ_m is the detuning of the detection beam from the $|j\rangle \leftrightarrow |e_m\rangle$ transition. We sum over m for all the excited states $|e_m\rangle$ in the $P_{3/2}$ state. The $P_{1/2}$ excited states are ignored in this case because they are ≈ 197 GHz away from the frequency of the detection beam. When Δ_m is comparable to half of the power broadened linewidth, Eq. (2.7) breaks down and we have to include an imaginary damping term, $i\gamma/2$, in the detuning [Loudon 95]. By adding this damping term to the detuning, the Kramers-Heisenberg formula reproduces the well-known total photon scattering rate in Eq. (2.6) for a two-level atom.

The time-dependent population transfer of each state is given by

$$\frac{\partial v_i}{\partial t} = \sum_j \Gamma^{\sigma^+}_{i,j} v_j - v_i \sum_j \Gamma^{\sigma^+}_{j,i} \tag{2.8}$$

that can be written as a matrix form:

$$\frac{\partial \mathbf{v}}{\partial t} = \mathbf{M}^{\sigma^+}\cdot\mathbf{v} \tag{2.9}$$

where $\mathbf{M}^{\sigma^+} = \mathbf{\Gamma}^{\sigma^+} - \mathbf{D}(\mathbf{1}^{\mathbf{T}}\cdot\mathbf{\Gamma}^{\sigma^+})$, $\mathbf{1}$ is a 8-by-1 matrix of ones, and $\mathbf{D}(\mathbf{x})$ is a diagonal matrix with $\mathbf{x}$ in the diagonal elements. First, we solve Eq. (2.9) using the Laplace transform approach. After taking the Laplace transform, it yields

$$s\mathbf{V}(s) - \mathbf{v}(0) = \mathbf{M}^{\sigma^+}\cdot\mathbf{V}(s) \tag{2.10}$$

where $\mathbf{V}(s)$ is the Laplace transform of $\mathbf{v}(t)$, $\mathbf{v}(0)$ is the initial condition, and s is the Laplace transform variable. Therefore, the solution can be easily obtained

$$\mathbf{V}(s) = -(\mathbf{M}^{\sigma^+} - s\mathbb{1})^{-1}\mathbf{v}(0) \tag{2.11}$$

where $\mathbb{1}$ is the identity matrix. For the given initial condition $\mathbf{v}(0)$, the time-domain solution $\mathbf{v}(t)$ can be calculated by taking the inverse Laplace transform of $\mathbf{V}(s)$. In the following, we show how to solve $\mathbf{v}(t)$.

We know from the control theory the term $-(\mathbf{M}^{\sigma^+} - s\mathbb{1})^{-1}$ represents a transfer function. The poles of the transfer function are the characteristic frequencies of the system. Here we write a single term as a sum of partial fractions:

$$\begin{aligned}\left[(\mathbf{M}^{\sigma^+} - s\mathbb{1})^{-1}\right]_{i,j} &= \frac{p_{i,j}(s)}{q(s)} \\ &= \sum_k \frac{b_{i,j}^{(k)}}{s+\omega_k} \end{aligned} \tag{2.12}$$

where $q(s) = \prod_k (s+\omega_k)$ is the characteristic polynomial with roots $-\omega_k$ (the characteristic frequency), $p_{i,j}(s)$ is a polynomial in s, and

$$\begin{aligned} b_{i,j}^{(k)} &= \lim_{s\to-\omega_k} \frac{(s+\omega_k)p_{i,j}(s)}{q(s)} \\ &= \frac{p_{i,j}(\omega_k)}{\prod_{l\neq k}(\omega_l - \omega_k)} \end{aligned} \tag{2.13}$$

are constants assuming $q(s)$ has no double roots that is the case for our detection system. Therefore, the time-domain solution is given by:

$$v_{i,j}(t) = \sum_{k=1}^{8} b_{i,j}^{(k)} e^{-\omega_k t} \tag{2.14}$$

These are rate equation solutions for the time-dependent populations of each state. We are concerned with the probability of detecting the ion in the $|F=2, m_F=2\rangle$ state at time t with the ion initially in other hyperfine states $|j\rangle$ at $t=0$. It is given by

$$P_{d\to b}(t) = v_{i=(2,2),j}(t) = \sum_{k=1}^{8} b_{i=(2,2),j}^{(k)} e^{-\omega_k t}. \tag{2.15}$$

A more general case would be including the polarization impurities in the detection beam. Ideally the polarization of the detection beam is purely σ^+, but it might have ϵ_{σ^-} admixture of $\hat{\sigma}^-$ polarization and ϵ_π admixture of $\hat{\pi}$ polarization. We define new rate matrices $\mathbf{\Gamma}^{\sigma^-}$ and $\mathbf{\Gamma}^{\pi}$ for $\hat{\sigma}^-$ and $\hat{\pi}$ polarization components respectively. Their matrix element and corresponding matrix $\mathbf{M}$ ($\mathbf{M}^{\pi}$ and $\mathbf{M}^{\sigma^-}$) are given by

$$\begin{aligned} \Gamma_{i,j}^{\sigma^-} &= \frac{g^2}{4}\gamma\left|\sum_m \frac{c_{i,j}^{(m)}}{\Delta_m}\right|^2, \quad \Gamma_{i,j}^{\pi} = \frac{g^2}{4}\gamma\left|\sum_m \frac{d_{i,j}^{(m)}}{\Delta_m}\right|^2 \\ \mathbf{M}^{\sigma^-} &= \mathbf{\Gamma}^{\sigma^-} - \mathbf{D}(\mathbf{1}^{\mathbf{T}}\cdot\mathbf{\Gamma}^{\sigma^-}), \quad \mathbf{M}^{\pi} = \mathbf{\Gamma}^{\pi} - \mathbf{D}(\mathbf{1}^{\mathbf{T}}\cdot\mathbf{\Gamma}^{\pi}) \end{aligned}$$

where $c_{i,j}^{(m)} = \sum_q \langle i|\mathbf{d}\cdot\hat{\sigma}^q|e_m\rangle\langle e_m|\mathbf{d}\cdot\hat{\sigma}^-|j\rangle/\mu^2$ and $d_{i,j}^{(m)} = \sum_q \langle i|\mathbf{d}\cdot\hat{\sigma}^q|e_m\rangle\langle e_m|\mathbf{d}\cdot\hat{\pi}|j\rangle/\mu^2$. Because we solve a differential equation with the same form as Eq. (2.9), we have to find a new matrix $\mathbf{M}$, which now is the sum over all the polarization components and can be defined as

$$\mathbf{M} = \frac{1}{(1-\epsilon_{\sigma^-}-\epsilon_\pi)^2+\epsilon_{\sigma^-}^2+\epsilon_\pi^2}\left[(1-\epsilon_{\sigma^-}-\epsilon_\pi)^2\mathbf{M}^{\sigma^+}+\epsilon_{\sigma^-}^2\mathbf{M}^{\sigma^-}+\epsilon_\pi^2\mathbf{M}^{\pi}\right] \tag{2.16}$$

Following the same procedures described above to solve $\frac{\partial \mathbf{v}}{\partial t} = \mathbf{M}\cdot\mathbf{v}$ for given initial conditions, the time-dependent populations of each state can be calculated.

We can now study the read-out error a bit further by looking at the distribution of photon counts for the dark state ion. This information is useful if we are going to optimize the qubit readout fidelity. We have seen from Eq. (2.15) that the probability of scattering from a dark state into the bright state is the sum over exponential terms. Therefore for a qubit initially in the dark state, we expect the probability distribution of collected photons to be a convolution of Poisson and exponential distributions [King 99]. We introduce a general way which can apply to different cases based on the derivations given by Acton *et al.* [Acton 05] and Langer [Langer 06].

Using Eq. (2.15), the probability that the ion leaves the dark state to the bright state between t and $t+dt$ is given by

$$|\dot{P}_{d\to b}(t)dt| = \sum_{k=1}^{8} b_{i=(2,2),j}^{(k)}\omega_k e^{-\omega_k t}dt \tag{2.17}$$

When the dark ion goes into the bright state at time t, the collected photons will obey Poisson statistics with a mean given by

$$\lambda(t) = \lambda_{bg} + (1-\frac{t}{\tau_D})\lambda_0 \tag{2.18}$$

where $\lambda_0 = \gamma_c\tau_D$ is the mean of the bright photon distribution (without background), and $\lambda_{bg} = r_{bg}\lambda_0$ is the mean of the background photon distribution. τ_D is the detection time, $\gamma_c = \zeta\frac{\gamma}{2}\frac{s_0}{1+s_0}$ is the rate of collecting photons in the closed transition in which ζ is the total detection efficiency, and r_{bg} is the rate of collecting background photons normalized by γ_c. We desire to transform from a probability distribution $\dot{P}_{d\to b}(t)dt$ to a probability distribution of Poissonian means, $g(\lambda)d\lambda$. We use Eq. (2.18) to get $t(\lambda)$ and then substitute into Eq. (2.17). This yields the probability that the collected photons from a dark ion produces a Poisson distribution with mean λ:

$$g(\lambda)d\lambda = \begin{cases} -\sum_k b_{i=(2,2),j}^{(k)}\frac{\omega_k}{\gamma_c}e^{-\frac{\omega_k}{\gamma_c}(\lambda_{bg}+\lambda_0-\lambda)}d\lambda, & \lambda_{bg}<\lambda\leq\lambda_{bg}+\lambda_0 \\ 1-\sum_k b_{i=(2,2),j}^{(k)}e^{-\omega_k\tau_D}, & \lambda=\lambda_{bg} \end{cases} \tag{2.19}$$

Here when $\lambda = \lambda_{bg}$, it means that the dark ion never enters the bright state, and the probability that the dark ion behaves like Poisson statistics with mean λ_{bg} is $1 - P_{d\to b}(\tau_D)$.

Therefore, the probability of detecting n photons when starting in the dark state is simply the convolution of the density of means $g(\lambda)$ with the Poisson distribution $P(n|\lambda) = \frac{e^{-\lambda}\lambda^n}{n!}$:

$$\begin{aligned} p_{\text{dark}}(n|j) &= \left(1 - \sum_k b^{(k)}_{i=(2,2),j} e^{-\omega_k \tau_D}\right) P(n|\lambda_{bg}) - \\ &\quad \int_{\lambda_{bg}}^{\lambda_{bg}+\lambda_0} \frac{e^{-\lambda}\lambda^n}{n!} \sum_k b^{(k)}_{i=(2,2),j} \frac{\omega_k}{\gamma_c} e^{-\frac{\omega_k}{\gamma_c}(\lambda_{bg}+\lambda_0-\lambda)} d\lambda \\ &= P(n|\lambda_{bg}) - \sum_k b^{(k)}_{i=(2,2),j} e^{-\omega_k \tau_D} \Bigg(P(n|\lambda_{bg}) + \\ &\quad \frac{\omega_k e^{-\frac{\omega_k}{\gamma_c}\lambda_{bg}}}{\gamma_c n!} \int_{\lambda_{bg}}^{\lambda_{bg}+\lambda_0} e^{\omega_k \lambda/\gamma_c} e^{-\lambda} \lambda^n d\lambda \Bigg) \end{aligned}$$

We can rewrite the above equation in terms of incomplete Gamma function as follows:

$$\begin{aligned} p_{\text{dark}}(n|j) &= P(n|r_{bg}\gamma_c\tau_D) - \sum_k b^{(k)}_{i=(2,2),j} e^{-\omega_k \tau_D} \Bigg(P(n|r_{bg}\gamma_c\tau_D) + \\ &\quad \frac{\omega_k \gamma_c^n e^{-\omega_k \tau_D r_{bg}}}{(\gamma_c - \omega_k)^{n+1}} \Big[\mathcal{P}(n+1, (\gamma_c - \omega_k)(1+r_{bg})\tau_D) \\ &\quad - \mathcal{P}(n+1, (\gamma_c - \omega_k) r_{bg} \tau_D \Big] \Bigg) \end{aligned} \tag{2.20}$$

where $\mathcal{P}(a,x) \equiv \frac{1}{(a-1)!}\int_0^x e^{-y} y^{a-1} dy$ is the incomplete Gamma function normalized such that $\mathcal{P}(a,\infty) = 1$.

2.4.2 Readout Error - Bright to Dark State Pumping

Similarly, the ion in the bright state can be optically pumped into a dark state due to imperfect detection beam polarization. This will cause the measurement error. If the polarization of the detection beam has a small fraction of $\hat{\pi}$ ($\hat{\sigma}^-$) polarization, the bright state ($|S_{1/2}, F = 2, m_F = 2\rangle$) can off-resonantly couple to the $|P_{3/2}, m_J = 1/2\rangle$ ($|P_{3/2}, m_J = -1/2\rangle$) state with the detuning of ≈ 225 (450) MHz for the magnetic we use (see Fig. 2.6) and then decay to a dark state. In the experiment, the detection beam is aligned parallel to the magnetic field in order to have purely $\hat{\sigma}^+$ light. However, if the optical alignment is not perfect, the polarization that the ion sees may contain $\hat{\pi}$ and $\hat{\sigma}^-$ components. We can reduce imperfect polarizations by tilting and rotating the quarter-wave plate in front of the vacuum chamber by minimizing the

amount of dark photon counts on the histogram for the ion prepared in the bright state.

This optical pumping process from the bright state to a dark state can be theoretically analyzed using the methods similar to that in the previous section. Here we are interested in the time-dependent population change in the $|F = 2, m_F = 2\rangle$ state, which is $P_b(t) = v_{i=(2,2),j=(2,2)}(t) = \sum_{k=1}^{8} b^{(k)}_{i=(2,2),j=(2,2)} e^{-\omega_k t}$ from Eq. (2.15). The probability density for the ion in the bright state between t and $t + dt$ is given by

$$|\dot{P}_b(t)dt| = \sum_{k=1}^{8} b^{(k)}_{i=(2,2),j=(2,2)} \omega_k e^{-\omega_k t} dt \tag{2.21}$$

If the ion leaves the bright state at time t, the collected photon will exhibit Poisson statistics with a mean given by

$$\lambda(t) = r_{bg}\gamma_c\tau_D + \gamma_c t \tag{2.22}$$

The probability that the collected photons from a bright ion produces a Poisson distribution with mean λ:

$$g(\lambda)d\lambda = \begin{cases} \sum_k b^{(k)}_{i=(2,2),j=(2,2)} \frac{\omega_k}{\gamma_c} e^{\frac{\omega_k}{\gamma_c}(\lambda_{bg}-\lambda)} d\lambda, & \lambda_{bg} \le \lambda < \lambda_{bg} + \lambda_0 \\ \sum_k b^{(k)}_{i=(2,2),j=(2,2)} e^{-\omega_k \tau_D}, & \lambda = \lambda_{bg} + \lambda_0 \end{cases} \tag{2.23}$$

Here when $\lambda = \lambda_{bg} + \lambda_0$, the bright ion never leaves the bright state, and the probability that the bright ion follows Poisson statistics is $P_b(t)$.

As before, the overall photon probability distribution will be a convolution of Poisson and exponential distributions. However the process is now reversed that after some time the bright ion is pumped into a dark state and emits no more photons. The probability of detecting n photons when starting in the bright state is:

$$\begin{aligned} p_{\text{bright}}(n) \;=\; & \sum_k b^{(k)}_{i=(2,2),j=(2,2)} e^{-\omega_k \tau_D} P(n|(1 + r_{bg})\gamma_c\tau_D) + \\ & \sum_k b^{(k)}_{i=(2,2),j=(2,2)} \frac{\omega_k \gamma_c^n e^{\omega_k \tau_D r_{bg}}}{(\gamma_c + \omega_k)^{n+1}} \Big[\mathcal{P}(n+1, (\gamma_c + \omega_k)(1 + r_{bg})\tau_D) \\ & - \mathcal{P}(n+1, (\gamma_c + \omega_k) r_{bg}\tau_D\Big] \end{aligned} \tag{2.24}$$

where the first term is the Poisson distribution from never leaving the cycling transition and the second term is the the distribution from pumping to a dark state.

2.4.3 Simulation Results and Discussion

Here we have provided a theoretical study about the qubit readout errors. In Chapter 6, we will give the discussions for the simulations, accompanying with experimental results.

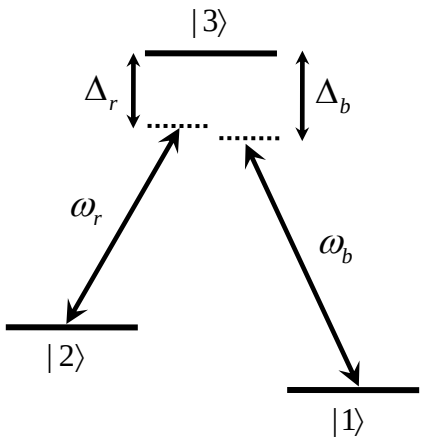

Figure 2.7: Energy level diagram for two-photon stimulated Raman transitions. The "blue" Raman beam couples levels $|3\rangle$ and $|1\rangle$ with a single-photon detuning $\Delta_b = \omega_b - \omega_{31}$. The "red" Raman beam couples levels $|3\rangle$ and $|2\rangle$ with a single-photon detuning $\Delta_r = \omega_r - \omega_{32}$. The two-photon detuning is defined as $\delta = \Delta_b - \Delta_r$.

2.5 Stimulated Raman Transitions

Since we encode the qubit into two of the hyperfine ground states, the qubit manipulations and coherent operations are realized by two-photon stimulated Raman transitions. We consider the energy level structure in the Λ-configuration, as shown in Fig. 2.7, where two ground states, $|\downarrow\rangle \equiv |1\rangle$ and $|\uparrow\rangle \equiv |2\rangle$, are coupled to an excited state $|e\rangle \equiv |3\rangle$ by two laser fields. These states have energies $\hbar\omega_1$, $\hbar\omega_2$, and $\hbar\omega_3$ respectively corresponding to an atomic Hamiltonian $\hat{H}_0 = \hbar\omega_1|1\rangle\langle 1| + \hbar\omega_2|2\rangle\langle 2| + \hbar\omega_3|3\rangle\langle 3|$. The $|1\rangle \leftrightarrow |3\rangle$ and $|2\rangle \leftrightarrow |3\rangle$ transitions are dipole allowed transitions. The two monochromatically laser fields are labeled with $\mathbf{E}_i = \hat{\epsilon}_i E_i \cos(\mathbf{k}_i \cdot \mathbf{r} - \omega_i t + \phi_i)$ for $i \in \{b, r\}$. Here, E_i and $\hat{\epsilon}_i$ are the amplitude and the polarization of the electric field, $\mathbf{k}_i$ is the wave vector, $\mathbf{r}$ is the position of the ion, and ω_i and ϕ_i are the frequency and the phase of the laser respectively. The goal is to show that under certain conditions, the internal states and motional states of the ion can be coherently controlled between states $|1\rangle$ and $|2\rangle$ without significantly populating the excited state. This is effectively mapped to a two-level system.

The electric field interacts with the atomic dipole, given by $\mathbf{d} = e\mathbf{r}$, which can be expressed in terms of the atomic eigenstates and the dipole matrix elements $\mu_{a,b} = \langle a|\mathbf{d}|b\rangle$:

$$\mathbf{d} = \mu_{1,3}|1\rangle\langle 3| + \mu_{3,1}|3\rangle\langle 1| + \mu_{2,3}|2\rangle\langle 3| + \mu_{3,2}|3\rangle\langle 2| \tag{2.25}$$

We have used the property that states $|1\rangle$, $|2\rangle$ and $|3\rangle$ have opposite parity such that $\langle 1|\mathbf{d}|1\rangle = \langle 2|\mathbf{d}|2\rangle = \langle 3|\mathbf{d}|3\rangle = 0$. The dynamics of the system is

governed by the full Hamiltonian for the three-level atom and classical fields:

$$\begin{aligned}
\hat{H} &= \hbar\omega_{21}|2\rangle\langle 2| + \hbar\omega_{31}|3\rangle\langle 3| + \mathbf{d}\cdot\sum_i \mathbf{E_i} \\
&= \hbar\omega_{21}|2\rangle\langle 2| + \hbar\omega_{31}|3\rangle\langle 3| + \\
&\quad \hbar g_b^*|1\rangle\langle 3|\frac{1}{2}\left(e^{i(\mathbf{k}_b\cdot\mathbf{r}-\omega_b t+\phi_b)} + e^{-i(\mathbf{k}_b\cdot\mathbf{r}-\omega_b t+\phi_b)}\right) + \\
&\quad \hbar g_b|3\rangle\langle 1|\frac{1}{2}\left(e^{i(\mathbf{k}_b\cdot\mathbf{r}-\omega_b t+\phi_b)} + e^{-i(\mathbf{k}_b\cdot\mathbf{r}-\omega_b t+\phi_b)}\right) + \\
&\quad \hbar g_r^*|2\rangle\langle 3|\frac{1}{2}\left(e^{i(\mathbf{k}_r\cdot\mathbf{r}-\omega_r t+\phi_r)} + e^{-i(\mathbf{k}_r\cdot\mathbf{r}-\omega_r t+\phi_r)}\right) + \\
&\quad \hbar g_r|3\rangle\langle 2|\frac{1}{2}\left(e^{i(\mathbf{k}_r\cdot\mathbf{r}-\omega_r t+\phi_r)} + e^{-i(\mathbf{k}_r\cdot\mathbf{r}-\omega_r t+\phi_r)}\right) \qquad (2.26)
\end{aligned}$$

where we define the single-photon Rabi frequencies as $g_b \equiv \frac{E_b\langle 3|\mathbf{d}\cdot\hat{\epsilon}_b|1\rangle}{\hbar}$ and $g_r \equiv \frac{E_r\langle 3|\mathbf{d}\cdot\hat{\epsilon}_r|2\rangle}{\hbar}$, and define $\omega_{21} = \omega_2 - \omega_1$ and $\omega_{31} = \omega_3 - \omega_1$ by setting the energy of $|1\rangle$ state to zero. We then transform the Hamiltonian to an appropriate rotating frame via the transformation $\hat{H}_{\rm rot} = \hat{U}\hat{H}\hat{U}^\dagger - i\hbar\hat{U}\frac{d\hat{U}^\dagger}{dt}$ with the unitary operator $\hat{U} = e^{i((\omega_b-\omega_r)|2\rangle\langle 2|+\omega_b|3\rangle\langle 3|)t}$. Equation (2.26) can be written as

$$\begin{aligned}
\hat{H}_{\rm rot} &= -\hbar\Delta|3\rangle\langle 3| - \hbar\delta|2\rangle\langle 2| + \\
&\quad \hbar\frac{g_b^*}{2}|1\rangle\langle 3|e^{-i(\mathbf{k}_b\cdot\mathbf{r}+\phi_b)} + \hbar\frac{g_b}{2}|3\rangle\langle 1|e^{i(\mathbf{k}_b\cdot\mathbf{r}+\phi_b)} + \\
&\quad \hbar\frac{g_r^*}{2}|2\rangle\langle 3|e^{-i(\mathbf{k}_r\cdot\mathbf{r}+\phi_r)} + \hbar\frac{g_r}{2}|3\rangle\langle 2|e^{i(\mathbf{k}_r\cdot\mathbf{r}+\phi_r)} \qquad (2.27)
\end{aligned}$$

where $\Delta = \Delta_b = \omega_b - \omega_{31}$ the single-photon detuning, $\delta = \Delta_b - \Delta_r$ is the two-photon detuning in which $\Delta_r = \omega_r - \omega_{32}$, and we have made the rotating-wave approximation (RWA) in which the high-frequency oscillating terms ($e^{\pm i2\omega_b t}$ and $e^{\pm i2\omega_r t}$) are omitted. The general form of the state

$$|\psi\rangle = c_1(t)|1\rangle + c_2(t)|2\rangle + c_3(t)|3\rangle$$

obeys the Schrödinger equation

$$i\hbar\frac{d}{dt}|\psi\rangle = \hat{H}_{\rm rot}|\psi\rangle$$

yielding equations of motion for the population amplitudes as follows:

$$i\dot{c}_1 = \frac{g_b^*}{2}c_3 e^{-i(\mathbf{k}_b\cdot\mathbf{r}+\phi_b)} \qquad (2.28)$$

$$i\dot{c}_2 = -\delta c_2 + \frac{g_r^*}{2}c_3 e^{-i(\mathbf{k}_r\cdot\mathbf{r}+\phi_r)} \qquad (2.29)$$

$$i\dot{c}_3 = -\Delta c_3 + \frac{g_b}{2}c_1 e^{i(\mathbf{k}_b\cdot\mathbf{r}+\phi_b)} + \frac{g_r}{2}c_2 e^{i(\mathbf{k}_r\cdot\mathbf{r}+\phi_r)} \qquad (2.30)$$

This Λ-system has a simple solution for large single-photon detuning $\Delta \gg g_b,\ g_r,\ \delta$. Since Δ is much larger than other time scales in the problem, to the lowest order in $g_{b,r}/\Delta$ the excited state amplitude will be constant, with

$$c_3 = \frac{g_b c_1 e^{i(\mathbf{k}_b \cdot \mathbf{r} + \phi_b)} + g_r c_2 e^{i(\mathbf{k}_r \cdot \mathbf{r} + \phi_r)}}{2\Delta} \tag{2.31}$$

Substituting c_3 back to Eqs. (2.28) and (2.29), we obtain the evolution of the probability amplitude for the two ground states

$$i\dot{c}_1 = \frac{|g_b|^2}{4\Delta} c_1 + \frac{g_b^* g_r e^{-i((\mathbf{k}_b - \mathbf{k}_r) \cdot \mathbf{r} + \phi_b - \phi_r)}}{4\Delta} c_2 \tag{2.32}$$

$$i\dot{c}_2 = \frac{g_b g_r^* e^{i((\mathbf{k}_b - \mathbf{k}_r) \cdot \mathbf{r} + \phi_b - \phi_r)}}{4\Delta} c_1 + (-\delta + \frac{|g_r|^2}{4\Delta}) c_2 \tag{2.33}$$

These equations are equivalent to the equations of motion for a two level system with a Rabi frequency

$$\Omega = \frac{g_b g_r^*}{2\Delta} e^{i((\mathbf{k}_b - \mathbf{k}_r) \cdot \mathbf{r} + \phi_b - \phi_r)}, \tag{2.34}$$

which is also called effective Rabi frequency for the Raman transition, Raman frequency or two-photon Rabi frequency, and AC Stark shifts

$$\delta_{sb} = \frac{|g_b|^2}{4\Delta} \tag{2.35}$$

$$\delta_{sr} = \frac{|g_r|^2}{4\Delta} \tag{2.36}$$

induced from the detuned laser fields. After rewriting Eqs. (2.32) and (2.33), we get

$$i\dot{c}_1 = \delta_{sb} c_1 + \frac{\Omega^*}{2} c_2 \tag{2.37}$$

$$i\dot{c}_2 = \frac{\Omega}{2} c_1 + (-\delta + \delta_{sr}) c_2 \tag{2.38}$$

The above equations of motion can be viewed as resulting from the Hamiltonian

$$\hat{H} = \hbar\delta_{sb}|1\rangle\langle 1| + \hbar(-\delta + \delta_{sr})|2\rangle\langle 2| + \frac{\hbar}{2}(\Omega|2\rangle\langle 1| + \Omega^*|1\rangle\langle 2|) \tag{2.39}$$

Basically the AC Stark shift terms can be removed by re-defining the energy level reference. To calculate the dynamics of a standard two-level system, again we choose the zero energy level in the middle of two states and introduce a detuning like $\delta' = \delta - \delta_{sr} + \delta_{sb}$ such that Eq. (2.39) can be rewritten as

$$\hat{H} = -\hbar\delta'|2\rangle\langle 2| + \frac{\hbar}{2}(\Omega|2\rangle\langle 1| + \Omega^*|1\rangle\langle 2|) \tag{2.40}$$

Using the unitary operator $\hat{U} = e^{-i\delta'|2\rangle\langle 2|t}$ and transferring Eq. (2.40) to a new rotating frame, the resulting Hamiltonian is

$$\hat{H}_I = \frac{\hbar}{2}\Omega_0 \left(|2\rangle\langle 1| e^{i(\Delta\mathbf{k}\cdot\mathbf{r}+\Delta\phi)} e^{-i\delta' t} + |1\rangle\langle 2| e^{-i(\Delta\mathbf{k}\cdot\mathbf{r}+\Delta\phi)} e^{i\delta' t} \right) \tag{2.41}$$

where $\Omega_0 = |\Omega| = \frac{g_b g_r^*}{2\Delta}$, $\Delta\mathbf{k} = \mathbf{k}_b - \mathbf{k}_r$, and $\Delta\phi = \phi_b - \phi_r$. This form is like the Hamiltonian for a two-level system in the interaction picture. The dynamics of the system is the well-known Rabi oscillations, where the time evolution of the population of the state behaves like a sinusoidal function at a rate given by the Rabi frequency Ω_0.

2.5.1 Multiple Excited States

The techniques for treating the three-level system are also applicable to the case in which the ground states are coupled to multiple excited states. Essentially this always happens in real atoms or ions. To illustrate how to extend the three-level calculation to multiple excited states, we consider an ion with two ground states (qubit states) as before and many excited states $|e\rangle$. Each excited state is coupled to $|1\rangle$ by the field $\mathbf{E}_b$ and coupled to $|2\rangle$ by the field $\mathbf{E}_r$. Equation (2.27) is modified to be

$$\begin{aligned}
\hat{H}_{\text{rot}} \;=\; & -\hbar \sum_m \Delta_m |e_m\rangle\langle e_m| - \hbar\delta |2\rangle\langle 2| + \\
& \hbar \sum_m \frac{g_{b,e_m}^*}{2} |1\rangle\langle e_m| e^{-i(\mathbf{k}_b\cdot\mathbf{r}+\phi_b)} + \hbar \sum_m \frac{g_{b,e_m}}{2} |e_m\rangle\langle 1| e^{i(\mathbf{k}_b\cdot\mathbf{r}+\phi_b)} + \\
& \hbar \sum_m \frac{g_{r,e_m}^*}{2} |2\rangle\langle e_m| e^{-i(\mathbf{k}_r\cdot\mathbf{r}+\phi_r)} + \hbar \sum_m \frac{g_{r,e_m}}{2} |e_m\rangle\langle 2| e^{i(\mathbf{k}_r\cdot\mathbf{r}+\phi_r)}
\end{aligned} \tag{2.42}$$

The derivation is basically the same as before, except for the summation of the excited states and the dependence of the detunings from different excited state. Following the same procedure above, we find that the Raman Rabi frequency and AC Stark shifts are now given by

$$\begin{aligned}
|\Omega| = \Omega_0 \;&=\; \sum_m \frac{g_{b,e_m} g_{r,e_m}^*}{2\Delta} \\
&=\; \frac{E_b E_r}{2\hbar^2} \sum_m \frac{\langle 2|\mathbf{d}\cdot\hat{\epsilon}_r|e_m\rangle\langle e_m|\mathbf{d}\cdot\hat{\epsilon}_b|1\rangle}{\Delta_m}
\end{aligned} \tag{2.43}$$

and

$$\delta_{sb} \;=\; \sum_m \frac{|g_{b,e_m}|^2}{4\Delta_m} = \frac{E_b^2}{4\hbar^2} \sum_m \frac{|\langle e_m|\mathbf{d}\cdot\hat{\epsilon}_b|1\rangle|^2}{\Delta_m} \tag{2.44}$$

$$\delta_{sr} \;=\; \sum_m \frac{|g_{r,e_m}|^2}{4\Delta_m} = \frac{E_r^2}{4\hbar^2} \sum_m \frac{|\langle e_m|\mathbf{d}\cdot\hat{\epsilon}_r|2\rangle|^2}{\Delta_m} \tag{2.45}$$

2.5.2 Ion's Motion

In the previous section we have showed that we can coherently drive the populations between two ground internal states of an ion by using two laser beams detuned from an excited state with a beatnote frequency close to the energy level splitting of the qubit. For the other degree of freedom, because the ion is strongly confined in a harmonic potential, its motion is quantized. Therefore, we can take the motional effects into account by adding the harmonic oscillator Hamiltonian $\hat{H}_{\rm osc} = \hbar\omega_z \hat{a}^\dagger \hat{a}$ to the base Hamiltonian $\hat{H}_0$, where we only consider ω_z, the vibrational frequency along the z axis. The motional-dependent term in Eq. (2.41) needs to be modified as $\Delta\mathbf{k}\cdot\mathbf{r} \to \Delta k_z \hat{z} = \eta(\hat{a}^\dagger + \hat{a})$ in which we only consider the motion in z-axis. Here $\eta = \Delta k_z z_0$ is the Lamb-Dicke parameter and $z_0 = \sqrt{\frac{\hbar}{2m\omega_z}}$ is the root mean squared extent of the oscillator ground state wavepacket.

Applying the transformation $e^{-i\hat{H}_{\rm osc}t/\hbar}\hat{H}_I e^{i\hat{H}_{\rm osc}t/\hbar}$ to Eq. (2.41) and making use of Baker Campbell Hausdorff formula, the interaction Hamiltonian in the interaction picture is

$$\hat{H}_I' = \frac{\hbar}{2}\Omega_0 \left|\uparrow\right\rangle \left\langle\downarrow\right| \exp\{i\eta(\hat{a}e^{-i\omega_z t} + \hat{a}^\dagger e^{i\omega_z t})\} e^{i(\phi-\delta' t)} + \text{h.c.} \tag{2.46}$$

where 'h.c.' means the hermitian conjugate of the first term, and $\Delta\phi$, $|1\rangle$ and $|2\rangle$ in Eq. (2.41) have been replaced with ϕ, $|\downarrow\rangle$, and $|\uparrow\rangle$ respectively. Depending on the laser detuning δ', the interaction Hamiltonian couples ion's internal and motional states ($|\downarrow, n\rangle$ and $|\uparrow, n+s\rangle$, where s is an integer and $|n\rangle$ are the eigenstates of the harmonic oscillator).

Rabi Frequencies

With the closure relation, an arbitrary operator $\hat{O}$ can be expressed in the form $\hat{O} = \sum_{n,n'} |n'\rangle\langle n'|\hat{O}|n\rangle\langle n|$ such that Eq. (2.46) can be written as

$$\begin{aligned}
\hat{H}_I' &= \sum_{n,n+s} \frac{\hbar}{2}\Omega_0 \langle n+s|e^{i\eta(\hat{a}e^{-i\omega_z t} + \hat{a}^\dagger e^{i\omega_z t})}|n\rangle \left|\uparrow, n+s\right\rangle\left\langle\downarrow, n\right| e^{i(\phi-\delta' t)} + \text{h.c.} \\
&= \sum_{n,n+s} \frac{\hbar}{2}\Omega_0 \langle n+s|\hat{D}(i\eta e^{i\omega_z t})|n\rangle \left|\uparrow, n+s\right\rangle\left\langle\downarrow, n\right| e^{i(\phi-\delta' t)} + \text{h.c.}
\end{aligned} \tag{2.47}$$

where $\hat{D}(\alpha) = e^{\alpha\hat{a}^\dagger - \alpha^*\hat{a}}$ denotes the displacement operator. We then determine the matrix elements of displacement operator. For $n+s \geq n$ ($s \geq 0$), we can show the result in the following by applying the Baker-Campbell-Hausdorff formula and basic properties of the annihilation operator:

$$\begin{aligned}
\langle n+s|\hat{D}(\alpha)|n\rangle &= e^{-|\alpha|^2/2}\langle n+s|e^{\alpha\hat{a}^\dagger}e^{\alpha^*\hat{a}}|n\rangle \\
&= e^{-|\alpha|^2/2}\alpha^s \sqrt{\frac{n!}{(n+s)!}} L_n^s(|\alpha|^2),
\end{aligned}$$

where $L_n^s(|\alpha|^2)$ are the generalized Laguerre polynomials. Analogously, for $n+s \leq n$ ($s \leq 0$), we obtain

$$\langle n+s|\hat{D}(\alpha)|n\rangle = e^{-|\alpha|^2/2}(-\alpha^*)^{-s}\sqrt{\frac{(n+s)!}{n!}}L_{n+s}^{-s}(|\alpha|^2),$$

At the end, it turns out that Eq. (2.47) is

$$\hat{H}_I' = \sum_{n,n+s} \frac{\hbar}{2}\Omega_{n+s,n} i^{|s|} |\uparrow, n+s\rangle\langle\downarrow, n| e^{i(s\omega_z - \delta' t + \phi)} + \text{h.c.} \qquad (2.48)$$

in which

$$\Omega_{n+s,n} = \Omega_0 e^{-\eta^2/2}\eta^{|s|}\sqrt{\frac{n_<!}{n_>!}}L_{n_<}^{|s|}(\eta^2) \qquad (2.49)$$

where $n_<$ ($n_>$) is the lesser (greater) of $n+s$ and n [Wineland 98]. The time evolution for the general state

$$|\Psi(t)\rangle = \sum_{n=0}^{\infty} c_{\downarrow,n}(t)|\downarrow, n\rangle + c_{\uparrow,n}(t)|\uparrow, n\rangle \qquad (2.50)$$

can be calculated by solving the Schrödinger equation with the Laplace transform method, yielding the solution

$$\begin{bmatrix} c_{\uparrow,n+s}(t) \\ c_{\downarrow,n}(t) \end{bmatrix} = U_n^s \begin{bmatrix} c_{\uparrow,n+s}(0) \\ c_{\downarrow,n}(0) \end{bmatrix} \qquad (2.51)$$

with

$$U_n^s = \begin{bmatrix} e^{-i(\delta_s/2)t}\left[\cos\left(\frac{X}{2}t\right) + i\frac{\delta_s}{X}\sin\left(\frac{X}{2}t\right)\right] & -i\frac{\Omega_{n+s,n}}{X}e^{i(\phi+|s|\pi/2-\delta_s t/2)}\sin\left(\frac{X}{2}t\right) \\ -i\frac{\Omega_{n+s,n}}{X}e^{-i(\phi+|s|\pi/2-\delta_s t/2)}\sin\left(\frac{X}{2}t\right) & e^{i(\delta_s/2)t}\left[\cos\left(\frac{X}{2}t\right) - i\frac{\delta_s}{X}\sin\left(\frac{X}{2}t\right)\right] \end{bmatrix} \qquad (2.52)$$

where $\delta_s = \delta' - s\omega_z$ and $X = \sqrt{\delta_s^2 + \Omega_{n+s,n}^2}$. This time-domain solution shows the generalized form of Rabi flopping between states $|\downarrow, n\rangle$ and $|\uparrow, n+s\rangle$.

Lamb-Dicke Approximation

Once the ions are cold, experiments are carried out in the Lamb-Dicke (LD) regime where the extension of the ion's wavefunction is much smaller than $1/k$. When the condition for the LD regime is satisfied, the exponent in Eq. (2.46) can be expanded to the first order in η, resulting in

$$\hat{H}_{I,\text{LD}}' = \frac{\hbar}{2}\Omega_0\hat{\sigma}_+\{1 + i\eta(\hat{a}e^{-i\omega_z t} + \hat{a}^\dagger e^{i\omega_z t})\}e^{i(\phi-\delta' t)} + \text{h.c.} \qquad (2.53)$$

where $\hat{\sigma}_+ \equiv |\uparrow\rangle\langle\downarrow|$ and $\hat{\sigma}_- \equiv |\downarrow\rangle\langle\uparrow|$ are the spin flip operators. There are three different types of coupling forming the basic coherent operations for all the

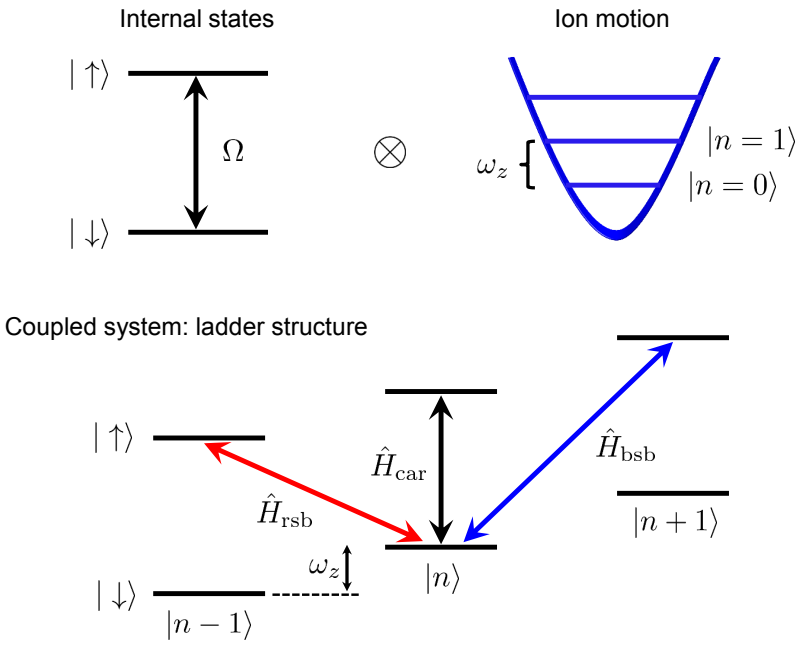

Figure 2.8: A two-level system coupled to a harmonic oscillator results in the ladder structure. Three types of couplings (carrier, blue sideband, and red sideband drives) are shown.

quantum information and quantum computation experiments using trapped ions. 1) When $\delta' = 0$, the Hamiltonian is simplified to

$$\hat{H}_{\mathrm{car}} = \frac{\hbar}{2}\Omega_0 \left(\hat{\sigma}_+ e^{i\phi} + \hat{\sigma}_- e^{-i\phi}\right) \tag{2.54}$$

which is called the carrier Hamiltonian and only drives the transition between two internal states without coupling to the ion's motion. 2) When $\delta' = -\omega_z$, the Hamiltonian becomes

$$\hat{H}_{\mathrm{rsb}} = \frac{\hbar}{2}\Omega_0\eta \left(\hat{a}\hat{\sigma}_+ e^{i\phi} + \hat{a}^\dagger\hat{\sigma}_- e^{-i\phi}\right) \tag{2.55}$$

This Hamiltonian is called the first red sideband Hamiltonian and equivalent to the famous Jaynes-Cummings Hamiltonian in quantum optics. It drives $|\downarrow, n\rangle \leftrightarrow |\uparrow, n-1\rangle$ transition with Rabi frequency $\Omega_{n-1,n} = \Omega_0\sqrt{n}\eta$. 3) When $\delta' = \omega_z$, which is the counterpart of the second type of coupling, the Hamiltonian is simplified to

$$\hat{H}_{\mathrm{rsb}} = \frac{\hbar}{2}\Omega_0\eta \left(\hat{a}^\dagger\hat{\sigma}_+ e^{i\phi} + \hat{a}\hat{\sigma}_- e^{-i\phi}\right) \tag{2.56}$$

This is the first blue sideband Hamiltonian or called anti-Jaynes-Cummings Hamiltonian, coupling $|\downarrow, n\rangle$ and $|\uparrow, n+1\rangle$ with Rabi frequency $\Omega_{n+1,n} =$

$\Omega_0\sqrt{n+1}\eta$. Figure 2.8 shows the ladder structure of a two-level system coupled to a harmonic oscillator and the three types of couplings are indicated. With proper use or certain combination of these coherent operations, one can perform a variety of experiments with trapped ions.

2.6 Quantum Gates

Although we haven't realized the two-qubit gate operations in our experiments yet, in this Section I will introduce the theoretical background of single-qubit and two-qubit gates using $^9Be^+$ ions. The reasons are that we have performed some theoretical studies for the gate error analysis (see next Section) as well as set up the apparatus that can be used for implementing the two-qubit gates (see Chapter 5).

2.6.1 Single-Qubit Quantum Gates

The single-qubit gate operations are implemented using the stimulated Raman transition described previously with two co-propagating Raman beams. The advantage of the co-propagating Raman beams is that the difference of two k vectors is close to zero, $(\mathbf{k}_b - \mathbf{k}_r) \approx 0$, which means this action is insensitive to the ion's motion ($\Delta\mathbf{k}\cdot\mathbf{r}$ is extremely small.). For the resonant carrier transitions ($\delta' = 0$ and $s = 0$), Eq. (2.51) is simplified to

$$\begin{bmatrix} c_{\uparrow,n}(t) \\ c_{\downarrow,n}(t) \end{bmatrix} = \hat{R}(\theta,\phi) \begin{bmatrix} c_{\uparrow,n}(0) \\ c_{\downarrow,n}(0) \end{bmatrix} \tag{2.57}$$

with

$$\hat{R}(\theta,\phi) = \begin{bmatrix} \cos\left(\frac{\theta}{2}\right) & -ie^{i\phi}\sin\left(\frac{\theta}{2}\right) \\ -ie^{-i\phi}\sin\left(\frac{\theta}{2}\right) & \cos\left(\frac{\theta}{2}\right) \end{bmatrix} \tag{2.58}$$

where $\theta \equiv \Omega_0 t$ and $\phi = \Delta\phi = \phi_b - \phi_r$ in the case of stimulated Raman transitions. The rotation matrices $\hat{R}(\pi,\phi)$ and $\hat{R}(\pi/2,\phi)$ are a π-pulse and a $\pi/2$-pulse respectively with a phase ϕ. The θ is varied by the laser pulse duration for a given Rabi frequency (laser intensity). The phase can be controlled by the differential phase between the two Raman beams generated from stable microwave sources. With suitable settings, we are able to perform arbitrary rotations about any axis on the Bloch sphere.

2.6.2 Two-Qubit Quantum Gates

The final element of the universal gate set is the two-ion entangling gate. Since we encode the quantum information onto the ion's spin states, an entangling operation is completed between two ions' spin states. The efficient way to obtain the entanglement of two ions is through their collective motion.

In this Section, I will mainly explain two gate operations using a state dependent force (SDF) as well as discuss some experimental issues. Both gates basically work in the same way but in different computational basis. The first one is the conditional phase gate in z basis of the spin states, namely the geometric phase gate (Z-phase gate or σ_z gate) [Leibfried 03b, Roos 08]; the second is called Mølmer-Sørensen gate (MS gate or σ_ϕ gate) [Mølmer 99, Benhelm 08a, Roos 08] operating in the basis other than z. The main idea is that the force acting on the two ions creates internal-state dependent displacement in the position-momentum ($x-p$) phase space. After completion of the force application, the trajectory of particular two-qubit states is a closed loop in the phase space while acquiring a state-dependent geometric phase proportional to the area of the loop. This geometric phase can lead to an entanglement between spin states.

Geometric Phase Gate

For $^9Be^+$ ions, the two-qubit operations are also performed using stimulated Raman transitions. Here the geometric phase gate uses a pair of non copropagating Raman beams illuminating on two ions. The frequency difference between the two Raman beams $\delta = \omega_a - \omega_b$ is set close to one of the vibrational frequencies of the ion chain. The fields couple each of the spin states via an the excited state with a large detuning Δ compared to the qubit splitting frequency $\omega_{\uparrow\downarrow}$ (See Fig. 2.9). With this arrangement, states $|\downarrow\rangle$ and $|\uparrow\rangle$ are not coupled by the laser beams because the beatnote frequency δ is far away from the qubit transition frequency $\omega_{\uparrow\downarrow}$. Thus we can think that transitions $|\downarrow\rangle \leftrightarrow |e\rangle$ and $|\uparrow\rangle \leftrightarrow |e\rangle$ are two independent two-level systems. The Hamiltonian for one of the two-level systems can be written as

$$\begin{aligned}
\hat{H} &= \hbar\omega_{e\downarrow} |e\rangle\langle e| + \\
&\quad \frac{\hbar g_a^*}{2} |\downarrow\rangle\langle e| \left(e^{i(\mathbf{k}_a\cdot\mathbf{r}-\omega_a t+\phi_a)} + e^{-i(\mathbf{k}_a\cdot\mathbf{r}-\omega_a t+\phi_a)}\right) + \\
&\quad \frac{\hbar g_a}{2} |e\rangle\langle\downarrow| \left(e^{i(\mathbf{k}_a\cdot\mathbf{r}-\omega_a t+\phi_a)} + e^{-i(\mathbf{k}_b\cdot\mathbf{r}-\omega_a t+\phi_a)}\right) + \\
&\quad \frac{\hbar g_b^*}{2} |\downarrow\rangle\langle e| \left(e^{i(\mathbf{k}_b\cdot\mathbf{r}-\omega_b t+\phi_b)} + e^{-i(\mathbf{k}_b\cdot\mathbf{r}-\omega_b t+\phi_b)}\right) + \\
&\quad \frac{\hbar g_b}{2} |e\rangle\langle\downarrow| \left(e^{i(\mathbf{k}_b\cdot\mathbf{r}-\omega_b t+\phi_b)} + e^{-i(\mathbf{k}_b\cdot\mathbf{r}-\omega_b t+\phi_b)}\right) \qquad (2.59)
\end{aligned}$$

Applying the RWA and adiabatic elimination of the excited state, the Hamiltonian in an appropriate rotating frame is

$$\hat{H}_I = \hbar\left[\delta_{s\downarrow} + \frac{\Omega_\downarrow}{2}\left(e^{i(\Delta\mathbf{k}\cdot\mathbf{r}-\delta t+\Delta\phi)} + \text{h.c.}\right)\right] |\downarrow\rangle\langle\downarrow| \qquad (2.60)$$

where $\Delta\mathbf{k} = \mathbf{k}_a - \mathbf{k}_b$, $\Delta\phi = \phi_a - \phi_b$, $\delta_{s\downarrow} = \frac{|g_a|^2+|g_b|^2}{4\Delta}$ is the time-averaged Stark shift on the level $|\downarrow\rangle$ and $\Omega_\downarrow = \frac{g_a g_b^*}{2\Delta}$ is the time-varying Stark shift due to the

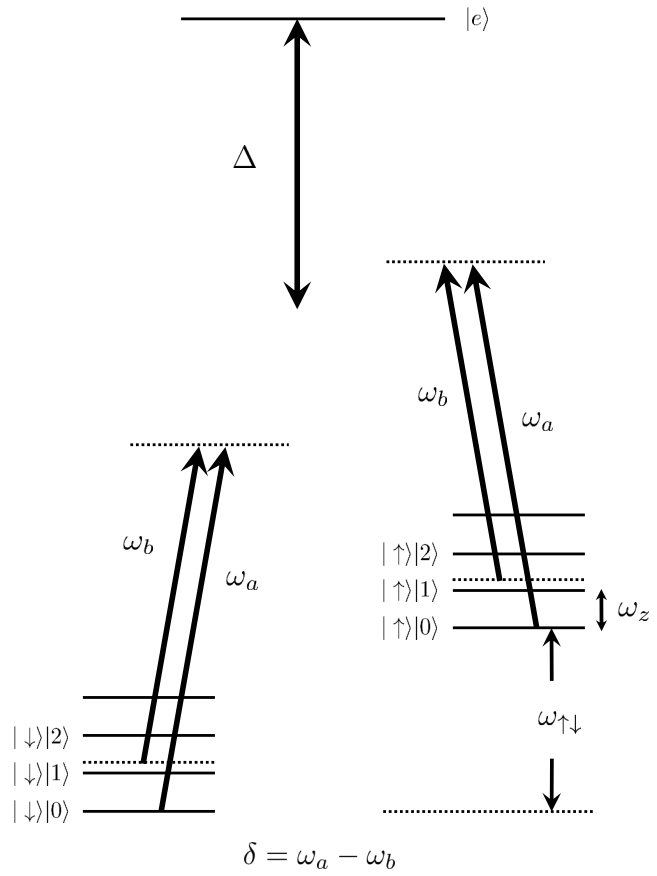

Figure 2.9: The energy levels and laser arrangements used for the geometric phase gate implementation, where $\Delta \gg \omega_{\uparrow\downarrow}$. The drawing is not to scale.

variation in the intensity created by the interference of two beams. Summing up both two-level systems, we obtain the total Hamiltonian for a single ion as follows:

$$\begin{aligned}\hat{H}_I &= \hbar\left[\delta_{s\downarrow} + \frac{\Omega_\downarrow}{2}\left(e^{i(\Delta\mathbf{k}\cdot\mathbf{r}-\delta t+\Delta\phi)} + \text{h.c.}\right)\right]|\downarrow\rangle\langle\downarrow| + \\ &\quad \hbar\left[\delta_{s\uparrow} + \frac{\Omega_\uparrow}{2}\left(e^{i(\Delta\mathbf{k}\cdot\mathbf{r}-\delta t+\Delta\phi)} + \text{h.c.}\right)\right]|\uparrow\rangle\langle\uparrow| \qquad (2.61)\end{aligned}$$

In our case it must consider multiple excited states such that the Rabi frequency and Stark shift terms need to be modified based on the analysis in Chapter 2.5.1:

$$\Omega_q = \frac{E_a E_b}{2\hbar^2}\sum_m \frac{\langle q|\mathbf{d}\cdot\hat{\epsilon}_a|e_m\rangle\langle e_m|\mathbf{d}\cdot\hat{\epsilon}_b|q\rangle}{\Delta_m} \qquad (2.62)$$

and

$$\delta_{sq} = \sum_{j=a,b} \frac{E_j^2}{4\hbar^2} \sum_m \frac{|\langle e_m|\mathbf{d}\cdot\hat{\epsilon}_j|q\rangle|^2}{\Delta_m} \tag{2.63}$$

where $q \in \{\downarrow,\uparrow\}$. By carefully choosing the polarizations for the two Raman beams, the time-averaged Stark shifts ($\delta_{s\downarrow}$ and $\delta_{s\uparrow}$) can be made equal such that there is no net time-averaged Stark shift between states $|\downarrow\rangle$ and $|\uparrow\rangle$ [Wineland 03, Leibfried 03b]. If one makes $\Omega_\downarrow \neq \Omega_\uparrow$, a differential Stark shift will result in a differential force between the two spin states. In the experiment, the goal is to make $|\Omega_\downarrow - \Omega_\uparrow|$ as large as possible. In the following discussions, we will ignore $\delta_{s\downarrow}$ and $\delta_{s\uparrow}$ terms because both do not affect the final result.

Using the same mathematical treatments in Chapter 2.5.2 for ion's motion, we find that the interaction Hamiltonian (Eq. (2.61)) with Lamb-Dicke approximation is

$$\hat{H}'_{I,\mathrm{LD}} = \sum_{q=\uparrow,\downarrow} \frac{\hbar}{2}\Omega_q\{1 + i\eta(\hat{a}e^{-i\omega_z t} + \hat{a}^\dagger e^{i\omega_z t})\}e^{i(\Delta\phi-\delta t)}|q\rangle\langle q| + \mathrm{h.c.}$$

After we simplify the equation and skip the fast oscillating terms by RWA, the remaining term is

$$\hat{H}'_{I,\mathrm{LD}} = \sum_{q=\uparrow,\downarrow} \frac{\hbar}{2} i\eta\Omega_q \left(\hat{a}^\dagger e^{i[(\omega_z-\delta)t+\Delta\phi]} - \hat{a}e^{-i[(\omega_z-\delta)t+\Delta\phi]}\right)|q\rangle\langle q| \tag{2.64}$$

When N ions are trapped in the same potential, there are N vibrational modes in each principal axis. For two ions, the two modes in the axial direction are the center-of-mass (COM) mode where two ions oscillate in phase and the stretch mode where the ions oscillate out of phase. Application of the gate operation to two ions on the stretch mode (the motional heating for this mode is lower [Leibfried 03b]) can be analyzed by summing over the individual Hamiltonian (Eq. (2.64)):

$$\begin{aligned}
\hat{H}_I &= (+1)\hat{H}'^{(1)}_{I,\mathrm{LD}} + (-1)\hat{H}'^{(2)}_{I,\mathrm{LD}} \\
&= \sum_{j=1,2}\sum_{q=\uparrow,\downarrow} \frac{\hbar}{2} i\eta(-1)^{j-1}\Omega_{qj}\left(\hat{a}^\dagger e^{i[(\omega_z-\delta)t+\phi_j]} - \hat{a}e^{-i[(\omega_z-\delta)t+\phi_j]}\right)|q_j\rangle\langle q_j| \\
&= \sum_{q=\uparrow,\downarrow}\left(\frac{F_{q1,q2}z_s}{2}\hat{a}^\dagger e^{i(\omega_z-\delta)t} + \frac{F^*_{q1,q2}z_s}{2}\hat{a}e^{-i(\omega_z-\delta)t}\right)|q_1q_2\rangle\langle q_1q_2|
\end{aligned} \tag{2.65}$$

where $F_{q1,q2}z_s = i\hbar\eta(\Omega_{q1}e^{i\phi_1} - \Omega_{q2}e^{i\phi_2})$ in which z_s is the root mean squared extent of the ground state wavepacket for the stretch mode and $F_{q1,q2}$ is the spin-state-dependent force on both ions associated with the computational

basis $|q_1 q_2\rangle$. For Eq. (2.65) it is important to notice that 1) the motional mode is common to both ions; 2) The phase $\phi_j = (\Delta\mathbf{k}\cdot\hat{z})z_j + \Delta\phi$ is different for two ions because they are in different locations (z_j denotes the location of the j^{th} ion along the z-axis). We can see that the optical phase difference $\phi_1 - \phi_2$ determines the phase difference between the forces. However if two ions are spaced by an integer multiple of the effective optical wavelength $\lambda_{\text{eff}} = 2\pi/|\Delta\mathbf{k}| \approx 215$ nm, they experience the same phase of the optical field, i.e. $\phi_1 = \phi_2$. The differential force would be determined by the the magnitude and the sign of Ω_{q1} and Ω_{q2}. This implies that when two spin states are the same there is no differential force. On the other hand, when the spin states are anti-aligned each ion would experience different forces because $\Omega_{\downarrow 1} \neq \Omega_{\uparrow 2}$ and $\Omega_{\downarrow 2} \neq \Omega_{\uparrow 1}$; 3) Once the ion-ion separation is adjusted to fulfill the condition mentioned above, then the sign of the individual Hamiltonian depends on which vibrational mode is driven. The sign of the Hamiltonian for the second ion is negative due to the use of the stretch mode.

We desire to calculate the time evolution for $\hat{H}_I$. The matrix elements $H_{q1,q2} = \frac{F_{q1,q2}z_s}{2}\hat{a}^\dagger e^{i(\omega_z-\delta)t} + \frac{F^*_{q1,q2}z_s}{2}\hat{a}e^{-i(\omega_z-\delta)t}$ are the motional parts corresponding to each computational eigenstate and are only located in the diagonal of the Hamiltonian matrix. $H_{q1,q2}$ does not commute with itself at different times. However for a very short time interval Δt the evolution of a wavefunction can still be written as $|\Psi(t+\Delta t)\rangle = \exp\left(-\frac{i}{\hbar}H_{q1,q2}\Delta t\right)|\Psi(t)\rangle$. It can be found that

$$\exp\left(-\frac{i}{\hbar}H_{q1,q2}\Delta t\right) = \exp\left(\Delta\alpha\hat{a}^\dagger - \Delta\alpha^*\hat{a}\right) = \hat{D}(\Delta\alpha)$$

where $\hat{D}(\alpha)$ is the displacement operator and the small displacements $\Delta\alpha = -\frac{i}{2\hbar}F_{q1,q2}z_s e^{i(\omega_z-\delta)t}\Delta t$ for which the real and the imaginary parts can be understood as its position and momentum parts in phase space. By repeatedly using the relation $\hat{D}(\alpha)\hat{D}(\beta) = \hat{D}(\alpha+\beta)\exp\left[i\text{Im}(\alpha\beta^*)\right]$ [Walls 94], we are able to add all the infinitesimal displacements to construct the time-evolution operator, resulting in

$$\begin{aligned}
\hat{U}(t) &= \hat{D}\left(\sum_{i=1}^{N}\Delta\alpha_i\right)\exp\left\{i\text{Im}\left[\sum_{j=2}^{N}\Delta\alpha_j\left(\sum_{k=1}^{j-1}\Delta\alpha_k\right)^*\right]\right\} \\
&= \hat{D}(\alpha)\exp\left(i\text{Im}\oint\alpha^* d\alpha\right) \\
&= \hat{D}(\alpha)\exp(i\Phi) \qquad (2.66)
\end{aligned}$$

with

$$\begin{aligned}
\alpha &= \int d\alpha = -\frac{i}{2\hbar}\int_0^t F_{q1,q2}z_s e^{i(\omega_z-\delta)t'}dt' \\
&= \frac{F_{q1,q2}z_s}{2\hbar(\omega_z-\delta)}\left(1 - e^{i(\omega_z-\delta)t}\right) \qquad (2.67)
\end{aligned}$$

For the gate time $\tau_{\text{gate}} = 2\pi/(\omega_z - \delta)$, we can see that the motional mode returns to its initial state ($\alpha(\tau_{\text{gate}}) = 0$) and its trajectory in phase space is a closed circle. The geometric phase that is acquired at the end of the gate time will be

$$\Phi = \text{Im} \int_0^\tau \alpha^*[d\alpha/dt']dt' = \frac{\pi}{2}\left(\frac{F_{q1,q2}z_s}{\hbar(\omega_z - \delta)}\right)^2 \tag{2.68}$$

Therefore, we know that Φ is a function of $F_{q1,q2}$, depending on the internal state of the ion. As we discussed above, to have a differential force on two ions is achieved by choosing a certain qubit pair and proper light polarizations of the Raman beams. This type of gate was implemented by Leibfried *et al.* [Leibfried 03b] in which they used the qubit states $|\uparrow\rangle \equiv |F = 1, m_F = -1\rangle$ and $|\downarrow\rangle \equiv |F = 2, m_F = -2\rangle$ and the polarizations $\hat{\epsilon}_b = (\hat{\sigma}^+ + \hat{\sigma}^-)/\sqrt{2}$ and $\hat{\epsilon}_r = (\hat{\sigma}^+ - \hat{\sigma}^-)/\sqrt{2}$, yielding $\Omega_\downarrow = -2\Omega_\uparrow$ at low magnetic fields [Wineland 03]. If the experiment is performed with the magnetic field at 119.45 G, the differential force is smaller. When $\Phi = \pi/2$, the outcome of the gate operation is

$$\begin{aligned}
|\uparrow_1\uparrow_2\rangle &\rightarrow |\uparrow_1\uparrow_2\rangle \\
|\uparrow_1\downarrow_2\rangle &\rightarrow e^{i\frac{\pi}{2}}|\uparrow_1\downarrow_2\rangle \\
|\downarrow_1\uparrow_2\rangle &\rightarrow e^{i\frac{\pi}{2}}|\downarrow_1\uparrow_2\rangle \\
|\downarrow_1\downarrow_2\rangle &\rightarrow |\downarrow_1\downarrow_2\rangle
\end{aligned}$$

Combined with some single-qubit rotations, we can obtain the final states equivalent to the results of a CNOT gate. Unfortunately the geometric phase gate works inefficiently for the field-independent qubits because the differential Stark shift of the pairs of the qubit state ($\Omega_\downarrow \sim \Omega_\uparrow$) is tiny.

Mølmer-Sørensen Gate

The other gate scheme proposed by Mølmer and Sørensen [Mølmer 99] is analogous to the geometric phase gate except it operates in a rotated basis and involves spin flips. The state-dependent force in this case is generated by simultaneously driving the blue and red motional sidebands of the spin-flip transition with equal and opposite detunings $\pm\delta'$ in Eq. (2.53) [Roos 08, Lee 05]. Two possible configurations are sketched in Fig. 2.10. The resulting interaction Hamiltonian can be written in the Lamb-Dicke approximation as

$$\hat{H}'_{I,\text{LD}} = -\frac{\hbar}{2}\eta\Omega\hat{\sigma}_{\frac{\pi}{2}-\phi_S}\left(\hat{a}^\dagger e^{i[(\omega_z-\delta')t+\phi_M]} + \hat{a}e^{-i[(\omega_z-\delta')t+\phi_M]}\right) \tag{2.69}$$

where $\hat{\sigma}_\phi \equiv \cos(\phi)\hat{\sigma}_x + \sin(\phi)\hat{\sigma}_y$ is a rotated Pauli matrix in the xy-plane, $\phi_S = \frac{1}{2}(\phi_B + \phi_R)$ is the phase associated with the spin state, and $\phi_M = \frac{1}{2}(\phi_B - \phi_R)$ is the phase associated with the motion. ϕ_B and ϕ_R are the phases of the Raman laser field for driving the blue and red sideband transitions. Here we have ignored three off-resonant terms. The most significant one of them drives

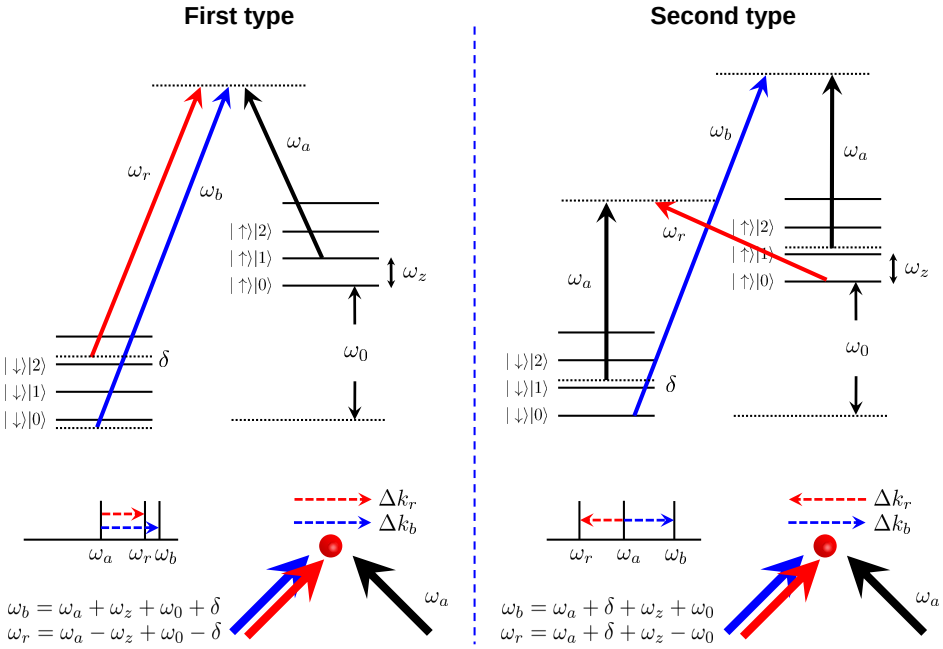

Figure 2.10: Two types of scheme that can be used to realize the MS gate operations.

the carrier transition off-resonantly that would cause more problems because its coupling strength is $1/\eta$ larger than the sideband coupling strength. In practice, this effect can be strongly suppressed by shaping the laser pulses [Roos 08, Benhelm 08a].

Following the same approach as for the geometric phase gate, we sum over the individual Hamiltonian for each ion so that we can write down an equation similar to Eq. (2.65) except that the computational basis has changed, meaning a differential force is now applied to the eigenstates of the spin operator $\hat{\sigma}_{\frac{\pi}{2}-\phi_S} \otimes \hat{\sigma}_{\frac{\pi}{2}-\phi_S}$. We can then calculate the dynamics of the system for the gate. Detailed derivations can be found in [Lee 05, Roos 08]. In a general case this gate scheme will produce the following outcome

$$\begin{aligned}
|\uparrow_1\uparrow_2\rangle_{\frac{\pi}{2}-\phi_S} &\rightarrow |\uparrow_1\uparrow_2\rangle_{\frac{\pi}{2}-\phi_S} \\
|\uparrow_1\downarrow_2\rangle_{\frac{\pi}{2}-\phi_S} &\rightarrow e^{i\frac{\pi}{2}} |\uparrow_1\downarrow_2\rangle_{\frac{\pi}{2}-\phi_S} \\
|\downarrow_1\uparrow_2\rangle_{\frac{\pi}{2}-\phi_S} &\rightarrow e^{i\frac{\pi}{2}} |\downarrow_1\uparrow_2\rangle_{\frac{\pi}{2}-\phi_S} \\
|\downarrow_1\downarrow_2\rangle_{\frac{\pi}{2}-\phi_S} &\rightarrow |\downarrow_1\downarrow_2\rangle_{\frac{\pi}{2}-\phi_S}
\end{aligned}$$

In the case when two ions are anti-aligned, each ion experiences an equal

force but in opposite direction, such that after the application of the gate a geometric phase is accumulated. For other cases, the phase might be only acquired by the ions aligned in the same direction.

If we take a specific example setting $\phi_S = 0$ (more discussions are given in the next paragraph), the time-evolution operator for the MS gate is $\hat{U}_{\mathrm{MS}}(t) = \exp\left(-i\frac{\pi}{8}\hat{S}_y^2\right)$, where $\hat{S}_y = \hat{\sigma}_y^{(1)} - \hat{\sigma}_y^{(2)}$ for working with the stretch mode. As a result, we obtain the above truth table in the $\hat{\sigma}_y \otimes \hat{\sigma}_y$ basis. Written in the $\hat{\sigma}_z \otimes \hat{\sigma}_z$ basis is shown below

$$\begin{aligned}
|\uparrow_1\uparrow_2\rangle &\rightarrow \frac{1}{\sqrt{2}}(|\uparrow_1\uparrow_2\rangle - i\,|\downarrow_1\downarrow_2\rangle)\\
|\uparrow_1\downarrow_2\rangle &\rightarrow \frac{1}{\sqrt{2}}(|\uparrow_1\downarrow_2\rangle + i\,|\downarrow_1\uparrow_2\rangle)\\
|\downarrow_1\uparrow_2\rangle &\rightarrow \frac{1}{\sqrt{2}}(|\downarrow_1\uparrow_2\rangle + i\,|\uparrow_1\downarrow_2\rangle)\\
|\downarrow_1\downarrow_2\rangle &\rightarrow \frac{1}{\sqrt{2}}(|\downarrow_1\downarrow_2\rangle - i\,|\uparrow_1\uparrow_2\rangle)
\end{aligned}$$

where the global phase $e^{-i\pi/4}$ is omitted. This gate has been implemented with a fidelity of 99.3 % using a quadrupole transition (optical qubits) in $^{40}Ca^+$ ion, where they used the COM mode instead [Benhelm 08a]. The groups at NIST and Maryland also realized this type of gate operation using stimulated Raman transitions [Gaebler 12, Haljan 05a].

Experimental Issue - Phase Coherence

As we have seen before, after completion of the gate the spin states of the two ions are entangled and are not entangled with any motional state. This implies that next gate operations do not have memory of the motional phase from the previous one, but the spin phase from previous gates is retained in the internal states of the qubits. Thus the spin phase needs to be stable throughout the whole quantum computational experiment and certainly both spin and motional phases have to be stable during a gate operation. In this section we would like to investigate these phases and how to minimize the effect of phase fluctuations on the coherence of the entangled state [Lee 05].

In Eq. (2.69), the spin phase $\phi_S = (\phi_B + \phi_R)/2$ determines the spin orientation to which the differential force is applied and the motional phase $\phi_M = (\phi_B - \phi_R)/2$ determines the direction of the trajectory of the motional mode in phase space. To be clear, we show two possible configurations for achieving the MS gate with the stimulated Raman transition. Figure 2.10(a) shows the standard configuration, where the red sideband is driven with two laser frequencies ω_r and ω_a and $\phi_R = \phi_r - \phi_a$, and for the blue sideband drive two frequencies are ω_b and ω_a so $\phi_B = \phi_b - \phi_a$; The second laser arrangement is illustrated in Fig.

2.10(b), where the frequency difference of ω_r and ω_b is twice the frequency splitting of the qubit with $\phi_B = \phi_b - \phi_a$ and $\phi_R = \phi_a - \phi_r$. It is noted that the sign of ϕ_R in the second case is changed because $\omega_a > \omega_r$ referred to the definitions in Chapter 2.5. ϕ_a, ϕ_b, and ϕ_r depends on the optical setup of the Raman beams and the phase that we apply to the AOM (Acousto-optic modulator, which is used to tune the laser frequency in tens of MHz range). Usually the phase of the AOM modulation can be controlled very stably. The main concern is the the beam path difference between two arms of the Raman beam setup in which one arm called A provides ω_a frequency component and the other called B generates ω_b and ω_r frequency components. The phase difference between two Raman beams will be $k_A x_A - k_B x_B$ related to ϕ_B and ϕ_R.

Let's look at Fig. 2.10(a), the spin phase is calculated to be $\phi_S = \phi_b + \phi_r - 2\phi_a$ so it is sensitive to the beam path fluctuations between arm A and B. This is called "phase sensitive geometry". Reversely, for the configuration shown in Fig.2.10(b) the spin phase is $\phi_S = \phi_b - \phi_r$, which is very small because ϕ_b and ϕ_r come from the same optical path and all the fluctuation will be common for both such that they cancel out in ϕ_S [Haljan 05b]. This is called "phase insensitive geometry". However the phase fluctuations due to changes in the path length difference is now imposed on the motional phase ϕ_M. If the motional phase fluctuates during the gate operation, the trajectories of the motional mode in phase space will rotate by an random angle depending on the change of ϕ_M. Therefore as long as ϕ_M does not change during the application of the gate the result will remain independent of the motional phase. The discussions above are about the beam path fluctuations and the next question would be how to make the relative ϕ_M phase the same or stable seen by two ions. This can be achieved by tuning the trapping potential appropriately such that the distance between two ions is an integer or half-integer multiple of the effective optical wavelength (the same as the geometric phase gate). With this adjustment two ions can see the same ϕ_M. Experimentally it will require stable beam pointing on the ions and stable DC electrode voltage [Langer 06].

2.7 Off-Resonant Spontaneous Photon Scattering

In the previous sections, we describe the requirements and tools about how to perform quantum control with $^9Be^+$ ions. However owing to imperfect control of the experiment and intrinsic properties of quantum physics, it is important to understand what may cause the decoherence of quantum information stored in the ions. For example, the classical noise like laser intensity fluctuations, laser frequency drifts, and unstable laser phases, can lead to decoherence of the qubit. In principle, these types of classical noise can be controlled to levels below a certain threshold. On the other hand, there is a fundamental source of decoherence arising from the spontaneous photon scattering as the ion in-

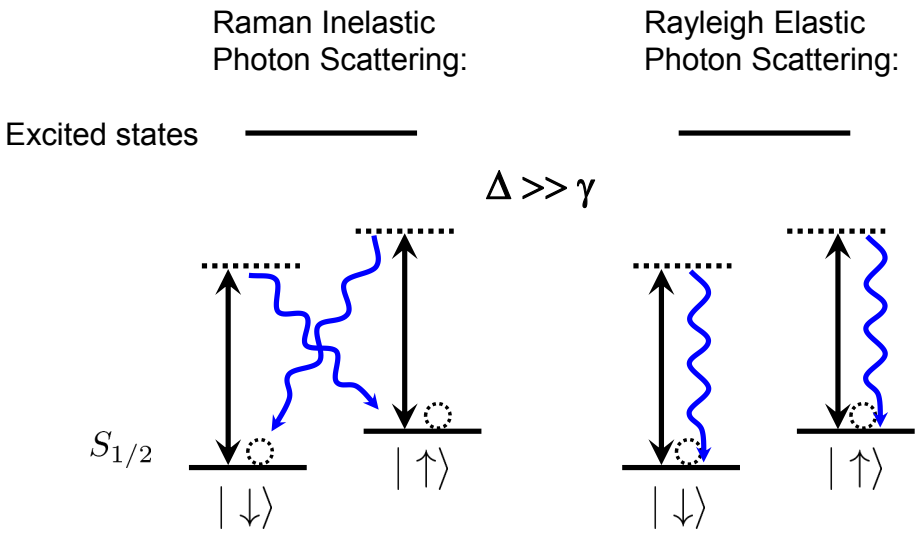

Figure 2.11: Illustration of two different photon scattering processes. The detuning of the Raman beams Δ is much larger than the natural linewidth of the excited states γ.

teracts with the quantum vacuum field [Wineland 98, Ozeri 07]. The photon scattering process for an ion can be categorized by two types: 1) Raman inelastic photon scattering; 2) Rayleigh elastic photon scattering. Both types of photon scattering mechanism for $^9Be^+$ ions have been theoretically and experimentally studied by the Ion Storage Group at NIST [Ozeri 05, Uys 10] and more explanations can be found in [Ozeri 07].

In this section, we only shortly introduce two types of the photon scattering process and then show some simulation results. The mechanism of both scattering events is illustrated in Fig. 2.11. Initially the ion is prepared in a superposition of two hyperfine ground states. After it interacts with an off-resonant laser beam (in our case, it's Raman beams), the ion has a probability being excited to the excited states and then the photon scattering occur.

For the Raman inelastic photon scattering the ion ends up in different internal states. If the frequency of the scattering photon is higher than that of the laser, the final state of the ion is the lower state, which is not a superposition state. It's the same that if the frequency of the scattering photon is lower than that of the laser, the final state of the ion is the higher state, also not a superposition. So the Raman scattering essentially projects the ion's state and destroys the coherence of superposition. In some sense, this process can be thought of a far-off-resonance optical pumping.

For the Rayleigh elastic photon scattering, the post-scattering state of the ion

does not change, meaning that the energy of the incident photon is conserved and the only change may be its direction. If the ion is initially prepared in a hyperfine superposition, the final state after the Rayleigh scattering process remains a coherent superposition and the scattered photon does not take away information about the quantum state of the ion. However, if the two hyperfine states have different Rayleigh scattering rates, the Rayleigh decoherence could be dominant even in the presence of the decoherence induced from the Raman scattering [Uys 10].

We consider a non-resonant laser field $\mathbf{E} = \hat{\epsilon}E\cos(\mathbf{k}\cdot\mathbf{r} - \omega t + \phi)$, where $\hat{\epsilon} \equiv \epsilon_+\hat{\sigma}^+ + \epsilon_0\hat{\pi} + \epsilon_-\hat{\sigma}^-$ is the polarization component of the light satisfying the normalization condition $\sum_{k\in\{+,0,-\}}\epsilon_k^2 = 1$. $\hat{\sigma}^+$ ($\hat{\sigma}^-$) is right (left) circularly polarized with respect to the quantization axis, which is defined as the direction of the magnetic field, and $\hat{\pi}$ component is parallel to the magnetic field. The rate of the photon scattering event from states $|i\rangle$ to $|f\rangle$ can be calculated using the Kramers-Heisenberg formula [Ozeri 05, Loudon 95]:

$$\Gamma_{i,f} = \frac{g^2}{4}\gamma\sum\nolimits_q\left|\frac{a_{i\to f}^{(1/2)}}{\Delta} + \frac{a_{i\to f}^{(3/2)}}{\Delta-\Delta_F}\right|^2 \tag{2.70}$$

where $g = \frac{E\mu}{\hbar} = \gamma\sqrt{\frac{s_0}{2}}$ is the single-photon Rabi frequency (E is the electric field amplitude of the laser beam, and $\mu = |\langle P_{3/2}, F' = 3, m'_F = 3|\mathbf{d}\cdot\hat{\sigma}^+|S_{1/2}, F = 2, m_F = 2\rangle|$ is the magnitude of the cycling transition electric-dipole moment.), the coefficient $a_{i\to f}^{(J)} = \sum_{e\in J}\langle f|\mathbf{d}\cdot\hat{\sigma}^q|e\rangle\langle e|\mathbf{d}\cdot\hat{\epsilon}|i\rangle/\mu^2$ is the normalized transition amplitude from state $|i\rangle$ to state $|f\rangle$ through an intermediate state $|e\rangle$ and here we sum over all the excited states $|e\rangle$ that belong to $P_{1/2}$ and $P_{3/2}$ states respectively. Δ is the laser detuning from the $S_{1/2} \leftrightarrow P_{1/2}$ transition and Δ_F is the frequency difference of $P_{1/2}$ and $P_{3/2}$ states. It is worth nothing that we consider the scattered photons with different polarizations do not interfere and thus we sum over different polarizations q of the scattering light after taking the modulus square of the amplitude. The only situation that the scattering photons can interfere is the emitting photons from $P_{1/2}$ and $P_{3/2}$ states decaying to the same final state with the same polarization due to a coherence between two P states[1]. The Raman scattering rate Γ_{Raman} is then given by summing over all the rates where $i \neq f$ for all the final states $|f\rangle$ as follows:

$$\Gamma_{\text{Raman}} = \sum_{f\neq i}\Gamma_{i,f} \tag{2.71}$$

The Rayleigh scattering rate is given by [Uys 10]

$$\Gamma_{\text{Rayleigh}} = \frac{g^2}{4}\gamma\sum\nolimits_q\left|\left(\frac{a_{u\to u}^{(1/2)}}{\Delta} + \frac{a_{u\to u}^{(3/2)}}{\Delta-\Delta_F}\right) - \left(\frac{a_{d\to d}^{(1/2)}}{\Delta} + \frac{a_{d\to d}^{(3/2)}}{\Delta-\Delta_F}\right)\right|^2 \tag{2.72}$$

[1]Private communication with NIST group.

where u and d stand for the qubit states $|\uparrow\rangle$ and $|\downarrow\rangle$. When the qubit states have different normalized transition amplitudes, or they have roughly equal transition strength but opposite sign, then the Rayleigh scattering rate can be comparable to the Raman scattering rate or even larger. Essentially both Raman and Rayleigh scattering rates can be written in an analytical form [Langer 06], but in here we try to avoid the redundant mathematics.

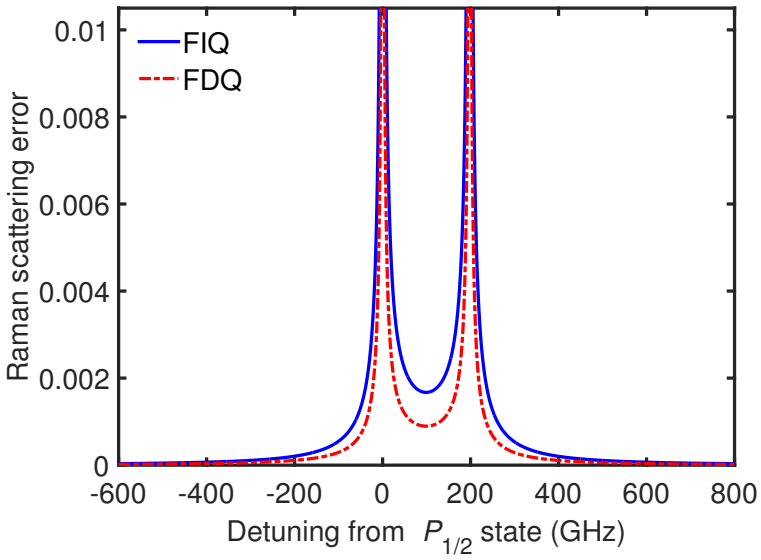

Figure 2.12: The calculated probability to scatter a Raman photon during a π rotation as a function of Raman detuning from the $P_{1/2}$ state. Two different qubits are considered here. FDQ: $|\uparrow\rangle \equiv \left|S_{1/2}, F=1, m_F=1\right\rangle$ and $|\downarrow\rangle \equiv \left|S_{1/2}, F=2, m_F=2\right\rangle$ and FIQ: $|\uparrow\rangle \equiv \left|S_{1/2}, F=1, m_F=1\right\rangle$ and $|\downarrow\rangle \equiv \left|S_{1/2}, F=2, m_F=0\right\rangle$. The polarizations of light used are $\hat{\epsilon}_b = \hat{\epsilon}_r = -\frac{1}{2}\hat{\sigma}^+ + \frac{1}{\sqrt{2}}\hat{\pi} + \frac{1}{2}\hat{\sigma}^-$. The laser powers and beam waist are fixed in the simulation.

Given the Raman and Rayleigh scattering rates, we are interested in the spontaneous scattering error during the gate operations. We can estimate this error by considering the probability of scattering event to occur during a gate time. First of all, we start from the single-qubit gate for which we just consider a π-pulse. The duration τ_π required to perform a π rotation is determined by the relation $\pi = |\Omega|\tau_\pi$, where $|\Omega|$ is the Raman Rabi frequency defined in Eq. (2.43). In some literatures τ_π can be found to be $\pi = 2|\Omega|\tau_\pi$ due to a factor of 2 difference in the definition of the Rabi frequency, but different ways of defining the Rabi frequency will not affect the results. The probability of scattering a photon through the Raman scattering process during the π time

is given by

$$P_{\text{err}}^{\text{S}} = \frac{1}{2}\left(\Gamma_{\text{Raman}}^{\uparrow,b} + \Gamma_{\text{Raman}}^{\uparrow,r} + \Gamma_{\text{Raman}}^{\downarrow,b} + \Gamma_{\text{Raman}}^{\downarrow,r}\right)\tau_\pi \tag{2.73}$$

$$= \frac{\pi}{2|\Omega|}\left(\Gamma_{\text{Raman}}^{\uparrow,b} + \Gamma_{\text{Raman}}^{\uparrow,r} + \Gamma_{\text{Raman}}^{\downarrow,b} + \Gamma_{\text{Raman}}^{\downarrow,r}\right) \tag{2.74}$$

Here we assume that the qubit stays in $|\uparrow\rangle$ and $|\downarrow\rangle$ states for the same amount of time so we take the average of the scattering rate of the two qubit states. Each qubit state experiences both blue and red Raman beams. Figure 2.12 shows the spontaneous scattering error for the field-dependent qubit ($|\uparrow\rangle \equiv |S_{1/2}, F = 1, m_F = 1\rangle$ and $|\downarrow\rangle \equiv |S_{1/2}, F = 2, m_F = 2\rangle$) and the field-independent qubit ($|\uparrow\rangle \equiv |S_{1/2}, F = 1, m_F = 1\rangle$ and $|\downarrow\rangle \equiv |S_{1/2}, F = 2, m_F = 0\rangle$) versus different Raman detunings. It is found that the probability to scatter a Raman photon gets down to $\sim 10^{-5}$ when $\Delta \gg \Delta_F$. This suggests that we can increase the detuning to reduce the Raman scattering probability, however the π time will be longer using the same laser power. There is no such thing as a free lunch. To maintain the same Rabi frequency (the same π time) and to reduce the Raman scattering error, we require more laser power which is technically challenging in general. In [Ozeri 07] the authors quantify what power is needed for a given spontaneous scattering error with different species of ions.

The two-qubit quantum gate is a key element for quantum computation and so far the error of the two-qubit gate operation is still higher than the fault-tolerant threshold. Here we show how to calculate the spontaneous scattering probability during the Mølmer-Sørensen gate operation for example. Since implementing the MS gate with $^9Be^+$ ions requires three beams (see Fig. 2.10(a)), the probability of scattering a photon through the Raman scattering process during the gate time τ_{gate} is given by

$$P_{\text{err}}^{\text{MS}} = 2 \times \frac{1}{2}\big(\Gamma_{\text{Raman}}^{\uparrow,r} + \Gamma_{\text{Raman}}^{\uparrow,b} + \Gamma_{\text{Raman}}^{\uparrow,a} + \Gamma_{\text{Raman}}^{\downarrow,r} + \Gamma_{\text{Raman}}^{\downarrow,b} + \Gamma_{\text{Raman}}^{\downarrow,a}\big)\tau_{\text{gate}} \tag{2.75}$$

where the factor of 2 accounts for two ions, the factor of $\frac{1}{2}$ comes from the same consideration for the single-qubit gate, and the gate time is given by $\tau_{\text{gate}} = 2\pi/|\omega_z - \delta'|$. For a gate operation, the Rabi frequency is set such that $\eta\Omega \approx |\omega_z - \delta'|/2$, thus $\tau_{\text{gate}} \approx \pi/(\eta\Omega)$. The Raman scattering probability during the MS gate duration as a function of detuning is plotted in Fig. 2.13. In the simulation, we keep the laser power fixed and assume a Lamb-Dicke parameter of $\eta = 0.25$. The laser beam polarizations used are $\hat{\epsilon}_b = \hat{\epsilon}_r = \frac{1}{\sqrt{2}}\hat{\sigma}^+ + \frac{1}{\sqrt{2}}\hat{\sigma}^-$ and $\hat{\epsilon}_a = -\frac{1}{2}\hat{\sigma}^+ + \frac{1}{\sqrt{2}}\hat{\pi} + \frac{1}{2}\hat{\sigma}^-$. We can see that the spontaneous scattering error also drops as the detuning is larger. The calculated errors for single- and two-qubit gates as well as the relative gate time are summarized in Table 2.1. If we demand the errors on the $< 10^{-3}$ level for a MS gate, the laser

detuning must be larger than 500 GHz red from the $P_{1/2}$ state. If we want to maintain the same Rabi frequency and reduce the error by increasing the laser detuning, we would require more laser power in each Raman beam given by the relative Rabi frequency ratio. This is why a high power laser source is useful in order to be able to perform fault-tolerant quantum computation (see Chapter 5.3). It is worth noting that if one performs a two-qubit gate consisting of one beryllium and one calcium ion for which the calcium qubit is driven by the 729 nm quadrupole transition, the Raman scattering error due to spontaneous emission can be reduced by factor of 2, compared to the same operation using two beryllium ions, because this error source is only contributed from the beryllium ion.

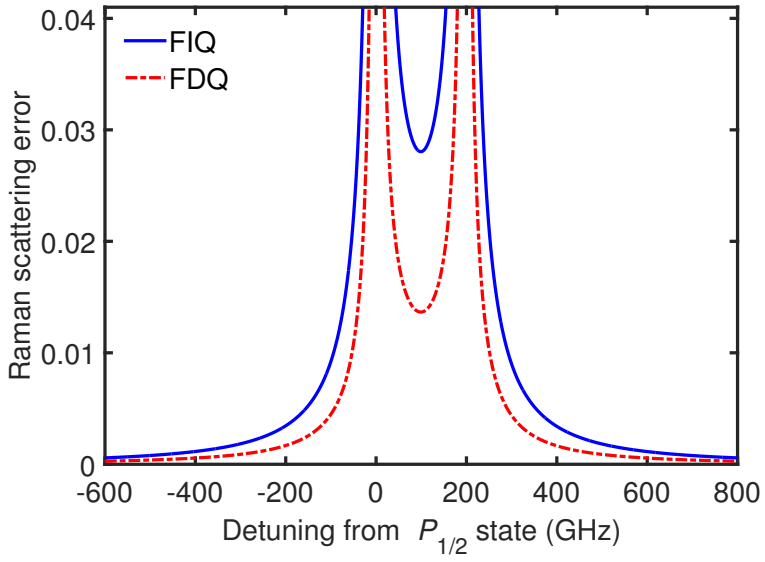

Figure 2.13: The calculated probability to scatter a Raman photon during a π rotation as a function of Raman detuning from the $P_{1/2}$ state. Two different qubits are considered here. FDQ: $|\uparrow\rangle \equiv |F=1, m_F=1\rangle$ and $|\downarrow\rangle \equiv |F=2, m_F=2\rangle$ and FIQ: $|\uparrow\rangle \equiv |F=1, m_F=1\rangle$ and $|\downarrow\rangle \equiv |F=2, m_F=0\rangle$. The polarizations of light used are $\hat{\epsilon}_b = \hat{\epsilon}_r = \frac{1}{\sqrt{2}}\hat{\sigma}^+ + \frac{1}{\sqrt{2}}\hat{\sigma}^-$ and $\hat{\epsilon}_a = -\frac{1}{2}\hat{\sigma}^+ + \frac{1}{\sqrt{2}}\hat{\pi} + \frac{1}{2}\hat{\sigma}^-$. The laser powers and beam waist are fixed in the simulation.

Until now, we have not considered the effect of Rayleigh scattering on the gate errors. These discussions are widely covered in [Ozeri 07]. The Rayleigh scattering is elastic so there is no energy transfer between the photon and the internal degree of freedom of the ion. The main effect of this type of scattering process is a momentum kick on the ion's motion because the ion experiences a recoil from the scattering photon. For the single-qubit gate, the two Raman beams are usually set up in a co-propagating configuration such that it

is insensitive to ion's motion. Therefore, we can say Rayleigh scattering has a negligible effect during the single-qubit gate operation. On the other hand, the Rayleigh scattering has more influence on the two-qubit gate. The recoil from the scattering photons perturbs the trajectory of ions' motion in phase space. Once the trajectory is distorted in phase space, not a complete circle anymore, this causes gate errors [Ozeri 07].

Δ (GHz)	MS gate Raman scattering error	π-pulse scattering error	Relative gate time
-600	5.74×10^{-4}	3.42×10^{-5}	6.015
-500	7.88×10^{-4}	4.69×10^{-5}	4.384
-400	1.10×10^{-3}	6.85×10^{-5}	3.005
-300	1.80×10^{-3}	1.10×10^{-4}	1.877
-200	3.50×10^{-3}	2.06×10^{-4}	1.000
-100	9.20×10^{-3}	5.50×10^{-4}	0.374
100	2.80×10^{-2}	1.70×10^{-3}	0.123
200	6.87×10^{-1}	4.10×10^{-2}	0.005
300	9.00×10^{-3}	5.35×10^{-4}	0.384
400	3.40×10^{-3}	2.03×10^{-4}	1.015
500	1.80×10^{-3}	1.08×10^{-4}	1.897
600	1.10×10^{-3}	6.79×10^{-5}	3.030

Table 2.1: The calculated results for the gate errors with respect to different detunings. In the simulation, the field-independent qubit is used, and we fix the laser power (10 mW in each Raman beam) and the laser beam waist ($w = 30$ μm). The polarizations of the light used for the MS gate are $\hat{\epsilon}_b = \hat{\epsilon}_r = \frac{1}{\sqrt{2}}\hat{\sigma}^+ + \frac{1}{\sqrt{2}}\hat{\sigma}^-$ and $\hat{\epsilon}_a = -\frac{1}{2}\hat{\sigma}^+ + \frac{1}{\sqrt{2}}\hat{\pi} + \frac{1}{2}\hat{\sigma}^-$, and for the single-qubit gate are $\hat{\epsilon}_b = \hat{\epsilon}_r = -\frac{1}{2}\hat{\sigma}^+ + \frac{1}{\sqrt{2}}\hat{\pi} + \frac{1}{2}\hat{\sigma}^-$. The gate error becomes large at $\Delta = 200$ GHz because this positive detuning from $P_{1/2}$ state is very close to $P_{3/2}$ state ($\Delta_F = 198$ GHz). The relative gate time shown here is the same for MS and sinlge-qubit gates, independent of the polarizations.

Chapter 3

The $^{40}Ca^{+}$ Qubit

The other ion species used in our group is calcium. Calcium ions have been used to perform a plenty of beautiful experiments [Blatt 12, Home 06a] and shown to be a well suited qubit candidate for quantum information science [Blatt 08]. For practical implementations, the laser sources required for control of calcium ions are all commercially available[1]. The calcium ion has many isotopes [Lucas 04a] in which we are in particular interested in the $^{40}Ca^{+}$ ion because its properties are most well-known, and it is easier to work with due to zero nuclear spin and it has maximum natural abundance.

In this chapter I will describe my main contributions to the calcium project, and the rest of the details about $^{40}Ca^{+}$ ions can be found in [Kienzler 15b]. First, I will introduce how to generate $^{40}Ca^{+}$ ions using the two-photon photoionization scheme. The atomic structure of $^{40}Ca^{+}$ ions, the required laser sources and how we identify the qubit are shortly discussed. Since we use a magnetic field of 119.45 G for the $^{9}Be^{+}$ ion in order to work with a field-independent qubit, this leads to the energy level splitting of the $^{40}Ca^{+}$ ion larger than the natural linewidth of the states. Under the circumstances, to efficiently control the $^{40}Ca^{+}$ ion requires more laser beams to address the transition than usual, this makes the system more complex than many previous setups. Therefore, we try to find optimal working parameters, like the laser intensity and detunings, by solving the optical Bloch equations for a multi-level atomic system. The results will be presented in the end.

3.1 Photoionization of Neutral Calcium Atoms

Photoionization has several advantages compared to electron bombardment [Lucas 04a], for example photoionization is isotope selective such that only the desired isotope of the ion species is loaded into the trap, there is no

[1] Toptica Photonics AG, http://www.toptica.com/

charging problem on the trap caused by the use of electron beams, and the efficiency of using photoionization is much higher, requiring lower densities of neutral atoms. The ionization energy of neutral calcium atoms is approximately 6.11 eV, corresponding to the required laser wavelength of 202.8 nm. This deep UV light is very hard to produce. In the typical experimental setup, generation of calcium ions is performed by a two-photon photoionization method. Two-photon photoionization of calcium for loading in a Paul trap was first demonstrated using laser light at 272 nm [Kjaergaard 00], later another approach was implemented using near 423 nm and 376 nm light instead [Gulde 01, Schuck 10]. The first approach needs a complicated laser system, by comparison the second technique is easier to manage because we can get the laser sources directly from laser diodes or from simple frequency conversion.

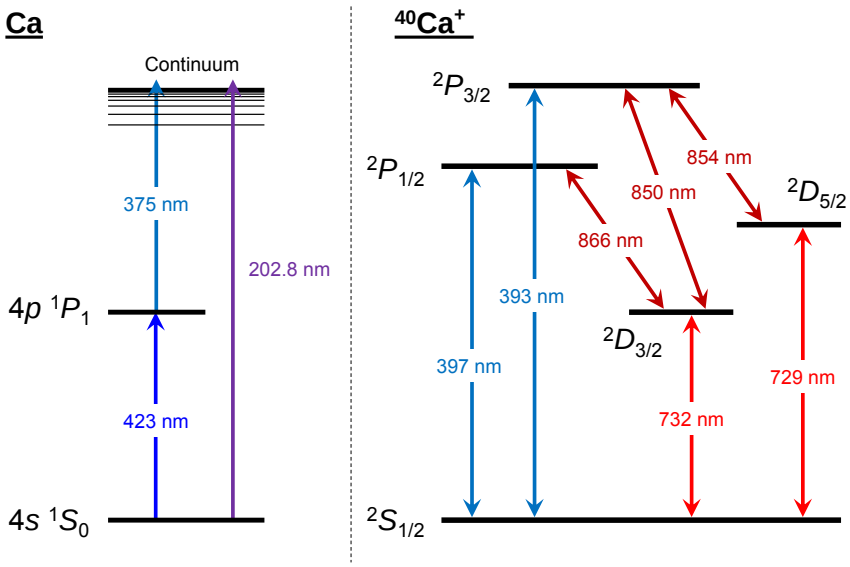

Figure 3.1: Left: Energy levels and light wavelengths used in the photoionization process of neutral calcium. Right: Energy level diagram and transition wavelengths of $^{40}Ca^{+}$ ions.

The energy levels and laser wavelengths used in the photoionization process of neutral calcium atoms is depicted in Fig. 3.1. In the first stage, we shine a laser at 422.7915 nm driving the transition from the ground $4s\ ^1S_0$ state to the $4p\ ^1P_1$ excited state. The linewidth of this dipole transition is $2\pi \times 34.7$ MHz, the laser frequency has to be tuned close to the resonance to enhance the excitation rate. Since the photoionization beam is $\approx 30^\circ$ to the normal of

the neutral calcium atomic beam, the laser frequency is Doppler shifted by ≈ 400 MHz in the reference frame of the atoms. One can check what the laser frequency should be by observing the neutral fluorescence from the calcium atoms. When the laser frequency is close to the atomic transition, we could see the atom cloud fluorescing on a camera. The 423 nm light is obtained by the second harmonic generation (SHG) from an 846 nm diode laser using a periodically poled potassium titanyl phosphate (PPKTP) waveguide chip. Here we monitor the frequency of the pump light on a wavelength meter. The SHG is performed within a compact fiber-in fiber-out module provided from AdvR (see Fig. 3.2). The temperature of the PPKTP waveguide needs to be controlled and stabilized to fulfill the phase matching condition. With an input power of roughly 100 mW at 846 nm, we are able to get maximally 4 mW output at 423 nm which includes the loss in the input and output fiber connectors. The saturation intensity of the $4s\ ^1S_0 \leftrightarrow 4p\ ^1P_1$ transition is 0.6 mW/mm^2 so the optical power required to drive this transition is only 10 µW with a beam waist of 70 µm. The 423 nm light power is sufficient for three trapped ion setups in our group. At the second stage of the photoionization process, the laser just needs high enough photon energies to excite the ion to a continuum state so the laser frequency is not that critical. Here we use a free running laser at 375 nm that is a simple laser module directly controlled by a computer. Typically the loading time of the ion is around a couple of minutes. The details of the atomic oven, which is used to produce the neutral calcium atoms, and the loading process can be found in [Kienzler 15b].

Figure 3.2: 846 nm to 423 nm frequency conversion module. It is a simple fiber-in and fiber-out device for which the temperature of the PPKTP waveguide chip inside needs to be stabilized for achieving the phase matching condition. The SHG temperature coefficient of the module is ≈ 0.06 nm/^{o}C.

3.2 Atomic Structure

Calcium ions have similar electrical structures to alkali neutral atoms, with a single valence electron. The energy level diagram of the $^{40}Ca^{+}$ ion and the corresponding transition wavelengths are shown in Fig. 3.1. It has a ground state $^2S_{1/2}$, and two excited states $^2P_{1/2}$ and $^2P_{3/2}$. In addition calcium ions have the low-lying $^2D_{3/2}$ and $^2D_{5/2}$ metastable states. This makes the odd-isotope of calcium ions difficult to use, and therefore we use an isotope with zero nuclear spin instead, which is the ^{40}Ca. Shown in Fig. 3.1, the $^2S_{1/2} \leftrightarrow {}^2P_{1/2}$, $^2S_{1/2} \leftrightarrow {}^2P_{3/2}$, $^2P_{1/2} \leftrightarrow {}^2D_{3/2}$, $^2P_{3/2} \leftrightarrow {}^2D_{3/2}$ and $^2P_{3/2} \leftrightarrow {}^2D_{5/2}$ transitions are dipole-allowed, where the lifetime of the $^2P_{1/2}$ and $^2P_{3/2}$ is $\sim$ 7 ns (the natural linewidth $\sim 2\pi \times 22.7$ MHz) [Jin 93], whereas the $^2D_{3/2}$ and the $^2D_{5/2}$ states are metastable with a lifetime of $\sim$ 1.1 s [Barton 00]. As we can see, the advantage of the calcium ion is that the laser sources required to drive all the possible transitions are all commercially available. All the laser frequencies are stabilized and locked to a reference cavity using the Pound-Drever-Hall technique [Drever 83].

Because of the lack of hyperfine structure in the $^{40}Ca^{+}$ ion, the energy level shift is linearly proportional to the applied magnetic field, given by $\Delta E = \mu_B g_J m_J B$, where $\mu_B = h \cdot 1.399624$ MHz/G is the Bohr magneton, g_J is the Landé g-factor, m_J is the quantum number of the total angular momentum projected on the z-axis, and B is the magnetic field. The energy splittings of each state with $B = 119.45$ G and the transition wavelengths relevant for this thesis are shown in Fig. 3.3.

In order to produce fluorescence from calcium ions as is required for Doppler cooling an ion and qubit readout, we use a combination of 397 nm and 866 nm light. The dynamics of the fluorescence generation is complicated by the presence of interference effects between the two light fields, and due to the large energy level splitting in the magnetic field of 119.45 G (these energy level splittings are larger than the natural linewidth of the transition). In order to find optimal settings for our lasers, we set up simulations of the $S_{1/2}$, $P_{1/2}$ and $D_{3/2}$ states using the master equation treatment where the ion interacts with classical electromagnetic fields while undergoing spontaneous emission. The details will be introduced in the next Section.

All coherent quantum operations make use of the quadrupole transition between these levels at 729 nm. The qubit states are encoded in the internal electronic states $|S_{1/2}, m_J = 1/2\rangle$ and $|D_{5/2}, m_J = 3/2\rangle$ that has lower sensitivity to magnetic field fluctuations compared to other qubit candidates while having a high coupling strength for our chosen beam direction [Kienzler 15b]. Compared to the qubit states we use in $^9Be^{+}$ ions, the one in $^{40}Ca^{+}$ is called an optical qubit which only relies on a single-photon transition. The main advantage of using an optical qubit for quantum computation is that there is no fundamental problem of the spontaneous emission during the coherent

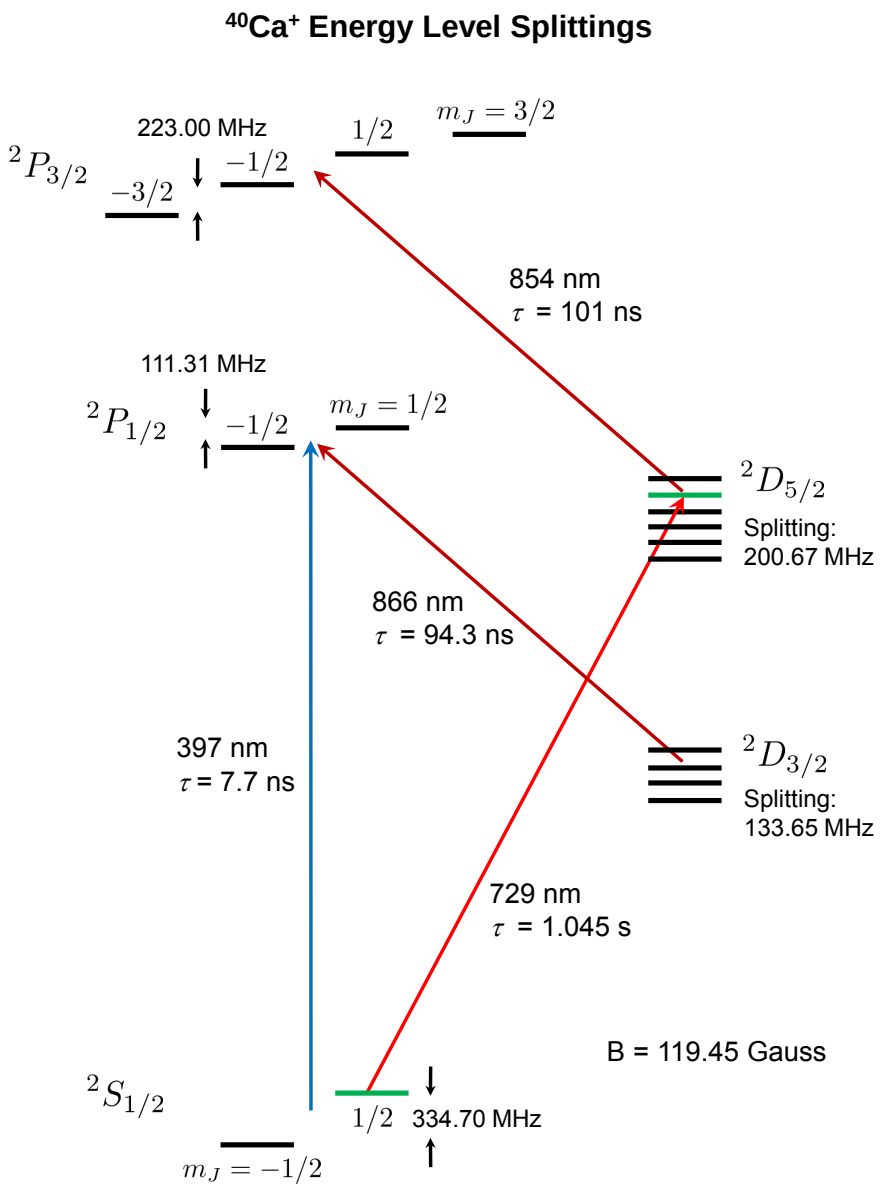

Figure 3.3: Transition wavelengths used in the experiments and the energy level splittings in an external magnetic field of 119.45 G. The qubit states are chosen from two internal electronic states $|S_{1/2}, m_J = 1/2\rangle$ and $|D_{5/2}, m_J = 3/2\rangle$, labeled with green.

operations as long as the time interval of the operations is shorter than the lifetime of the $D_{5/2}$ states. However, using an optical qubit needs very good laser frequency stability due to the narrow linewidth of the metastable state. In our

case the qubit coherence time is also limited by magnetic field fluctuations.

The qubit initialization is carried out by both the 854 nm laser light that repumps the population from the $D_{5/2}$ state back to the $S_{1/2}$ and the 397 nm light that resets the population from $|S_{1/2}, m_J = -1/2\rangle$ to $|S_{1/2}, m_J = 1/2\rangle$ through the $P_{1/2}$ excited state. The 397 nm light used in the qubit initialization is vertically polarized for which the ion experiences both $\hat{\sigma}^+$ and $\hat{\sigma}^-$ polarization components according to our beam configurations (see Fig. 5.2). If the laser frequency is tuned on resonance for the $\hat{\sigma}^+$ component, then the $\hat{\sigma}^-$ component is about 446 MHz blue detuned with respect to its transition. Hence, the effect of this off-resonant drive on the qubit initialization process can be ignored to first order when using the 397 nm power below one saturation intensity. The saturation intensity for each dipole transition is calculated with the formula $I_{\text{sat}} = \frac{\hbar\omega^3\Gamma}{12\pi c^2} \times 10^{-3}$ mW/mm^2. They are $I_{\text{sat}} = 0.466$ mW/mm^2 for the 397 nm transition and $I_{\text{sat}} = 0.003$ mW/mm^2 for both 866 nm and 854 nm transitions.

3.3 Optical Bloch Equations for an Eight-Level Atomic System

As mentioned before, the application of the 866 nm and 397 nm light fields is responsible for the Doppler cooling and the qubit readout, requiring a high rate of photon scattering. Therefore, how to obtain fluorescence from the ion as much as possible becomes an important issue in the experiment. For the trapped ion groups who work with the calcium ions, we use a relatively high magnetic fields of 119.45 G. This makes the resonance fluorescence more difficult to control due to large energy level splittings. In this case, we use more laser beams with different frequencies and polarizations. Meanwhile we need to avoid the dark resonance generated from two laser fields due to quantum interference effects. Here we set up a numerical simulation for an eight-level atomic system by solving the optical Bloch equations. By doing so, we are able to find optimal parameters for our laser settings.

The energy levels involved in the problem are shown in Fig. 3.4. We denote the levels from $|1\rangle$ to $|8\rangle$, which are the Zeeman sublevels in $S_{1/2}$, $P_{1/2}$ and $D_{3/2}$ states. The 397 nm laser field contains two frequencies with the polarization $\hat{\pi}$ and $\hat{\sigma}^+/\hat{\sigma}^-$ for each frequency. The 866 nm light field has two frequency components as well and both are circularly polarized. The optical setups are described in [Kienzler 15b]. Here we focus on the simulations. The Hamiltonian describing the total system is given by

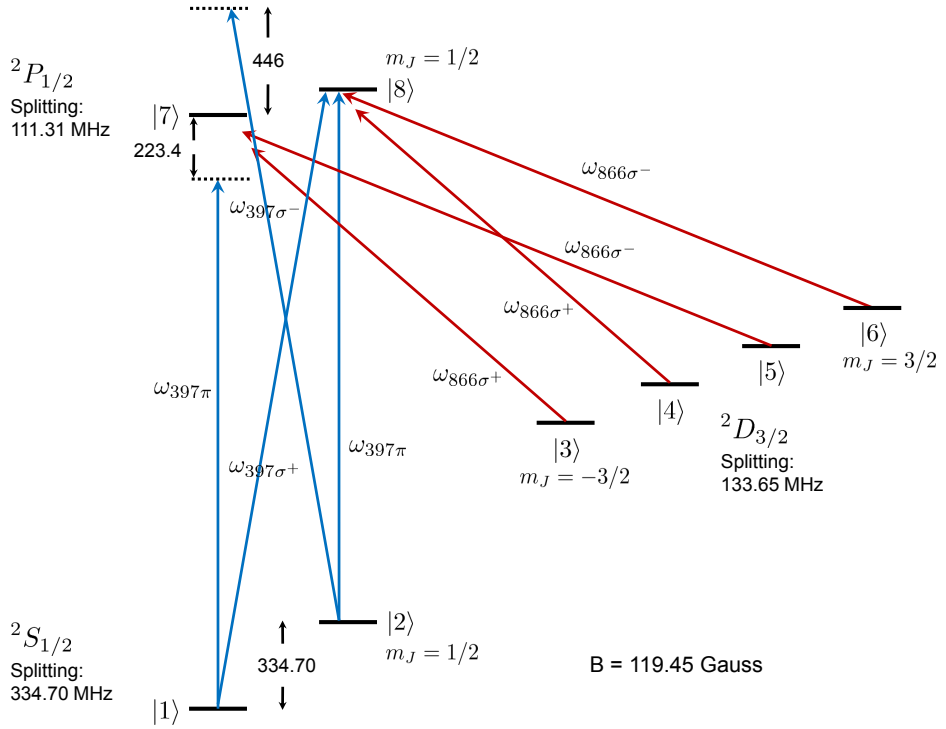

Figure 3.4: The energy levels used in the simulation of optical Bloch equations. The frequency and polarization of the laser beams are shown. For the simulations, we define $\Delta_{397\sigma^+} \equiv \omega_{397\sigma^+} - (\omega_8 - \omega_1)$, $\Delta_{397\pi} \equiv \omega_{397\pi} - (\omega_8 - \omega_2)$, $\Delta_{866\sigma^-} \equiv \omega_{866\sigma^-} - (\omega_8 - \omega_6)$, and $\omega_{866\sigma^+} = \omega_{866\sigma^-} + \omega_{\mathrm{AOM}}$. It should be noted that the laser configurations in the real situation are much more complicated than that we consider in the simulation. The frequency $\omega_{866\sigma^+} = \omega_{866\sigma^-} + \omega_{\mathrm{AOM}}$ that couples the $|8\rangle \leftrightarrow |4\rangle$ transition is not purely $\hat{\sigma}^+$ polarized and also has the $\hat{\sigma}^-$ polarization component. Therefore, for example the $|8\rangle \leftrightarrow |6\rangle$ transition is not only driven by one frequency component ($\omega_{866\sigma^-}$) but also driven by $\omega_{866\sigma^-} + \omega_{\mathrm{AOM}}$. This would make the problem quite hard to solve.

$$\begin{aligned}\hat{H} &= \hat{H}_a + \hat{H}_l \\ &= \sum_{a=1}^{8} \hbar\omega_a |a\rangle\langle a| + \mathbf{d}\cdot\sum_i \mathbf{E_i} \end{aligned} \tag{3.1}$$

where $\hat{H}_a$ is the atomic Hamiltonian and $\hat{H}_l$ is the Hamiltonian of the interactions mediated by the applied light fields. The dipole operator $\mathbf{d}$ is defined as a form similar to Eq. (2.25), $\mathbf{E}_i = \hat{\epsilon}_i E_i \cos(\mathbf{k}_i\cdot\mathbf{r} - \omega_i t + \phi_i)$ for $i \in \{397\sigma^+, 397\pi, 866\sigma^+, 866\sigma^-\}$ are the monochromatically laser fields, where E_i and $\hat{\epsilon}_i$ are the amplitude and the polarization of the electric field, $\mathbf{k}_i$ is the wave vector, $\mathbf{r}$ is the position of the ion, and ω_i and ϕ_i are the frequency and the phase of the laser respectively. The spatial dependence $\mathbf{k}_i\cdot\mathbf{r}$ can be neglected using the dipole approximation. The laser phase is not crucial in the following discussions so we drop it. Therefore the matrix elements of the interaction term $(\hat{H}_l)_{mn} = \langle m|\hat{H}_l|n\rangle$ can be written as

$$\begin{aligned}
(\hat{H}_l)_{17} &= (\hat{H}_l)_{71} = \hbar\Omega_{397\pi}\cos(\omega_{397\pi}t) \\
(\hat{H}_l)_{18} &= (\hat{H}_l)_{81} = \hbar\Omega_{397\sigma^+}\cos(\omega_{397\sigma^+}t) \\
(\hat{H}_l)_{28} &= (\hat{H}_l)_{82} = \hbar\Omega_{397\pi}\cos(\omega_{397\pi}t) \\
(\hat{H}_l)_{37} &= (\hat{H}_l)_{73} = \hbar\Omega_{866\sigma^+}\cos(\omega_{866\sigma^+}t) \\
(\hat{H}_l)_{48} &= (\hat{H}_l)_{84} = \hbar\Omega_{866\sigma^+}\cos(\omega_{866\sigma^+}t) \\
(\hat{H}_l)_{57} &= (\hat{H}_l)_{75} = \hbar\Omega_{866\sigma^-}\cos(\omega_{866\sigma^-}t) \\
(\hat{H}_l)_{68} &= (\hat{H}_l)_{86} = \hbar\Omega_{866\sigma^-}\cos(\omega_{866\sigma^-}t)
\end{aligned}$$

where the Rabi frequency is $\Omega_i \equiv \frac{E_i\langle J', m'_J|\mathbf{d}\cdot\hat{\epsilon}_i|J, m_J\rangle}{\hbar}$. Here we do not consider the transition $|2\rangle \leftrightarrow |7\rangle$ driven by the $397\sigma^-$ light because its frequency is 446 MHz off-resonant from the level $|7\rangle$. We choose the zero energy point at level $|8\rangle$ and then transfer the Hamiltonian $\hat{H}$ into a rotating frame by using the operator

$$\begin{aligned}\hat{U} = \exp\Big[&-i\big(\omega_{397\sigma^+}|1\rangle\langle 1| + \omega_{397\pi}|2\rangle\langle 2| + (\omega_{866\sigma^+} - \omega_{397\pi} + \omega_{397\sigma^+})|3\rangle\langle 3| \\ &+\omega_{866\sigma^+}|4\rangle\langle 4| + (\omega_{866\sigma^-} - \omega_{397\pi} + \omega_{397\sigma^+})|5\rangle\langle 5| + \omega_{866\sigma^-}|6\rangle\langle 6| + \\ &(\omega_{397\sigma^+} - \omega_{397\pi})|7\rangle\langle 7|\big)t\Big]\end{aligned}$$

After the application of the rotating wave approximation and some algebraic simplification, the matrix elements of the Hamiltonian in an appropriate ro-

tating frame are

$$
\begin{aligned}
&(\hat{H}_{\text{rot}})_{17} = (\hat{H}_{\text{rot}})_{71} = \frac{\hbar\Omega_{397\pi}}{2} \qquad (\hat{H}_{\text{rot}})_{18} = (\hat{H}_{\text{rot}})_{81} = \frac{\hbar\Omega_{397\sigma^+}}{2} \\
&(\hat{H}_{\text{rot}})_{28} = (\hat{H}_{\text{rot}})_{82} = \frac{\hbar\Omega_{397\pi}}{2} \qquad (\hat{H}_{\text{rot}})_{37} = (\hat{H}_{\text{rot}})_{73} = \frac{\hbar\Omega_{866\sigma^+}}{2} \\
&(\hat{H}_{\text{rot}})_{48} = (\hat{H}_{\text{rot}})_{84} = \frac{\hbar\Omega_{866\sigma^+}}{2} \qquad (\hat{H}_{\text{rot}})_{57} = (\hat{H}_{\text{rot}})_{75} = \frac{\hbar\Omega_{866\sigma^-}}{2} \\
&(\hat{H}_{\text{rot}})_{68} = (\hat{H}_{\text{rot}})_{86} = \frac{\hbar\Omega_{866\sigma^-}}{2} \\
&(\hat{H}_{\text{rot}})_{11} = \hbar\Delta_{397\sigma^+} \qquad (\hat{H}_{\text{rot}})_{22} = \hbar\Delta_{397\pi} \\
&(\hat{H}_{\text{rot}})_{33} = \hbar\left(-\Delta_{397\pi} + \Delta_{397\sigma^+} + \Delta_{866\sigma^-} + \omega_{\text{AOM}} - \frac{2}{5}u\right) \\
&(\hat{H}_{\text{rot}})_{44} = \hbar\left(\Delta_{866\sigma^-} + \omega_{\text{AOM}} - \frac{8}{5}u\right) \\
&(\hat{H}_{\text{rot}})_{55} = \hbar\left(-\Delta_{397\pi} + \Delta_{397\sigma^+} + \Delta_{866\sigma^-} + \omega_{\text{AOM}} + \frac{6}{5}u\right) \\
&(\hat{H}_{\text{rot}})_{66} = \hbar\Delta_{866\sigma^-} \qquad (\hat{H}_{\text{rot}})_{77} = \hbar\left(\Delta_{397\sigma^+} - \Delta_{397\pi} + \frac{4}{3}u\right)
\end{aligned}
$$

where the laser detunings are defined as follows: $\Delta_{397\sigma^+} \equiv \omega_{397\sigma^+} - (\omega_8 - \omega_1)$, $\Delta_{397\pi} \equiv \omega_{397\pi} - (\omega_8 - \omega_2)$ and $\Delta_{866\sigma^-} \equiv \omega_{866\sigma^-} - (\omega_8 - \omega_6)$, and we introduce a parameter $u = \frac{\mu_B B}{\hbar} = 2\pi \times 1.3994 \times B$ MHz to simplify the expression. The frequency $\omega_{866\sigma^+} = \omega_{866\sigma^-} + \omega_{\text{AOM}}$, where ω_{AOM} is the frequency shifts by using an acousto-optic modulator (AOM). The quantity $g_J u$ is the energy splitting between two Zeeman levels (for example $\omega_6 = \omega_4 + 2g_J(D_{3/2})u.$). To calculate the Rabi frequency given the laser parameters from the laboratory, we use the equation in [King 08]

$$
\Omega_i = \sqrt{\frac{3\lambda^3\gamma P}{2\hbar c\pi^3 w_0^2}}(-1)^{J'+J+J_>-m_J}\sqrt{2J'+1}\begin{pmatrix} J' & k & J \\ m'_J & q & m_J \end{pmatrix}
$$

where λ is the wavelength, γ is the spontaneous decay rate of the excited state, P and w_0 are the power and the $1/e^2$ beam waist of the laser light respectively, $J_>$ is the larger of J' and J. The matrix $\begin{pmatrix} J' & k & J \\ m'_J & q & m_J \end{pmatrix}$ is the Wigner 3-j symbol. For photons, the angular momentum $k = 1$ and $q \in \{-1, 0, 1\}$ is associated with the polarizations of the light field $\{\hat{\sigma}^-, \hat{\pi}, \hat{\sigma}^+\}$.

Until now, our discussions have been about a closed quantum system, which evolves unitarily. However, the reality is that the ion can also decay from an excited state in the absence of any applied laser field - the spontaneous emission, arising from the atom interaction with the vacuum modes of the field. To account for spontaneous decay and dephasing processes, we resort to the density matrix approach that provides a tool to efficiently describe a

quantum system interacting with its environment [Cohen-Tannoudji 92]. The equation of motion is expressed by

$$\frac{d\rho}{dt} = -\frac{i}{\hbar}\left[\hat{H}_{\mathrm{rot}}, \rho\right] + \mathcal{L}(\rho) \tag{3.2}$$

where ρ is the atomic density matrix for an eight-level system and $\mathcal{L}(\rho)$ is the Louvillian operator accounting for spontaneous decay and dephasing effects, and has the form

$$\mathcal{L}(\rho) = -\frac{1}{2}\sum_{m}\left(\hat{L}_m^{\dagger}\hat{L}_m\rho + \rho\hat{L}_m^{\dagger}\hat{L}_m - 2\hat{L}_m\rho\hat{L}_m^{\dagger}\right) \tag{3.3}$$

where the damping operators $\hat{L}_m$ describe different decay and dephasing processes. Equation (3.2) is known as the master equation in the Lindblad form and can be used to study the evolution of open quantum systems coupled to Markovian reservoirs like the vacuum modes of the field.

The total spontaneous emission rates of $P_{1/2} \rightarrow S_{1/2}$ and $P_{1/2} \rightarrow D_{3/2}$ are written as

$$\begin{aligned} \gamma_{PS} &= \gamma_{71} + \gamma_{72} \\ &= \gamma_{81} + \gamma_{82} \\ \gamma_{PD} &= \gamma_{73} + \gamma_{74} + \gamma_{75} \\ &= \gamma_{84} + \gamma_{85} + \gamma_{86} \end{aligned}$$

where γ_{mn} is the decay rate from the level $|m\rangle$ to $|n\rangle$ and can be calculated with

$$\gamma_{mn} = \frac{\omega_{mn}^3}{3\pi\epsilon_0\hbar c^3}|\langle m|\mathbf{d}|n\rangle|^2 \tag{3.4}$$

where ω_{mn} is the atomic transition frequency and $|\langle m|\mathbf{d}|n\rangle|$ is related to the Clebsch-Gordon coefficient of the transition $|m\rangle \leftrightarrow |n\rangle$. The corresponding damping operators are $\hat{L}_{PS} = \sqrt{\gamma_{PS}}|S\rangle\langle P|$ and $\hat{L}_{PD} = \sqrt{\gamma_{PD}}|D\rangle\langle P|$.

However in the Zeeman-split multi-level system we need to meticulously determine the operator $\hat{L}_m$ due to the presence of not only the optical coherence effects (e.g. coherence between level $|1\rangle$ and $|8\rangle$) but also the coherence effects between two Zeeman sublevels (e.g. coherence between level $|1\rangle$ and $|2\rangle$) [Cohen-Tannoudji 77]. This means that the spontaneous decay (damping) operator splits into three operators for three different possible polarizations of the emitted photons. The one for $P_{1/2} \rightarrow S_{1/2}$ are given by

$$\hat{L}_{PS\sigma^+} = \sqrt{\gamma_{PS}}\sqrt{\frac{2}{3}}|1\rangle\langle 8| \tag{3.5}$$

$$\hat{L}_{PS\pi} = \sqrt{\gamma_{PS}}\left(\sqrt{\frac{1}{3}}|1\rangle\langle 7| - \sqrt{\frac{1}{3}}|2\rangle\langle 8|\right) \tag{3.6}$$

$$\hat{L}_{PS\sigma^-} = -\sqrt{\gamma_{PS}}\sqrt{\frac{2}{3}}|2\rangle\langle 7| \tag{3.7}$$

This shows the coherence ρ_{12} is coupled to ρ_{78} through the π-photon transitions, yielding the damping of the Zeeman coherence $\langle 1|\frac{d\rho}{dt}|2\rangle = -\frac{1}{3}\gamma_{PS}\rho_{78}$ which was calculated and explained by Cohen-Tannoudji [Cohen-Tannoudji 77]. For $P_{1/2} \rightarrow D_{3/2}$, the relevant Lindblad operators are

$$\hat{L}_{PD\sigma^+} = \sqrt{\gamma_{PD}}\left(\sqrt{\frac{1}{2}}|3\rangle\langle 7| + \sqrt{\frac{1}{6}}|4\rangle\langle 8|\right) \tag{3.8}$$

$$\hat{L}_{PD\pi} = -\sqrt{\gamma_{PD}}\left(\sqrt{\frac{1}{3}}|4\rangle\langle 7| + \sqrt{\frac{1}{3}}|5\rangle\langle 8|\right) \tag{3.9}$$

$$\hat{L}_{PD\sigma^-} = \sqrt{\gamma_{PD}}\left(\sqrt{\frac{1}{2}}|5\rangle\langle 7| + \sqrt{\frac{1}{6}}|6\rangle\langle 8|\right) \tag{3.10}$$

In general there are also processes which decrease the coherences without changing the populations. These are typically incorporated into the master equation by setting dephasing rates. One source to cause such decoherence is the finite laser linewidth. The damping operators can be expressed by

$$\hat{L}_{397} = \sqrt{\gamma_{397}}\left(|1\rangle\langle 1| + |2\rangle\langle 2|\right) \tag{3.11}$$

$$\hat{L}_{866} = \sqrt{\gamma_{866}}\left(|3\rangle\langle 3| + |4\rangle\langle 4| + |5\rangle\langle 5| + |6\rangle\langle 6|\right) \tag{3.12}$$

where γ_{397} and γ_{866} are the linewidth of the 397 nm and 866 nm laser fields respectively.

To solve Eq. (3.2), we use the methods given in [Oberst 99]. One can convert the N-by-N density matrix into a N^2-by-1 vector and then simplify the equation ending up with the form

$$\frac{d\rho}{dt} = \mathbf{M}\cdot\rho \tag{3.13}$$

where $\mathbf{M}$ is a matrix with a dimension of $N^2 \times N^2$. The matrix elements of $\mathbf{M}$ are given by

$$M_{rs,kj} = -\frac{i}{\hbar}\left(\tilde{H}_{rk}\delta_{js} - \tilde{H}^{\dagger}_{js}\delta_{rk}\right) + \sum_m (L_m)_{rk}(L^{\dagger}_m)_{js} \tag{3.14}$$

where $\tilde{H} = H - \frac{i}{2\hbar}\sum_m \hat{L}^{\dagger}_m\hat{L}_m$ and (r, s, k, j) are indices from 1 to 8 in our case. These differential equations are called optical Bloch equations. Given the initial condition $\rho(0)$, the time-dependent solution, $\rho(t)$, can be calculated with

$$\rho(t) = e^{\mathbf{M}t}\rho(0) \tag{3.15}$$

This method is quite time consuming. However, if we are only interested in the steady state of the dynamics, $\rho(\infty)$ is a constant, a more efficient way of

calculating it is by replacing one of the Bloch equations with the normalization condition $\sum_{i=1}^{8} \rho_{ii} = 1$ such that the steady-state solutions can be obtained by solving a system of linear equations [Oberst 99]. We desire to have the populations in $P_{1/2}$ state $(\rho_{77} + \rho_{88})$ as high as possible, meaning that more photons can scatter.

Results and Discussions

In the experiments, we typically use 7.5 μW with a beam waist of 70 μm for both 397 nm detection beams, corresponding to near one saturation intensity, and $20 - 30$ μW with the same beam waist for both 866 nm laser beams that is highly saturated for this transition. Figure 3.5 shows the steady-state populations in the $P_{1/2}$ state as a function of the detuning of the 866 nm laser light for different detuning settings of the 397 nm beams. The maximum $P_{1/2}$ state population and the position of dark resonances strongly depends on the detunings of the 397 nm beams. We can see that there are four dark resonances formed by the Λ-type system, from left to right $|2\rangle - |8\rangle - |6\rangle$, $|1\rangle - |8\rangle - |6\rangle$, $|2\rangle - |8\rangle - |4\rangle$, and $|1\rangle - |8\rangle - |4\rangle$.

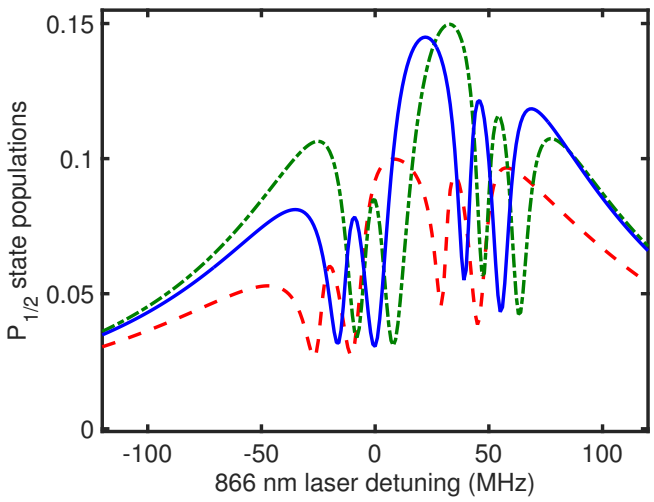

Figure 3.5: The $P_{1/2}$ state populations as a function of 866 nm laser detuning. The parameters used here are $\Delta_{397\pi} = -26$ MHz and $\Delta_{397\sigma^+} = -10$ MHz for red dashed line; $\Delta_{397\pi} = -8$ MHz and $\Delta_{397\sigma^+} = 8$ MHz for green dash-dot line; $\Delta_{397\pi} = -16$ MHz and $\Delta_{397\sigma^+} = 0$ MHz for blue solid line. All three settings make the frequency difference between two 397 nm laser beams the same. ω_{AOM} is fixed at 212 MHz for all cases. The laser linewidth is assumed to be 685 kHz for both wavelengths. There are four dark resonances and each is formed by a Λ-type system, see texts.

Figure 3.6 shows the steady-state populations in the $P_{1/2}$ state as a function

of the detuning of the 397 nm laser light. This type of spectrum can be measured by scanning the reference cavity used to lock the frequency of the 397 nm laser so both frequency components are scanned in common. Here both 397 nm laser beams have a frequency difference of 16 MHz to avoid the dark resonance created by themselves. For the red curve in Fig. 3.6, we choose $\Delta_{866\sigma^-} = 25$ MHz. The green curve is obtained by setting $\Delta_{866\sigma^-} = 80$ MHz. Although the red curve has a higher maximum population, we prefer to use the setting of the green one, making the 866 nm laser far blue detuned from the resonance. The reasons are that the dark resonances in the red curve are located on both sides of the main resonant peak, for which the one on the left would affect the Doppler cooling, and the linewidth of the red curve is narrower so if the laser frequency of the detection beam is chosen to be on the resonance peak, then it is more sensitive to the frequency fluctuations. The experimental result is shown in Fig. 3.6(b) for comparison, i.e. the experimental parameters might be different from those used in the simulation.

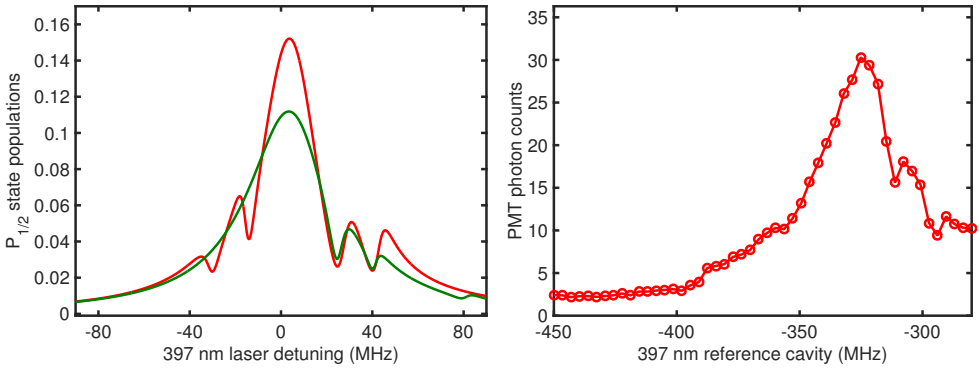

(a) (b)

Figure 3.6: The $P_{1/2}$ state populations as a function of 397 nm laser detuning. (a) The parameters used here are $\Delta_{866\sigma^-} = 25$ MHz for the red curve and $\Delta_{866\sigma^-} = 80$ MHz for the green one. Other parameters are the same as those in Fig. 3.5. (b) The experimental result is shown for comparison. This is similar to the green curve in (a) because the 866 nm laser frequency is set to be far blue detuned as described in the text.

The frequency of each 397 nm polarization component can be scanned by using a high-bandwidth AOM. Depending on the center frequency of the AOM, the scanning range is usually $\pm 15 - 20$ % of the center frequency without losing diffraction efficiency. Figure 3.7 shows the $P_{1/2}$ state populations versus the detuning of the 397 nm σ^+ beam. The dark resonance at $\Delta_{397\sigma^+} = -14$ MHz is generated from the 397 nm σ^+ and π components. The second dark resonance at $\Delta_{397\sigma^+} \approx 25$ MHz is formed by the 397 nm σ^+ and the 866 nm σ^+

components when we choose $\Delta_{866\sigma^-} = 80$ MHz and $\omega_{\mathrm{AOM}} = -212$ MHz. As we can learn from the simulation results (Figs. 3.5, 3.6 and 3.7), the position of the dark resonances depends on the detuning of both laser beams. Therefore, the parameters we use for the experiments are compromise between high populations in the $P_{1/2}$ state and avoiding a dark resonance.

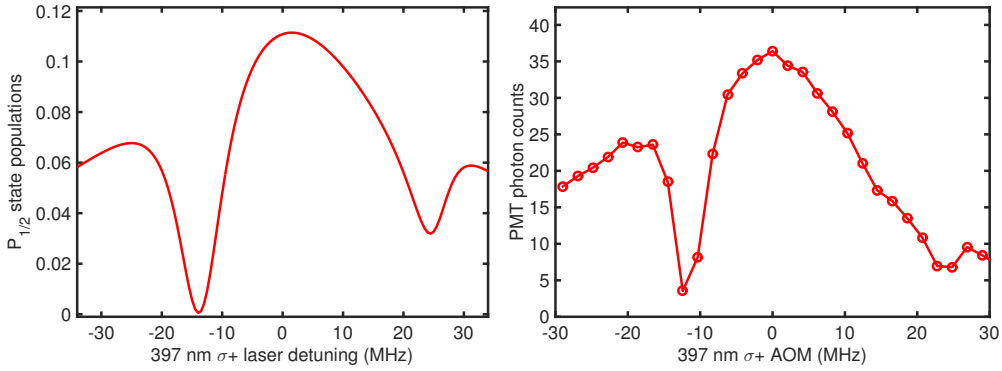

(a) (b)

Figure 3.7: The $P_{1/2}$ state populations as a function of 397 nm $\hat{\sigma^{+}}$ laser detuning. (a) The parameters used here are $\Delta_{866\sigma^-} = 80$ MHz and $\Delta_{397\pi} = -14$ MHz. Other parameters are the same as those in Fig. 3.5. (b) The experimental result is shown for comparison. The profile on the right part is relatively lower than the simulation result. This might be due to the decrease of the AOM diffraction efficiency when the AOM's frequency is close to the boundary of the scannable range.

Chapter 4

Ion Trap and Imaging System

In our group, we aim for a high-fidelity control of a mixed-species ion chain for implementing quantum information processing and quantum simulation. Building up a new experimental system for two ion species is quite challenging. The experimental setup consists of five parts, which are the ion trap placed in a ultra-high vacuum chamber, the voltage waveforms for transporting, splitting and combining the ions, the imaging system for fluorescence detection and qubit readout, the laser systems for manipulating the ions, and the computer control system for controlling the experiments. All the apparatus needs to take very careful design and should be suitable for two ion species. In this chapter, I will introduce the trapping principles and then the ion trap which we use for the works covered in the thesis. The trap was designed and built by Daniel Kienzler [Kienzler 15b]. The design and features of the imaging system for both species of ions will be discussed in detail. In the end, I will shortly mention the computer control system that we used to program the experimental sequence and handle the laser pulses. The technologies that have been developed in the past few years will enable us to realize flexible control of trapped ions for quantum physics studies.

4.1 Ion Trap

4.1.1 Trapping Principles

Three-dimensional confinement of charged particles requires a potential energy minimum at some point in space and the corresponding force is pointing toward that minimum in all three dimensions. Such confinement can be created with electric fields. It follows $F = -\nabla U$, where $U = q\Phi$ is the potential energy. In general Φ takes a quadratic form in the Cartesian coordinates as $\Phi(x, y, z) = \frac{\Phi_0}{R^2}(Ax^2 + By^2 + Cz^2)$, where A, B, and C are constants, and R is the normalizing factor. However, it is not possible to trap charged particles with only the static electric fields according to Earnshaw's theorem. A simple

explanation is that if Φ has to satisfy Laplace's equation $\nabla^2\Phi = 0$, we must need $A + B + C = 0$. It is possible to trap in two dimensions with $A, B > 0$ for $q > 0$, but the third dimension will be anti-trapping ($C < 0$). The solution is to use the time-varying fields instead.

The potential used for a linear Paul trap [Wineland 98] near the center has a following form:

$$\begin{aligned}\Phi(x,y,z,t) &= \Phi_{\mathrm{RF}} + \Phi_{\mathrm{DC}} \\ &= \frac{1}{2}V_0\cos\left(\Omega_{\mathrm{RF}}t\right)\left(\frac{x^2-y^2}{R^2}\right) + \frac{\kappa U_0}{2}\left(2z^2 - x^2 - y^2\right) \quad (4.1)\end{aligned}$$

where $V_0\cos\left(\Omega_{\mathrm{RF}}t\right)$ is the potential applied to the diagonally opposite RF electrodes which are placed a distance R from the axis of the trap and responsible for the confinement in the radial plane (x and y directions), and U_0 is the static potential applied to the DC electrodes in order to provide axial confinement of the ions (z direction). κ is the geometry factor. The equations of motion for an ion with mass m and charge q are given by

$$\ddot{u} = \frac{F}{m} = \frac{qE}{m} = -\frac{q}{m}\frac{\partial\Phi}{\partial u}, \qquad u \in \{x, y, z\} \quad (4.2)$$

Along the z direction, the ion's motion is simple harmonic motion with the oscillation frequency $\omega_z = \sqrt{2\kappa q U_0/m}$. In the x and y directions, the equations of motion can be transformed to the standard form of the Mathieu differential equation as follows:

$$\frac{d^2u}{d\xi^2} + \left(a_u + 2q_u\cos\left(2\xi\right)\right)u = 0, \qquad u \in \{x, y\} \quad (4.3)$$

where $\xi = \frac{\Omega_{\mathrm{RF}}t}{2}$, $a_x = a_y = \frac{4q\kappa U_0}{m\Omega_{\mathrm{RF}}^2}$ is a measure of the strength of the static potential, and $q_x = -q_y = \frac{2qV_0}{m\Omega_{\mathrm{RF}}^2R^2}$ quantifies the strength of the RF potential. Equation (4.3) can be solved by using the Floquet theorem [Leibfried 03b, Wineland 98]. Typically, we have the condition $a_u < q_u \ll 1$ so the solution to the first order in a_u and q_u is given by

$$u(t) = A_u\cos\left(\beta_u\frac{\Omega_{\mathrm{RF}}}{2}t\right)\left[1 + \frac{q_u}{2}\cos\left(\Omega_{\mathrm{RF}}t\right)\right] \quad (4.4)$$

where A_u is determined by the initial condition and $\beta_u = \sqrt{a_u + q_u^2/2}$. Under the conditions $a_u < q_u \ll 1$, we can see that the frequency $\beta_u\Omega_{\mathrm{RF}}/2 \ll \Omega_{\mathrm{RF}}$. The first term which has a larger amplitude and slower motion (frequency at $\beta_u\Omega_{\mathrm{RF}}/2$) is the "secular" motion of the ion, and the second term with a smaller amplitude and faster motion (frequency at Ω_{RF}) is called the "micromotion". When the confinement in x and y directions is much stronger than

the axial confinement, the secular motional frequency can be approximated by

$$\omega_u \simeq \frac{|q_u|}{2\sqrt{2}}\Omega_{\mathrm{RF}} = \frac{qV_0}{\sqrt{2}m\Omega_{\mathrm{RF}}R^2}, \qquad u \in \{x, y\}. \tag{4.5}$$

In our case, due to a complex trap geometry Equation (4.1) can not be used to describe the total potential. The degeneracy of the two secular frequencies can be broken by adding an axial trapping potential. The RF potential which provides radial confinement is cylindrically symmetric. Once we have the static field for the axial confinement, this potential is overlaid on radial component and deforms the net potential seen by the ion, breaking the cylindrical symmetry [Amini 11]. When designing a trap, the condition $\omega_{x,y} < \Omega_{\mathrm{RF}}/5$ should be satisfied in order to ensure stability.

Pseudopotential Approximation

The pseudopotential approximation [Dehmelt 68] is a heuristic approach that gives an insight into the radial confinement as well as provides a useful tool for the simulation of ion traps. We consider an ion with mass m and charge q in an oscillating electric field $\mathbf{E}(\mathbf{u}, t) = \mathbf{E}(\mathbf{u})\cos(\Omega_{\mathrm{RF}}t)$, where $\mathbf{u} = x\hat{x}+y\hat{y}+z\hat{z}$ is the position vector. Under the assumption that the mean ion position changes negligibly in duration $2\pi/\Omega_{\mathrm{RF}}$, the equation of motion can be written as

$$\frac{\partial^2 \mathbf{u}_\mu}{\partial t^2} = \frac{q\mathbf{E}(\mathbf{u})}{m}\cos(\Omega_{\mathrm{RF}}t) \tag{4.6}$$

This is actually the equation of motion for the ion's micromotion, and its solution is

$$\mathbf{u}_\mu = -\frac{q\mathbf{E}(\mathbf{u})}{m\Omega_{\mathrm{RF}}^2}\cos(\Omega_{\mathrm{RF}}t) \tag{4.7}$$

The pseudopotential Φ_{pseudo} governed from the kinetic energy of the ion is now given by

$$q\Phi_{\mathrm{pseudo}} = \langle KE\rangle = \frac{1}{2}m\langle v_\mu\rangle^2 = \frac{q^2|\mathbf{E}(\mathbf{u})|^2}{4m\Omega_{\mathrm{RF}}^2} \tag{4.8}$$

From Φ_{RF} in Eq. (4.1), we are able to calculate $\mathbf{E}(\mathbf{u})$ for a linear RF trap, which is $\mathbf{E}(\mathbf{u}) = -\frac{V_0}{2}\nabla\left(\frac{x^2-y^2}{R^2}\right) = -V_0\left(\frac{x\hat{x}-y\hat{y}}{R^2}\right)$. Therefore the pseudopotential for a linear RF trap is

$$q\Phi_{\mathrm{pseudo}} = \frac{q^2V_0^2}{4m\Omega_{\mathrm{RF}}^2R^4}\left(x^2+y^2\right) = \frac{1}{2}m(\omega_x^2x^2+\omega_y^2y^2) \tag{4.9}$$

We obtain the secular frequency $\omega_x = \omega_y = \frac{qV_0}{\sqrt{2}m\Omega_{\mathrm{RF}}R^2}$, which agrees with the solution of the Mathieu equation in the limit $a_u, q_u^2 \ll 1$.

4.1.2 Micromotion

If the pseudopotential at the equilibrium position of an ion is not zero, the ion will have micromotion oscillating at the RF driving frequency. There are two types of micromotion in Paul traps: 1) Complex trap structures or not well aligned trap electrodes can have a residual component of the RF field in the axial direction. In this case, the minimum of the pseudopotential is not zero. Since this effect is caused by the trap itself, we name this kind of micromotion as "intrinsic" micromotion [Amini 11]. 2) In the presence of stray electric fields at the pseudopotential minimum, this stray field displaces the equilibrium position of an ion away from the center. This type of micromotion can be nulled by applying compensation fields to extra electrodes and is called "excess" micromotion. The extra electrodes should be allowed to have independent control of the compensation fields along each radial principal axis. However, for a given stray field the displacement will be different for ions with different mass such that a mixed-species ion chain would not co-align along the axial direction (illustrated in Fig. 4.1). This will lead to a change of the mode structure such that the mode's amplitude and frequency are changed. Therefore it is very important to know how to compensate the stray field completely when working with two species of ions [Home 13]. Several methods have been tried out for the calcium and beryllium ion individually. These techniques and measurement results will be discussed in Chapter 6.

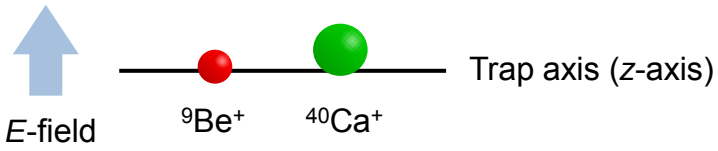

Figure 4.1: Owing to a stray E-field, a two-species ion crystal is displaced in the radial plane from the pseudopotential minimum, resulting in excess micromotion. The heavier mass ions get larger displacements because they experience weaker confinement from the pseudopotential.

4.1.3 Three-Dimensional Segmented Linear Paul Trap

In our group, a segmented linear Paul trap is used to simultaneously trap both beryllium and calcium ions. The general goal is relevant for scaling up quantum information processing based on trapped ions as well as flexible control of both ion species. The ion trap used for the experiments of this thesis is shown in Fig. 4.2. The trap was designed and fabricated by Daniel Kienzler. Detailed design considerations and recipe for making the trap can be found in his thesis [Kienzler 15b]. Here I only summarize the new features

of the trap.

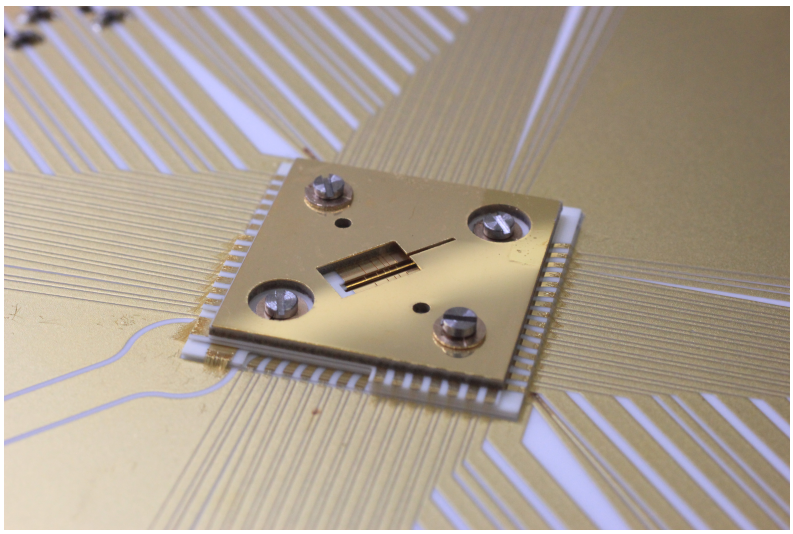

Figure 4.2: A three-dimensional segmented linear Paul trap. This is made of laser machined alumina wafers with electroplated gold. The picture shown here is that all trap wafers are assembled on the filterboard.

The main part of the trap consists of four gold plated alumina wafers, as shown in Fig. 4.3(a). The middle two wafers form the linear Paul trap, for which both the RF electrodes and DC electrodes reside at two opposite corners of the typical four-rod quadrupole configuration. We design and optimize a segmented structure for DC electrodes, providing two zones for loading ions, three zones for quantum control, and two zones for shuttle and separation of ion strings (Fig. 4.3(b)). Two loading zones are located at both ends of the trap, where one beryllium and one calcium atomic oven are installed. This gives us more flexibility for two-species ion loading. The other benefit is that if the oven on one side is broken or empty, we still have a backup.

Three experimental zones could be used to realize a simple version of the "quantum charge-coupled device (QCCD) architecture" [Kielpinski 02] in which the ion string loaded in a segmented trap can be transported to different zones for cooling/storage/qubit readout, and the quantum control can be performed in specific zones. Between two experimental zones, there is a zone consisting of three electrodes which are used to shuttle, separate and combine the ions. The electrode widths are optimized to achieve highest confinement during the process of splitting the ion chain [Home 06b, Kienzler 15b].

Typically two bias electrodes are used in order to null stray electric fields transverse to the trap axis that induce the excess micromotion. With this approach only one point along the trap axis can be optimally compensated.

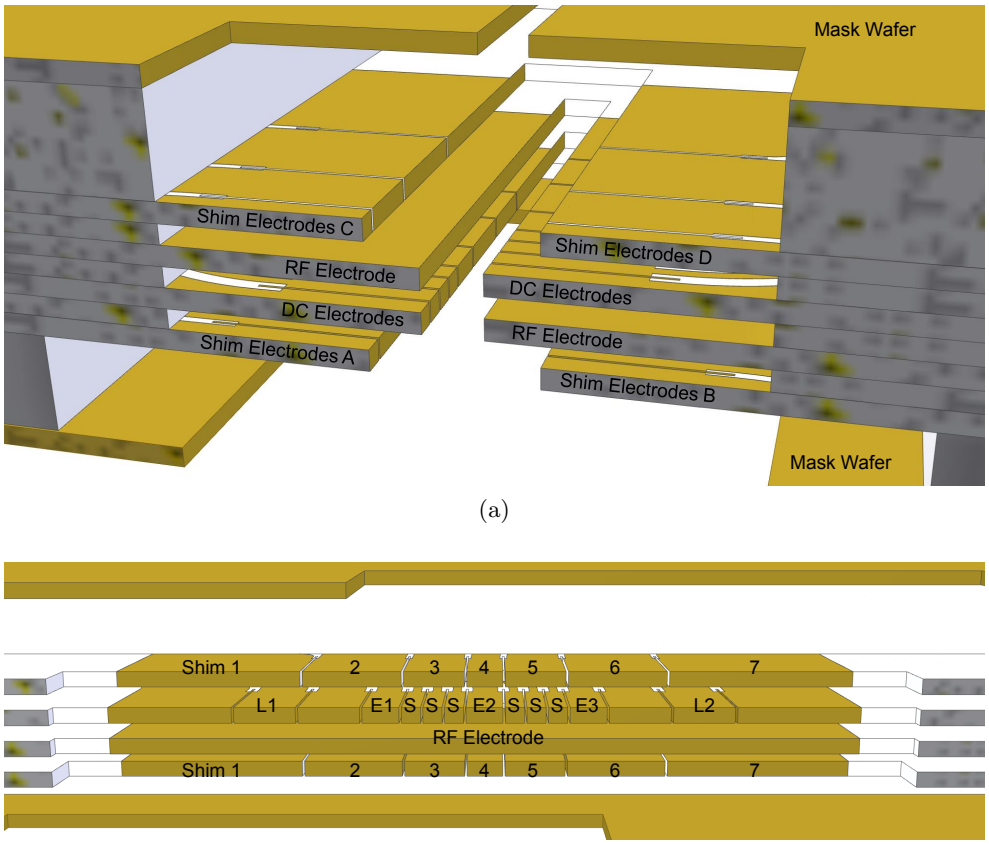

(a)

(b)

Figure 4.3: Schematic diagram of the 3-D segmented trap. (a) Cut transverse to the trap axis. (b) Cut along the trap axis. L: loading zone, S: shuttling and splitting zone, and E: experimental zone. The width of the L, S, and E electrodes are 500 µm, 155 µm, and 300 µm. All the gaps between two electrodes are 20 µm. (These CAD drawings are made by Daniel Kienzler)

However the stray field can not be guaranteed to be the same at different points on the trap axis. Therefore a segmented bias wafer is used on both sides of the trap. Each shim electrode has seven segments, shown in Fig. 4.3(b), such that we can compensate the excess micromotion in different regions. The use of these shim electrodes to minimize the micromotion is discussed in Chapter 6.6.

4.1.4 DC Voltage Source

The axial confinement is achieved by applying a set of voltages to segmented DC electrodes that create a trapping potential. Changing the voltage on each DC electrode is able to move the ion along the axial direction. In our

group, we have two approaches for the DC voltage source. The first one is the use of AD5371 DAC board[1]. The AD5371 board contains 40-channel 14-bit DACs. The device provides buffered voltage outputs with a maximum span of 20 V. In our case, we restrict the output voltage range between −10 V and +10 V. This device is divided into five groups of eight DACs. Three offset DACs allow the output range of the groups to be adjusted. This board can be controlled through the SPI interface. Initially the communication to this device was implemented by Ben Keitch. The idea was that the computer control system directly controls the AD5371 board with an intermediate buffer board, but eventually we decided to use an Arduino Uno board[2], which is a microcontroller board based on the ATmega328 chip[3], to control the DAC channels. This provides a stable and reliable solution for the DC voltages. However, it is not fast enough for performing voltage updates within a single experimental sequence.

For this reason, a high-speed and low noise DAC board has been designed and constructed in our group. It is called Direct Ethernet Adjustable Transport Hardware (DEATH). For the readers who are interested, all the details about the design, specifications and characterizations of DEATH can be found in Ludwig de Clercq's thesis [de Clercq 15]. Currently, we are using DEATH for the DC electrodes and still using AD5371 for the shim electrodes.

4.2 Imaging System

The imaging system in the trapped ion experiments plays an important role because it is responsible for imaging the ions which are trapped, and collecting photons during the qubit readout. The system should be near diffraction limited in order to resolve single trapped particles which are a few microns apart. In the following, I will describe how we set up our imaging system in detail.

Requirements

We desire to have two high numerical-aperture (NA) objectives in the vacuum chamber for imaging trapped ions and collecting the fluorescence emitted from them. These two in-vacuum objectives are movable along three dimensions such that we can image the ions in different zones as well as adjust the focal length and height of the objective. Some specifications we required for the high NA objective design are listed below:

- Compatible with UHV.

[1] Analog, www.analog.com
[2] Arduino, www.arduino.cc
[3] www.atmel.com/Images/doc8161.pdf

- Ion-objective distance: 30 mm. This is determined by the optical access to the ion.
- NA: 0.45, corresponding to $\simeq 5.3\%$ of 4π solid angle.
- Field of view: 100 microns
- Depth of focus: 20 microns
- Magnification: 40
- Total working distance: 1 meter

Design

Designing a high NA objective with near-diffraction-limit resolution is challenging for two different wavelengths. The design program we use in the group is Zemax, which integrates all the features required to conceptualize, design, optimize, analyze, tolerance, and document any optical system. It is widely used in the optics industry as a standard design tool. The version we have is for design of a sequential optical system.

Sequential ray-tracing could be used to model almost all imaging systems. It is fast, flexible, and easy to optimize. The "sequential" means that rays are traced through a pre-defined sequence of surfaces while traveling from the object surface to the image surface. The starting point of designing such an objective, which satisfies the above criteria, is to refer to other groups' setup [Benhelm 08b, Hijlkema 07, Alt 02]. They used a multi-lens system to compensate the aberrations of one surface with the aberrations of other ones. This is because single spherical lenses always introduce spherical aberrations.

We start from a system with five lenses, where the initial radii of curvature of lens surfaces and lens thickness are obtained from commercially available products, and then try to optimize the radii of curvature of the lens surfaces and the distances between the lenses. However, the problem we faced was that we couldn't optimize the objective for both wavelengths at the same time. The final design and lens manufacturing were made by Sill Optics, where they apply the function of "Multi-Configuration" in Zemax, which we were not aware of, to simultaneously optimize the imaging system for the wavelengths of 313 nm and 397 nm. Two additional lenses are placed in each imaging path outside the vacuum chamber in order to reduce the back-focal distance and calibrate the image quality, as shown in Figs. 4.3(a) and 4.3(b) for the schematic diagrams. The multi-lens in-vacuum objective is common for both wavelengths. The NA in the final design is 0.41, corresponding to $\simeq 4.4\%$ of 4π solid angle. The total working distance is one meter for both. The detailed lens data can be found in Appendix B.

The in-vacuum objective is "designed" as an infinity-corrected optical system, in which a light beam from a object passes through the objective lens which

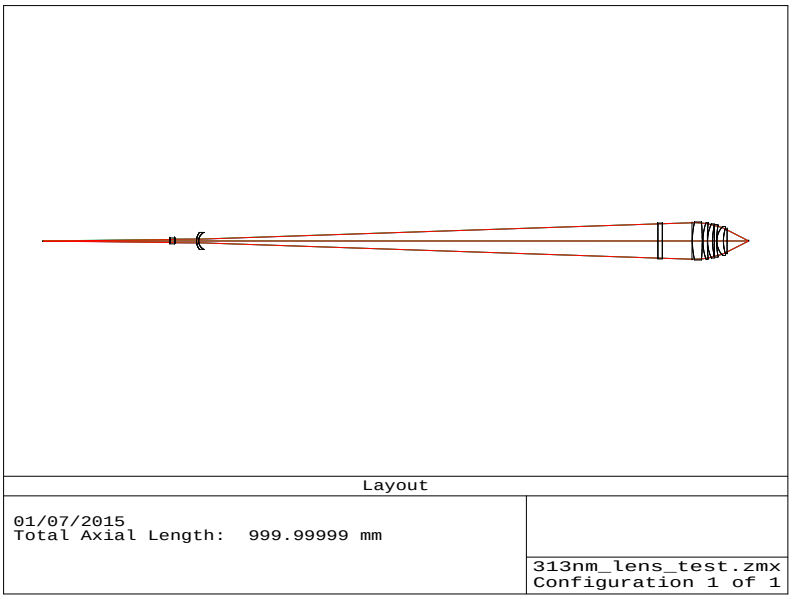
Layout
01/07/2015
Total Axial Length: 999.99999 mm
313nm_lens_test.zmx
Configuration 1 of 1

(a)

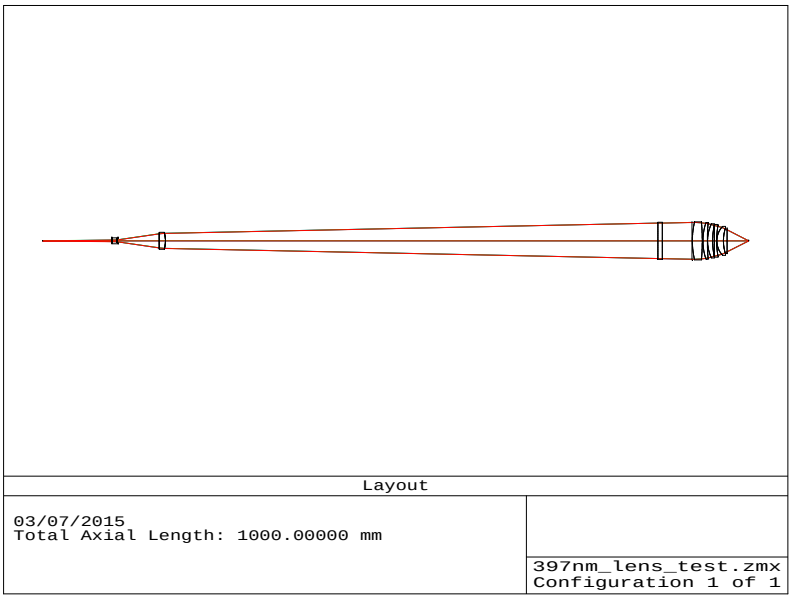
Layout
03/07/2015
Total Axial Length: 1000.00000 mm
397nm_lens_test.zmx
Configuration 1 of 1

(b)

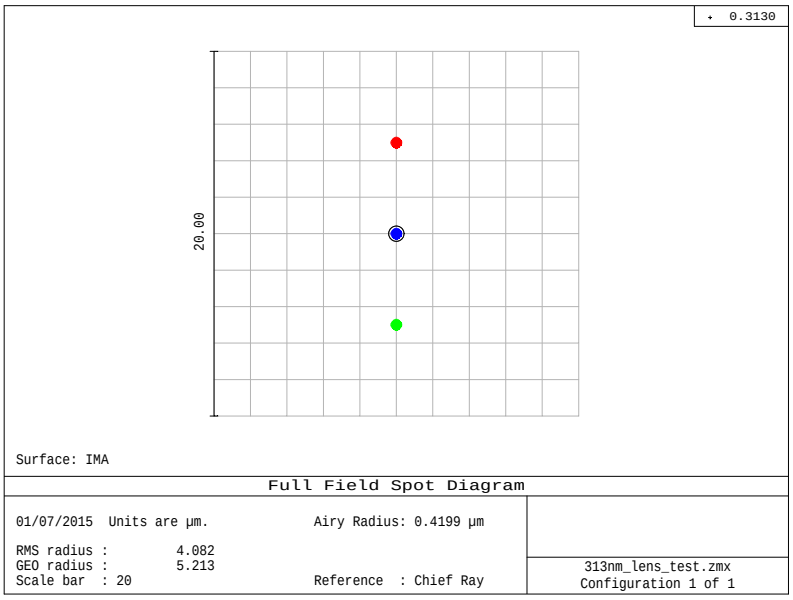

(c)

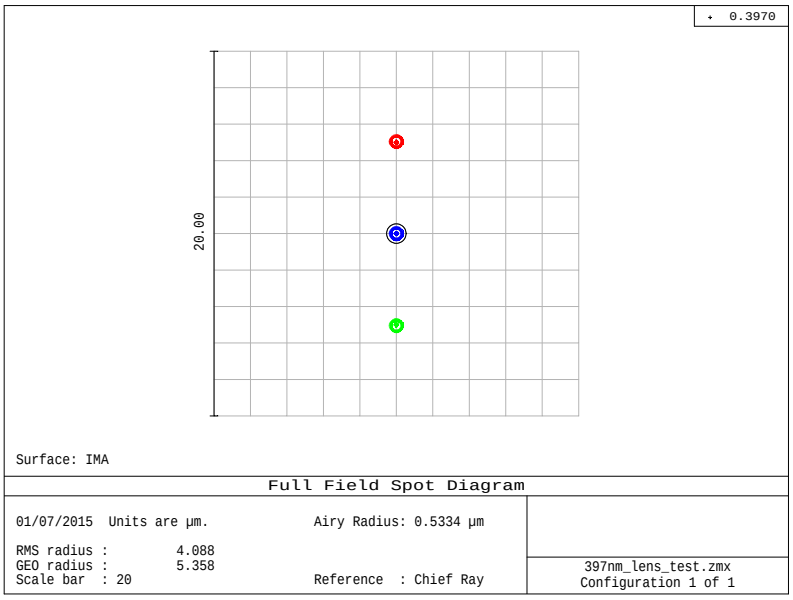

(d)

Figure 4.3: The imaging system design. (a) The layout of the lens design for 313 nm light field. (b) The layout of the lens design for 397 nm light field. (c) Simulated spot diagram for 313 nm light field. (d) Simulated spot diagram for 397 nm light field. Three objects are set 200 µm apart.

does not form an image and enters as an infinity parallel beam in the additional image forming lenses (though in our case the objective does not make a perfect infinity parallel beam, see below). In a finite correction optical system, the objective lens forms an image by itself. An infinity-corrected objective lens has the following advantages: 1) A magnification remains the same when the distance between the objective lens and the additional lens is changed. 2) If a flat plate like the viewport in our case is inserted between the objective lens and the additional lens, the parfocal point is unchanged and delivers no image shifts. The two advantages mentioned are significant for configuring a near-diffraction-limited optical system as well as for designing a microscope optical system.

Figures 4.3(c) and 4.3(d) show the simulation results of both imaging systems respectively. The objects are set to a separation of 200 μm and it forms the image of 5 μm apart, which is what we should expect because the magnification is 1/40 (in reverse). All the image spots are within the airy disk, which is a black circle at the center and is an indication of the diffraction limit. By reversing the whole system (see Figs. 4.3(a) and 4.3(b)), this is the real situation where the two ions are now the objects with 5 μm apart. The image also matches our specifications and we are able to resolve both ions, as shown in Figs. 4.3(c) and 4.3(d).

We then examine how sensitive the focal point is in order to understand the alignment tolerances of the system. We can simulate the spot diagram at different positions crossing the focus. Figures 4.3(a) and 4.3(b) show that it is quite sensitive if we try to adjust the distance between the ion and the objective. As we can see, with a defocus of 10 μm, the image is already much larger than the airy disk. Conversely, if we fix the ion-objective distance, the tolerance of moving the image plane is in the range of millimeters, as shown in Figs. 4.3(c) and 4.3(d).

Construction

Figure 4.4 shows the assembly of the in-vacuum objectives. There are two identical imaging systems in our setup, located on two sides of the trap. On one side the objective can image from zone L1 to the center of the trap; on the other side, the imaging region is from zone L2 to the center. The total movable range of the vacuum bellows is around 3 mm.

Inside the chamber, the objective is screwed in an aluminum mechanical mount. The whole part is mounted on the flexible vacuum bellows, as shown in the CAD drawing (see Fig. 4.5). As mentioned above, we need the capability to adjust the objective in three dimensions, including the height, the focal distance, and the axial direction along the trap. Therefore, we attach a three-dimensional translation stage to the bellows. A motorized translation

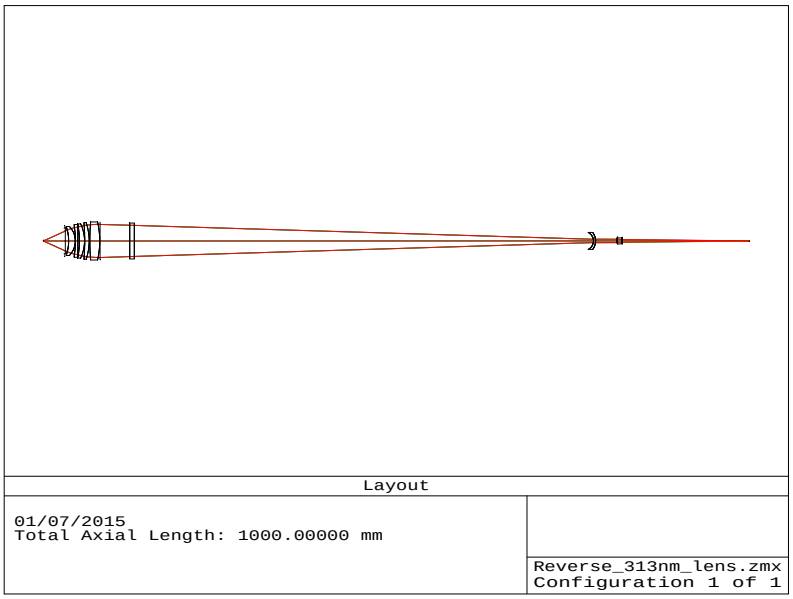
Layout
01/07/2015
Total Axial Length: 1000.00000 mm
Reverse_313nm_lens.zmx
Configuration 1 of 1

(a)

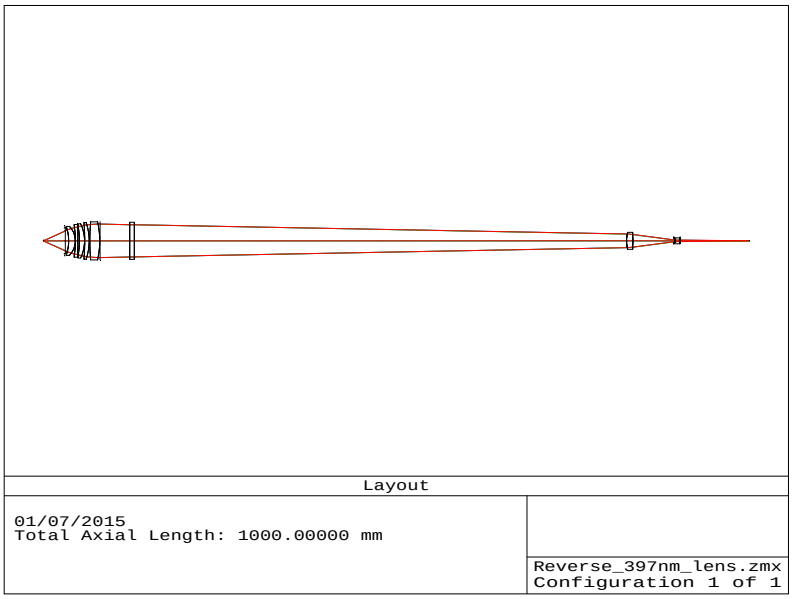
Layout
01/07/2015
Total Axial Length: 1000.00000 mm
Reverse_397nm_lens.zmx
Configuration 1 of 1

(b)

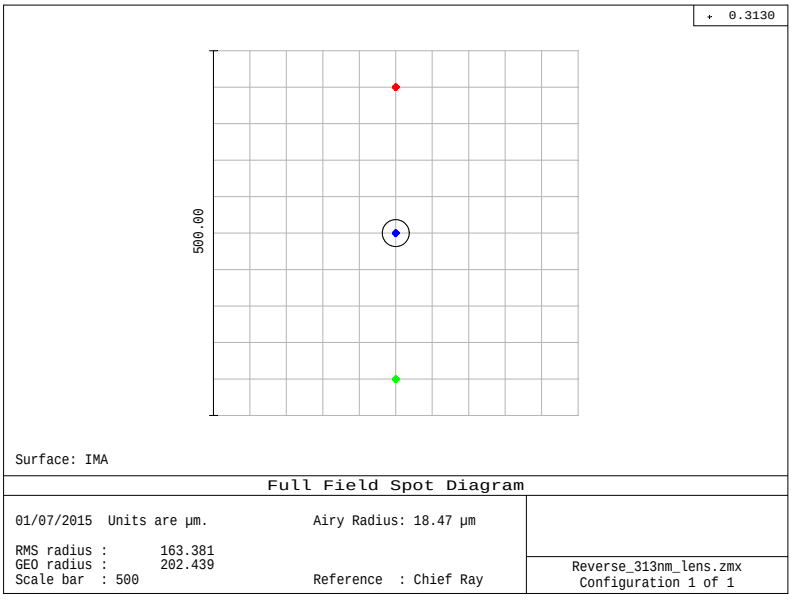

(c)

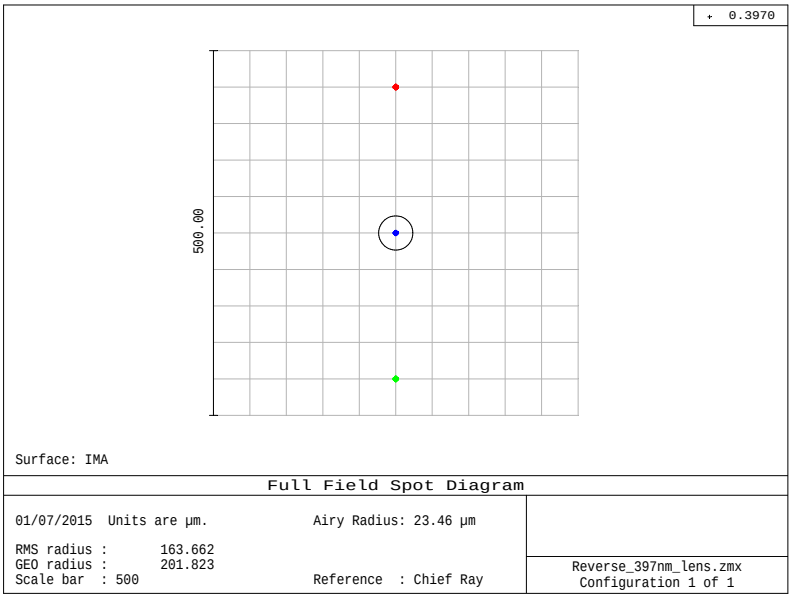

(d)

Figure 4.3: Reversed imaging system. (a) The layout of the lens design for 313 nm light field. (b) The layout of the lens design for 397 nm light field. (c) Simulated spot diagram for 313 nm light field. (d) Simulated spot diagram for 397 nm light field. Three objects are set 5 µm apart, which is a typical ion-ion spacing.

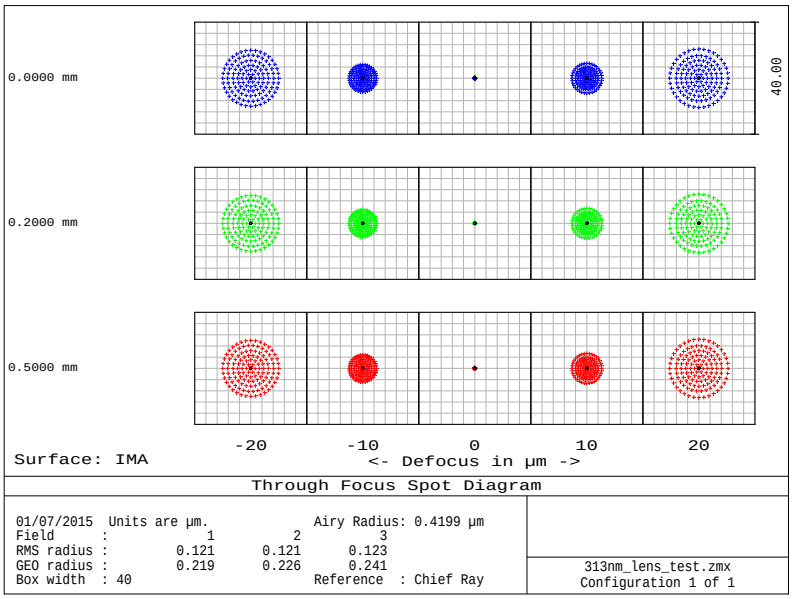
0.0000 mm
0.2000 mm
0.5000 mm
40.00
-20
-10
0
10
20
Surface: IMA
<- Defocus in µm ->
Through Focus Spot Diagram
01/07/2015 Units are µm.
Airy Radius: 0.4199 µm
Field : 1 2 3
RMS radius : 0.121 0.121 0.123
GEO radius : 0.219 0.226 0.241
Box width : 40
Reference : Chief Ray
313nm_lens_test.zmx
Configuration 1 of 1

(a)

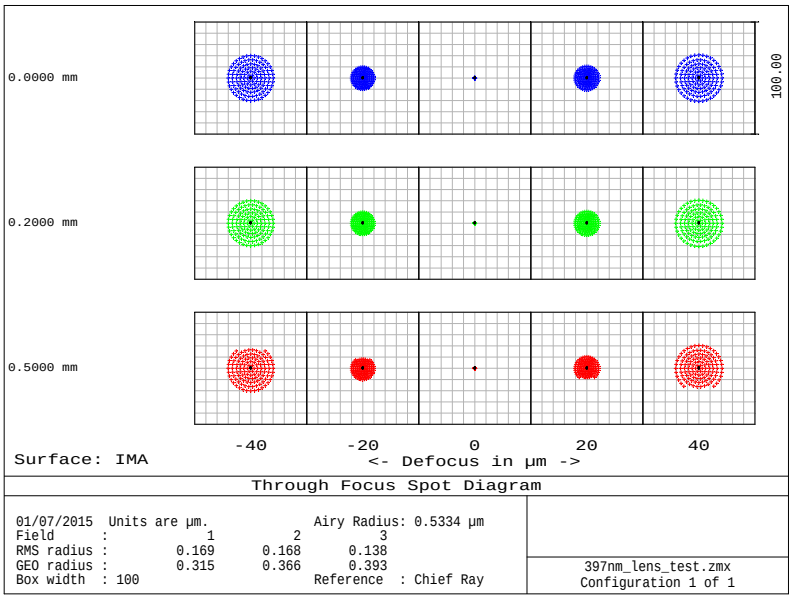
0.0000 mm
0.2000 mm
0.5000 mm
100.00
-40
-20
0
20
40
Surface: IMA
<- Defocus in µm ->
Through Focus Spot Diagram
01/07/2015 Units are µm.
Airy Radius: 0.5334 µm
Field : 1 2 3
RMS radius : 0.169 0.168 0.138
GEO radius : 0.315 0.366 0.393
Box width : 100
Reference : Chief Ray
397nm_lens_test.zmx
Configuration 1 of 1

(b)

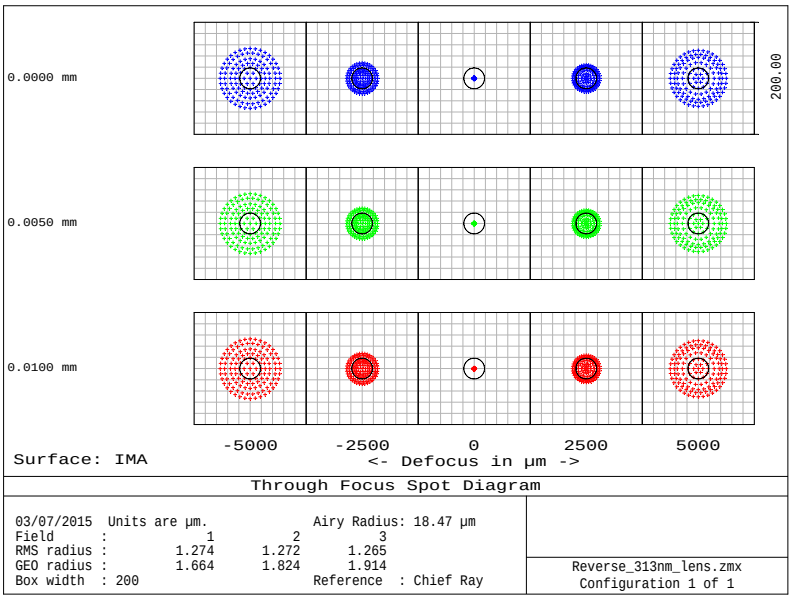

(c)

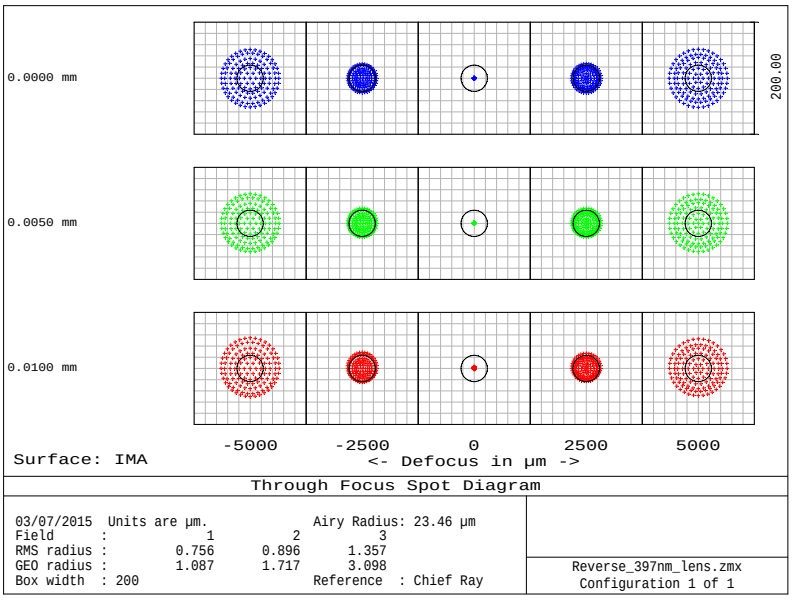

(d)

Figure 4.3: Simulated spot diagrams for the defocus. (a) for 313 nm light field. (b) for 397 nm light field. Reversed the system, and the defocus effect is less sensitive, shown in (c) for 313 nm and (d) for 397 nm.

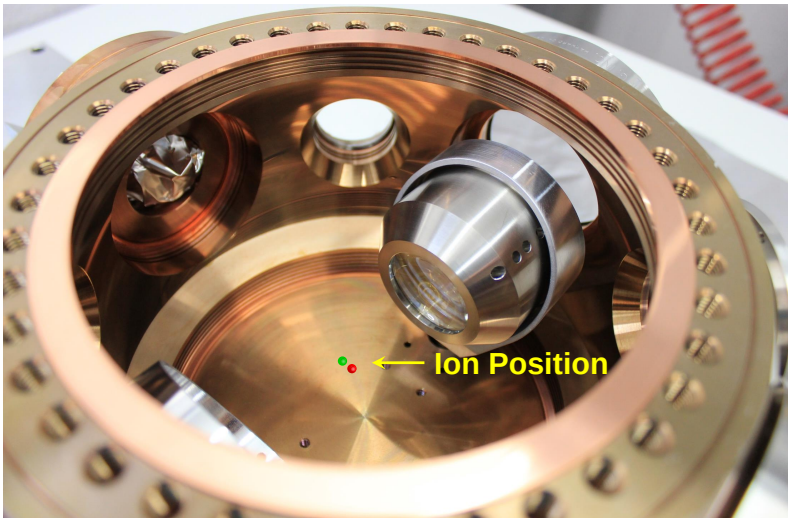

Figure 4.4: Two identical objectives are set up in the vacuum can and a cartoon of where the ions should be. The trap is not mounted in the vacuum chamber and is not shown here.

stage is used for the axial direction for the fine and fast tuning of the position. The other two axes are manually controlled.

Figure 4.6 shows the schematic diagram of a single imaging system. Outside the vacuum, both wavelength light fields pass through a vacuum viewport and hit a dichroic beamsplitter[4]. The diameter of the dichroic beamsplitter is 3 inches and is mounted 45° with respect to the optical table. The light field at 313 nm from beryllium ions reflects from the dichroic mirror and the 397 nm light field from calcium ions is transmitted. On each arm, there is a pair of lenses as mentioned before, followed by a flip mirror (not shown in the schematics) to guide the light field into a camera or a photomultiplier tube (PMT). Additionally, we insert a dichroic filter[5] to filter out the 866 and 854 nm scattering light during the qubit readout.

The camera we choose to image the ions is iXon X3 DU897 Electron multiplying CCD from Andor. It has a pixel number of 512×512 with each pixel size of 16×16 μm^2. A magnification of 40 onto a pixel size of 16 μm should give us 12.5 pixels between ions for two ions 5 μm apart. Obtained from the simulation, the diffraction limit is around 1 μm in diameter (double the airy radius), and the image would produce a spot size of $40 \times 1/16 = 2.5$ pixels.

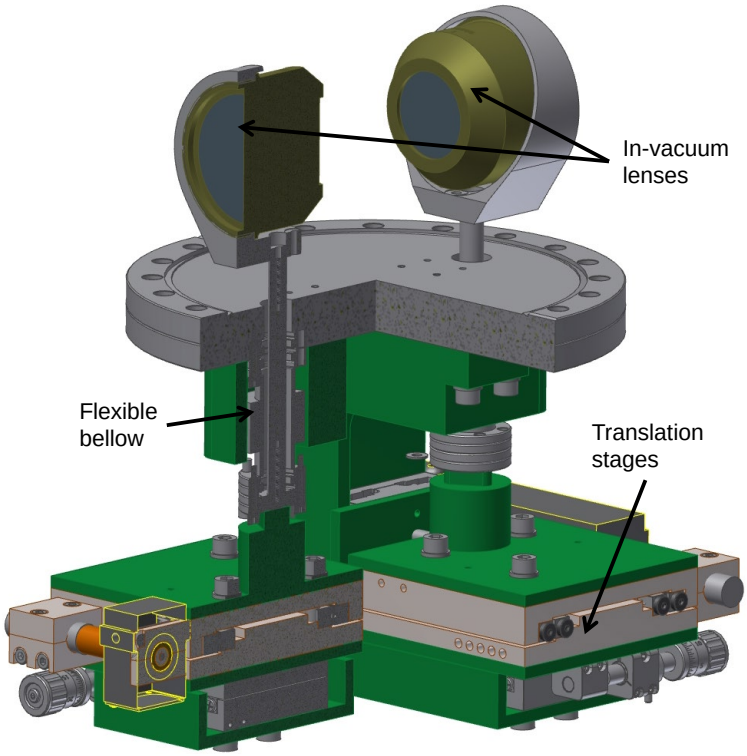

Figure 4.5: Drawing of the assembly of the in-vacuum objectives. Two objectives are mounted on the vacuum bellows separately inside the chamber. A three-dimensional translation stage is attached to the vacuum bellows outside the chamber. The ion trap is placed between the objectives, not shown here. (Figure by courtesy of Daniel Kienzler)

First Steps

We unfortunately did not measure the transmission of all the optical elements for 313 and 397 nm light fields. It would be good if we know how much loss we have when performing the qubit readout. Before we tried loading ions, some works have been done as follows. First, we have to get the position of the objective right because as described above the distance between the objective and the ion is critical. Here we shine and monitor both 313 and 397 nm light on the trap electrodes simultaneously as shown in Fig. 4.7. By doing so, we could align the position of the imaging system well for both beam paths. In the end, the object is moved back to compensate for the distance of the electrode front surface and the location of the ion.

[4] Altechna, www.altechna.com

[5] Semrock, FF01-405/150, alternatively FF01-390/18, which filters out the 423 nm light too.

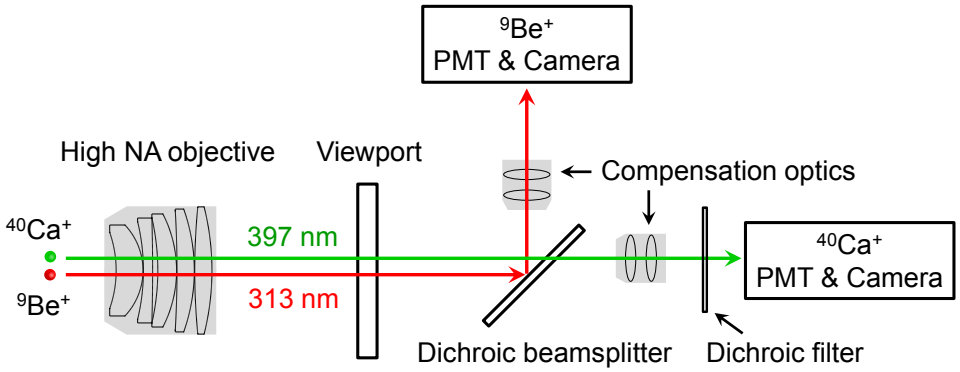

Figure 4.6: Schematics of the whole imaging system on one side of the trap. The second imaging system on the other side is identical to this.

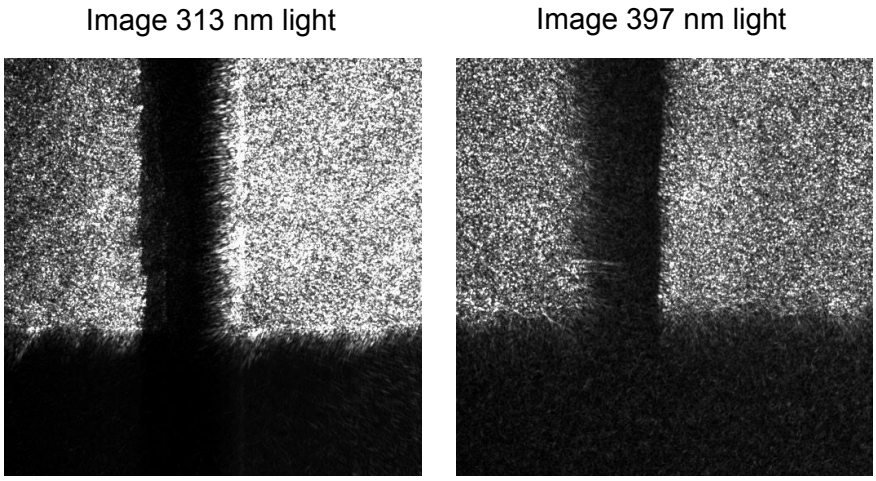

Figure 4.7: Illuminating 313 and 397 nm laser fields on the electrode simultaneously for aligning the imaging system.

Second, in order to observe the neutral fluorescence from the calcium atoms at 423 nm, we can use the same imaging system. According to the Zemax simulation, the diffraction limited resolution can also be achieved for the 423 nm light field by translating the objective by 0.32 mm backwards. Figure 4.8 shows the atom cloud fluorescing at 423 nm on the calcium camera.

Ion Imaging

After the laser systems (see Chapter 5) and the control system (see Section 4.3) were prepared and ready to use, we successfully loaded a two-species ion

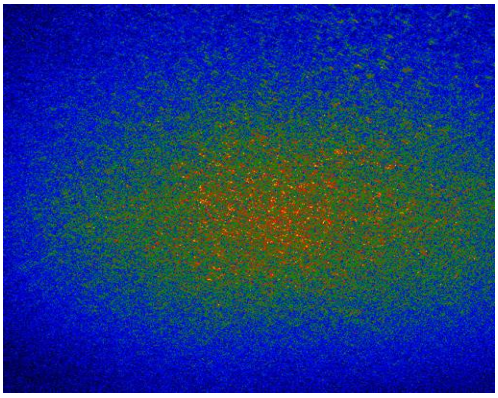

Figure 4.8: Neutral calcium fluorescence at 423 nm is observed by translating the objective by 0.32 mm.

chain in the segmented ion trap. As shown in Fig. 4.9, the ion chain contains two calcium ions and one beryllium ion. They were imaged simultaneously on separate cameras. On the calcium camera, the picture shows two calcium ions, and the dark region in the middle is where the single beryllium ion is located. The details of loading process can be found in Chapter 6.

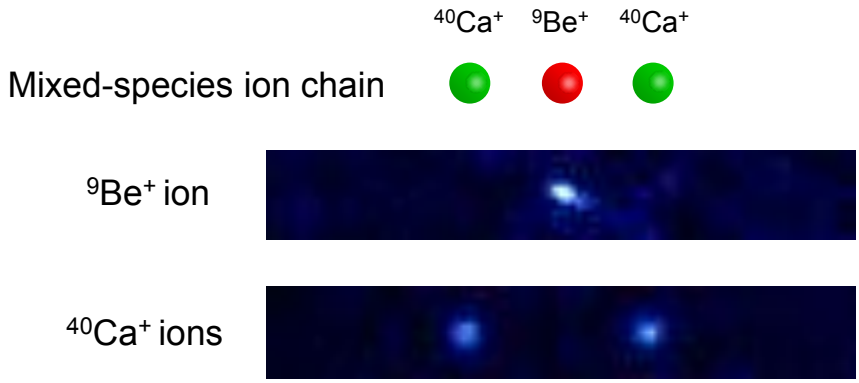

Figure 4.9: Pictures of two $^{40}Ca^+$ ions and one $^{9}Be^+$ ion trapped simultaneously in the same potential well. The calcium camera shows the image of two trapped $^{40}Ca^+$ ions, and a dark $^{9}Be^+$ ion in the middle can not be observed. The beryllium camera shows a single trapped $^{9}Be^+$ ion surrounded by the two dark $^{40}Ca^+$ ions.

Figure 4.10 shows the image of an ion string, where we can see each ion has a fan-shaped tail. We notice that the image quality is very sensitive to a tilt to the objective. This effect is then examined in the simulation. We consider a case in which the objective has a tilt of 0.2°. Figure 4.10 shows

the simulated spot diagram for the calcium arm, for which I set three objects with 5 µm apart. It can be seen that the resulting image also has a tail and is not circularly symmetric anymore. The direction of the tail depends on where the objective is tilted. Consequently, we need to take special care of the objective during the vacuum bake-out and mounting of the components in order to avoid any tilt. This slightly image distortion does not cause severe problems in our experiments.

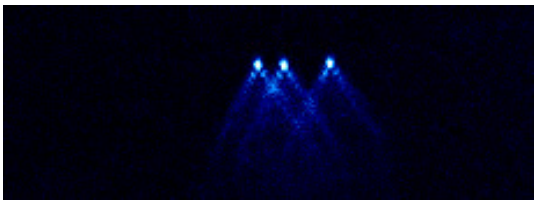

(a)

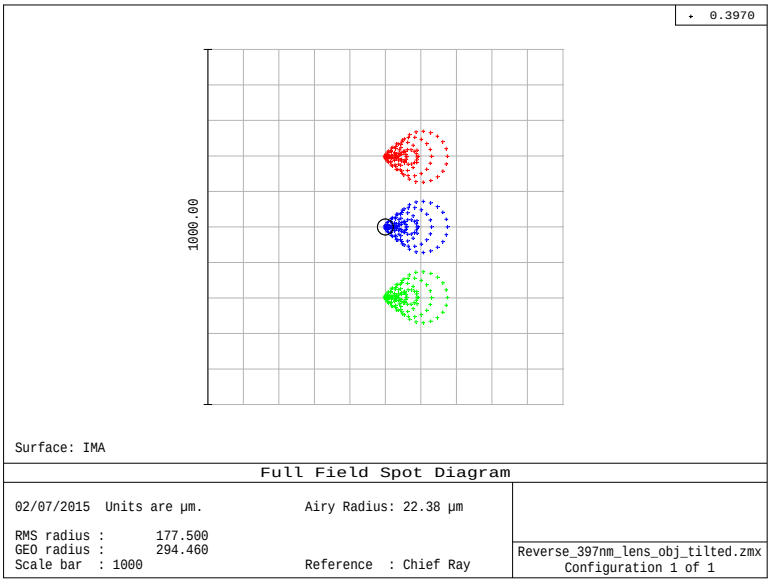

(b)

Figure 4.10: (a) Image of three $^{40}Ca^{+}$ ions. There is a dark ion in the trap, and each ion has a fan-shaped tail. (b) Simulation of the spot diagram in case the objective is tilted. The parameter used here is the tilted angle of 0.2°.

Photon Detection

We use PMTs from Hamamatsu[6], and the model we have is H10682-210. It has an active area of 8 mm in diameter. The count sensitivity at 397 nm and 313 nm is 6×10^5 and 4×10^5 $s^{-1}pW^{-1}$, respectively. These values have taken the quantum efficiency and collection efficiency into account. As a result, the total detection efficiency of the PMT per photon is 30 % for 397 nm and is around 26.5 % for 313 nm .

The total detection efficiency ζ used in Chapter 2.4 can be calculated with

$$\begin{aligned} \zeta &= \text{effective solid angle } 4.4\% \times \\ &\quad \text{PMT quantum efficiency } 26.5\% \times \\ &\quad \text{assuming } 15\% \text{ loss in optics and windows } (1 - 15\%) \\ &\simeq 0.01 \end{aligned}$$

We can now estimate the mean photon number which is collected during the qubit readout if the ion is in the bright state. In the case of beryllium ions, from Eq. (2.6) we have the photon scattering rate $\Gamma = \gamma/6$ with $s_0 = 0.5$. So the mean photon number we detect can be estimated by $N = \zeta\tau_D\Gamma \simeq 40$ photons with the duration of the detection pulse $\tau_D = 200$ µs. For calcium ions, $\Gamma = \gamma\rho_{P_{1/2}}$, where $\rho_{P_{1/2}}$ is the $P_{1/2}$ state populations, and we can see from the simulation results in Chapter 3.3 the maximum $\rho_{P_{1/2}}$ under our working conditions is around 0.1. Therefore, the mean photon number we can collect during the calcium qubit readout is $N \simeq 30$. Both estimations agree with what we observe in the experiment. We use this detection time of 200 µs in order to better distinguish the ion being dark or bright. A more careful study about the qubit readout fidelity of $^9Be^+$ ions is given in Chapter 6.2.

4.3 Experimental Control

The experiments we are doing in our group require a high level of control. In general, well-controlled laser frequency and phase, the duration of the laser pulse, voltage waveforms, and digital acquisition of data are necessary. To accommodate all of the required capabilities, we employ a field programmable gate array (FPGA) based experiment controller for use in the experiments with trapped ions.

The core of the computer control system uses the ML507 evaluation plateform[7], which contains Virtex-5 FPGAs and a PowerPC 440 processor. The FPGA-based control system can produce a timing-critical pulse sequence. It is convenient to program and powerful, where the users write a pulse sequence

[6]Hamamatsu, www.hamamatsu.com
[7]Xilinx, www.xilinx.com

in C/C++. The ML507 board is controlled via ethernet through a graphical user interface (GUI) on a standard PC. The GUI software we use is called "Ionizer", which allows users to set the parameters and run the experiments. It was originally developed by NIST Ion Storage Group and further improved by Ben Keitch, Vlad Negnevitsky and Matteo Marinelli. The codes of the GUI software were written in QT and C++.

The laser pulse duration is controlled by a TTL pulse (transistor-transistor logic) output from FPGA. The TTL pulse controls RF-switches, which switch on and off RF signals passing to the AOM in the laser setup. The laser frequency, phase and amplitude are modulated with the RF signal which is sent into the AOM from direct digital synthesizer (DDS) boards[8].

As a temporary solution used in our phase of experiments, the DDS boards are preloaded with frequency, phase and amplitude settings. They allow a TTL signal for a DDS channel to switch to another setting, where the phase is referenced to the first setting. These RF signals are sent to the AOMs for modulating the frequency, phase and amplitude of the laser in an experimental sequence. The limitations are that we can not update parameters (except time) during a sequence, there are only two profiles per DDS channel, and it uses an USB connection, which is slow. In this temporary setup, the phase switched between two DDS profiles is not coherent, and the starting phase of the first pulse of a DDS channel is random and the following pulses have a absolute phase reference to the first one if we keep running the same profile.

The whole computer control system is now upgraded, including the firmware of the DDS board and the FPGA board. Now the new system is much more flexible and powerful. The phase, frequency and amplitude sent to one AOM can be changed only with one DDS channel while running an experimental sequence, which we could not do in the past. This will facilitate more complex experiments in the future.

[8]Enterpoint, Milldown DDS board, www.enterpoint.co.uk

Chapter 5

Beryllium Laser Systems

Lasers are used for ionization, cooling and quantum state manipulation of ions. A stable and controllable laser system is an indispensable part for all of the experiments with trapped ions or atoms. In our group, since we work with two species of ions, more wavelengths and setups are involved in the laser systems. During my PhD, I developed laser systems and setup all the beam lines for control of beryllium ions. In this chapter, I will first describe an overview of our laser setup configuration and then focus on the work that I have done. Some of the sections are covered in our publication [Lo 14]. The calcium laser systems used in our group include contributions from many people. The details can be found in [Kienzler 15b, Sepiol 12, Lindenfelser 11].

One of the major challenges of working with beryllium is that the lowest-energy transitions for excitation from the ground state of both the ion and the atom require wavelengths in the ultraviolet (UV) region of the spectrum, at 313 and 235 nm respectively (Fig. 5.1). As a result, most experiments performed until now have required frequency doubled dye lasers for control of the ion. Photoionization of neutral beryllium has been previously performed using a frequency-quadrupled pulsed Titanium-Sapphire laser [Blakestad 10]. These laser systems are expensive and complex, motivating the use of alternative approaches. Here I will present a new setup for generating continuous-wave (CW) 235 nm light for photoionization of beryllium atoms based on two stages of frequency doubling of light from a diode laser. In addition, for controlling beryllium ions, we follow the approach demonstrated by Wilson *et al.* [Wilson 11] to generate three desired UV wavelengths at 313 nm starting from four infrared (IR) fiber-laser sources. The latter complements recent developments using telecom lasers at 1565 nm [Vasilyev 11] or diode lasers at 626 nm [Ball 13], with the advantage that the powers we achieve are far higher. I will present how we stabilize the frequency of the 313 nm light. Once the light at the fundamental laser frequency has been generated, it is delivered to the ions via acousto-optic modulators (AOMs) for frequency fine-tuning and laser

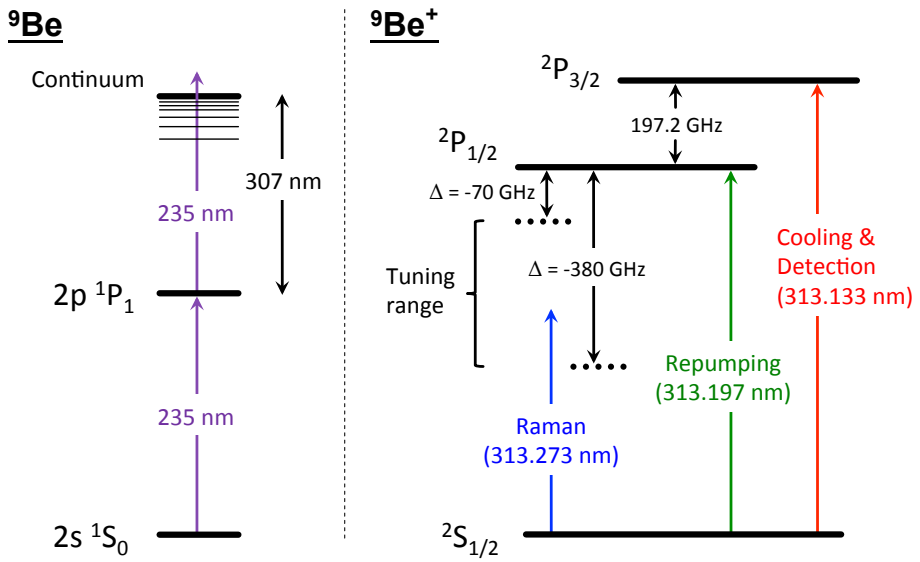

Figure 5.1: Relevant level schemes in beryllium. Left: two-photon ionization process by resonant excitation from $^1S_0$ to $^1P_1$ in neutral ^{9}Be. Right: ^{9}Be$^+$ energy levels addressed during trapping and manipulation.

pulse control. I will describe three AOM beam line setups for control of beryllium ions, including cooling/detection beams, repumping beams, and Raman beams.

5.1 Overview

Our vacuum chamber has 6 optical ports which can be accessed by the laser beams. A schematic of the laser arrangements is shown in Fig. 5.2. We combine calcium and beryllium laser beams on the dichroic beamsplitter which is the same as the one in the imaging system. This dichroic beamsplitter is designed for 397 nm and 313 nm light fields. It also works for all the calcium laser wavelengths with some power loss. However, the coating of this dichroic beamsplitter does not reflect 235 nm light. For Port 1, we use a dichroic beamsplitter[1] for which the reflection band is from 230 to 325 nm and the transmission band is from 380 nm to near-infrared. The calcium laser beams entering from this port are linearly polarized. For the horizontal polarization component, the ion experiences $\hat{\pi}$ polarized light. If the laser is vertically polarized, the ion will experience a superposition of $\hat{\sigma}^+$ and $\hat{\sigma}^-$.

For the cooling, detection, and repumping beams applied to beryllium ions, we require pure $\hat{\sigma}^+$ polarized light. This requirement can only be fulfilled by

[1]Semrock FF347-Di01, www.semrock.com

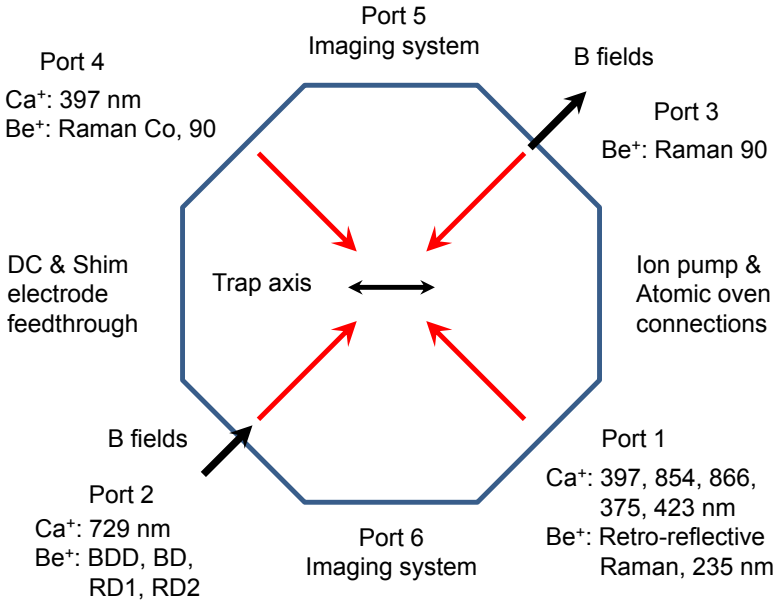

Figure 5.2: Laser beam configurations near the vacuum chamber.

sending the laser beam parallel to the magnetic field. Here we use Port 2, as shown in Fig. 5.2. The 729 nm laser beam for calcium qubit manipulations uses the same port, but the polarization of this beam is not critical for our particular choice of beam direction relative to the magnetic field [Roos 00b].

The Raman beams for controlling the beryllium qubit are illuminated from Port 3 and 4. To drive a single-qubit rotation, two co-propagating Raman beams are sent from Port 3. Implementation of sideband cooling or a two qubit gate with beryllium ions needs two Raman beams perpendicular to each other or counter-propagated, where the difference of two k vectors is non-zero. Therefore, one beam is sent from Port 3 and the other one is sent from Port 4.

Apart from the regular setup described above, the additional 397 nm laser beam in Port 4 is used for electromagnetically-induced-transparency (EIT) cooling [Roos 00a], and we retro-reflect the two co-propating Raman beams from Port 1 to demonstrate parallel single-qubit quantum operations using transported ions [de Clercq 15].

5.2 Laser Source at 235 nm

Ionization of neutral beryllium atoms requires an energy of 9.3 eV, corresponding to a wavelength of 133 nm. Since this wavelength lies in the vacuum UV,

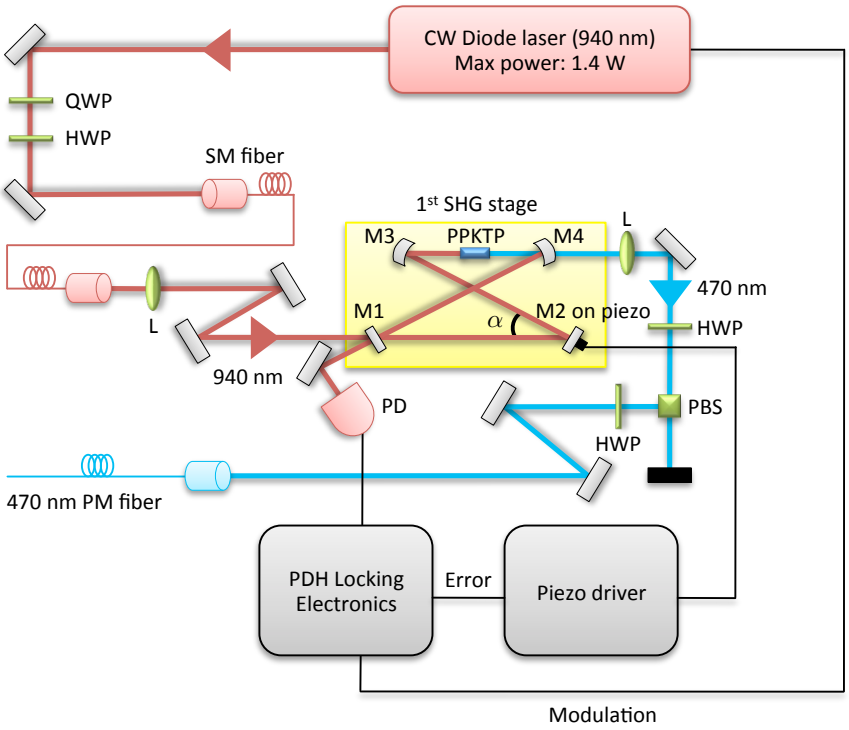

Figure 5.3: First SHG stage: 940 to 470 nm. Notation: L, lens; QWP, quarter-wave plate; HWP, half-wave plate; Mi, cavity mirrors; PBS, polarizing beam-splitter; PD, photodiode; SM fiber, single-mode fiber; PM fiber, polarization-maintaining fiber; α, full-opening angle. Also shown are the locking electronics. For details, see text.

it is desirable to remove the electron using a two-photon excitation scheme. The photoionization cross-section is enhanced if the first stage of excitation is performed on resonance with an allowed transition in the neutral atom [Kjaergaard 00, Lucas 04b]. Furthermore, resonance-enhanced photoionization is convenient in that it is species selective. For these reasons we choose to use two photons at 235 nm, the first of which is resonant with the $^1S_0 \leftrightarrow {}^1P_1$ transition of neutral beryllium (Fig. 5.1, left). In what follows we describe our 235 nm laser source, obtained by means of two stages of second-harmonic generation (SHG) starting from a commercial 940 nm diode laser with a tapered amplifier (TA)[2].

5.2.1 First SHG Stage: 940 to 470 nm

The first stage of frequency doubling converts 940 into 470 nm light. A schematic of the experimental setup is shown in Fig. 5.3. The Toptica TA unit can deliver up to 1.4 W at 940 nm. We first pass this light through a single-mode (SM) fiber to clean up the spatial mode, resulting in up to 700 mW which can be sent to a bowtie cavity for power build-up. The frequency conversion is performed using a periodically-poled potassium titanyl phosphate (PPKTP) crystal, chosen due to its high non-linearity and transparency at both 940 and 470 nm. The PPKTP crystal[3] has a 5.95 µm poling period and is temperature stabilized close to 21°C for quasi-phase matching (QPM).

The cavity was designed by Joseba Alonso. The cavity's geometry is optimized to achieve high conversion efficiency while minimizing the dependence of the second-harmonic output power on the short arm optical length (M3-M4) [Wilson 11]. QPM is intrinsically free of walk-off (the Poynting and propagation vectors of the second-harmonic field are parallel), so a value for the Boyd-Kleinmann focusing parameter of $\xi = 2.84$ should yield the maximum conversion efficiency [Boyd 68]. This parameter is defined as $\xi \equiv l_c/b$, with l_c the crystal length and $b = 2\pi n_\omega w^2/\lambda$ the confocal parameter of the laser beam. Here n_ω is the refractive index of the crystal sampled by the input light (of wavelength λ) and w the waist size of the beam in the crystal. Based on previous observations of thermal lensing effects in a similar system operated at 922 nm by Le-Targat *et al.* [Targat 05], we designed the cavity for a larger waist of $w = 50$ µm ($\xi = 0.98$) to reduce the intensity of the generated blue light inside the crystal. The curved mirrors introduce astigmatism to the beam, which we minimize by using a small opening angle $\alpha \approx 11°$ (see Fig. 5.3), limited by geometric constraints imposed by the mirror-mounts. The transmission of the input coupling mirror M1 was chosen to be $T_1 = 14.5$ % in order to account for the expected cavity losses, and thus achieve an optimal impedance matching to the cavity for a predicted input power of $P_{940} = 600$ mW. More details of the cavity design are given in Table 5.1.

The length of the cavity is locked to the pump laser using the Pound-Drever-Hall (PDH) technique [Drever 83]. The 940 nm diode is phase-modulated at 15.6 MHz via a bias-tee input to the diode current. The light reflected from the cavity is collected by a fast photodiode and the signal is demodulated and filtered. The error signal thereby produced is used to feed back on the piezoelectric stack to which M2 is glued.

The results for this first stage of frequency doubling are shown in Fig. 5.4, including both the second-harmonic output power P_{470} and the ratio $\eta_{470} =$

[2]Toptica, www.toptica.com
[3]Raicol Crystal Ltd., raicol.com

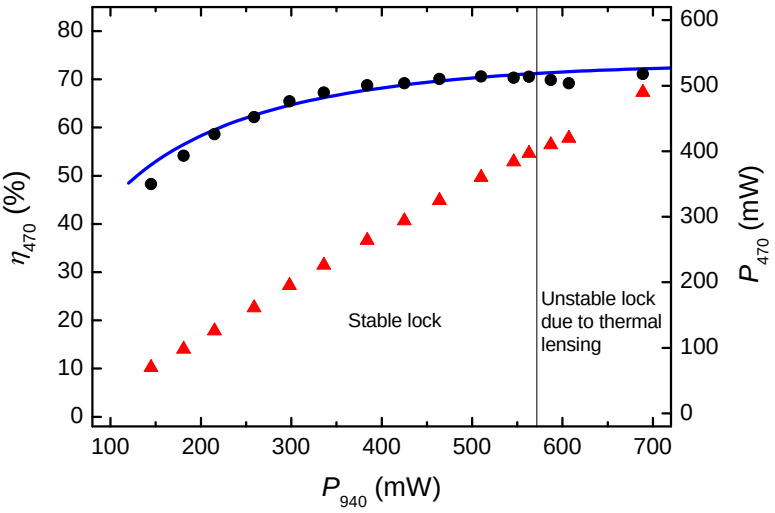

Figure 5.4: Measured net power at 470 nm (triangles, referred to the right axis) and the power ratio of the 940 → 470 nm doubling cavity (circles, referred to the left axis) as a function of the pump power. The solid line corresponds to the theoretical prediction of η_{470} based on Eq. (C.5) in the Appendix C. To the right of the vertical line the cavity becomes unstable (see text).

P_{470}/P_{940} as a function of the input power P_{940}. The solid line results from the theoretical calculation using the theory given by Le-Targat *et al.* [Targat 05], which generalized the seminal work of Boyd and Kleinmann [Boyd 68] to a situation including an optical cavity [Freegarde 01]. Our calculations use the cavity parameters and the crystal properties provided by the manufacturer. These are displayed in Tables 5.1 and C.1. The theory is summarized in the appendix.

It is worth noting that, as was observed previously in a similar system operated at 466 nm [Targat 05], the output power is limited by thermal lensing induced by absorption of the 470 nm light in the crystal. Our cavity becomes unstable for $P_{470} > 400$ mW. For stable operation, we set $P_{940} \approx 500$ mW and obtain $P_{470} \approx 350$ mW ($\eta_{470} \approx 70$ %).

5.2.2 Second SHG Stage: 470 to 235 nm

The 470 nm light generated in the first SHG stage is sent through a 30 m long polarization-maintaining (PM) fiber (OZ Optics) to a neighboring laboratory. The output mode of the fiber is matched to the spatial mode of the second bowtie cavity with a two-lens telescope, and the polarization is cleaned using a polarizing beam-splitter (PBS) cube (see Fig. 5.5). Input-coupling losses and absorption in the fiber result in a maximum value of ≈ 140 mW of light incident on the 470→235 nm cavity.

Table 5.1: Details of the cavities for SHG of 470 and 235 nm light. All mirror coatings were provided by Layertec GmbH. $w_{\mathrm{h,v}}$ are the horizontal and vertical beam waists.

		940→470 nm	470→235 nm
Crystal	Material	PPKTP	BBO
	Phase-matching	QPM (type I)	CPM (type I)
	Dimensions	$1 \times 2 \times 30$ mm^3	$4 \times 4 \times 10$ mm^3
	Phase-matching angles θ/ϕ	90/0°	58.15/0°
	Surfaces	AR coated @ 940 nm	Brewster-cut (59.25°)
	Temperature stabilization	0.1°C (@ 21°C)	Not stabilized
Mirrors	Radius of curvature M3 & M4	100 mm	38 mm
	Reflectivity M1	85.5 %	99.0 %
	Coating M2-M4	Sputter	Ion-beam sputter
Cavity	Long arm length	399 mm	320 mm
	Crystal-mirror distance	50 mm	18 mm
	Full opening angle (α)	11.0°	33.8°
	Mean waist short/long arm	50/212 µm	18/145 µm
	Elipticity short/long arm ($w_{\mathrm{h}}/w_{\mathrm{v}}$)	0.99/0.96	1.53/1.00
	Full spectral range (FSR)	560 MHz	805 MHz
	Linewidth	43 MHz	2.7 MHz
	Finesse ($\mathcal{F}$)	13	300

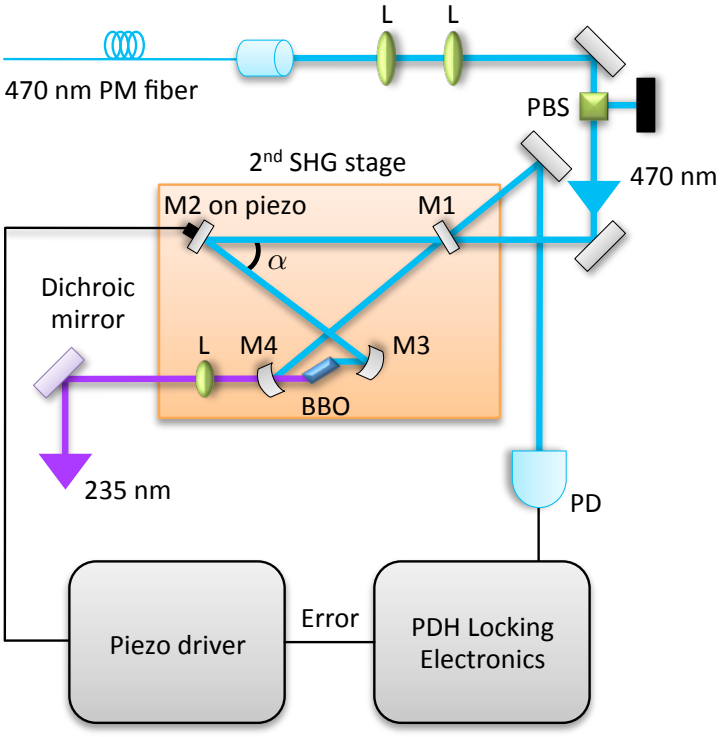

Figure 5.5: Second SHG stage: 470 to 235 nm. Labels are as in Fig. 5.3. For details, see text.

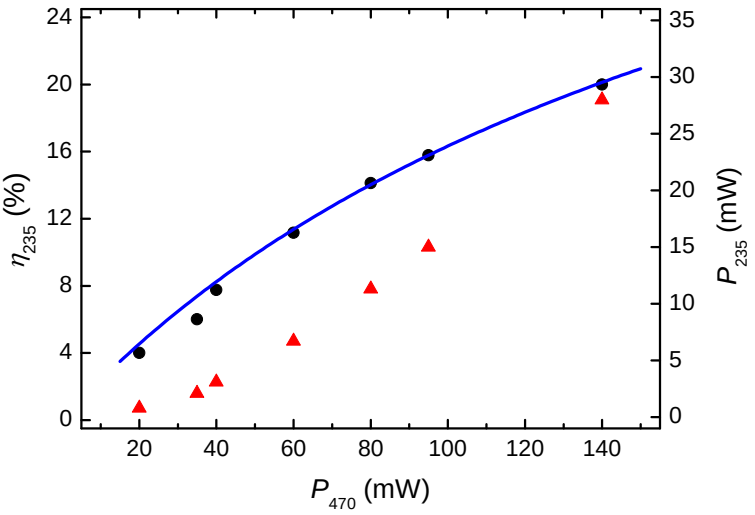

Figure 5.6: Measured net power at 235 nm (triangles, referred to the right axis) and the power ratio of the 470→235 nm doubling cavity (circles, referred to the left axis) versus the pump power at 470 nm. The solid line corresponds to the theoretical prediction of η_{235} based on Eq. (C.5) in the Appendix C.

For this SHG stage we use a BBO crystal (Castech Inc.) Brewster-cut for 470 nm which achieves critical type-I phase matching (CPM) at an angle of 58.15°. This cavity was also designed to optimize the conversion efficiency of the frequency doubling while being insensitive to changes in the positions of the focusing mirrors M3 & M4 [Wilson 11]. By contrast with the first frequency-doubling stage, the use of angle phase-matching intrinsically results in walk-off which limits the length of the conversion region of the crystal. The optimized cavity parameters are given in Table 5.1. The length of the cavity is also stabilized using the PDH method in order to keep it on resonance with the pump laser. Since the modulation frequency applied to the diode laser (15.6 MHz) is comparable to the linewidth of the 940→470 nm cavity, the 470 nm light also exhibits modulation sidebands at 15.6 MHz and can be directly used for the PDH locking scheme.

Figure 5.6 shows the UV output power P_{235} along with the power ratio $\eta_{235} = P_{235}/P_{470}$ as a function of the input power P_{470}. Note that we define P_{235} and η_{235} in terms of the net second-harmonic power at the output of the cavity. With $P_{470} \approx 140$ mW, we obtain $P_{235} \approx 28$ mW ($\eta_{235} \approx 20$ %). Considering the 22 % reflection at the output surface of the Brewster-cut BBO crystal, the total UV light generated is ≈ 36 mW. The theoretical curve is calculated using the values given in Table C.1, yielding $\Gamma_{\text{eff}} \approx 1.6 \times 10^{-4}$ W^{-1}. The level of agreement between the measured values of η_{235} and those predicted by the theory is reasonable given the assumptions made in the theory, which include

perfect phase-matching of a circular beam and no absorption in the crystal (see Table C.1).

The counter-propagating fundamental mode of a bowtie cavity can be excited by any back-reflecting element in the cavity, which can lead to considerable back-circulating power if the finesse $\mathcal{F}$ of the cavity is high [Hemmerich 90]. In the 470→235 nm cavity, we observe that light is emitted along a direction which is consistent with this effect. This leads to a reduction in η_{235} and an unstable output power. The back-circulation could likely be eliminated by reducing the reflectivity of M1 if required [Hemmerich 90]. Since photoionization does not require high stability or high power, we have currently chosen not to pursue this.

The power we achieve is comparable to the average power of the pulsed laser used in [Blakestad 10], and considerably higher than values which have been previously used to perform photoionization of other atomic species [Lucas 04b, Kjaergaard 00]. The $^1\mathrm{S}_0 \leftrightarrow ^1\mathrm{P}_1$ transition of neutral beryllium atoms has a saturation intensity of $8.9\,\mathrm{mW/mm^2}$, corresponding to $70\,\mu\mathrm{W}$ for a beam waist of $50\,\mu\mathrm{m}$.

5.3 Laser Source at 313 nm

Quantum control experiments using beryllium ions require near resonant light for Doppler cooling and optical pumping and, in our case, a far-detuned Raman laser for coherent manipulations [Wineland 98]. As shown in Fig. 5.1 (right), the wavelengths of the $^2S_{1/2} \leftrightarrow {}^2P_{3/2}$ and $^2S_{1/2} \leftrightarrow {}^2P_{1/2}$ transitions are at 313.133 nm and 313.197 nm, respectively. We have chosen to operate our Raman laser system at a wavelength between 313.221 and 313.322 nm, detuned to the red of the $^2P_{1/2}$ manifold by between -380 and -70 GHz. Small detunings allow for lower power for a given Raman transition rate, but lead to more spontaneous scattering of photons which will induce errors in the quantum state manipulation. Therefore, for high-fidelity control of a quantum system, a large detuning from the excited state is preferable [Ozeri 07]. The laser systems to generate all three wavelengths are shown schematically in Fig. 5.7.

5.3.1 SFG Stage: Infrared to 626 nm

To produce the three UV wavelengths we require, we start from four fiber lasers[4] at 1550.65 nm, 1050.56 nm, 1551.44 nm and 1050.98 nm which can be thermally tuned over a range of 80 GHz and fine-tuned over ±150 MHz by means of an internal piezoelectric element. The laser outputs (PM fibers) are terminated with an integrated beam-collimation system, producing beams

[4]NP Photonics, www.npphotonics.com

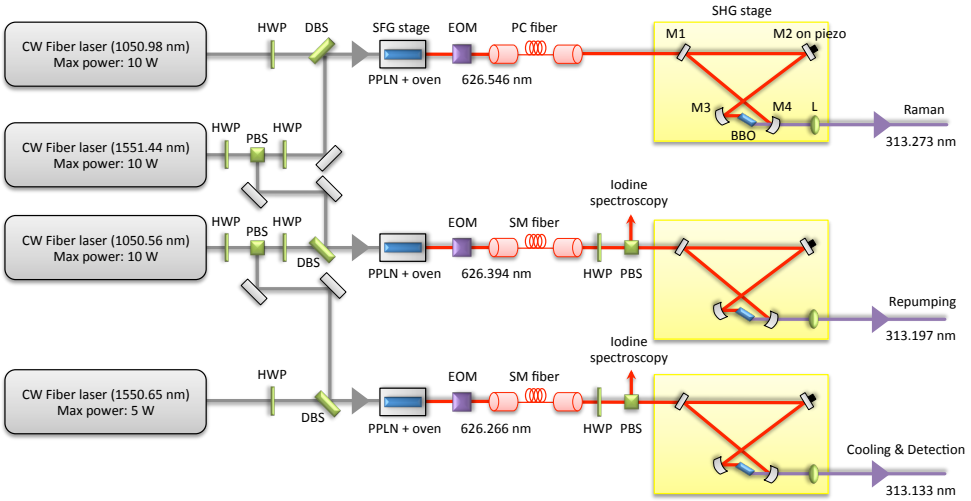

Figure 5.7: Setup for generating three wavelengths at 313 nm for Doppler cooling, optical pumping and coherent manipulations of beryllium ions. Notation: DBS, dichroic beam-splitter; EOM, electro-optic modulator; PC fiber, photonic-crystal fiber; the rest are as in Fig. 5.3. The locking electronics and focusing lenses are not shown. The wavelengths indicated for the Raman setup are approximately in the middle of the range of operation. For details, see text.

of diameters between 3 and 4 mm. The sum-frequency generation (SFG) is performed using magnesium-oxide-doped periodically-poled lithium niobate (MgO:PPLN) crystals[5]. Each crystal contains three different poling periods of around 11.5 µm on strips 1 mm wide which run down the length of the 4 cm long crystal. The PPLN crystals are maintained at a constant operating temperature in order to achieve the phase-matching condition for maximizing the conversion efficiency. In our case, we obtain maximal 626 nm output power for temperatures close to 180°C, stabilized to within ±0.01°C. In order to access the highest non-linear coefficient of the crystal, the polarization axis of the light is parallel to the thickness of the crystal.

The 1050.56 nm light is shared between the cooling and repumping setups (Fig. 5.7). The power ratio can be tuned by rotating the half-wave plate in front of the PBS. The same mechanism applies for the 1551.44 nm laser, which is split between the repumping and Raman setups. In all three setups, two of the fiber-laser outputs (pump beams) are overlapped using a dichroic element after passing through independent beam-shaping telescopes (not shown in the figure) that focus the beam to an optimal waist inside the crystal. The beam waist that maximizes the conversion efficiency was experimentally found to

[5]Covesion Ltd., www.covesion.com

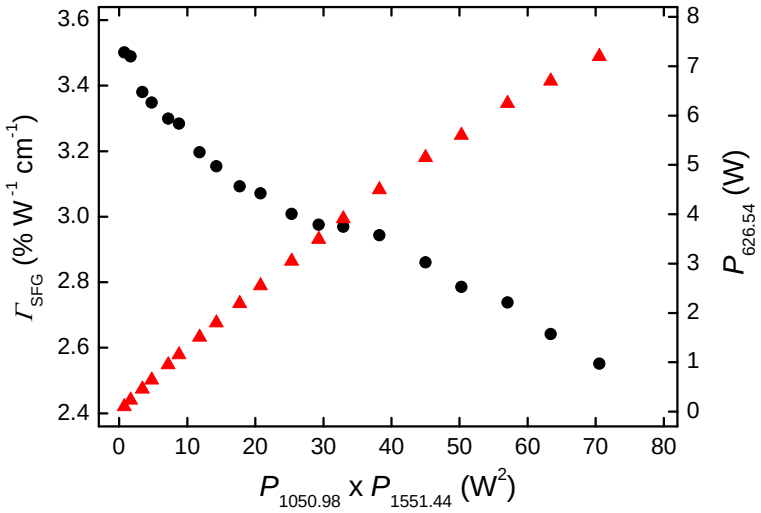

Figure 5.8: Net power of 626 nm light measured at the output as a function of the product of pump powers (triangles, referred to the right axis). Also shown (circles, referred to the left axis) is the sum-frequency-generation efficiency per unit length of the crystal.

be 58 ± 5 µm at the center of the crystal. This is larger than the 40 µm predicted from the Boyd-Kleinmann theory. A possible explanation for this difference could be phase mismatch or imperfect spatial-mode overlap arising from absorption-induced heating in the crystal [Batchko 98].

All SFG setups exhibit similar performance. For the Raman light (SFG of the 1050.98 nm and 1551.44 nm) the output power for different products of the pump powers is plotted in Fig. 5.8. We have generated up to 7.2 W of red light at 626.54 nm using pump powers of 8.5 W at 1050.98 nm and 8.3 W at 1551.44 nm. Also shown is the conversion efficiency per unit length

$$\Gamma_{\mathrm{SFG}} = \frac{P_{626}}{P_{1051} P_{1551} l_{\mathrm{c}}}, \tag{5.1}$$

which characterizes the performance of the non-linear crystal. We find a maximum value of $\Gamma_{\mathrm{SFG}} \approx 3.5$ % W^{-1}cm^{-1}, which is reduced to ≈ 2.5 % W^{-1}cm^{-1} at the highest output power, possibly due to absorption-induced heating in the crystal. To test whether these effects are more prominent in the IR or the visible light, we measured Γ_{SFG} for different combinations of pump powers with a constant product $P_{1050.98} \times P_{1551.44}$, which would be expected to produce the same amount of red light. The results (see Fig. 5.10) show that the conversion efficiency is lowest when $P_{1551.44} > P_{1050.98}$. The Pearson correlation coefficients $\mathcal{R}_\lambda$ between Γ_{SFG} and the pump powers are $\mathcal{R}_{1050.98} \approx -0.5$ and $\mathcal{R}_{1551.44} \approx -0.9$, indicating that the absorption of the 1551.44 nm light contributes most to thermal effects.

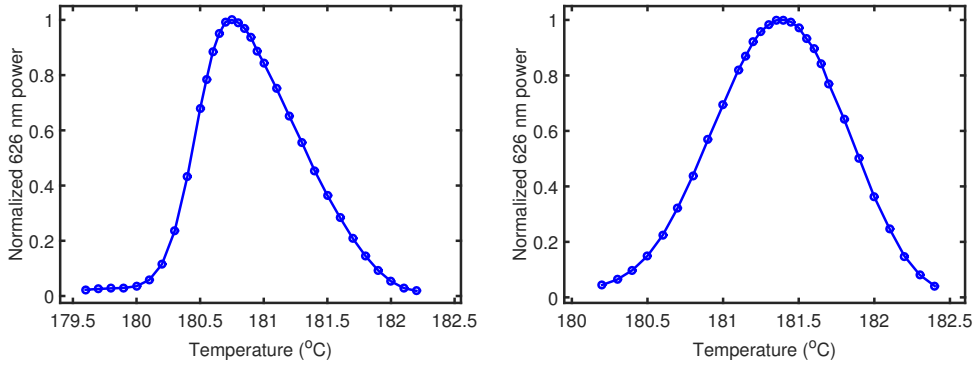

(a) (b)

Figure 5.9: Temperature dependence of the Raman sum frequency generation setup. The 626 nm power is normalized to 1. The PPLN nonlinear crystal is mounted in the oven and the temperature is controlled with a PID-regulated thermoelectric in a step of 0.01° (a) High pump powers. (b) Low pump powers.

We also measure the temperature dependence of the SFG in the Raman setup with two different pump power settings. Figure 5.9 shows the experimental results, where the 626 nm power is normalized to 1 for both cases. We can see that with high pump powers the temperature of getting maximum conversion efficiency goes down. This can be explained by the fact that higher pump power heats up the nonlinear crystal more strongly. So we should set the temperature lower in order to fulfill the phase-matching condition. The observed asymmetry in the case of high pump powers is due to spread of the wavevectors in the focused beam, since the phase-matching conditions are fulfilled at different temperatures for different wavevector components of the pump beam [Schuck 10, Gibson 98].

At an output power of ≈ 7 W the drift was observed to be below 0.2 % per hour over 10 hours of operation. After running this system for more than a year at a variety of input and output powers, we have seen little change in the conversion efficiency, and no realignment of the optical components has been required.

Since the detection and repumping beams must provide light resonant with the ${}^2S_{1/2} \leftrightarrow {}^2P_{3/2}$ and ${}^2S_{1/2} \leftrightarrow {}^2P_{1/2}$ transitions, the absolute frequencies of these lasers must be actively stabilized. The transition linewidths are $\gamma/2\pi \approx 19.4$ MHz, so we aim for frequency stability on the level of a megahertz. To that end, a small portion of the 626 nm light is picked off and sent through an optical fiber to a Doppler-free saturated-absorption-spectroscopy setup with an iodine cell [Demtroeder 82, King 99]. This will be discussed later in this chapter. However, in the Raman setup the stability of the absolute frequency

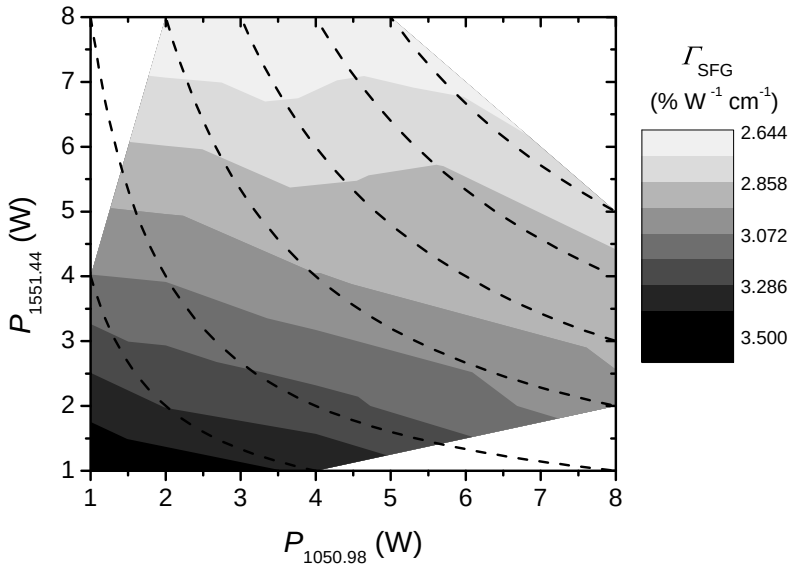

Figure 5.10: Conversion efficiency per unit length of the crystal measured for different pump powers. The dashed lines correspond to combinations of $P_{1551.44}$ and $P_{1050.98}$ with a constant product. The data points were taken along these curves.

is not as critical due to the large detuning from resonance, and the natural stability of the fiber lasers (which we have measured to drift by less than 60 MHz over a day) is sufficient for our purposes.

5.3.2 SHG stage: 626 to 313 nm

The beams from the SFG setups are coupled into high-power SM fibers and sent to frequency doubling cavities for conversion to 313 nm. The coupling efficiency is ≈ 90 % in the repumping and cooling setups excluding the loss in the fiber collimators (5 m long SM fibers[6]). This is because the high quality Gaussian modes of the pump beams produced by the fiber lasers is transferred to the 626 nm light. Measurement of the spatial mode of the output 626 nm light is shown in Fig. 5.11, measured with a beam profiler. The power transmitted through the fibers saturates at ≈ 2 W due to stimulated Brillouin scattering [Agrawal 07]. It is interesting that we observe the frequency of the reflected light from the fiber is shifted by 27 GHz, which is measured with a wavelength meter. In order to avoid this problem in the Raman setup, where we require higher powers, we use a photonic-crystal fiber[7]. The limitation is in this case the coupling efficiency into the fiber, which is ≈ 60 %.

[6]OZ Optics, www.ozoptics.com
[7]NKT Photonics, www.nktphotonics.com

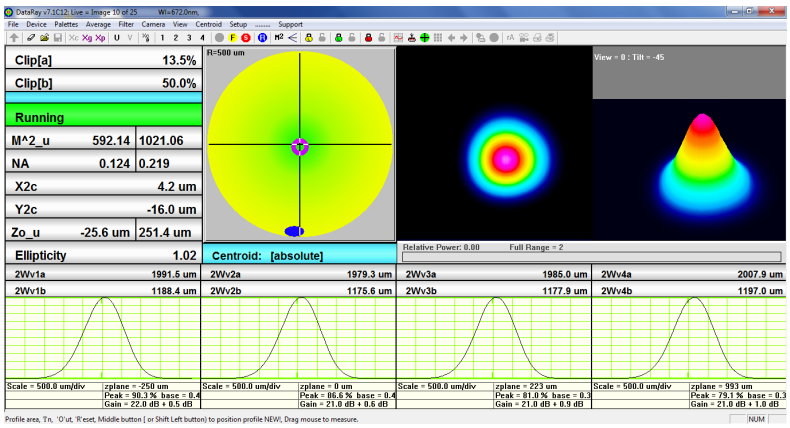

Figure 5.11: The beam profile of the 626 nm light measured with a beam profiler.

SHG from 626 to 313 nm is performed in all three cases using a BBO crystal Brewster-cut for 626 nm with a phase-matching angle of 38.35°. The crystals are placed in bowtie cavities ($FSR \approx 845$ MHz and $\mathcal{F} \approx 275$) for pump-power enhancement. The beam waists in the BBO crystals are 36.7 (23.6) µm for the horizontal (vertical) direction. The design and properties of the doubling cavities are very similar to those reported by [Wilson 11] except that we use a Pound-Drever-Hall rather than Hänsch-Couillaud scheme to stabilize the cavity length. In order to generate the required modulation for the PDH stabilization, we pass the 626 nm beams through electro-optic phase modulators (Qubig) placed directly after the PPLN crystals and driven at frequencies closed to 125 MHz. All of the SHG conversion setups are similar, so below we give explicit details for the Raman setup, for which we work with the highest powers.

Figure 5.12 shows the 313 nm output power P_{313} and the power ratio $\eta_{313} = P_{313}/P_{626}$ as a function of the power P_{626} coupled into the Raman doubling cavity. As before, P_{313} and η_{313} are defined in terms of the net second-harmonic power delivered by the system. The maximum output power obtained is ≈ 1.95 W, with $P_{626} \approx 3.8$ W ($\eta_{313} \approx 52$ %). Including the 20 % reflection at the output facet of the Brewster-cut BBO crystal, overall ≈ 2.4 W at 313 nm are produced. The parameters for the theoretical calculation of Eq. (C.5) are given in Table C.1.

In order to characterize the long-term performance of the UV light production, we have monitored the stability of the 313 nm power. For these tests, output powers up to $P_{313} \approx 1$ W ($P_{626} \approx 2.2$ W) were used. Observed drifts were below 0.5 % per hour during 8 hours of continuous operation.

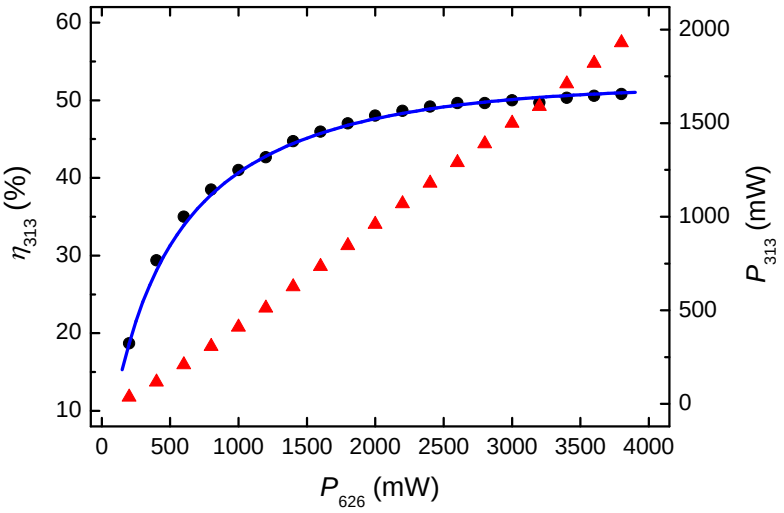

Figure 5.12: Measured net power at 313 nm (triangles, referred to the right axis) and the power ratio of the 626→313 nm Raman doubling cavity (circles, referred to the left axis) versus the input power at 626 nm. The solid line corresponds to the theoretical prediction of η_{313} based on Eq. (C.5) in the Appendix C.

5.4 Iodine Spectroscopy

Since the detection and repumping beams provide light resonant with the $^2S_{1/2} \leftrightarrow {}^2P_{3/2}$ and $^2S_{1/2} \leftrightarrow {}^2P_{1/2}$ transitions of the beryllium ion, the absolute frequencies of these lasers must be actively stabilized. The transition linewidths are $\gamma/2\pi \approx 19.4$ MHz, so we aim for frequency stability on the level of a megahertz. To that end, precision spectroscopy can be used to provide a very stable frequency reference for a laser. Here we do not stabilize the frequency of 313 nm light directly. Instead a small portion of the 626 nm light is picked off and sent through a single-mode fiber to a Doppler-free saturated absorption spectroscopy setup with an iodine vapor cell [Demtroeder 82, King 99].

The optical setup is shown in Fig. 5.13. The 626 nm light out of fiber first passes through a half-wave plate and a PBS, where the half-wave plate is used to clean up the polarization of the light and make sure the transmitted power is maximum. Then the beam is focused into an AOM, followed by another lens collimating the beam. It is passed through a quarter-wave plate and reflected from a mirror. The polarization of the light in the second pass has changed from horizontally polarized to vertically polarized by passing through quarter-wave plate twice. It is then picked off from the reflection port of the PBS. This double-pass configuration is different from the one we use for the UV light (see next Section) since the AOM for this wavelength can take any

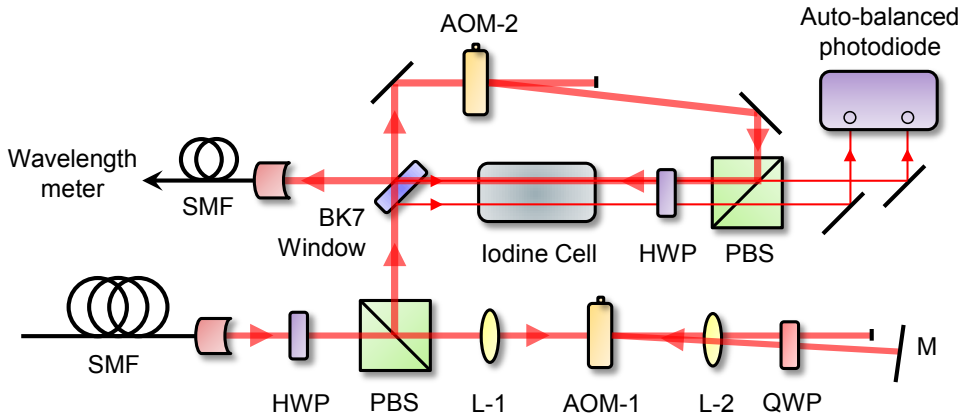

Figure 5.13: The optical setup for the iodine saturated absorption spectroscopy. For details, see text.

polarization with no change in the diffraction efficiency. This double-pass AOM produces a frequency offset of $\Delta f = -2 \times 388.5$ MHz and allows us to change the frequency offset between the laser light and the iodine lock. The beam reflected from the PBS passes through a 5-mm thick glass window (approximately 5 % reflectance per surface). Two weak reflected beams are the probe and reference beams for the saturated absorption spectroscopy. The transmitted beam, which is called pump beam, has more power and passes through another single-pass AOM. The radio frequency applied to this AOM is $f_a = 80$ MHz, which is added to the light and is frequency modulated at 15 kHz with a frequency deviation of 125 kHz[8]. By frequency modulating the pump beam, we are able to detect the resulting variation signal at the modulation frequency using standard phase-sensitive detection techniques, yielding the error signal. We also monitor the frequency of the pump beam transmitted through the glass window in the end, as shown in Fig. 5.13.

The saturated absorption spectroscopy is performed with iodine molecules in a 10 cm-long glass vapor cell. The probe beam is counter-propagated and overlapped with the pump beam inside the iodine cell. The strong pump beam "burns a hole" in the velocity class that it interacts with, saturating iodine populations. When the laser is at a right frequency, both probe and pump beams interact with molecules with the same velocity class along the beam axis. Because of the hole burning, only few molecules can be excited by the probe beam. Therefore when we measure the probe signal, there is less absorption. This effect only happens in a very small frequency range around the transition frequency and allows saturated absorption spectroscopy

[8]This is the maximum deviation given by the Rohde&Schwarz SMC100A RF signal generator depending on the set RF frequency.

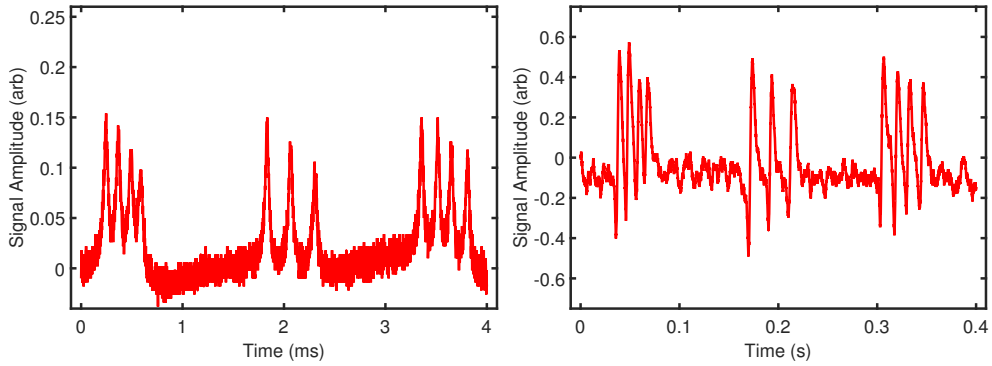

(a) (b)

Figure 5.14: (a) The Doppler-free saturated absorption profile as we scan the laser frequency. (b) The derivative of the absorption resolved from a lock-in amplifier. It has a sharp zero-crossing and can be used as the error signal for frequency locking.

to achieve sharp frequency resolution. If the laser frequency is scanned, a normal Doppler-broadened absorption profile is observed with a sharp peak at a transition frequency. On the other hand, the reference beam is just traveled through the iodine cell so the photodiode only measures a Doppler-broadened absorption profile. Both the probe and reference beams are sent to a New-Focus Nirvana auto-balanced photodiode, which subtracts common-mode changes such as the laser intensity fluctuations. The output is only the narrow and Doppler-free saturated absorption signal and is then sent to a lock-in amplifier for demodulation. In the end we obtain the derivative of the Doppler-free saturated absorption signal, which has a steep zero-crossing at the maximum of the input signal and can be used as the error signal for frequency locking. The 626 nm light can be locked to one of the molecular hyperfine features of the iodine vapor. Feedback control of the laser frequency is performed using the piezoelectric element in one of the fiber lasers.

Figure 5.14(a) shows the Doppler-free saturated absorption signal from the photodiode as we sweep the piezo of the 1550.65 nm fiber laser and Fig. 5.14(b) shows its derivative resolved from the lock-in amplifier. Each peak in Fig. 5.14(a) is a hyperfine feature in one of the iodine lines. For the beryllium detection setup, we lock the 626 nm light to the line #961 of the "Iodine atlas" [Gerstenkorn 78]. Since the piezoelectric element in our fiber laser can only be scanned around ±150 MHz, this is not broad enough to observe all the hyperfine features of this specific line. Therefore I take the measurement results from Brian King's thesis [King 99], where they used the same iodine line as we do. The spectrum of the iodine line #961 is shown in Fig. 5.15, where the laser frequency is locked to hyperfine feature "g", for which the

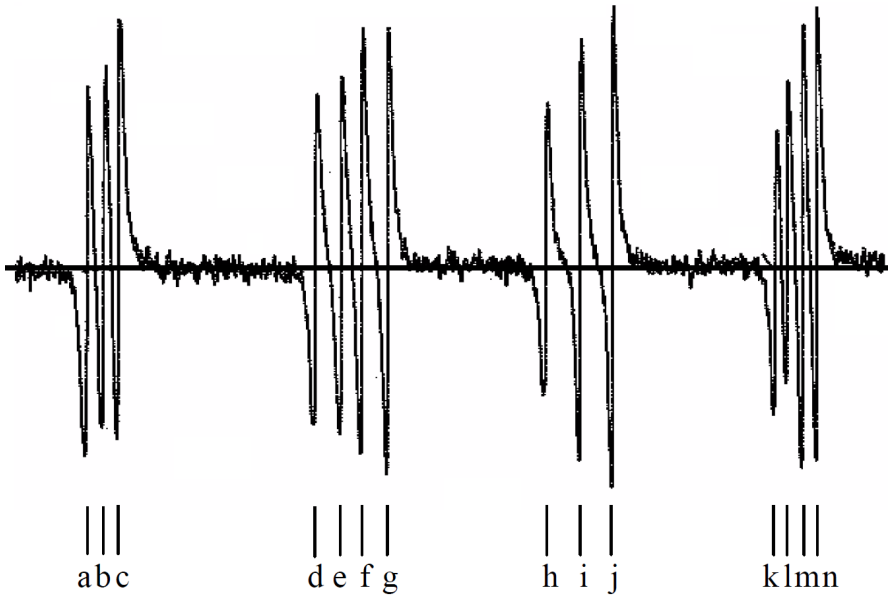

Figure 5.15: Portion of the iodine spectrum of the line #961. Features "o" through "u" are not shown. Due to some technical limitations, we can not measure this broad range of the spectrum. This figure is taken from Brian King's thesis [King 99]. The laser frequency is locked to hyperfine feature "g".

frequency we measured is 478.6976 − 478.6977 THz. Once the laser frequency is locked, we measure that the frequency drift is less than 1 MHz during a day using the ion. For the repumping setup, the design of beam lines is the same as the other, except the AOMs' driving frequencies are different. Here the radio frequencies driving the double-pass AOM-1 and the single-pass AOM-2 are 115 and 100 MHz respectively. We lock the laser frequency to the hyperfine feature "a" of the iodine line #954, as shown in Fig. 5.16 for the full spectrum (taken from [King 99]). The frequency is read to be 478.5991 THz from the wavelength meter.

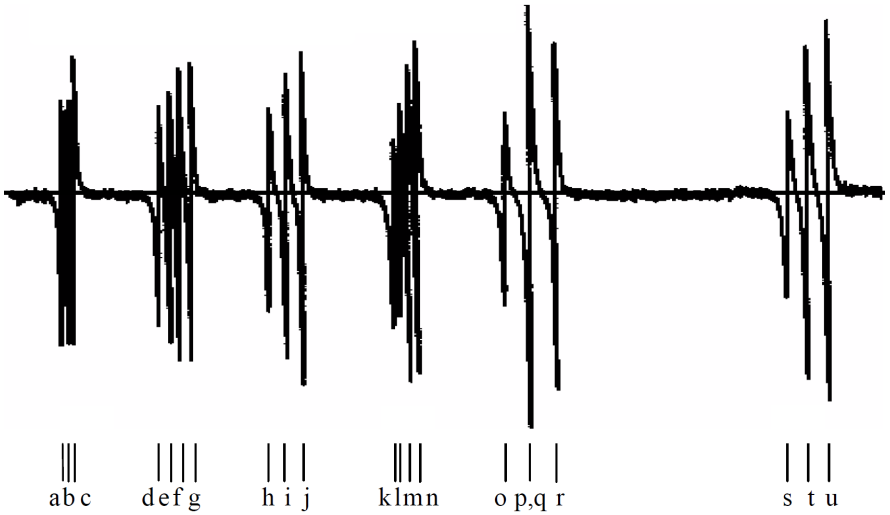

Figure 5.16: Complete iodine spectrum of the line #954. This figure is taken from Brian King's thesis [King 99]. The repumping laser is locked to feature "a".

5.5 Beryllium Doppler Cooling/Detection Beam Lines

In Chapter 2.3 and 2.4, we have described that the pre-cooling and Doppler cooling processes are carried out by the "Blue Doppler Detuned" (BDD) beam tuned 600 MHz to the red of the $|S_{1/2}, F = 2, m_F = 2\rangle \leftrightarrow |P_{3/2}, F' = 3, m'_F = 3\rangle$ cycling transition, and the near-resonant "Blue Doppler" (BD) beam, which is red detuned $\gamma/2$ ($\gamma = 2\pi \times 19.4$ MHz, the natural linewidth of the excited state) from the same transition. Qubit readout performed by state-dependent fluorescence uses the BD beam with the frequency tuned to the resonance of the cycling transition.

The laser beam line is schematically shown in Fig. 5.17. The 313 nm light generated from the frequency doubling cavity is vertically polarized and has frequency f_0. It's first passes through a continuously running double-pass AOM-1. This deflected beam is focused onto a right-angle prism[9] and passed a second time through AOM-1. In total, the laser frequency is shifted by $+80 \times 2$ MHz, resulting in $f_1 = f_0 + 160$ MHz. The retro-reflected beam is displaced vertically from the incident beam so it can be picked off with a mirror after the double-pass setup. Around 10 % of the light is then picked off for the intensity stabilization, for which the error signal produced is used to feed back to the RF power supplied to the AOM-1. Then the main laser beam is sent to a tunable double-pass AOM-2 and a fixed-frequency double-pass AOM-3. The AOM-2 provides the frequency shift from $+160 \times 2$ to $+240 \times 2$ MHz,

[9] Altechna, with fluoride coatings at 313 nm, which has much higher damage threshold

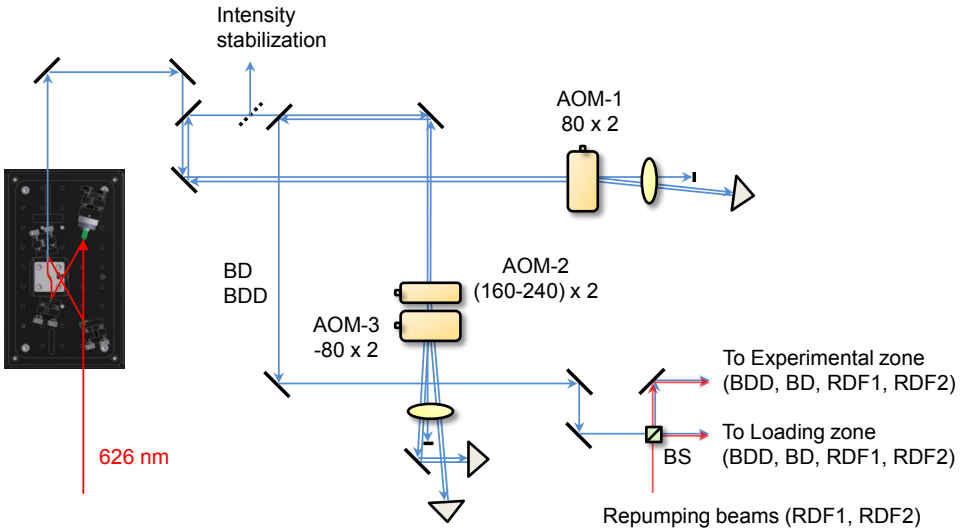

Figure 5.17: Blue Doppler (BD) beam line. The two frequency components in the BD beam line (BD and BDD) are generated with three AOMs. The beam line is combined with the Red Doppler (RD) beam line prior to being sent to the trap. For details, see text.

generating the laser frequency required for BD and detection beams. In our case, the frequency of the BD beam is $f_2 = f_1 + 424$ MHz and the frequency of the detection beam is $f_2 = f_1 + 430$ MHz after passing through the AOM-2 twice. The BDD (pre-cooling) beam is formed in a similar manner using AOM-3, which takes the zeroth-order beam from the AOM-2. We apply the frequency of 80 MHz to the AOM-3 and use its minus first-order diffraction, providing $f_3 = f_1 - 160$ MHz $= f_0$, which is equal to 600 MHz red detuned with respect to the cycling transition frequency. The power of laser pulses is adjusted by controlling the AOM diffraction efficiency which depends on the RF power supplied to it. When the RF power is turned off completely, the AOM does not diffract light, meaning the laser pulse is off. Both AOM-2 and AOM-3 serve as a switch for the cooling and detection beams.

The main advantage of our setup is that the Doppler cooling and detection beams need very low power so in the pre-cooling stage the zeroth-order beam from the AOM-2 still has a lot of power, which can be used for the stronger pre-cooling beam. After the pre-cooling step, AOM-3 is switched off. Therefore no far-detuned frequency component can affect the ion in the subsequent experiment, and the BD beam power remains unchanged. One example is that the Ion Storage Group at NIST observed that in a different setup the leakage light of the BDD and BD beams could cause a systematic Stark shift of the qubit transition [Langer 06]. These two frequency components (f_2 and

f_3) of light are overlapped after the double-pass setup and then combined with the repumping beams on a 50/50 beamsplitter. In the beam path prior to the beamsplitter, we use a 50-μm pinhole to shape the beam profile as well as to make sure BD and BDD beams are well overlapped. Lastly one arm is guided into the loading zone, and the light of the other arm is shone into the experimental zone through Port 2, see Fig. 5.2. To create the $\hat{\sigma}^+$ polarization, a quarter-wave plate is placed immediately after a Glan-Laser α-BBO polarizer[10] and before the final focusing lens, which has a focal length of 200 mm. One technical issue, which should be noticed, is that all the AOMs we use for the 313 nm light[11] only deflect light with a high efficiency when the polarization of the incident beam is perpendicular to the mounting surface of the AOM. This is the reason for the retro-reflective arrangement using a right-angle prism.

The saturation intensity is about 0.76 mW/mm^2 for ^{9}Be$^+$ ion. In the experiment, the intensity of the detection (Doppler cooling) beam is set to roughly half (below half) of the saturation intensity ($\approx$ 3 µW in 60 µm waist in our case). The BDD beam needs higher power than others because its frequency is far detuned from resonance. The laser power used is approximately 200 µW with roughly the same beam waist as the BD beam. The typical experimental parameters are: around 240 mW of 626 nm light is measured directly after the SM fiber output, about 120 mW at 626 nm is delivered to an iodine spectroscopy setup, 100 mW red light is sent to the frequency doubling cavity, and around 9 mW at 313 nm is generated. Each AOM has approximately 75 % − 85 % single-pass diffraction efficiency.

5.6 Beryllium Repumping Beam Lines

As described in Chapter 2.3 and 2.4, the "Red Doppler F1" (RDF1) beam coupled to the $|S_{1/2}, F = 1, m_F = 1\rangle \leftrightarrow |P_{1/2}, F' = 2, m'_F = 2\rangle$ transition and the "Red Doppler F2" (RDF2) beam driving the $|S_{1/2}, F = 2, m_F = 1\rangle \leftrightarrow |P_{1/2}, F' = 2, m'_F = 2\rangle$ transition are responsible for optically pumping to the $|S_{1/2}, F = 2, m_F = 2\rangle$ state.

The beam layout is illustrated in Fig. 5.18. The 313.197 nm light (frequency f_0) generated from the frequency doubling cavity is split using a polarizing beamsplitter (PBS, which is a Glan-Laser polarizer) establishing the RDF1 and RDF2 beam lines. The power ratio between these two branches can be adjusted by the half-wave plate in front of the PBS. The reflected light from the PBS is sent to two double-pass AOMs (AOM-1 and AOM-2) with a frequency shift of $+188 \times 2$ MHz in each, resulting in the frequency of $f_2 = f_0 + 752$ MHz. This is used for the RDF2 beam. For the transmitted light from the PBS, the

[10] Thorlabs, GLB10-UV
[11] IntraAction, www.intraaction.com

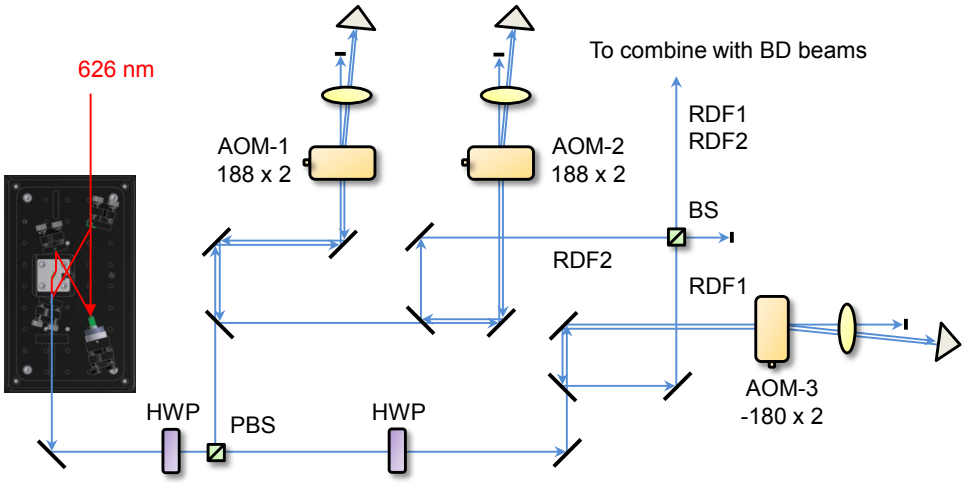

Figure 5.18: Red Doppler (Repumping) beam line. The RD beam line consists of the RDF1 beam and the RDF2 beam separated by 1112 MHz, which is close to the frequency splitting between $|S_{1/2}, F = 1, m_F = 1\rangle$ and $|S_{1/2}, F = 2, m_F = 1\rangle$ states at the magnetic field of 119.45 G. The beam line is combined with the Blue Doppler (BD) beam line prior to being sent to the trap. For details, see text.

polarization is corrected with a half-wave plate before it is sent to the double-pass AOM-3. This AOM-3 subtracts 360 MHz from f_0 providing the frequency component for the RDF1 beam ($f_3 = f_0 - 360$ MHz). The frequency difference between RDF1 and RDF2 beams is $\Delta f = f_2 - f_3 = 1112$ MHz, which is close to the frequency splitting of 1120 MHz between $|S_{1/2}, F = 1, m_F = 1\rangle$ and $|S_{1/2}, F = 2, m_F = 1\rangle$ states at the magnetic field of 119.45 G. Experimentally, we do not set the frequency difference Δf exactly the same as the atomic splitting frequency because if $\Delta f = 1120$ MHz these two beams will form a dark resonance, which creates a coherent population trapping (CPT) or an EIT effect. We have observed this phenomenon in the experiment and the optical pumping efficiency is reduced significantly. The RDF1 and RDF2 beams are switched on and off using the AOM-3 and AOM-2 respectively and are combined on a 50/50 beamsplitter. In the setup shown here, we inevitably lose 50 % of power in each beam (In principle, we can use the beams output from two ports of the beamsplitter in two different trapped zones such that we do not waste 50 % of the power, but then the setup will need to be changed.). Prior to the combined BD/RD beam lines, we also align the overlap of the RDF1 and RDF2 beams and shape the beam profile with help of a 30-μm pinhole. The red light power used in this beam line is very similar to what we have in the BD beam lines. We can obtain more than 400 µW in both RDF1 and RDF2 beams, which is much higher than the saturation intensity.

Finally, the BD/BDD and RDF1/RDF2 beams are carefully aligned to overlap on the 50/50 beamsplitter. Each output from the beamsplitter contains light from any or all of these frequencies. By switching the RF power to the above-mentioned AOMs, we can control which light is shone onto the ion. The light going to both loading and experimental zones will be identical and synchronous. When working with ions in the experimental zone, we block the loading beam to avoid any scattering light.

5.7 Beryllium Raman Beam Lines

The frequencies required to drive the Raman transition for beryllium qubit manipulations span a range of $\approx 1000 - 1400$ MHz. Especially three various frequency differences are concerned: 1) To initialize the field-independent qubit (FIQ), we drive a Raman π-pulse coherently transferring all the population from the $|S_{1/2}, F = 2, m_F = 2\rangle$ state to the $|S_{1/2}, F = 1, m_F = 1\rangle$ state. The frequency difference between two Raman beams is 1018 MHz. 2) The frequency splitting of two Raman beams to drive the FIQ is 1207 MHz. 3) Before the measurement, it is necessary to shelve the dark state ion, the $|\downarrow\rangle \equiv |S_{1/2}, F = 2, m_F = 0\rangle$ state in FIQ, to $|S_{1/2}, F = 1, m_F = -1\rangle$ state, in order to improve the read-out fidelity. The splitting frequency required for the shelving pulse is 1370 MHz. More discussions of each operation are covered in Chapter 2.

There are two sets of Raman beams, the co-carrier (CC) and the Co-90 beams. The CC beams are aligned such that they co-propagate, making transitions driven by this beam pair insensitive to the ion's motion. For the Co-90 beams, two Raman beams are set up perpendicular to each other, and Δk points along the axial mode of motion.

The Raman setup is depicted in Fig. 5.19. The CC and Co-90 beams originate from the same frequency doubling cavity. The 313 nm light is passed through a continuously running AOM, in which the zeroth-order diffracted beam is picked off and sent to a photodiode for intensity stabilization. The zeroth-order beam is focused into a 25-μm pinhole for cleaning the optical spatial mode and is then split into two paths by the PBS. The power in each path can be tuned by rotating the half-wave plate before the PBS. The transmitted beam passes through a tunable double-pass AOM-1. This chosen AOM model, a so-called high-bandwidth deflector AOM, features a similar diffraction efficiency in the radio frequency range from 250 MHz to 350 MHz. After this double-pass setup, the laser frequency becomes $f_1 = f_0 + 2 \times f_a$, where f_0 and f_a are the frequency of the incident beam and the radio frequency that is applied to the AOM respectively. The light reflected from the PBS is sent to a tunable double-pass AOM-2, which has the same specifications as AOM-1. The only dissimilarity is that here the minus first-order diffraction is

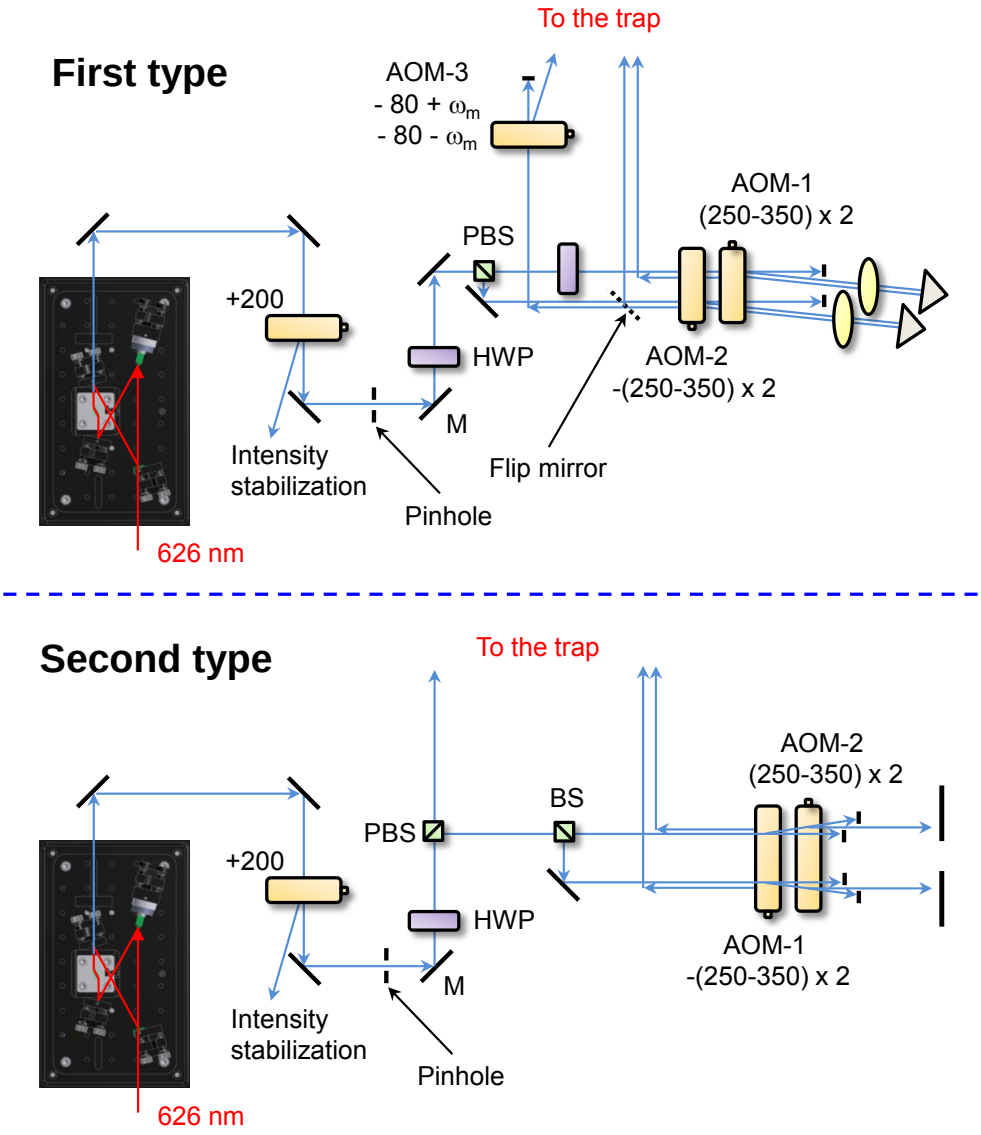

Figure 5.19: Raman beam line. Two types of setups are shown. The first type is the setup we have currently. The second type is still in a testing stage. It is a phase insensitive configuration. For details, see text.

used. The resulting frequency of this beam is $f_2 = f_0 - 2 \times f_a$. As a result, the frequency difference between these two beams can be set to any frequency in the range from 1000 to 1400 MHz. For the CC drive, these two beams are combined on a PBS (not shown in the figure) and delivered to the trap perpendicular to the B-field (Port 4 in Fig. 5.2).

For the Co-90 beam configuration, the laser beam after the double-pass AOM-2 is sent to the single-pass AOM-3, where the flip mirror is removed (see Fig. 5.19). In the setup, we focus the beam into the AOM-3. The aim is that for the MS gate operations we can apply two radio frequency tones to the AOM-3 at the same focusing point on the ion. Basically, a point object, which is focusing point in the AOM, is imaged to the ion. It is also possible to supply only one radio frequency tone to the AOM-3. The frequency shift of the light picked up by the AOM-3 can be compensated by the AOM-2 due to its high bandwidth and a double-pass setup. We should be aware that the first-type setup shown here is sensitive to the optical phase fluctuations arising from the beam path length difference (see Chapter 2.6.2 for theoretical discussions). So we try to shorten the total beam path length and make the path length difference between two Raman beams as small as possible.

In this setup, we typically work with an input power of 350 mW at 626 nm to the doubling cavity, obtaining $\approx$ 90 mW 313 nm light. Due to power losses in the pinhole (nearly 40 %) and other optical elements as well as 80 % AOM diffraction efficiency in single pass, we have around 10 mW for each Raman beam measured before delivering to the trap. If we want to make the optical power balanced in the Co-90 configuration, we have to set the power unequal in each branch by rotating the half-wave plate in order to account for the power loss in the AOM-3.

Another approach would be to use the so-called "phase insensitive" geometry for implementing a two-qubit gate operation. If we recall the theoretical discussions in Chapter 2.6.2, the phase insensitive configuration requires the frequency difference of two Raman beams twice the frequency splitting of the qubit ($\simeq$ 2.4 GHz). Typically to produce this large frequency shift with a single AOM is technically difficult, and it is unattainable at UV wavelengths. Therefore, we think of a possibility to achieve this large frequency splitting using the same AOMs we have. The second type setup shown in Fig. 5.19 should work, though we only tested AOMs' diffraction efficiency. The beam line before the PBS remains unchanged. The reflected beam from the PBS is then split into two paths by a 50/50 beamsplitter. Both AOM-1 and AOM-2 are placed side by side in an opposite orientation. Owing to the advantage of a large active aperture of the AOM, both beams $\sim$ 1.5 cm apart can pass through. We just consider one beam for now. When it passes through AOM-1, the minus first-order deflected beam has $-f_a$ frequency shifts. The frequency of this beam is then shifted $-f_a$ again in the AOM-2, followed by a mirror retro-

reflecting the beam. Meanwhile, the same amount of frequency is added to the other beam. Each beam passes twice through each AOM so this quad-pass AOM setup can produce a frequency difference between two Raman beams in the range from 2000 to 2800 MHz, which satisfies our requirement. From the test performed using 200 MHz AOMs, the overall diffraction efficiency for each beam is ≈ 40 %. After the quad-pass setup, two beams could be sent to the trap from the Port 4. For a two-qubit operation, one needs the transmitted beam from the PBS, but in this path additional AOMs are required for switching on and off this beam and tuning the frequency. It is then sent to the ion through the other port. This type of setup has more limitations, one example is the construction of CC beams, and we would need to further think about the experimental setups to make them useable.

Chapter 6

$^9Be^+$ Qubit Control and Measurement

In order to understand the performance of the new experimental system that we have built, we rely on some basic techniques to characterize it. This chapter provides characterization measurements mainly for a single beryllium ion. The measurements for a single $^{40}Ca^+$ ion are given in Daniel Kienzler's thesis [Kienzler 15b]. Several methods are used for the micromotion compensation and applied to both ion species. These experimental techniques and calibrations are useful tools and the first steps towards high-fidelity qubit manipulations.

6.1 Ion Loading

To demonstrate the combined use of our photoionization and cooling laser systems, we load beryllium ions into a micro-fabricated segmented trap. As a source for $^9Be^+$ production we make use of a beryllium wire tightly coiled around a tungsten wire. The tungsten is heated by running an electrical current through it, which in turn heats the beryllium up [Blakestad 10]. Neutral atoms are desorbed in this way, and then collimated to travel through the trapping area envisioned for loading. The neutral atom beam is illuminated simultaneously with 235 nm light (for two-photon photoionization process) and two $\hat{\sigma}^+$-polarized 313 nm beams. The first one is red detuned by ≈ 10 MHz from the $\left|S_{1/2}, F = 2, m_F = 2\right\rangle \leftrightarrow \left|P_{3/2}, F' = 3, m'_F = 3\right\rangle$ ion transition for Doppler cooling. The second is driven at higher power and is red-detuned by ≈ 600 MHz for efficient cooling during the loading process (when ions are most energetic) as well as repumping. The trapped ions are monitored throughout the process by means of a CCD-camera with which we image $^9Be^+$ ions fluorescence at 313 nm (See Fig. 4.9). For loading, the electric current applied to the beryllium oven is 0.63 A (2 V), with which we can load a single ion in less than 2 minutes. We use powers of 235 nm light in the range of 70–80 μW with an estimated beam waist of 50 μm. Photoionization of $^9Be^+$ atoms with

the 235 nm light should be more efficient than ionization with an electron gun. This continuous-wave laser with such a short wavelength could lead to electrically charging the trap electrodes so careful shaping and positioning of the beam are necessary in order to load ions reliably in the trap.

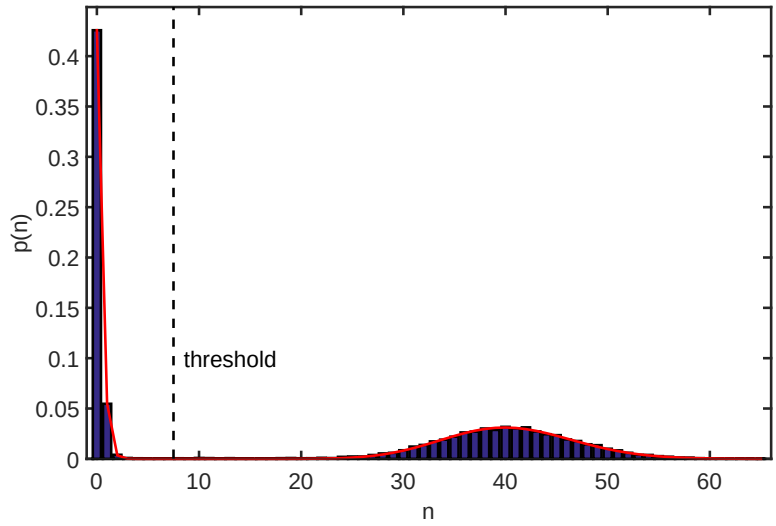

Figure 6.1: Typical photon number histogram for a single trapped ion with 200 µs detection time. This plot contains 20000 single-shot measurements in total. We use a threshold to determine whether the ion is in a bright state or dark state. When the ion is dark, no photon can be detected so ideally it behaves like a Poisson distribution with a mean close to zero (the region below the threshold). If the ion is bright, we are able to collect a lot of fluorescence following the Poisson distribution as well (the region above the threshold).

6.2 Qubit Readout/Fluorescence Detection

For the ^{9}Be$^+$ ion, a projective measurement for the qubit readout is performed using the $\left|S_{1/2}, F=2, m_F=2\right\rangle \leftrightarrow \left|P_{3/2}, F'=3, m'_F=3\right\rangle$ cycling transition to detect the probability of the ion being in the bright state $|b\rangle = \left|S_{1/2}, F=2, m_F=2\right\rangle$. In our experiments, as discussed in Chapter 4.2 if the ion is in the bright state $|b\rangle$, we are able to collect on average 40 photons within a 200 µs detection time on a photo-multiplier tube (PMT), as shown in Fig. 6.1. With the same detection interval the background photon count for the ion being in the dark state is around 0.13, which comes from the scattering light of the detection beam.

For each data point in the projective measurement, we repeat the experiment several hundred times to get the statistics and then use this to estimate the

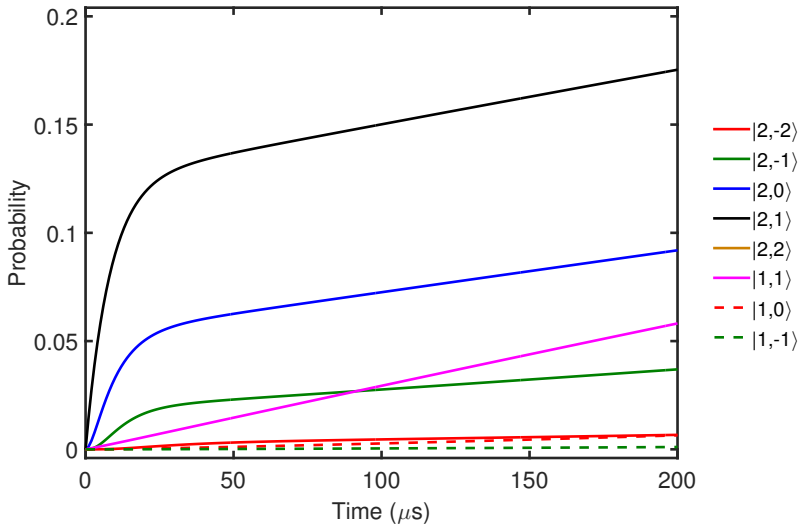

(a)

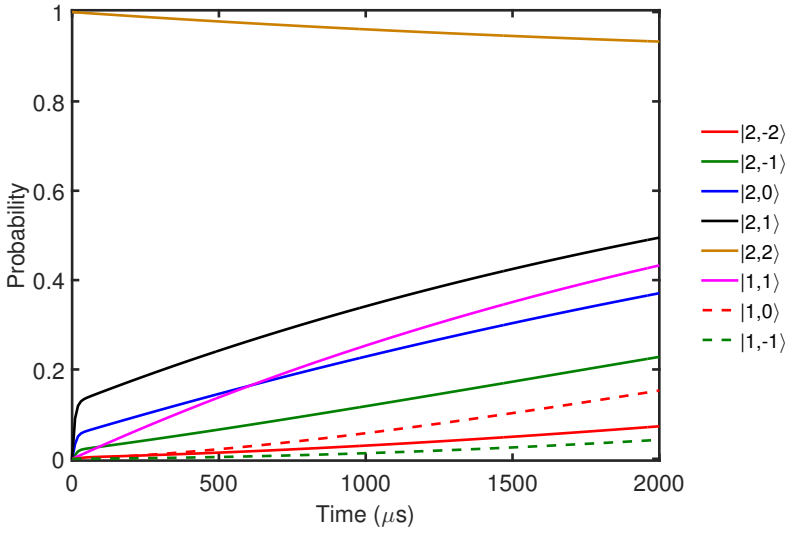

(b)

Figure 6.2: Simulation of the probability of a $^9Be^+$ ion being in $\left|S_{1/2}, F = 2, m_F = 2\right\rangle$ state at time t given different initial starting states when the detection beam intensity is set to 0.5 saturation. The calculated based on Eq. (2.15). (a) Ideal case, where the detection beam is purely $\hat{\sigma}^+$ polarized. (b) 5 % admixture of both $\hat{\sigma}^-$ and $\hat{\pi}$ polarization components in the detection beam. The use of 5 % admixture, which is much higher than the realistic value, and a longer time scale is to show the population leakage from the bright to dark state.

probability of the qubit of being $|\downarrow\rangle$ or $|\uparrow\rangle$. The statistics of the collected photons for both bright and dark states of the ion obeys a Poisson distribution. Figure 6.1 shows the typical histogram obtained for a single trapped ^{9}Be$^+$ ion. If the qubit is measured in a superposition of bright and dark, the histogram will look like Fig. 6.1. We then use a sum of two Poisson distributions to fit the histogram which contains all the data in order to get two mean photon numbers (bright and dark means). There are two ways to determine the probability $P(\downarrow)$ for each data point: 1) For given means, we can fit the histogram with a weighted sum of two Poisson distributions and use the weights. 2) From the means, the threshold that is used to distinguish the qubit being bright or dark can be determined. For each data point, if the photon count in the single-shot measurement is above the threshold, set this measurement to 1; otherwise it's 0. In both cases, the results of N experiments is then binomially distributed. We can then calculate the probability. Given a probability P, the error bar is the statistical uncertainty of a binomial distribution and is defined as a standard error of the mean (S.E.M.), which is

$$\text{S.E.M.} = \sqrt{\frac{P(1-P)}{N}} \tag{6.1}$$

6.2.1 Readout Error Analysis

In Chapter 2.4, we have described that the main source of the read-out error is the leakage of the qubits initially in the dark state into the cycling transition by off-resonant coupling to other excited states (other than the one in the closed transition) during measurement. The second source is that an ion in the bright state can be optically pumped into a dark state due to imperfect detection beam polarization. Figure 6.2 shows the probability of a ^{9}Be$^+$ ion to be in $\left|S_{1/2}, F=2, m_F=2\right\rangle$ state at time t given different initial conditions, plotted using Eq. (2.15). In Fig. 6.2(a), we consider an ideal case where the detection beam is a purely $\hat{\sigma}^+$ light ($\epsilon_{\sigma^-} = \epsilon_\pi = 0$) and the saturation parameter is set to $s_0 = 0.5$. The simulated results with imperfect detection polarizations are plotted in Fig. 6.2(b) for which we use 5 % admixture of both $\hat{\sigma}^-$ and $\hat{\pi}$ polarizations ($\epsilon_{\sigma^-} = \epsilon_\pi = 5\ \%$) and the same saturation parameter as in (a). We can see that after some time the population in state $\left|S_{1/2}, F=2, m_F=2\right\rangle$ is transferred to other hyperfine states due to the depumping by the $\hat{\sigma}^-$ and $\hat{\pi}$ polarized light. For the ion initially in the $\left|S_{1/2}, F=2, m_F=2\right\rangle$ state, the population is transferred to the $\left|S_{1/2}, F=1, m_F=1\right\rangle$ state with a highest probability. In a good polarizer, the polarization impurity can be suppressed to below 10^{-4} but this is not easily achievable for light passing through vacuum windows. For a cautious estimate, with 1 % admixture of both $\hat{\sigma}^-$ and $\hat{\pi}$ polarizations, 2×10^{-4} of the population is lost in a 200 μs detection time.

We experimentally examine the readout error by driving single qubit rotation on the carrier transition using co-propagating Raman beams. Two dif-

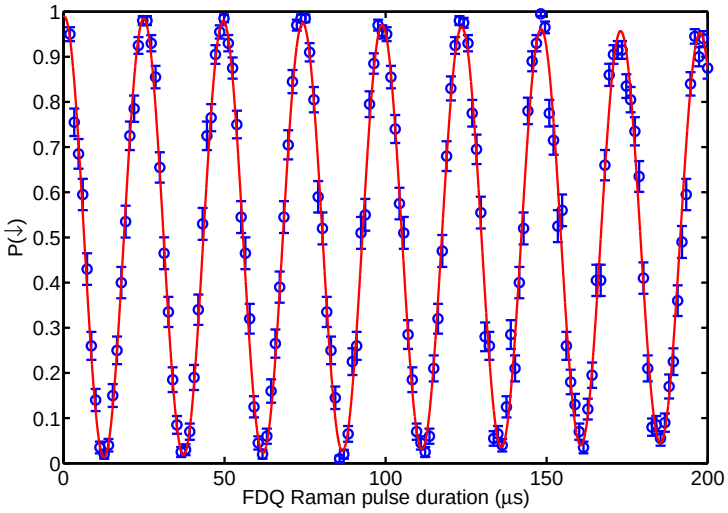

Figure 6.3: The Rabi flopping curve performed on the FDQ.

ferent qubit candidates are employed. 1) The field-dependent qubit (FDQ): $|\uparrow\rangle \equiv \left|S_{1/2}, F=1, m_F=1\right\rangle$ and $|b\rangle \equiv \left|S_{1/2}, F=2, m_F=2\right\rangle$. 2) The field-independent qubit (FIQ): $|\uparrow\rangle \equiv |S_{1/2}, F=1, m_F=1\rangle$ and $|\downarrow\rangle \equiv |S_{1/2}, F=2, m_F=0\rangle$.

The sequence of the experiment is that the ion is initially prepared in the $|b\rangle$ state by optical pumping (see Chapter 6.3) and then a Raman pulse is applied for different pulse durations, followed by the projective measurement. Figure 6.3 shows the data performed on the FDQ with a detection time of 120 μs. The dark state of the FDQ is $|\uparrow\rangle$. After a π-pulse transferring all the population to the dark state, we see that the first minimum of the Rabi flopping curve (π-pulse time) still has a probability $P(\downarrow)$ of around 2 %. This might be an indication of population leakage from the dark to the bright state due to the off-resonant excitation or infidelity in the π-pulse. If we compare with the simulation results in Fig. 6.2(a), at 120 μs the state $\left|S_{1/2}, F=1, m_F=1\right\rangle$ has some probabilities (≈ 2.5 %) entering the cycling transition and contributing to the photon counts.

To work with the FIQ, we need to apply a Raman π-pulse after the optical pumping to $|b\rangle$ in order to initialize the qubit in the $|\uparrow\rangle$ state. Before the qubit readout, we apply another Raman π-pulse bringing the population in $|\uparrow\rangle$ back to the bright state $|b\rangle$ for detection. Figure 6.4 shows the results of an intermediate probe pulse, which drives Rabi oscillations on the FIQ. The dark state in FIQ is $\left|S_{1/2}, F=2, m_F=0\right\rangle$. We can see that after a π-pulse there is a probability of around 8 % detecting photons, which is also close to the theoretical prediction as shown in Fig. 6.2(a) at 120 μs.

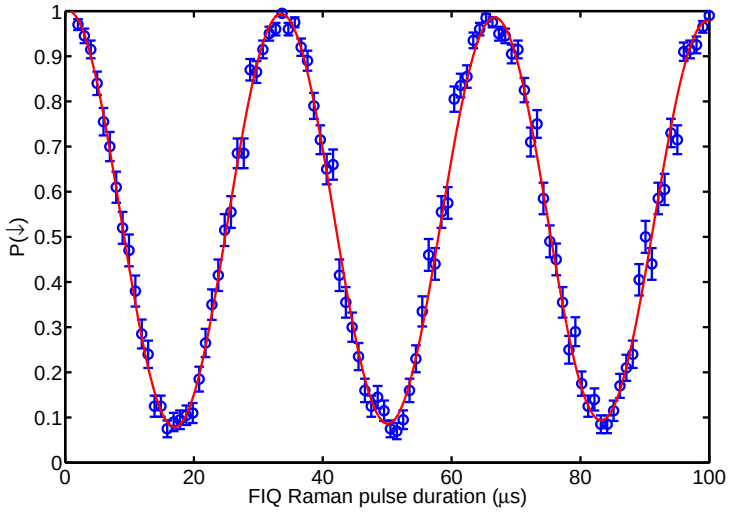

Figure 6.4: The Rabi flopping curve performed on the FIQ without shelving the dark state ion. For details, see text.

6.2.2 Improving Readout Fidelity Through Shelving

From the simulation and experimental results shown above, we can see after some time the ion initially in other hyperfine states can enter the cycling transition with a certain probability due to off-resonant pumping. However this repumping of the dark state ion can be suppressed by transferring the population to another state which is even darker. The darker state would require more scattering events than that the original dark state needs to get into the cycling transition. The basic idea is illustrated in Fig. 6.5. If the dark state is in $\left|S_{1/2}, F=1, m_F=1\right\rangle$, although the detection beam is off-resonantly driving this state to $P_{3/2}$ transition, only one scattering event can lead to pump the population into the bright $\left|S_{1/2}, F=2, m_F=2\right\rangle$ state. In contrast, if the dark state is in $\left|S_{1/2}, F=1, m_F=-1\right\rangle$, the detection beam is further off resonant and also it takes a minimum of three scattering events to pump this state into the bright state. From Fig. 6.2 we see that with a fixed detection time the ion in the $\left|S_{1/2}, F=1, m_F=-1\right\rangle$ state has a lowest probability to be pumped to the bright state. Therefore prior to detection we can shelve the state $|\downarrow\rangle \equiv \left|S_{1/2}, F=2, m_F=0\right\rangle$ for FIQ to state $\left|S_{1/2}, F=1, m_F=-1\right\rangle$ to improve the readout fidelity. Results from Rabi oscillations on the FIQ using shelving are shown in Fig. 6.6. We perform the single qubit rotation on the FIQ, but a shelving Raman π-pulse is applied before the qubit readout. Thus the population in $|\downarrow\rangle$ is transferred to the state $\left|S_{1/2}, F=1, m_F=-1\right\rangle$ for shelving. The contrast compared to Fig. 6.4 is significantly improved. We also notice that the bright state is still not perfectly bright. This might be due to imperfect polarizations in the detection beam as well as imperfect

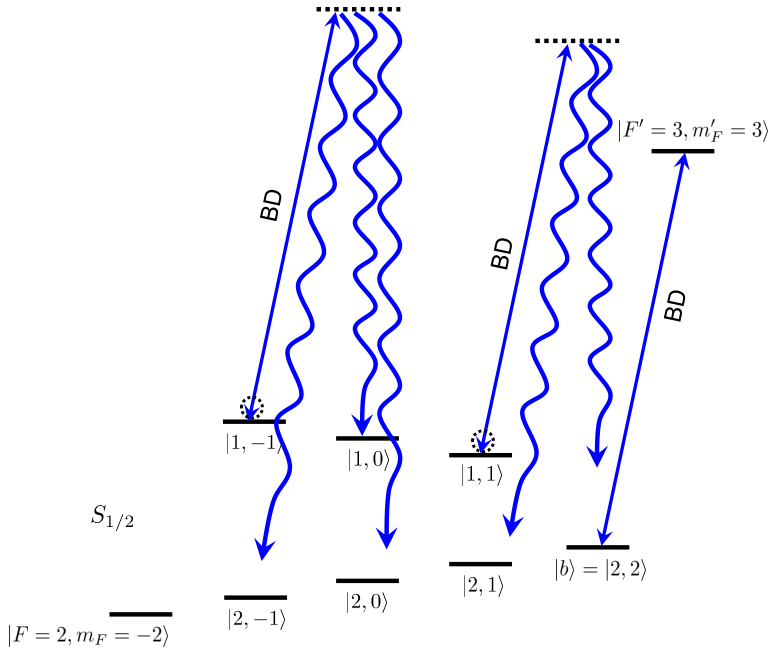

Figure 6.5: Shelving the dark state of the ion for enhancing the readout fidelity. If the dark ion is in state $\left|S_{1/2}, F=1, m_F=1\right\rangle$, it only needs one scattering event to enter the cycling transition by the off-resonantly driving within the detection time. By comparison the state $\left|S_{1/2}, F=1, m_F=-1\right\rangle$ has a less probability to be pumped into the bright state because it requires more than three scattering events during the detection interval.

population transfer from $\left|S_{1/2}, F=1, m_F=1\right\rangle$ to $\left|S_{1/2}, F=2, m_F=2\right\rangle$.

6.2.3 Optimal Detection Time for Readout Fidelity

One can optimize the readout fidelity by choosing an appropriate experimental parameters. Before we go into the details, we look at the simulation results for the distribution of photon counts. Figure 6.7(a) plots the probability distribution for an ion initially in different dark states $|j\rangle$ using Eq. (2.20). The parameters used for this plot are listed in the figure caption. Because the ion should ideally be dark, the probability at $n=0$ is near 1, which is not displayed in the figure. However, it shows that there are some probabilities of detecting many photons due to the dark to bright state leakage.

The probability distribution for the bright state ion (Eq. (2.24)) is shown in Fig. 6.7(b). We can see without the imperfect polarizations the photon counts exhibit a Poisson distribution with a given mean. If we take some polarization impurities into account, the bright state will start being opti-

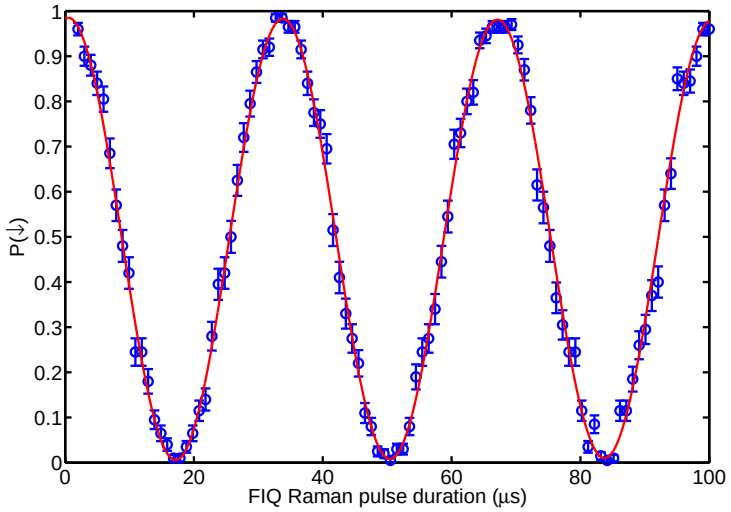

Figure 6.6: The Rabi flopping curve performed on the FIQ by the use of the shelving scheme for the dark state ion. The shelving Raman pulse transfers the dark state ion from $\left|S_{1/2}, F=2, m_F=0\right\rangle$ to $\left|S_{1/2}, F=1, m_F=-1\right\rangle$ state in order to improve the readout error. We can compare to Fig. 6.4 to see the improvement.

cally pumped to a dark state and the probability of getting lower counts increases. According to the selection rules, the bright state ion can be only pumped into $\left|S_{1/2}, F=1, m_F=1\right\rangle$ and $\left|S_{1/2}, F=2, m_F=1\right\rangle$ through the $\left|P_{3/2}, m_J=1/2\right\rangle$ and $\left|P_{3/2}, m_J=-1/2\right\rangle$ states by $\hat{\pi}$ and $\hat{\sigma}^-$ polarized light. Because the transition driven by the $\hat{\pi}$ polarization components is closer to resonance than the $\hat{\sigma}-$ polarized transition, we calculate the worst case assuming all of the impure polarization is $\hat{\pi}$.

The expected total histogram for a single ion is the sum of $p_{\text{bright}}(n)$ and $p_{\text{dark}}(n|j)$ with a given probability of the ion being bright $P(|b\rangle)$. It is written as

$$p_{\text{total}} = P(|b\rangle)p_{\text{bright}}(n) + (1 - P(|b\rangle))p_{\text{dark}}(n|j) \tag{6.2}$$

where $p_{\text{dark}}(n|j)$ is from Eq. (2.20) and $p_{\text{bright}}(n)$ is from Eq. (2.24). Previously we have mentioned how the typical histogram looks like. The bright state scatters many photons, whereas the dark state scatters a much smaller number of photons. Experimentally, we collect fluorescence for a fixed detection time τ_D. Afterwards we set a threshold for the number of collected photons n_c such that if more than n_c photons have been collected, we determine that the ion is projected into the bright state. Likewise, if we collect less than n_c photons, we claim that the ion was projected into a dark state.

The probability of falsely determining a bright ion being dark is given by

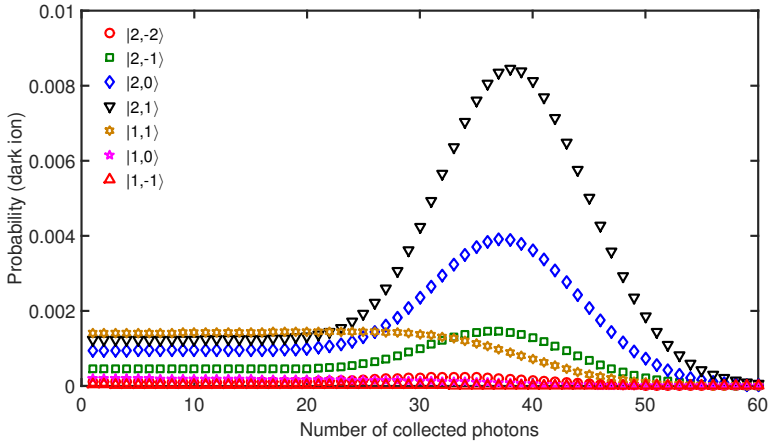

(a)

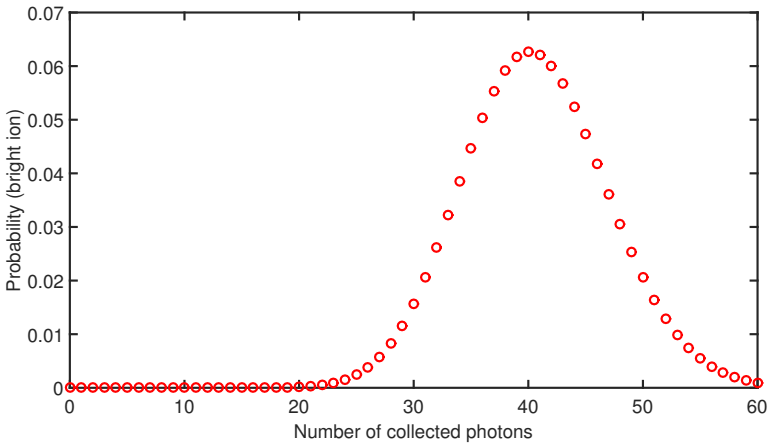

(b)

Figure 6.7: Theoretical photon count histogram for an ion that starts in: (a) different dark states; and (b) the bright state. Parameters used for both plots are $s_0 = 0.5$, $r_{bg} = 0$, $\zeta = 0.01$, and $\tau_D = 200$ µs. In (a), it shows that no matter where the initial dark state is, after some time the ion always has a probability to enter the cycling transition and then contributes photon counts. This will induce readout error.

$\sum_{n=0}^{n_c} p_{\text{bright}}(n)$. Likewise, the probability of falsely determining that an ion in the dark state $|j\rangle$ is bright is given by $\sum_{n=n_c+1}^{\infty} p_{\text{dark}}(n|j) = 1 - \sum_{n=0}^{n_c} p_{\text{dark}}(n|j)$. The measurement error is defined as the average of these two. It is obvious that the error is a function of τ_D and n_c, depending on state $|j\rangle$ as well. From the discussions before, we know that $\left|S_{1/2}, F = 1, m_F = -1\right\rangle$ is the optimum dark state, and then we are concerned with how to minimize the measurement errors by searching for optimum τ_D and n_c. Several numerical

methods can be applied to calculate the minimum error. If we restrict $n_c \geq 5$, with the detection efficiency $\zeta = 0.01$ and the saturation parameter $s_0 = 0.5$ the minimum error of 1.5×10^{-4} can be achieved at the detection time of 104 μs, which should be combined with the use of shelving technique.

Using standard optical setup for measurements and shelving the dark state ion to a "darker" hyperfine state, we can in principle obtain measurement errors below the fault-tolerance threshold [Steane 03, Knill 05]. If one would like to improve the readout fidelity, the alternative technique is the measurement via photon arrival times. Instead of collecting the photon numbers using a fixed detection time, here the arrival times of the photons $\{t_k\}$ are recorded into the measurement system. The advantage is that there is more information in the set $\{t_k\}$ than in the number of photons detected. The theoretical background of this technique and how to implement it were well explained in [Langer 06, Myerson 08]. The author shows that in the presence of background photons they can achieve approximately a factor of 3 improvement in the average error using the photon arrival times versus counting the number of collected photons with a fixed detection time.

6.3 Optical Pumping

Optical pumping is usually used to reset/initialize the qubit in the $|S_{1/2}, F = 2, m_F = 2\rangle$ state and is achieved by applying the RDF1 and RDF2 beams, coupled to the $|S_{1/2}, F = 1, m_F = 1\rangle \leftrightarrow |P_{1/2}, F' = 2, m'_F = 2\rangle$ and the $|S_{1/2}, F = 2, m_F = 1\rangle \leftrightarrow |P_{1/2}, F' = 2, m'_F = 2\rangle$ transitions respectively[1]. To investigate the dynamics of the optical pumping process, one can solve rate equations for all allowed transitions. In the simulation we set the frequency difference between RDF1 and RDF2 beams to 1112 MHz and the intensity of each beam to 5 saturation intensities. Figure 6.8 shows the time evolution of the probability for an ion initially in different states being pumped to the $|S_{1/2}, F = 2, m_F = 2\rangle$ state. We can see that around 3 μs is sufficient for the optical pumping from either the $|S_{1/2}, F = 2, m_F = 1\rangle$ or the $|S_{1/2}, F = 1, m_F = 1\rangle$ state since only one photon scattering event is required.

Experimentally the way we optimize the optical pumping efficiency is that we apply a Raman π-pulse transferring all the populations from the $|S_{1/2}, F = 2, m_F = 2\rangle$ state to $|S_{1/2}, F = 1, m_F = 1\rangle$ state, followed by an optical pumping pulse, where both RDF1 and RDF2 beams are switched on simultaneously. We scanned the frequency of the RDF1 or RDF2 beam such that we can choose an appropriate frequency to avoid a dark resonance formed by two beams. Once the dark resonance is created, the population is trapped in the $|S_{1/2}, F = 2, m_F = 1\rangle$ and $|S_{1/2}, F = 1, m_F = 1\rangle$ states, and is not

[1] Without using these two beams, the high-power far-detuned BDD beams, coupled the $S_{1/2}$ and $P_{3/2}$ states, can also serve as a repumping beam, see Chapter 2.3.

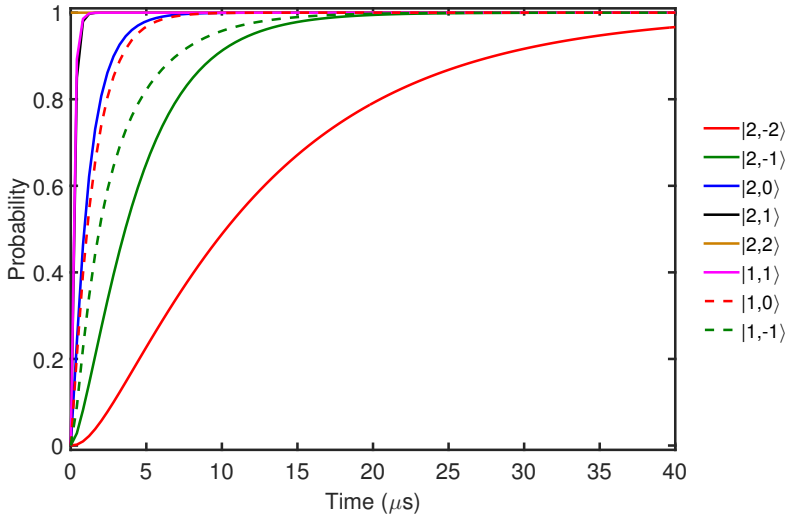

Figure 6.8: Rate equation simulation of the optical pumping for an ion initially in different states being pumped to the $\left|S_{1/2}, F = 2, m_F = 2\right\rangle$ state.

pumped back to the $|S_{1/2}, F = 2, m_F = 2\rangle$ state. Figure 6.9 shows the AOM frequency scan of the RDF2 beam when the AOM frequency of the RDF1 beam is set to 180 MHz (the experimental setup is shown in Chapter 5.6) and the pulse duration of the RDF1 and RDF2 beams is set to 3 μs. The dip at 190.2 MHz indicates the dark resonance. Therefore, we use 188 MHz for the AOM frequency for the RDF2 beam, resulting in 1112 MHz frequency difference between RDF1 and RDF2.

Figure 6.10 shows the population in the $|\downarrow\rangle \equiv \left|S_{1/2}, F = 2, m_F = 2\right\rangle$ state as a function of the optical pumping duration before and after the optimization of laser frequency using the same optical power. To get a characteristic time scale for the optical pumping process, we fit the data in Fig. 6.10(a) with the form $A(2-e^{-t/\tau_1}-e^{-t/\tau_2})$, where A, τ_1 and τ_2 are fit variables. Because a dark resonance is created in this case, we find that we should use two exponential terms to obtain a better fit, giving two time scales $\tau_1 = 0.6$ μs and $\tau_2 = 23$ μs. In Fig. 6.10(b), the data are fitted with this form $A(1 - e^{-t/\tau_1})$, yielding $\tau_1 = 0.54$ μs. After the optimization, the optical pumping is more efficient. We choose 5 μs as the optical pumping duration in the experiments such that ≈ 99.99 % of the population are pumped to the $\left|S_{1/2}, F = 2, m_F = 2\right\rangle$ state. Compared to the simulation, this is still a bit longer than the theoretical prediction. It is possible that there is a common frequency offset for both RDF1 and RDF2 beams, for example if we lock the 626 nm laser frequency to the wrong iodine hyperfine feature, so both beams have some detunings to the transition frequencies. Or we over estimated the laser intensity of the pumping beams in the simulation. The switching time of the AOMs might

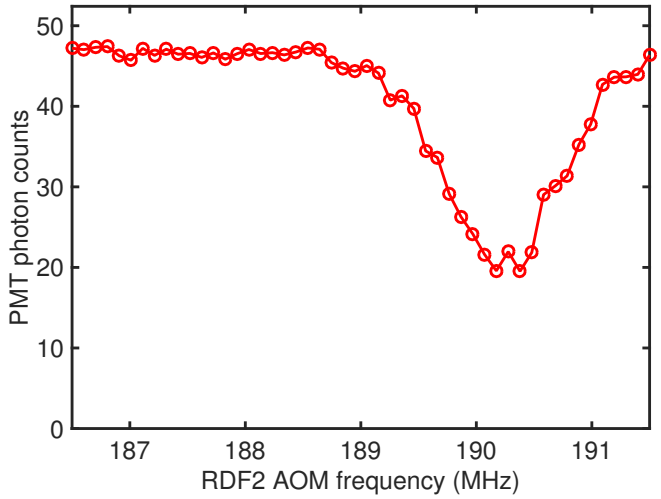

Figure 6.9: RDF2 AOM frequency scan. There is a dark resonance created with the RDF1 beam, where the frequency difference between two beams is similar and equal to the energy level splitting of $\left|S_{1/2}, F = 2, m_F = 1\right\rangle$ and $\left|S_{1/2}, F = 1, m_F = 1\right\rangle$ states.

also limit the optical pumping time (but not at the several μs level).

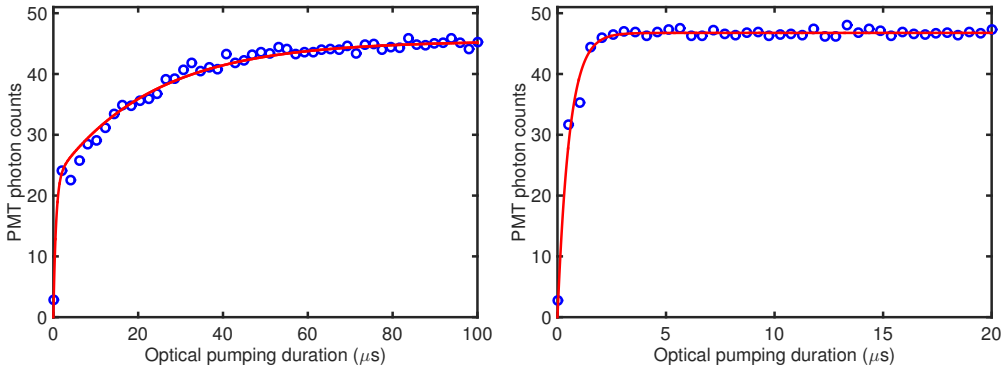

(a) (b)

Figure 6.10: The optical pumping process (a) before and (b) after optimization. For details, see text.

6.4 Resolved Sideband Cooling

After pre- and Doppler cooling, the ion is cooled to a temperature of $T_D \simeq \hbar\gamma/(2k_B)$ when the laser detuning is set to $-\gamma/2$. Here $\gamma = 2\pi \times 19.4$ MHz is the natural linewidth of the transition and k_B is the Boltzmann constant. For $^9Be^+$ ions, $T_{\min} \simeq 0.47$ mK. The mean energy of the ion is given by $\langle E\rangle \simeq k_B T = \hbar\omega_m(\langle n\rangle + 1/2)$, where ω_m is the ion's vibrational frequency. Therefore, the minimal phonon number is equal to

$$\langle n\rangle = \frac{1}{2}\left(\frac{\gamma}{\omega_m} - 1\right) \tag{6.3}$$

For a single $^9Be^+$ ion, the typical axial frequency we use in our experiment is $\omega_z \approx 2\pi \times 3 - 4$ MHz, so $\langle n\rangle \simeq 2 - 3$.

One can use the resolved sideband Raman cooling method to further cool the motion of the ion to the ground state. Cooling to the motional ground state is not only a requirement for some experiments [Cirac 95, Monroe 95b, Meekhof 96]. Once the frequency splittings between the vibrational levels of the oscillator is larger than the linewidth of the relevant atomic transition, the spectral sidebands are well-resolved. As a result, when absorbing on the first sideband, energy conservation requires that the motional state change by the one quanta along with the electronic state transition.

The procedure is listed below:

1. Begin with the ion in the state $|\downarrow\rangle|n\rangle$, which ion's motion has a thermal distribution.
2. Apply a π-pulse on the red sideband via stimulated Raman transitions, which drives $|\downarrow\rangle|n\rangle \rightarrow |\uparrow\rangle|n-1\rangle$ transition.
3. Reset the ion to $|\downarrow\rangle|n-1\rangle$ by using the optical pumping which couples state $|\uparrow\rangle|n-1\rangle$ to the excited state. In the Lamb-Dicke regime, the motional state does not change during the repumping process. Thus, the ion has reduced its vibrational energies by about one quanta.
4. Repeat Step 2 and 3.

After many cycles, it is possible to find the ion in the motional ground state with a high probability.

In our experiments, the resolved sideband cooling is performed with the field-dependent qubit, where $|\uparrow\rangle \equiv |S_{1/2}, F = 1, m_F = 1\rangle$ and $|\downarrow\rangle \equiv |S_{1/2}, F = 2, m_F = 2\rangle$ states are used (see Chapter 2.2). Because the ion's motion is in a thermal distribution after Doppler cooling, around 50 % of motional states that the ion is occupied are greater than the mean phonon number $\langle n\rangle$ calculated above. The Rabi frequency driving the $|\downarrow\rangle|n\rangle \rightarrow |\uparrow\rangle|n-1\rangle$ transition is different based on the starting motional state (see Eq. (2.49)). In order

to perform the sideband cooling more efficiently, we vary the duration of the red-sideband pulse during the cooling process. First we check the π-time ($\tau_\pi = \pi/|\Omega_{\mathrm{rsb}}|$) of the Rabi flop trace on the red sideband measured directly after Doppler cooling. This gives us roughly the duration of the initial red-sideband pulse (τ_i). The duration of the final pulse (τ_f) can be estimated from the π-time of the carrier Rabi flops divided by the Lamb-Dicke parameter. The duration of the red-sideband pulse in the n_{th} cooling cycle is given by $\tau_n = \left(\frac{\tau_f - \tau_i}{N} n + \tau_i\right)$, where N is the number of the cooling cycle. In our case, $N = 30$ is sufficient to cool the ion close to the ground state.

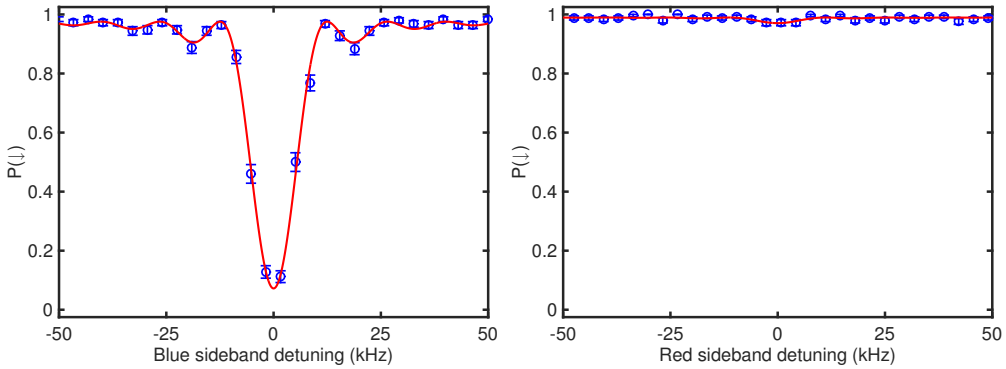

(a) (b)

Figure 6.11: Motional sideband absorption spectrum of a single ^{9}Be$^+$ ion after resolved sideband cooling. Here only the axial mode is cooled. The vibrational frequency of this mode is 2.7 MHz. The inferred mean phonon number $\langle n \rangle$ after the sideband cooling is approximately 0.03 ± 0.01 using Eq. (6.4).

When an ion is in electronic state $|\downarrow\rangle$ and has a thermal state distribution, the mean phonon number $\langle n \rangle$ can be determined by the ratio of the transition probabilities to $P(\uparrow)$ for the red and blue sidebands, given by

$$\langle n \rangle = \frac{P_{\uparrow,\mathrm{rsb}}/P_{\uparrow,\mathrm{bsb}}}{1 - P_{\uparrow,\mathrm{rsb}}/P_{\uparrow,\mathrm{bsb}}} \tag{6.4}$$

where $P_{\uparrow,\mathrm{rsb}}$ ($P_{\uparrow,\mathrm{bsb}}$) is the probability that the ion in the $|\uparrow\rangle$ state after excitation on the red (blue) sideband [Leibfried 03a]. This is independent of pulse duration, Rabi frequency, and Lamb-Dicke parameter [Turchette 00a]. The ratio $P_{\uparrow,\mathrm{rsb}}/P_{\uparrow,\mathrm{bsb}}$ can be inferred from a frequency scan over both sidebands while keeping the Rabi frequency and pulse duration constant. Figure 6.11 shows the blue and red sideband spectrum immediately after the ground state cooling. We measured the probability of the ion being in $|\downarrow\rangle$ state. Assuming

the laser pulse is a square profile, the data are fitted with the following form

$$P(\downarrow) = a + b\frac{\Omega_{\rm sb}^2}{\Omega_{\rm sb}^2 + \Delta^2}\sin^2\left(\frac{1}{2}\sqrt{\Omega_{\rm sb}^2 + \Delta^2}\,t\right) \tag{6.5}$$

where Δ is the laser detuning with respect to the sideband transition. The Rabi frequency for the sideband transition $\Omega_{\rm sb}$, and the parameters a and b are fit variables. For the red sideband drive, there is no excitation if the ion is in the electronic state $|\downarrow\rangle$ and motional ground state $|n = 0\rangle$. The mean phonon number $\langle n\rangle \simeq 0.03 \pm 0.01$ after the sideband cooling.

6.5 Spin Coherence - Robust Quantum Memory

A qubit with long coherence time is an excellent standing point for quantum information processing. In ion trap experiments, one of the principal problems in the laboratory is that the magnetic field fluctuates [Barrett 04]. As discussed in Chapter 2.2, we can use a first-order magnetic-field-independent transition in order to obtain a long-lived qubit.

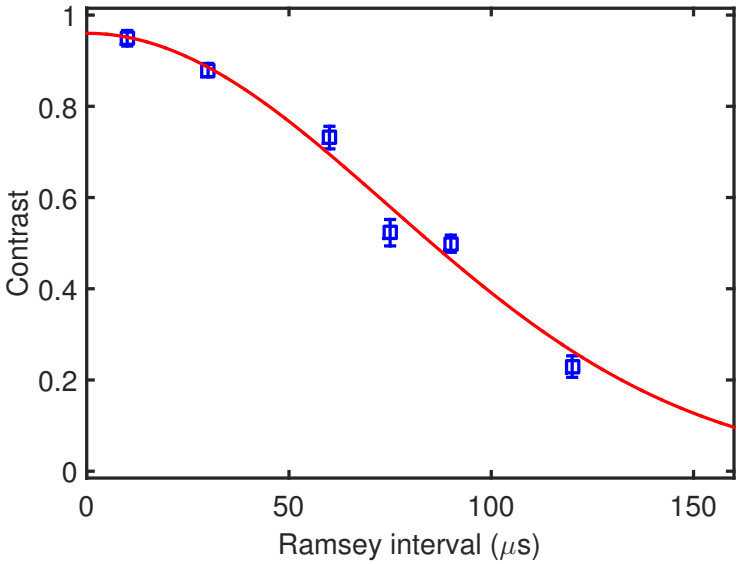

Figure 6.12: Contrast versus Ramsey interval T_R. Each data point represents the fitted contrast C for a phase scan for different T_R. The red curve is a weighted least-squares fit to the data using a Gaussian decay form.

To characterize the spin coherence, we perform a Ramsey experiment. The field-independent qubit (FIQ) we use is encoded as $|\uparrow\rangle \equiv \left|S_{1/2}, F = 1, m_F = 1\right\rangle$ and $|\downarrow\rangle \equiv \left|S_{1/2}, F = 2, m_F = 0\right\rangle$. 2) For the field-dependent qubit (FDQ), those states are chosen as $|\uparrow\rangle \equiv \left|S_{1/2}, F = 1, m_F = 1\right\rangle$ and $|b\rangle = |\downarrow\rangle \equiv$

$\left|S_{1/2}, F = 2, m_F = 2\right\rangle$. Coherent rotations between states $|b\rangle \leftrightarrow |\uparrow\rangle$ for FDQ and $|\downarrow\rangle \leftrightarrow |\uparrow\rangle$ for FIQ can be represented on the Bloch sphere (see Eq. (2.58)). The ion is Doppler cooled and prepared in the state $|\downarrow\rangle$. The Ramsey sequence is the following: we apply the rotation $\hat{R}(\frac{\pi}{2}, 0)$, creating the superposition state $|\Psi_1\rangle = \frac{1}{\sqrt{2}}(|\downarrow\rangle - i\,|\uparrow\rangle)$, and wait for the Ramsey interval T_R. During the wait time, the state evolves to $|\Psi_2\rangle = \frac{1}{\sqrt{2}}(e^{i\phi_D}\,|\downarrow\rangle - i\,|\uparrow\rangle)$. The phase $\phi_D = \int_0^{T_R}(\omega_R(t) - \omega_0(t))dt$, where ω_R is the two Raman beams' frequency difference and Ω_0 is the qubit transition frequency. The frequency driving the AOM for the Raman beams is derived from a stable 1 GHz frequency reference which is locked to a rubidium clock. The qubit transition frequency might drift due to the magnetic field fluctuations. After a certain Ramsey interval, a second $\pi/2$-pulse is then applied with ϕ varied, providing the rotation $\hat{R}(\frac{\pi}{2}, \phi)$. In the end, we perform a projective measurement for the probability of being in $|\downarrow\rangle$, yielding

$$P(\downarrow) = \frac{1}{2}(1 - \cos(\phi_D + \phi)) \tag{6.6}$$

The experiment is repeated many times and for different ϕ. The measured $P(\downarrow)$ should behave like a cosine wave. Any fluctuation in ϕ_D during many measurements, either generated by an unstable local oscillator or an unstable qubit frequency, can reduce the contrast of the obtained signal. We then fit the data using the function $f = \frac{1}{2}(a - b\cos(\phi_D + \phi))$, where the parameter a allows for an offset in the fit (very close to 1), b is the amplitude of the cosine wave, and ϕ_D is flowing for an offset in phase. The contrast of the Ramsey experiment is determined by $C = |b|$.

Figure 6.12 shows the extracted contrast for different Ramsey intervals performed on the FDQ. The reduced contrast as the Ramsey interval gets longer indicates spin decoherence. The spin decoherence can be modelled by a Gaussian or an exponential decay depending on the spectral properties of the noise [Home 06c]. We find that this data set can be fitted better with a Gaussian decay form $C(T_R) = Ae^{-T_R^2/\tau_s^2}$, where A is a constant and τ_s is the spin coherence time. We obtain $A = 0.96$ and $\tau_s = 105.5 \pm 4.1$ µs from the fit. The Gaussian form suggests that the noise spectrum is dominated by slow fluctuations compared to the Ramsey interval T_R. In our case, the frequency spectrum of the magnetic field noise are mainly peaked at 10 Hz, 110 Hz, and 50 Hz and its harmonics. It is also interesting to compare this spin coherence time of FDQ to ≈ 160 µs which is the coherence time of the calcium ion performing the same measurement. Because for the ^{40}Ca$^+$ ion the sensitivity of the qubit transition frequency to the magnetic field is ≈ 1.12 kHz/mG and for the ^{9}Be$^+$ FDQ, the transition frequency changes ≈ 1.76 kHz/mG around $B = 119.45$ G, the beryllium FDQ coherence time is shorter than the calcium one as we expect.

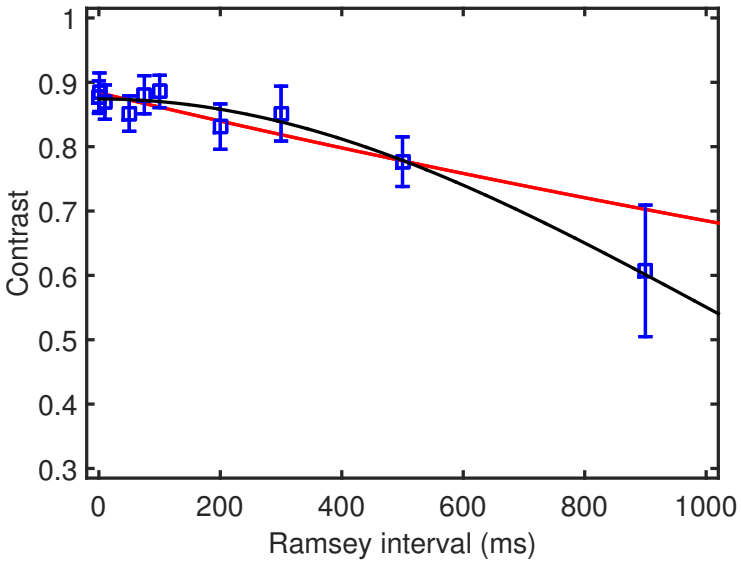

Figure 6.13: The same Ramsey experiment working with the FIQ. The red curve is a weighted least-squares fit to the data using a exponential decay form $C(T_R) = Ae^{-T_R/\tau_s}$, and the black curve is the same fit to the data using a Gaussian decay form $C(T_R) = Ae^{-T_R^2/\tau_s^2}$. The fit results are $A = 0.87$ and $\tau_s = 1.5 \pm 0.8$ seconds with the reduced $\chi^2 \approx 0.24$ for the black curve, and $A = 0.88$ and $\tau_s = 3.9 \pm 0.8$ seconds with the reduced $\chi^2 \approx 0.44$ for the red curve.

Figure 6.13 shows the same Ramsey experiment performed on the FIQ. It is clearly seen that the spin coherence is improved about 4 orders of magnitude. Here we use both a Gaussian and an exponential decay $C(T_R) = Ae^{-T_R/\tau_s}$ functions to fit this data set. In this case the frequency components of the magnetic field noise are already larger than the inverse of the Ramsey interval T_R [Home 06c]. Obtained from two fits, $A = 0.87$ and $\tau_s = 1.5 \pm 0.8$ seconds with the reduced $\chi^2 \approx 0.24$ using the Gaussian decay form, and $A = 0.88$ and $\tau_s = 3.9 \pm 0.8$ seconds with the reduced $\chi^2 \approx 0.44$ using the exponential decay function. The coherence time of the FIQ is much longer than the time scale of any quantum operations for our experiments. In principle, we can further improve this coherence time by calibrating the magnetic field more precisely to reach the field-independent point and stabilizing the Raman beam paths better. Active magnetic field stabilization might also help.

6.6 Micromotion Compensation

As mentioned in Chapter 4, two types of micromotion are present in Paul traps. When working with two-species ion chain, the micromotion compensation be-

comes even more crucial. Due to the mass difference, the stray fields distort the equilibrium positions of the ions in the crystal such that the frequencies and eigenvectors of the normal modes of the ion chain are changed. In this section, we will show some methods that we have tried in order to understand and null the micromotion for a single trapped ion in our 3-D segmented trap.

6.6.1 Intrinsic Micromotion

The first type of micromotion is called "intrinsic" micromotion [Amini 11], which is caused by complex trap geometries or not well aligned trap electrodes resulting in a residual component of the RF field present in the axial direction. This can be modeled by considering a RF field ($E_{\mathrm{RF}} \cos(\Omega_{\mathrm{RF}} t)$) along the axial direction. The treatment would be similar to Eq. (4.6), but now only the z component is taken into account. The solution is given by

$$z = -z_\mu \cos(\Omega_{\mathrm{RF}} t) \tag{6.7}$$

where $z_\mu = \frac{qE_{\mathrm{RF}}}{m\Omega_{\mathrm{RF}}^2}$ is the amplitude of the intrinsic micromotion. This reveals that the intrinsic micromotion amplitude is mass dependent and is smaller for heavier ions for the same trap conditions.

The intrinsic micromotion can not be nulled out by applying compensation fields. We attempt to find a position where the intrinsic micromotion is minimal by moving the ion along the axial direction. In the experiment we move the ion along the axial direction by changing the voltage of the DC electrodes. To measure the axial micromotion, we drive the Raman transitions using the Co-90 beam configuration because the k-vector difference points along the axial mode of motion only. In the presence of the axial micromotion we can drive a transition on the micromotion sideband when the frequency difference between two Raman beams is tuned to be $\omega_{\uparrow\downarrow} + n\Omega_{\mathrm{RF}}$, where $\omega_{\uparrow\downarrow}$ is the qubit transition frequency, n is an integer, and Ω_{RF} is the frequency of the RF drive of the trap. Here since the ion experiences a frequency-modulated laser field due to the micromotion, the effective Rabi frequency in the Raman transition (Eq. (2.34)) is scaled by the factor

$$\sum_n \sum_m J_n(\beta) J_m(-\beta) e^{i(n-m)\Omega_{\mathrm{RF}} t} \tag{6.8}$$

where $J_n(\beta)$ is the Bessel function of the first kind, and β is the modulation index. Its sign depends on the our laser setup configuration. In the case of the Co-90 beams, both Raman beams get frequency modulated. For the carrier transition ($m = n$) the effective Rabi frequency is scaled by $\sum_n J_n(\beta) J_n(-\beta)$, and for the first micromotion sideband ($m = n \pm 1$) the scaling factor is then $\sum_n J_n(\beta) J_{n\pm1}(-\beta)$. Figure 6.14 plots the scaling factor for the effective Rabi frequency as a function of the modulation index for different micromotion sidebands. In the experiment, once we move the ion to a new position, we

apply a Raman pulse to drive Rabi flops on the carrier and the first micromotion sideband, and then record the π-time of each data set. Ideally, if there is no micromotion ($\beta = 0$), we couldn't observe any Rabi oscillation on the micromotion sideband. Accordingly, we try to find a position where the π-time for the micromotion transition is the longest. The measurement results are shown in Fig. 6.15. We take the ratio of the carrier π-time to the micromotion π-time versus different positions along the axial direction. The minimum we measured is about one, showing that the modulation index is at one of the crossing points of blue and red curves in Fig. 6.14. We did perform the same measurement on the second and third micromotion sideband to gain more information after we took the data which is shown. However, the modulation index depends on the RF power we put into the trap, and so far we have not found a position without any intrinsic micromotion and the minimum modulation index inferred from the experimental data is about one.

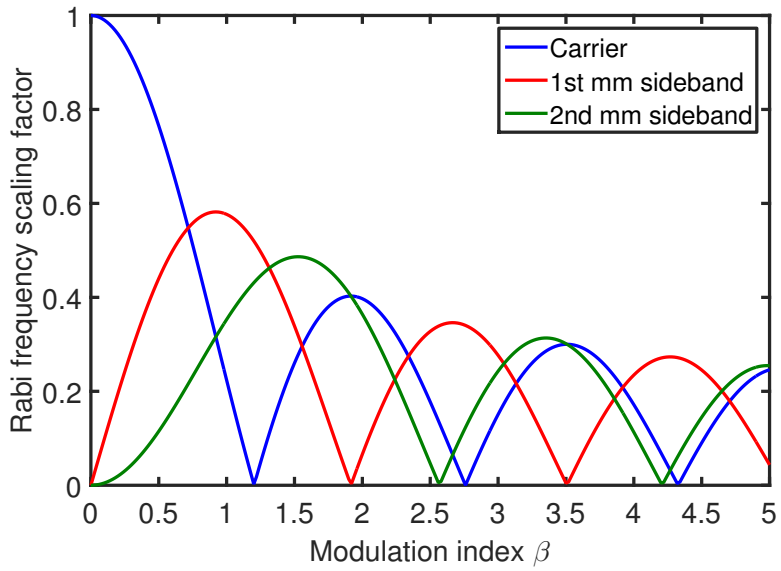

Figure 6.14: Plot Eq. (6.8) as a function of modulation index β for the carrier and first two sidebands. For the blue curve, the intrinsic micromotion can influence the Rabi frequency driving the carrier transition depending on the amplitude of β.

6.6.2 Excess Micromotion

The second type of micromotion is called "excess" micromotion, resulted from stray electric fields at the pseudopotential minimum. The field displaces the equilibrium position of an ion away from the pseudopotential minimum. This type of micromotion can be nulled by applying compensation fields to extra

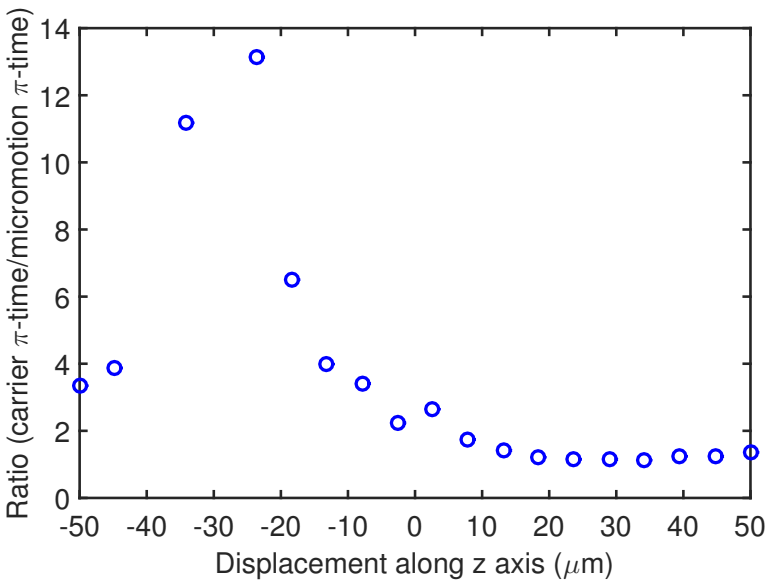

Figure 6.15: The ratio of the carrier π-time to the micromotion π-time versus different displacements along the axial direction. Ideally this ratio is zero if there is no intrinsic micromotion.

electrodes (as shown in Chapter 4). These extra electrodes should have independent control of the compensation fields along each radial principal axis. For a given stray field E_{dc}, the displacement of the ion x_{d} in the radial plane from the trap center and the resulting excess micromotion amplitude x_μ can be calculated as [Berkeland 98]:

$$x_{\mathrm{d}} = \frac{qE_{\mathrm{dc}}}{m\omega_x^2} \tag{6.9}$$

$$x_\mu \simeq \sqrt{2}\frac{\omega_x}{\Omega_{\mathrm{RF}}}x_{\mathrm{d}} \tag{6.10}$$

where ω_x is the radial secular frequency and can be obtained from Eq. (4.5). After algebraic simplifications with Eq. (4.5), we can find that x_μ is independent of mass although x_{d} is different for different ion's mass (heavier ions get larger displacements).

Both excess and intrinsic micromotion can influence the efficiency of Doppler cooling, ion fluorescence, and Raman transitions [Berkeland 98]. The reason is that an ion with micromotion experiences a frequency-modulated laser field due to the first-order Doppler shift. This modulation creates sidebands to the laser frequency as seen by the ion at integer multiples of Ω_{RF}. Therefore the intensity of the laser beam is suppressed at the carrier frequency depending on the strength of the modulation, which can be parametrized by an modulation

index β. It is given by

$$\beta = \mathbf{k} \cdot \mathbf{u}_\mu = |\mathbf{k}||\mathbf{u}_\mu| \cos(\theta) \tag{6.11}$$

where $\mathbf{u}_\mu = x_\mu \hat{x} + y_\mu \hat{y} + z_\mu \hat{z}$ is the micromotion amplitude, $\mathbf{k}$ is the wave vector of the laser beam, and θ is the angle between $\mathbf{k}$ and $\mathbf{u}_\mu$. In the rest frame of the ion, the laser field has the following form

$$\mathbf{E}(t) = \mathrm{Re}\left\{ \mathbf{E}_0 e^{i\mathbf{k}\cdot\mathbf{u}_0} \sum_{n=-\infty}^{\infty} J_n(\beta) e^{-i\omega_l + in(\Omega_{\mathrm{RF}} t + \pi/2)} \right\} \tag{6.12}$$

where $\mathbf{E}_0$ and ω_l are the amplitude and frequency of the electric field of the laser beam, $\mathbf{u}_0$ is the ion's position without any micromotion, $J_n(\beta)$ is the Bessel function of the first kind, n is an integer. As discussed in [Berkeland 98], the steady-state population of the excited state for a two-level system is

$$P_e = \sum_{n=-\infty}^{\infty} \frac{(gJ_n(\beta)/2)^2}{(-\Delta + n\Omega_{\mathrm{RF}})^2 + (\gamma/2)^2 + (gJ_n(\beta))^2/2} \tag{6.13}$$

where g is the Rabi frequency, Δ is the laser detuning with respect to the resonance frequency of the ion at rest and γ is the spontaneous decay rate of the excited state. Without any micromotion $\beta = 0$, Equation (6.13) reduces to the well-known steady state solution to the optical Bloch equations for a two-level system [Foot 04]. This equation is only valid in the low laser intensity limit ($g \ll \gamma$). We should also notice that if micromotion is perpendicular to the laser beam direction, the modulation index will be zero and the micromotion can not be probed. Figure 6.16 shows the the theoretical prediction for the spectrum based on Eq. (6.13) as a function of the probe beam frequency. It can be seen that the micromotion induces sidebands of the probing laser at integer multiples of the RF driving frequency. When the modulation index $\beta = 1.43$, the carrier and first micromotion sideband have equal strength. The aim for the experiment is to have β as small as possible in order to minimize the aforementioned influences to the ion.

Several methods are available to null the excess micromotion [Berkeland 98]. We diagnose the excess micromotion by three different approaches: 1) Fluorescence spectroscopy, 2) Micromotion mapping, and 3) RF tickle. In the work of this thesis, the excess micromotion compensation is performed by applying the DC voltage to the shim electrodes which create compensation fields along the vertical and horizontal directions. Figure 6.17 shows the side view of the trap, where each side contains two shim electrodes (A&B or C&D). Ideally the ion can be pushed back to the center from any position in the radial plane. The vertical and horizontal compensation fields are generated by $\alpha = (V_A + V_C) - (V_B + V_D)$ and $\beta = (V_A + V_B) - (V_C + V_D)$ respectively,

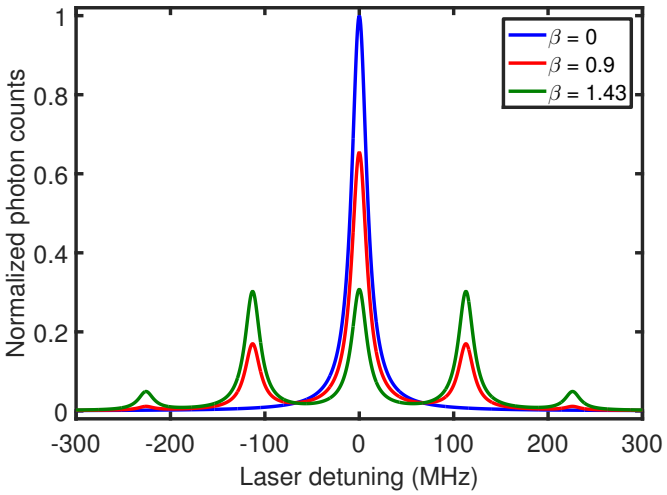

Figure 6.16: Effect of micromotion on the spectrum of P_e. Here various values of modulation index β are plotted and the probe laser power is much lower than the saturation intensity.

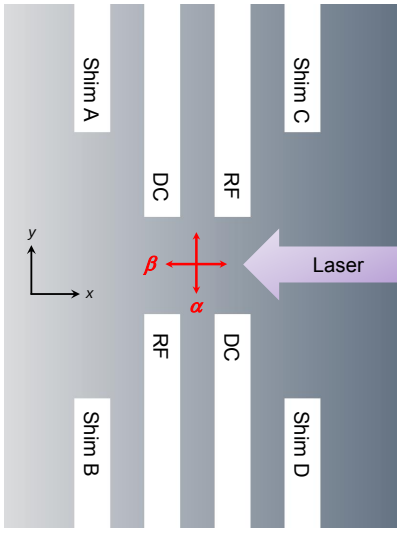

Figure 6.17: The side view of the trap. α and β are the compensation fields along the vertical and horizontal direction for nulling the stray fields and are generated by applying DC voltages to the shim electrodes (A, B, C, and D). The arrows indicate the direction of the field and do not scale to the field strength.

resulting in the voltage of each shim electrode as follows:

$$V_A = \frac{\alpha}{4} + \frac{\beta}{4} \tag{6.14}$$

$$V_B = -\frac{\alpha}{4} + \frac{\beta}{4} \tag{6.15}$$

$$V_C = \frac{\alpha}{4} - \frac{\beta}{4} \tag{6.16}$$

$$V_D = -\frac{\alpha}{4} - \frac{\beta}{4} \tag{6.17}$$

It should be noticed that the field in the horizontal direction (β) is ten times stronger than that in the vertical direction (α) due to the trap geometry.

Fluorescence Spectroscopy

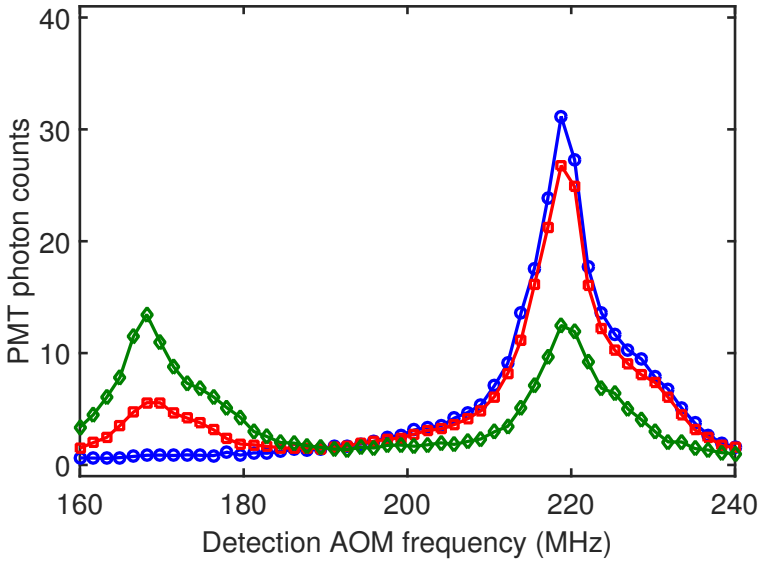

Figure 6.18: The frequency scan of the detection beam. Three traces corresponds to different shim voltages used for micromotion compensation. The RF drive frequency is $\Omega_{\mathrm{RF}} \approx 2\pi \times 110\,\mathrm{MHz}$ in this case. In the presence of micromotion, there is a sideband at the RF drive frequency. This AOM is in a double-pass setup so the frequency should be doubled. The blue trace shows that the micromotion is well compensated along the propagating direction of the laser beam. The green trace indicates that the modulation index is around 1.43 since the carrier and first micromotion sideband have nearly equal strength.

The first method we tried is the use of fluorescence spectroscopy with the detection beam, as shown in Fig. 6.18. The frequency of the detection beam is scanned using the AOM. Ideally we obtain a Lorentzian profile centered at the atomic resonance as derived in Eq. (6.13) with $\beta = 0$. However in the presence of micromotion we can see a sideband appeared at the RF driving frequency. Owing to the limited bandwidth of the AOM, we are not able to observe higher-order micromotion sidebands. To null the stray fields, we apply voltages (α and β) on the shim electrodes, which generate compensation fields, while setting the laser frequency at the micromotion sideband until the sideband signal is minimized. This method is simple, but it can not guarantee that the ion is really at the center of the pseudopotential because

the micromotion is only minimized along the propagating direction of the detection beam, which is at 45° with respect to the trap axis (see Fig. 5.2). For this method, one can fully compensate the stray fields using three laser beams which are illuminated to the ion from three directions perpendicular to each other, so each laser beam is sensitive to micromotion along its direction of propagation. However one axis is not accessible in our setup.

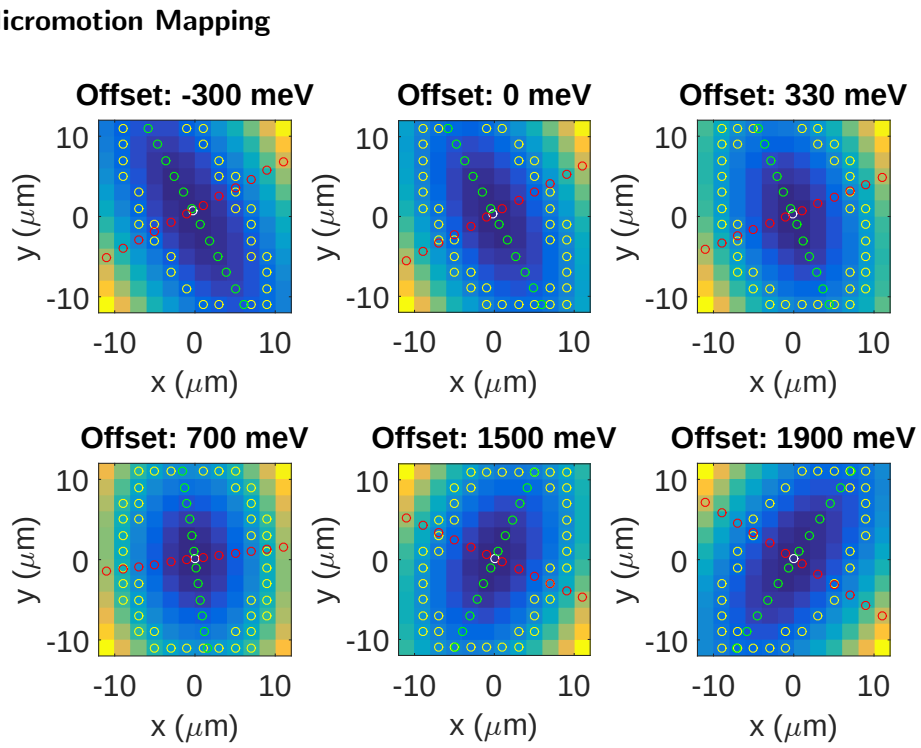

Figure 6.19: The simulated pseudopotential in the radial plane with different DC potential offsets. It can be seen that the principal axes in the $x-y$ plane are rotated depending on the DC potential offsets. This would affect the micromotion as well as the efficiency of laser cooling.

In a 3-D segmented traps, it is possible to rotate the principal axes in the radial $(x-y)$ plane by applying different static voltages to the DC electrodes (different DC potential offsets) [Madsen 06]. Normally the principal axes of an ion trap are chosen for efficient laser cooling. If the laser wave vector $\mathbf{k}$ has a component along each of the three principal axes, it can cool ion's three motional modes. Figure 6.19 shows simulation results of the superimposed pseudo- and static potential in the radial plane for different DC potential offsets. Here we keep the axial frequency constant and only the DC potential offset differs. As the radial principal axes are rotated, the shape and orien-

tation of the total potential changes. In the experiment, we observe that the required compensation field for minimizing the micromotion changes depending on the DC potential offsets, or equivalently the rotation of the radial principal axes. The measurement results for the $^{40}Ca^{+}$ and $^{9}Be^{+}$ ion are shown in Fig. 6.20. For each DC potential offset, we picked a range of values of α and performed a scan of β for each. Then we recorded the β value that produces the maximal fluorescence. It shows that there is a crossing point among different data sets. We think the α and β value at this point is the optimal setting for micromotion compensation because it is independent of the tilt of the radial principal axes. Nevertheless, this mapping method only provides information about micromotion along the direction of the detection beam.

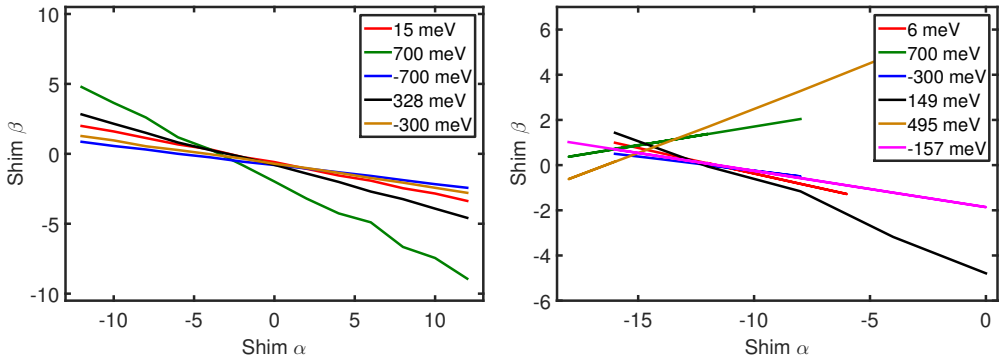

(a) (b)

Figure 6.20: Mapping of the compensation fields for different DC potential offsets (rotating the principal axes in the radial plane). (a) Work on a single $^{40}Ca^{+}$ ion. (b) A single $^{9}Be^{+}$ ion.

RF Tickle

The last approach, which is also the most precise one, is the RF tickle technique [Ibaraki 11]. The trap RF drive is amplitude modulated at ion's secular frequency. Once the ion is not at the RF null, this amplitude modulated RF field can excite ion's motion. This provides us a clean measurement that is independent of the laser beam directions. The setup is illustrated in Fig. 6.21. The modulation signal starts from two DDS channels. The outputs from DDSs are mixed and then passed through a low-pass (LP) filter. The remaining signal $m(t)$ only contains the few-MHz secular frequency component. The RF signal driving the trap is the carrier signal that is split into two paths with a power splitter (PS). The carrier signal in one path is multiplied with the modulation signal in a mixer, and then combined with the carrier signal from

the other path, resulting in an amplitude modulated signal. This modulated signal is then sent to the resonator and has three components: the carrier $c(t)$ with frequency Ω_{RF} and two sidebands with frequencies $\Omega_{RF} + \omega_m$ and $\Omega_{RF} - \omega_m$, where Ω_{RF} and ω_m are the frequency of the RF drive and the ion's secular motion. The advantage of this setup is that the power of the carrier RF component remains unchanged with and without amplitude modulation so the ion's motional frequency is not affected by our micromotion detection.

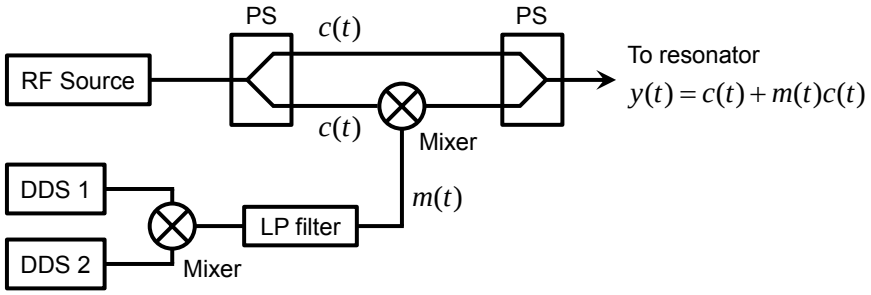

Figure 6.21: The setup for RF tickle measurement. PS: power splitter and LP filter: low-pass filter. For details, see texts.

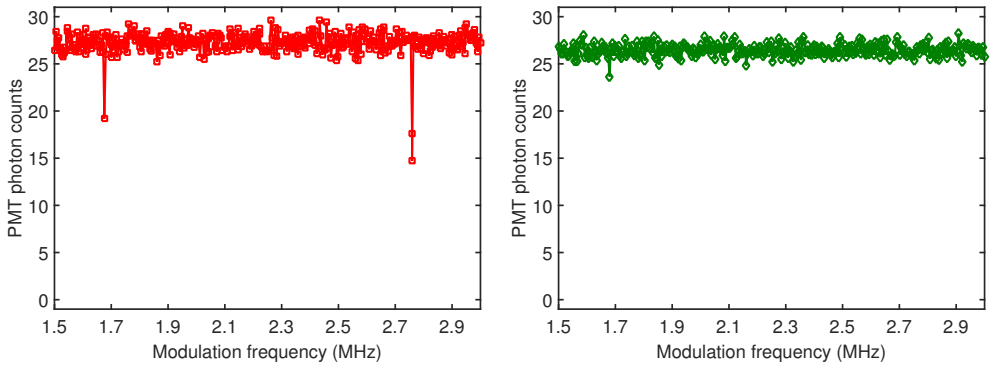

Figure 6.22: Micromotion compensation using RF tickle technique. (a) Before minimization of micromotion. We can see dips at two radial mode frequencies. (b) After minimization of micromotion.

After the ion is Doppler cooled, the RF tickling signal is applied, followed by the qubit readout. This measurement is only performed on the $^{40}Ca^{+}$ ion. The motional frequency of the radial modes of the $^{9}Be^{+}$ ion is too high

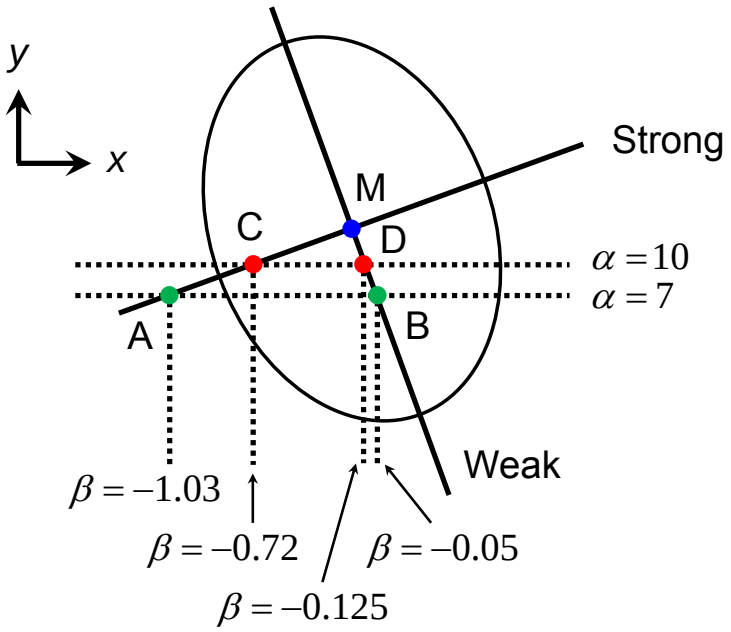

Figure 6.23: The summary of the RF tickle measurement. We draw a cartoon of the pseudopotential, which is tilted, and two principal axes of the radial confinement for the ion. The α and β values for the points A, B, C, and D are obtained from the 2-D scan. From which, we can calculate the required voltage settings (α and β) at the crossing point M, where ideally is the pseudopotential minimum.

($\sim$ 10 MHz) such that the sidebands of the modulated signal would be filtered out by the resonator for which the half-power linewidth is around 1 MHz in our case. One the other hand, if we null the stray fields such that the calcium ion is at the pseudopotential minimum, the beryllium should be the same. We first perform a frequency scan without applying any compensation field. The spectrum is shown in Fig. 6.22(a). There are two dips corresponding to the motional frequency of two radial modes. The next step is that we picked an α value and perform a 2-D scan in which the y axis is the β value and the x axis is the tickle frequency scanned over two radial modes[2]. For $\alpha = 7$, it is found that $\beta = -1.03$ can make the micromotion vanish for the weak radial mode. This means the ion is either at the center of the pseudopotential or on the principal axis of the strong radial confinement. For the same α, making the micromotion vanish for the strong radial mode needs $\beta = -0.05$. Since two β

[2]Since when we change the shim voltage, the motional frequency of the ion slightly shifts. Therefore 2-D scan is needed in this measurement. For some technical reasons, the raw 2-D scan data was not recorded by the computer so it can not be shown here. Only the screenshot pictures and notes were saved. These data shown were taken on 24.10.2014.

values are not the same, so we can conclude that in the first case the ion is on the principal axis of the strong radial confinement while the weak radial mode can not be excited. In the latter one, the ion is on the principal axis of the weak radial confinement. Next, we chose the other $\alpha = 10$ and followed the same procedures. The results are summarized in Fig. 6.23 for clarification. We can determine a linear equation from two points on the principal axis of strong radial confinement and two points on the principal axis of weak radial confinement. The crossing point of these two linear equations will be the pseudopotential minimum. After calculating α and β at the crossing point and set them in the experiment, we repeated the RF tickle measurement again. We found the micromotion is well compensated, as shown in Fig. 6.22(b).

6.7 Conclusions

In this chapter we began with the loading procedure for the $^9Be^+$ ions. Basic techniques and calibrations required for $^9Be^+$ qubit manipulations were described. We demonstrated $^9Be^+$ ion ground state cooling and created long-lived quantum memories using first-order magnetic-field-independent hyperfine transitions. The results with $^9Be^+$ qubits showed a coherence time of ≈ 1.5 s. In principle, this coherence time can be further improved by fine tuning the magnetic field to get the field-independent point and stabilizing the Raman beam path better, for example we can cover the setup with a box to suppress the influence from the environment.

The most severe problem we faced was the micromotion of the ion. The stray fields in the trap can cause a variety of problems for quantum control of trapped ions especially for mixed-species ion chains. For the intrinsic (axial) micromotion which can not be nulled with additional compensation fields, we moved the ion along the axial direction trying to find a position where this type of micromotion is minimum. However, there is no minimal point where it is zero, probed with non-copropagating Raman beams (the wavevector difference along the axial direction)[3]. The excess micromotion can be minimized by applying voltages to shim electrodes which generate compensation fields. In our experiment, we tried three methods, in two of which we relied on the fluorescence detection. The minimization of micromotion is only along the propagating direction of the probe field, which is at 45° with respect to the axial direction. In this case, the ion is not at the pseudopotential minimum even after we have maximal fluorescence counts. The lighter beryllium ion has much larger axial micromotion than the heavier calcium ion. The intrinsic micromotion always has a component projecting onto the propagating direction of the probe field. Consequently, to cancel out this vector projection of the

[3]Meanwhile, we also notice that the group at NIST also has strong axial micromotion in one of their traps. However they recently show that they can use the second micromotion sideband to perform high-fidelity quantum control of multiple qubits.

intrinsic micromotion on the probe field direction, different shim voltage settings are required for two ion species. It is quite hard for us to find a common shim voltage setting for both ion species. If we use the shim voltage setting of the calcium ion, we lose the fluorescence from the readout of the beryllium ion, and vice versa. The third method we used is the RF tickle. By amplitude modulating the trap RF field and optimizing the shim voltage settings, we could make the ion sit at the pseudopotential minimum. However, this optimal shim voltage setting does not reflect on the fluorescence detection of the beryllium ion due to the presence of intrinsic micromotion.

Our aim is to achieve high-fidelity control of two-species ion chains. Although the calcium and beryllium ions have not been operated together, this chapter combined with the characterizations for the calcium ion covered in [Kienzler 15b] provides the basic elements we need for control of both species of ions. Before writing the thesis, the beryllium ion system has been used for demonstrating the single-qubit transport gate for the first time. The details will be presented in Ludwig de Clercq's forthcoming Ph.D. thesis [de Clercq 15].

Chapter 7

Squeezed Schrödinger's Cat States

The creation and study of nonclassical states of spin systems coupled to a harmonic oscillator has provided fundamental insights into the nature of decoherence and the quantum-classical transition. These states and their control form the basis of experimental developments in quantum information processing and quantum metrology [Monroe 95a, Wineland 13, Haroche 13]. Two of the most commonly considered states of the oscillator are squeezed states and superpositions of coherent states of opposite phase, which are commonly referred to as "Schrödinger's cat" (SC) states. Squeezed states involve reduction of the fluctuations in one quadrature of the oscillator below the ground state uncertainty, which has been used to increase sensitivity in interferometers [Collaboration 11, Aasi 13]. SC states provide a complementary sensitivity to environmental influences by separating the two parts of the state by a large distance in phase space. These states have been created in microwave and optical cavities [Vlastakis 13, Haroche 13], where they are typically not entangled with another system, and also with trapped ions [Monroe 96, McDonnell 07, Haljan 05a, Wineland 13], where all experiments performed have involved entanglement between the oscillator state and the internal electronic states of the ion. SC states have recently been used as sensitive detectors for photon scattering recoil events at the single photon level [Hempel 13].

This Chapter presents our recent results in which we use a single trapped $^{40}Ca^{+}$ ion to combine for the first time highly squeezed states with superpositions of distinct atomic wavepackets commonly referred to as Schrödinger's cat states. This work demonstrates direct measurements on the squeezed state of the ion, revealing key features of the squeezed nature in phase space. The coherence of the squeezed Schrödinger's cat states is verified by recombining the squeezed wavepackets, which we measure through the revival of the spin coherence. I will first review how to prepare the squeezed vacuum state of an ion's motion by reservoir engineering, a technique covered in more detail in the

thesis of Daniel Keinzler [Kienzler 15b]. Then the creation and measurement of the squeezed Schrödinger's cat states will be presented. The results shown in this chapter are covered in our recent publications [Kienzler 15a, Lo 15].

7.1 Dissipative Quantum State Preparation

7.1.1 Reservoir Engineering

Reservoir engineering is a method in which specially designed couplings between a system of interest and an environment, which is the vacuum modes of the electromagnetic field, can be used to generate quantum superposition states of the system as the steady state of the dissipative process. Following the proposals [Cirac 93a, Poyatos 96], we have developed techniques to prepare quantum harmonic states of a single trapped $^{40}Ca^{+}$ ion, including coherent states, squeezed states and displaced-squeezed states [Kienzler 15a]. Basically the process is implemented by introducing an artificial decay channel for the spin states in form of an effective zero temperature reservoir, combined with engineered spin-oscillator couplings.

In the analysis, we consider the system shown in Fig. 7.1(a), where the ion's motion is described by a quantum harmonic oscillator and the internal state of the ion is restricted to a three-level system containing two long-lived qubit states and one short-lived excited state. Two qubit states are denoted by $|\uparrow\rangle$ and $|\downarrow\rangle$ driven by laser fields with a Rabi frequency Ω, and the state $|e\rangle$ represents the short-lived excited state of the ion with a spontaneous decay rate of γ. The state $|\uparrow\rangle$ can couple to the state $|e\rangle$ by a laser field with a coupling strength (Rabi frequency) $\Omega_{e\uparrow}$, generating an artificial decay channel from $|\uparrow\rangle$ to $|\downarrow\rangle$. The effective spontaneous emission rate for the state $|\uparrow\rangle$ is given by $\gamma_{\uparrow} \approx \Omega_{e\uparrow}^2/\gamma$ [Haroche 06]. Here γ is supposed to be much larger than the emission rate from $|e\rangle$ to $|\uparrow\rangle$ and the Rabi frequency $\Omega_{e\uparrow}$. In the Lamb-Dicke regime, the effect of the photon recoil from the spontaneous emission on the ion's motional state can be neglected.

The dynamics of the whole system can be described by a master equation:

$$\frac{d\rho}{dt} = -\frac{i}{\hbar}\left[\hat{H}, \rho\right] + \mathcal{L}(\rho) \tag{7.1}$$

where ρ is the total density matrix for the ion and $\hat{H}$ the general spin-motion coupling Hamiltonian, given by

$$\hat{H} = \frac{\hbar}{2}\Omega\left(\hat{K}\hat{\sigma}_{+} + \hat{K}^{\dagger}\hat{\sigma}_{-}\right) \tag{7.2}$$

where $\hat{\sigma}_{+} = |\uparrow\rangle\langle\downarrow|$ and $\hat{\sigma}_{-} = |\downarrow\rangle\langle\uparrow|$ are the spin flip operators and $\hat{K}$ ($\hat{K}^{\dagger}$) is a general motional annihilation (creation) operator. The Louvillian operator

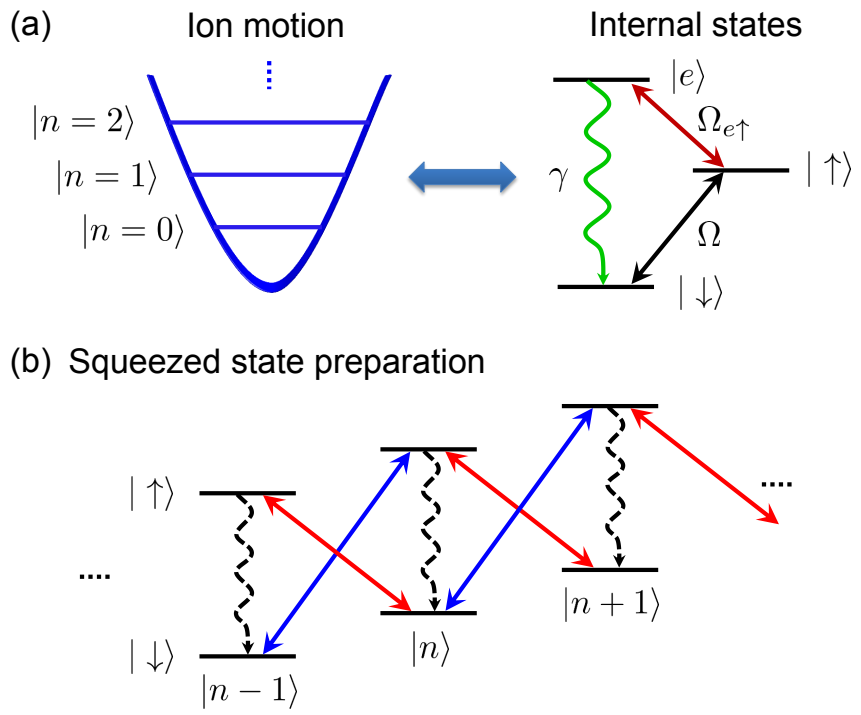

Figure 7.1: (a) The system we consider for dissipative quantum state preparation. (b) The transitions involved in the squeezed vacuum state preparation. The blue (red) motional sideband is marked with blue (red) arrows. The decay is labeled with dash lines. The steady state of the process is reached when the total probability amplitude of exciting the state $|\uparrow, n\rangle$ from $|\downarrow, n-1\rangle$ and $|\downarrow, n+1\rangle$ vanish.

$\mathcal{L}(\rho)$ describes the decay process with the form

$$\mathcal{L}(\rho) = \gamma_{\uparrow}\hat{\sigma}_{-}\rho\hat{\sigma}_{+} - \frac{\gamma_{\uparrow}}{2}\left(\rho\hat{\sigma}_{+}\hat{\sigma}_{-} + \hat{\sigma}_{+}\hat{\sigma}_{-}\rho\right) \tag{7.3}$$

In general, solving this master equation is difficult and requires numerical computations. We only consider a limiting case in which $\gamma_{\uparrow} \gg \Omega$ the effective qubit decay rate is much larger than the coupling strength. Therefore we can adiabatically eliminate the spin population in $|\uparrow\rangle$. By introducing the partial matrix elements of the density operator $\hat{\rho}_{ij} = \langle i|\,\hat{\rho}\,|j\rangle$, where $\{i,j\} \in \{\uparrow,\downarrow\}$, the density matrix can be re-written as

$$\hat{\rho} = \hat{\rho}_{\downarrow\downarrow}\,|\downarrow\rangle\langle\downarrow| + \hat{\rho}_{\downarrow\uparrow}\,|\downarrow\rangle\langle\uparrow| + \hat{\rho}_{\uparrow\downarrow}\,|\uparrow\rangle\langle\downarrow| + \hat{\rho}_{\uparrow\uparrow}\,|\uparrow\rangle\langle\uparrow| \tag{7.4}$$

These density operators $\hat{\rho}_{ij}$ still act on the motional state of the ion. Inserting Eq. (7.4) into Eq. (7.1), we can obtain four evolution equations for $\hat{\rho}_{ij}$

[Haroche 06, Kienzler 15b]. After applying adiabatic elimination and some algebraic simplification, the evolution equation for $\hat{\rho}_{\downarrow\downarrow}$ is

$$\frac{d\hat{\rho}_{\downarrow\downarrow}}{dt} = \frac{\Omega^2}{\gamma_\uparrow}\hat{K}\rho_{\downarrow\downarrow}\hat{K}^\dagger - \frac{1}{2}\frac{\Omega^2}{\gamma_\uparrow}\left(\rho_{\downarrow\downarrow}\hat{K}^\dagger\hat{K} + \hat{K}^\dagger\hat{K}\rho_{\downarrow\downarrow}\right) \tag{7.5}$$

This shows that the evolution equation for the ion's motion takes a Lindblad form with a decay rate of $\frac{\Omega^2}{\gamma_\uparrow}$. The Lindblad operator is expressed by $\hat{L} = \frac{\Omega}{\sqrt{\gamma_\uparrow}}\hat{K}$. The ion's motion undergoes relaxation processes until it reaches the final state $|\psi\rangle$ satisfying $\hat{L}\,|\psi\rangle = 0$. This dissipative state preparation can be easily understood in the resolved sideband cooling for which $\hat{K} = \hat{a}$ is the annihilation operator of the harmonic oscillator, resulting a Hamiltonian for the red sideband drive. After several dissipative pumping cycles, the ion can be cooled to its motional ground state ($\hat{a}\,|0\rangle = 0$). However this method can be extended to generate quantum superposition states of the harmonic oscillator by engineering the operator $\hat{K}$ [Kienzler 15a, Poyatos 96].

7.1.2 Squeezed Vacuum State Preparation

In the work on squeezed cats, we work with squeezed vacuum states. To obtain these, we start with the relation $\hat{a}\,|0\rangle = 0$, where $|0\rangle$ is the ground state of the harmonic oscillator. Now we introduce an unitary operator $\hat{U}$ such that $\hat{U}\hat{a}\hat{U}^\dagger\hat{U}\,|0\rangle = 0$ is still valid. The state of interest is defined as $|\psi\rangle = \hat{U}\,|0\rangle$ and the general motional annihilation operator becomes $\hat{K} = \hat{U}\hat{a}\hat{U}^\dagger$.

The squeezed vacuum state $|\xi\rangle$ is defined by the action of the squeezing operator $\hat{S}(\xi) = e^{(\xi^*\hat{a}^{\,2} - \xi\hat{a}^{\dagger\,2})/2}$ on the motional ground state $|0\rangle$, where $\xi = re^{i\phi_s}$ with r and ϕ_s real parameters, which define the magnitude and the direction of the squeezing in phase space. In order to generate squeezed vacuum states as the desired state of the pumping process, we implement a coupling Hamiltonian of the form given in Eq. (7.2), with the operator $\hat{K} = \hat{S}(\xi)\hat{a}\,\hat{S}^\dagger(\xi) = \cosh r\hat{a} + e^{i\phi_s}\sinh r\hat{a}^\dagger$. This requires simultaneous application of laser fields resonant with both the red motional sideband transition ($\hat{H}_{\mathrm{rsb}} = \frac{\hbar}{2}\Omega_r(\hat{\sigma}_+\hat{a}e^{i\phi_r} + \mathrm{h.c.})$) and the blue motional sideband transition ($\hat{H}_{\mathrm{bsb}} = \frac{\hbar}{2}\Omega_b(\hat{\sigma}_+\hat{a}^\dagger e^{i\phi_b} + \mathrm{h.c.})$). The ratio of the Rabi frequencies on these transitions gives the strength of the squeezing through $r = \tanh^{-1}\frac{\Omega_b}{\Omega_r}$ while the phase is given by the phase difference between the two frequency components of the laser $\phi_s = \phi_b - \phi_r$.

The squeezed state stabilization can also be understood as a quantum interference process. Figure 7.1(b) shows the ladder structure involved in the squeezed state pumping process. The blue (red) motional sideband couples the states $|\downarrow, n-1\rangle$ ($|\downarrow, n+1\rangle$) and $|\uparrow, n\rangle$. The evolution stops when the total transition probability amplitude is zero. The following condition must be fulfilled:

$$c_{n-1}\,\langle\uparrow, n|\,\hat{H}_{\mathrm{bsb}}\,|\downarrow, n-1\rangle + c_{n+1}\,\langle\uparrow, n|\,\hat{H}_{\mathrm{rsb}}\,|\downarrow, n+1\rangle = 0 \tag{7.6}$$

Using the definitions of the Hamiltonian above, this condition can be simplified to

$$c_{n-1}\Omega_b\sqrt{n} + c_{n+1}\Omega_r\sqrt{n+1} = 0 \tag{7.7}$$

There are two sets of solution, one contains only even phonon states and the other contains only odd phonon states. As we can see, only the even solution includes the ground state of the harmonic oscillator so this case is considered here. Taking normalization into account, the solution of this recurrence relation is [Gerry 05]

$$c_n = c_{2m} = (-1)^m \frac{\sqrt{(2m)!}}{2^m m!} \frac{(e^{i\phi_s \tanh r})^m}{\sqrt{\cosh r}} \tag{7.8}$$

where $r = \tanh^{-1}\frac{\Omega_b}{\Omega_r}$, which is consistent with the one we obtained above. Therefore the squeezed vacuum state is

$$|\xi\rangle = \frac{1}{\sqrt{\cosh r}} \sum_{m=0}^{\infty} (-1)^m \frac{\sqrt{(2m)!}}{2^m m!} e^{im\phi_s} (\tanh r)^m |2m\rangle \tag{7.9}$$

The probability distribution $p(n)$ is now given by

$$p(n) = p(2m) = |\langle 2m|\,\xi\rangle|^2 = \frac{(2m)!}{2^{2m}(m!)^2} \frac{(\tanh r)^{2m}}{\cosh r} \tag{7.10}$$

$$p(n) = p(2m+1) = 0 \tag{7.11}$$

The probability vanishes for all odd n.

7.2 Creation of Squeezed Schrödinger's Cat States

7.2.1 Theoretical Description

We use state-dependent forces (SDFs) to create superpositions of distinct squeezed oscillator wavepackets which are entangled with a pseudo-spin encoded in the electronic states of a single trapped ion. We will refer to these states as squeezed wavepacket entangled states (SWES) in the rest of this chapter.

A SDF is performed by simultaneously driving the red $|\downarrow\rangle|n\rangle \leftrightarrow |\uparrow\rangle|n-1\rangle$ and blue $|\downarrow\rangle|n\rangle \leftrightarrow |\uparrow\rangle|n+1\rangle$ motional sidebands of the spin flip transition [Monroe 96]. The resulting interaction Hamiltonian can be written in the Lamb-Dicke approximation as

$$\hat{H}_D = \hbar\frac{\Omega}{2}\hat{\sigma}_x \left(\hat{a}^\dagger e^{-i\phi_D/2} + \hat{a}\, e^{i\phi_D/2}\right) , \tag{7.12}$$

where Ω is the strength of the SDF, ϕ_D is the relative phase of the two light fields, and $\hat{\sigma}_x \equiv |+\rangle\langle +| - |-\rangle\langle -|$ with $|\pm\rangle = (|\uparrow\rangle \pm |\downarrow\rangle)/\sqrt{2}$. For an ion

prepared in $|+\rangle$, this Hamiltonian results in displacement of the motional state in phase space by an amount $\alpha(\tau) = -i\Omega e^{-i\phi_D/2}\tau/2$ which is given in units of the r.m.s. extent of the harmonic oscillator ground state. An ion prepared in $|-\rangle$ will be displaced by the same amount in the opposite direction. In the following equations, we use α in place of $\alpha(\tau)$ for simplicity. Starting from the state $|\downarrow\rangle|\xi\rangle$, application of the SDF ideally results in the SWES

$$|\psi(\alpha)\rangle = \frac{1}{\sqrt{2}}\left(|+\rangle|\alpha,\xi\rangle - |-\rangle|-\alpha,\xi\rangle\right), \tag{7.13}$$

where we use the notation $|\alpha,\xi\rangle = \hat{D}(\alpha)\hat{S}(\xi)|0\rangle$ with the displacement operator $\hat{D}(\alpha) = e^{\alpha\hat{a}^\dagger - \alpha^*\hat{a}}$. A projective measurement of the spin performed in the $\hat{\sigma}_z$ basis gives the probability of being $|\downarrow\rangle$ as $P(\downarrow) = (1+X)/2$, where $X = \langle\alpha,\xi| - \alpha,\xi\rangle = \langle-\alpha,\xi|\,\alpha,\xi\rangle$ gives the overlap between the two displaced motional states, which can be written as

$$X(\alpha,\xi) = e^{-2|\alpha|^2\left(\exp(2r)\cos^2(\Delta\phi)+\exp(-2r)\sin^2(\Delta\phi)\right)} \tag{7.14}$$

where $\Delta\phi = \arg(\alpha) - \phi_s/2$. When $\Delta\phi = 0$, the SDF is aligned with the squeezed quadrature of the state, while for $\Delta\phi = \pi/2$, the SDF is aligned with the anti-squeezed quadrature. At displacements for which X gives a measurable signal, monitoring the spin population as a function of the force duration τ for different choices of $\Delta\phi$ allows us to characterise the spatial variation of the initial squeezed wavepacket [Hao-Sheng 05, Gerritsma 10, Casanova 12]. For values of $|\alpha|^2$ which are greater than the wavepacket variance along the direction of the force, the state in Eq. (7.13) is a distinct superposition of squeezed wavepackets which have overlap close to zero and are entangled with the internal state. For $r = 0$ (no squeezing) the state reduces to the familiar "Schrödinger's cat" states which have been produced in previous work [Monroe 96, McDonnell 07, Haljan 05a, Wineland 13]. For $r > 0$ the superposed oscillator states are the displaced-squeezed states [Caves 81, Yuen 76].

7.2.2 Experimental Details

The experiments make use of a segmented linear Paul trap with an ion-electrode distance of ≈ 185 μm. Motional heating rates from the ground state for a $^{40}Ca^+$ ion in this trap have been measured to be 10 ± 1 quanta/s, and the coherence time for the number state superposition $(|0\rangle + |1\rangle)/\sqrt{2}$ has been measured to be 32 ± 3 ms [Kienzler 15b]. This experiment uses a single trapped $^{40}Ca^+$ ion, which mechanically oscillates on its axial vibrational mode with a frequency close to $\omega_z/(2\pi) = 2.1$ MHz. This mode is well resolved from all other modes. The first step of each experimental run involves cooling all modes of motion of the ion close to the Doppler limit using laser light at 397 and 866 nm. We encode a pseudo-spin system in the internal electronic states $|\downarrow\rangle \equiv \left|S_{1/2}, M_J = 1/2\right\rangle$ and $|\uparrow\rangle \equiv \left|D_{5/2}, M_J = 3/2\right\rangle$. This transition is

resolved by 200 MHz from all other internal state transitions in the applied magnetic field of 119.6 G. All coherent manipulations, including the squeezed state preparation and the SDF, make use of the quadrupole transition between these levels at 729 nm, with a Lamb-Dicke parameter of $\eta \simeq 0.05$ for the axial mode. This is small enough that the experiments are well described using the Lamb-Dicke approximation [Wineland 98]. A discussion of this approximation is given in Chapter 7.2.4.

The state-dependent forces (SDFs) and the reservoir engineering in our experiment require the application of a bichromatic light field. We generate both frequency components using acousto-optic-modulators (AOMs) starting from a single laser stabilized to an ultra-high-finesse optical cavity with a resulting linewidth < 600 Hz (at which point magnetic field fluctuations limit the qubit coherence). We apply pulses of 729 nm laser light using a double-pass AOM to which we apply a single radio-frequency tone, followed by a single-pass AOM to which two radio-frequency tones are applied. Following this second AOM, both frequency components are coupled into the same single-mode fiber before delivery to the ion. The double-pass AOM is used to switch on and off the light. Optical pumping to $|\downarrow\rangle$ is implemented using a combination of linearly polarized light fields at 854 nm, 397 nm and 866 nm. The internal state of the ion is read out by state-dependent fluorescence using laser fields at 397 nm and 866nm.

7.2.3 Experimental Results and Discussions

First Measurement

We apply the SDF directly after the squeezed vacuum state has been prepared by reservoir engineering and the internal state has been prepared in $|\downarrow\rangle$ by optical pumping (in the ideal case, the ion is already in the correct state and this step has no effect). Figure 7.2 shows the results of measuring $\langle\hat{\sigma}_z\rangle$ after applying displacements along the two principal axes of the squeezed state alongside the same measurement made using an ion prepared in the motional ground state. In order to extract relevant parameters regarding the SDF and the squeezing, we fit the data using $P(\downarrow) = (A + BX(\alpha, \xi))/2$, where the parameters A and B account for experimental imperfections such as shot-to-shot magnetic field fluctuations (see Chapter 7.2.5 for discussions). Fitting the ground state data with r fixed to zero allows us to extract $\Omega/(2\pi) = 13.25 \pm 0.40$ kHz (here and in the rest of the paper, all errors are given as s.e.m.). We then fix this in performing independent fits to the squeezed-state data for $\Delta\phi = 0$ and $\Delta\phi = \pi/2$. Each of these fits allows us to extract an estimate for the squeezing parameter r. For both the squeezed and anti-squeezed quadratures we obtain consistent values with a mean of $r = 1.08 \pm 0.03$, corresponding to 9.4 dB reduction in the squeezed quadrature variance. The inset shows the spin population as a function of the SDF phase ϕ_D with

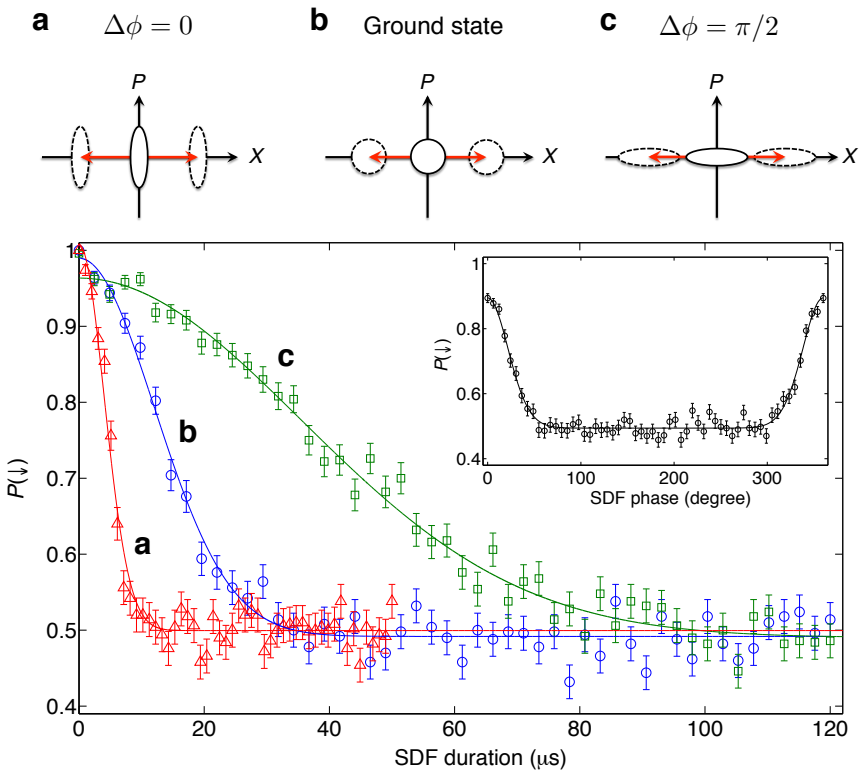

Figure 7.2: **Spin-population evolution due to spin-motion entanglement.** Projective measurement of the spin in the $\hat{\sigma}_z$ basis as a function of SDF duration. **a**, Forces parallel to the squeezed quadrature (red triangles). **b**, An ion initially prepared in the motional ground state (blue circles). **c**, Forces parallel to the anti-squeezed quadrature (green squares). The inset shows a scan of the phase of the SDF for an initial squeezed state with the force duration fixed to 20 μs. Each data point is the result of > 300 repetitions of the experimental sequence. The given error bars indicate one standard error of the mean, and are generated under the assumption that the dominant source of fluctuations is quantum projection noise.

the SDF duration fixed to 20 μs. This is also fitted using the same equation described above, and we obtain $r = 1.13 \pm 0.03$.

The loss of overlap between the two wavepackets indicates that a SWES has been created. In order to verify that these states are coherent superpositions, we recombine the wavepackets by applying a second "return" SDF pulse for which the phase of both the red and blue sideband laser frequency components is shifted by π relative to the first. This reverses the direction of the force applied to the motional states for both the $|+\rangle$ and $|-\rangle$ spin states. In the ideal case a state displaced to $\alpha(\tau_1)$ by a first SDF pulse of duration τ_1 has

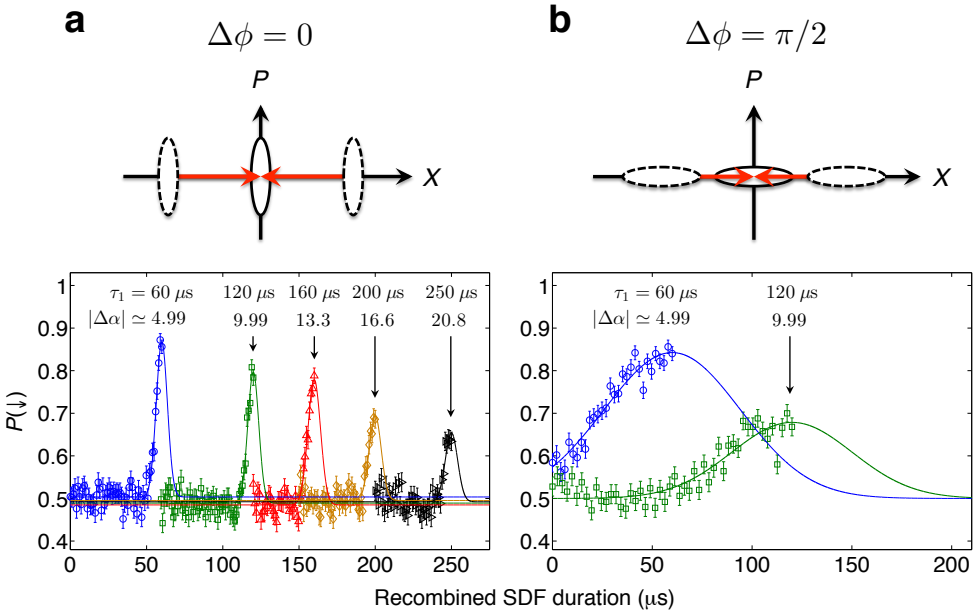

Figure 7.3: **Revival of the spin coherence.** Spin populations as a function of the duration of the second SDF pulse with the spin phase shifted by π relative to the first pulse. **a**, Forces parallel to the squeezed quadrature. **b**, Forces parallel to the anti-squeezed quadrature. In all cases an increase in the spin population is seen at the time when the two motional states are overlapped, which corresponds to the time τ_1 used for the first SDF pulse. The value of τ_1 and the corresponding $|\Delta\alpha|$ calculated from the measured Rabi frequency are written above the revival of each dataset. The fractional error on the mean of each of the estimated $|\Delta\alpha|$ is approximately 3%. The solid lines are fitted curves using the same form as using in the fits in Fig. 7.2 with the overlap function $X(\delta\alpha, \xi)$. The obtained values of r are consistent with the data in Fig. 7.2. The definition of error bars is the same as in Fig. 7.2.

a final displacement of $\delta\alpha = \alpha(\tau_1) - \alpha(\tau_2)$ after the return pulse of duration τ_2. For $\tau_1 = \tau_2$, $\delta\alpha = 0$ and the measured probability of finding the spin state in $|\downarrow\rangle$ is 1. In the presence of decoherence and imperfect control, the probability with which the ion returns to the $|\downarrow\rangle$ state will be reduced. In Fig. 7.3 we show revivals in the spin coherence for the same initial squeezed vacuum state as was used for the data in Fig. 7.2. The data include a range of different τ_1. For the data where the force was applied along the squeezed axis of the state ($\Delta\phi = 0$), partial revival of the coherence is observed for SDF durations up to 250 μs. For $\tau_1 = 250$ μs the maximum separation of the two distinct oscillator wavepackets is $|\Delta\alpha| > 19$, which is 56 times the

r.m.s width of the squeezed wavepacket in phase space. The amplitude of revival of this state is similar to what we observe when applying the SDF to a ground state cooled ion. The loss of coherence as a function of the displacement duration is consistent with the effects of magnetic-field induced spin dephasing and motional heating [Turchette 00b, Hempel 13]. When the force is applied along the anti-squeezed quadrature ($\Delta\phi = \pi/2$), we observe that the strength of the revival decays more rapidly than for displacements with $\Delta\phi = 0$. Simulations of the dynamics using a quantum Monte-Carlo wavefunction approach including sampling over a magnetic field distribution indicate that this is caused by shot-to-shot fluctuations of the magnetic field (see Chapter 7.2.5).

Second Measurement

We are also able to monitor the number state distributions of the motional wavepackets as a function of the duration of the SDF. This provides a second measurement of the parameters of the SDF and the initial squeezed wavepacket which has similarities with the homodyne measurement used in optics [Breitenbach 97, Ourjoumtsev 07]. In order to do this, we optically pump the spin state into $|\downarrow\rangle$ after applying the SDF. This procedure destroys the phase relationship between the two motional wavepackets, resulting in the mixed oscillator state $\hat{\rho}_{\text{mixed}} = \left(|\alpha,\xi\rangle\langle\alpha,\xi| + |-\alpha,\xi\rangle\langle-\alpha,\xi|\right)/2$ (we estimate the photon recoil during optical pumping results in a reduction in the fidelity of our experimental state relative to $\hat{\rho}_{\text{mixed}}$ by $< 3\%$, which would not be observable in our measurements). The two parts of this mixture have the same number state distribution, which is that of a displaced-squeezed state [Caves 81, Yuen 76]. In order to extract this distribution, we drive Rabi oscillations on the blue-sideband transition [Meekhof 96] and monitor the subsequent spin population in the $\hat{\sigma}_z$ basis. Figure 7.4 shows this evolution for SDF durations of $\tau = 0$, 30, 60 and 120 µs. For $\tau = 30$ and 60 µs, the results from displacements applied parallel to the two principal axes of the squeezed state are shown ($\Delta\phi = 0$ and $\pi/2$). We obtain the number state probability distribution $p(n)$ from the spin state population by fitting the data using a form $P(\downarrow) = bt + \frac{1}{2}\sum_n p(n)(1 + e^{-\gamma t}\cos(\Omega_{n,n+1}t))$, where t is the blue-sideband pulse duration, $\Omega_{n,n+1}$ is the Rabi frequency for the transition between the $|\downarrow\rangle|n\rangle$ and $|\uparrow\rangle|n+1\rangle$ states and γ is a phenomenological decay parameter [Meekhof 96, Leibfried 03a]. The parameter b accounts for gradual pumping of population into the state $|\uparrow\rangle|0\rangle$ due to frequency noise on our laser [Di Fidio 00, Kienzler 15a]. It is negligible when $p(0)$ is small. The resulting $p(n)$ are then fitted using the theoretical form for the displaced-squeezed states (see Chapter 7.2.6). The number state distributions show a clear dependence on the phase of the force, which is also reflected in the spin population evolution. Figure shows the Mandel Q parameters of the experimentally obtained number state distributions, defined as $Q = \langle(\Delta n)^2\rangle/\langle n\rangle - 1$ in which $\langle(\Delta n)^2\rangle$

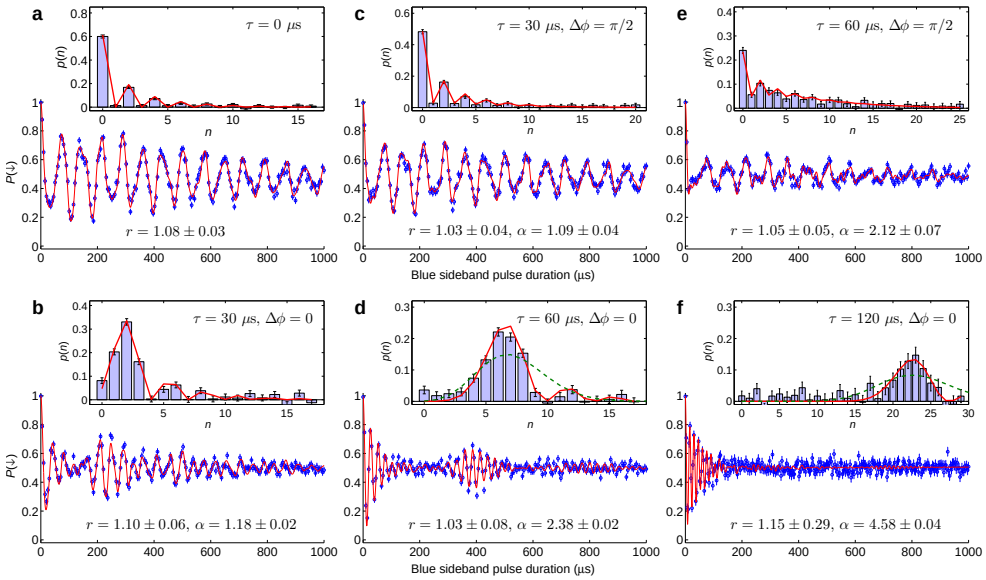

Figure 7.4: **Evolution of displaced-squeezed state mixtures.** The observed blue-sideband oscillations and the corresponding number state probability distributions for the SDF applied along the two principal axes of the squeezed state and with different durations. **a**, Initial squeezed vacuum state. **b, d, f**, Forces parallel to the squeezed quadrature. **c, e**, Forces parallel to the anti-squeezed quadrature. For $\tau = 30$ μs the obtained parameters are consistent within statistical errors. For $\tau = 60$ μs the displacement along the anti-squeezed quadrature (**e**) results in a large spread in the number state probability distribution, with the result that in the fitting r and α are positively correlated - the errors stated do not take account of this. We think that this accounts for the apparent discrepancy between the values of r and α obtained for $\tau = 60$ μs. The green-dashed line in the inset of **d** and **f** is the Poisson distribution for the same $\langle n \rangle$ as the created displaced-squeezed state mixture, which is given by $\langle n \rangle = |\alpha|^2 + \sinh^2 r$ [Caves 81]. Each data point is the average of 500 repeats of the experimental sequence. The definition of error bars is the same as in Fig. 7.2.

and $\langle n \rangle$ are the variance and mean of $p(n)$ respectively [Mandel 79]. The solid lines are the theoretical curves given by Caves [Caves 81] for $r = 1.08$, and are in agreement with our experimental results. For displacements along the short axis of the squeezed state (Fig. 7.4), the collapse and revival behaviour of the time evolution of $P(\downarrow)$ is reminiscent of the Jaynes-Cummings Hamiltonian applied to a coherent state [Haroche 06], but it exhibits a higher number of oscillations before the "collapse" for a state of the same $\langle n \rangle$. This is surprising since the statistics of the state is not sub-Poissonian. We attribute this to the fact that this distribution is more peaked than that of a coherent state with

the same $\langle n \rangle$, which is obvious when the two distributions are plotted over one another (Figs. 7.4(d) and 7.4(f)). The increased variance of the squeezed state then arises from the extra populations at high n, which are too small to make a visible contribution to the Rabi oscillations. For the squeezing parameter in our experiments sub-Poissonian statistics would only be observed for $|\alpha| > 3$. For $\tau = 120$ µs we obtain a consistent value of r and $|\alpha| = 4.6$ only in the case where we include a fit parameter for scaling of the theoretical probability distribution, obtaining a fitted scaling of 0.81 ± 0.10 (see Chapter 7.2.6). The reconstruction of the number state distribution is incomplete, since we cannot extract populations with $n > 29$ due to frequency crowding in the $\sqrt{n+1}$ dependence of the Jaynes-Cummings dynamics. As a result, we do not include these results in Fig. . Measurement techniques made in a squeezed-state basis [Kienzler 15a] could avoid this problem, however these are beyond our current experimental capabilities for states of this size.

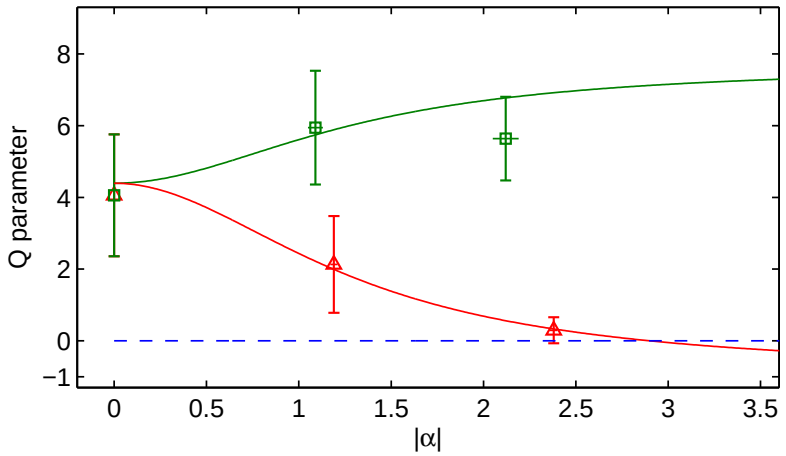

Figure 7.5: **Mandel Q parameter for the displaced-squeezed states.** Shown are the results for displacements along the squeezed quadrature (red triangles) and the anti-squeezed quadrature (green squares). All the values are calculated from the experimental data given in Fig. 7.4, taking the propagation of error into account. The solid lines are theoretical curves for displacements along the squeezed (red) and anti-squeezed (green) quadratures of an initial state with $r = 1.08$. The values of $|\alpha|$ are obtained from fits to the respective $p(n)$ (Fig. 7.4), with error bars comparable to the size of the symbol. The point at $|\alpha| = 0$ is the squeezed vacuum state.

7.2.4 Validity of Lamb-Dicke Approximation

The 729 nm laser beam enters the trap at 45 degrees to the z axis of the trap resulting in a Lamb-Dicke parameter of $\eta \simeq 0.05$ for the axial mode. For

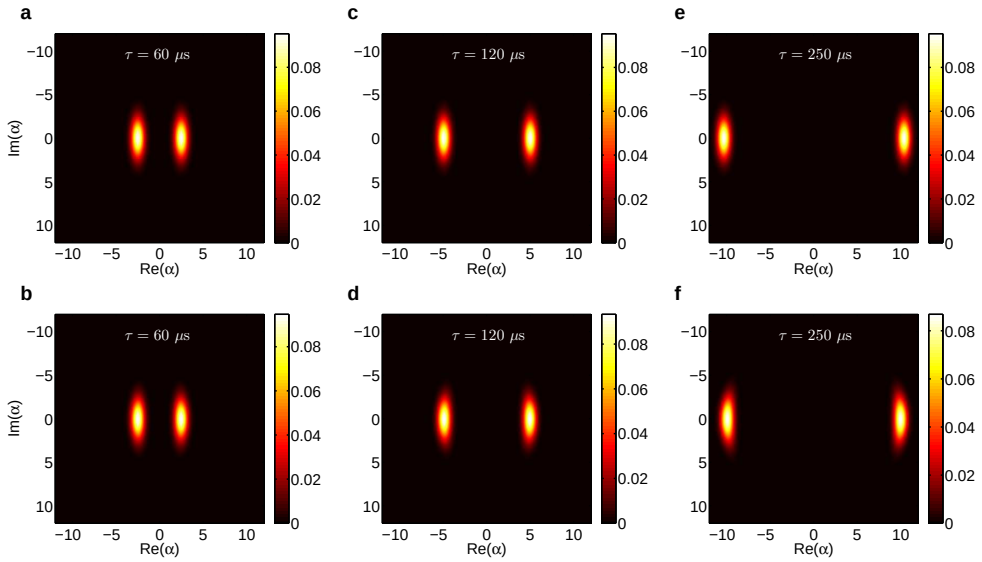

Figure 7.6: **Quasi-probability distributions for displaced-squeezed states in phase space using LDA and non-LDA: a, c, e**, The simulation results using LDA with different SDF durations. **b, d, f**, The results simulated using the full Hamiltonian.

this Lamb-Dicke parameter, we have verified whether for displacements up to $|\alpha| = 9.75$ the dynamics can be well described with the Lamb-Dicke Approximation (LDA). We simulate the wavepacket dynamics using the interaction Hamiltonian with and without LDA. In the simulation, we apply the SDF to an ion prepared in $|\downarrow\rangle|\xi\rangle$. The interaction Hamiltonian for a single trapped ion coupled to a single-frequency laser field can be written as [Leibfried 03a]

$$\hat{H}_I = \frac{\hbar}{2}\Omega_0\hat{\sigma}_+\exp\{i\eta(\hat{a}\,e^{-i\omega_z t} + \hat{a}^\dagger\,e^{i\omega_z t})\}e^{i(\phi-\delta t)} + \text{h.c.},$$

where Ω_0 is the interaction strength, $\hat{\sigma}_+ = |\uparrow\rangle\langle\downarrow|$, $\hat{a}$ and $\hat{a}^\dagger$ are motional annihilation and creation operators, ω_z is the vibrational frequency of the ion, ϕ is the phase of the laser, and $\delta = \omega_l - \omega_a$ the detuning of the laser from the atomic transition. In the laboratory, the application of the SDF involves simultaneously driving both the blue and red sideband transitions resonantly resulting in the Hamiltonian $\hat{H}_{\text{tot}} = \hat{H}_{\text{bsb}} + \hat{H}_{\text{rsb}}$, where $\delta = \omega_z$ in $\hat{H}_{\text{bsb}}$ and $\delta = -\omega_z$ in $\hat{H}_{\text{rsb}}$. Starting from $|\downarrow\rangle|\xi\rangle$, the evolution of the state can not be solved analytically. We perform a numerical simulation in which we retain only the resonant terms in the Hamiltonian. Figure 7.6 shows the quasi-probability distributions in phase space for chosen values of the SDF duration τ. These are compared to results obtained using the LDA. For $\tau = 60$ μs both cases are similar, resulting in $|\alpha| \simeq 2.4$. For $\tau = 250$ μs the squeezed state wavepackets are slightly distorted and the displacement is 4 % smaller for the

full simulation than for the LDA form. Considering the levels of error arising from imperfect control and decoherence for forces of this duration, we do not consider this effect to be significant in our experiments.

7.2.5 Simulations for the Coherence of Squeezed Cats

After creating SWESs, we deduce that coherence is retained throughout the creation of the state by applying a second SDF pulse to the ion, which recombines the two separated wavepackets and disentangles the spin from the motion. The revival in the spin coherence is not perfect due to decoherence and imperfect control in the experiment. One dominant source causing decoherence of the superpositions is spin decoherence due to magnetic field fluctuations. We have performed quantum Monte-Carlo wavefunction simulations to investigate the coherence of the SWES in the presence of such a decoherence mechanism. We simulate the effect of a sinusoidal fluctuation of the magnetic field on a timescale long compared to the duration of the coherent control sequence, which is consistent with the noise which we observe on our magnetic field coil supply and from ambient fluctuations due to electronics equipment in the room. The amplitude of these fluctuations is set to $\simeq 2.2$ mG, giving rise to the spin coherence time of ≈ 180 μs which we have measured using Ramsey experiments on the spin alone. Since the frequency of fluctuations is slow compared to the sequence length, we fix the field for each run of the simulation, but sample its value from a probability distribution derived from a sinusoidal oscillation. In Fig. 7.7 we show the effect of a single shot taken at a fixed qubit-oscillator detuning of 1.5 kHz, while in Fig. 7.8 we show the average over the distribution. In both figures results are shown for the SDF applied along the two principal axes of the squeezed vacuum state as well as for the motional ground state using force durations of 60 and 120 μs. We also show the results of applying the second SDF pulse resulting in partial revival of the spin coherence. It can be clearly seen that when the SDF is applied along the anti-squeezed quadrature, the strength of the revival decays more rapidly, and $P(\downarrow)$ oscillates around 0.5. This effect can be seen in the data shown in Fig. 7.3.

7.2.6 Number State Probability Distributions for the Displaced-Squeezed State

For Fig. 7.4, we characterize the probability distribution for the number states of the oscillator. This is performed by driving the blue-sideband transition $|\downarrow\rangle|n\rangle \leftrightarrow |\uparrow\rangle|n+1\rangle$ and fitting the obtained spin population evolution using

$$P(\downarrow) = bt + \frac{1}{2}\sum_n p(n)(1 + e^{-\gamma t}\cos(\Omega_{n,n+1}t)), \tag{7.15}$$

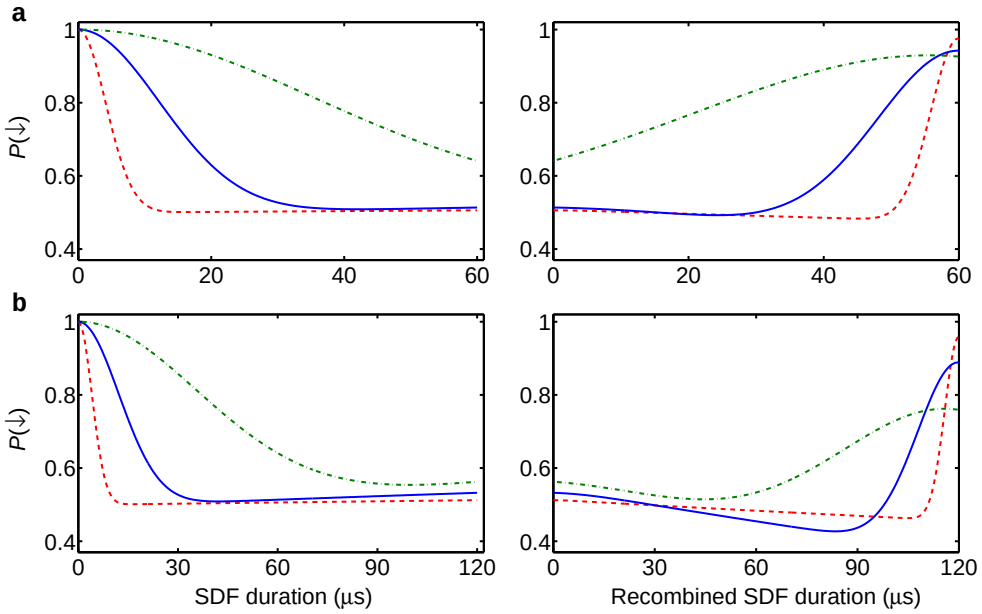

Figure 7.7: **Coherence of cat states with fixed magnetic field noise:** The magnetic-field-induced energy-level-shift of 1.5 kHz is used in this simulation. **a**, The duration of both SDF pulses is 60 μs. **b**, The duration of both SDF pulses is 120 μs. Red-dashed and green-dash-dot curves show the SDF aligned along the squeezed and anti-squeezed quadratures. The blue trace is for the SDF applied to a ground state cooled ion.

where t is the blue-sideband pulse duration, $p(n)$ are the number state probabilities for the motional state we concern, and γ is an empirical decay parameter [Meekhof 96, Leibfried 03a]. In the results presented here we do not scale this decay parameter with n as was done by [Meekhof 96]. We have also fitted the data including such a scaling and see consistent results. The Rabi frequency coupling $|\downarrow\rangle|n\rangle$ to $|\uparrow\rangle|n+1\rangle$ is $\Omega_{n,n+1} = \Omega_0|\langle n|e^{i\eta(\hat{a}^\dagger+\hat{a})}|n+1\rangle| = \Omega_0 e^{-\eta^2/2}\eta L_n^1(\eta^2)/\sqrt{n+1}$. For small n, this scales as $\sqrt{n+1}$, but since the states include significant populations at higher n we use the complete form including the generalized Laguerre polynomial $L_n^1(x)$. The parameter b in the first term accounts for a gradual pumping of population into the state $|\uparrow\rangle|0\rangle$ which is not involved in the dynamics of the blue-sideband pulse [Di Fidio 00, Kienzler 15a]. This effect is negligible when $p(0)$ is small.

After extracting $p(n)$ from $P(\downarrow)$, we fit it using the number state probability

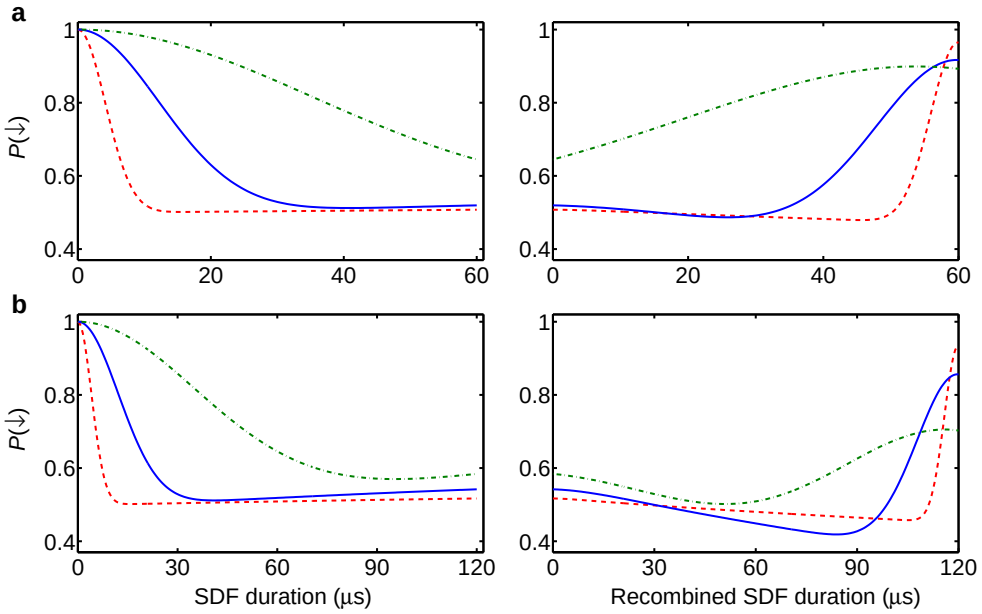

Figure 7.8: **Coherence of cat states with a magnetic field fluctuation distribution:** Assuming the magnetic field exhibits a 50-Hz sinusoidal pattern with an amplitude of 2.2 mG, this plot shows the simulation results by taking an average over 100 samples on the field distribution. **a**, The duration of both SDF pulses is 60 μs. **b**, The duration of both SDF pulses is 120 μs. Definitions of the curve specification are the same as Fig. 7.7.

distribution for the displaced-squeezed state [Gerry 05],

$$p(n) = \kappa \frac{(\frac{1}{2}\tanh r)^n}{n!\cosh r} \exp\left[-|\alpha|^2 - \frac{1}{2}(\alpha^{*2}e^{i\phi_s} + \alpha^2 e^{-i\phi_s})\tanh r\right] \times \left|H_n\left[\frac{\alpha\cosh r + \alpha^* e^{i\phi_s}\sinh r}{\sqrt{e^{i\phi_s}\sinh 2r}}\right]\right|^2$$

where κ is a constant which accounts for the infidelity of the state during the application of SDF and the $H_n(x)$ are the Hermite polynomials. The direction of the SDF is aligned along either the squeezing quadrature or the anti-squeezing quadrature of the state. Therefore, we set $\arg(\alpha) = 0$ and fix $\phi_s = 0$ and π for fitting the data of the short axis and the long axis of the squeezed state, respectively. This allows us to obtain the values of r and $|\alpha|$ for the state we created. For the cases of smaller displacements (from Figs. 7.4(a) to (e)), we set $\kappa = 1$. For the data set of $|\alpha| \simeq 4.6$ (Fig. 7.4(f)), κ is a fitting parameter which gives us a value of 0.81 ± 0.1. We note that in this case 4 % of the expected population lies above $n = 29$ but we are not able to extract these populations from our data.

The Mandel Q parameter [Mandel 79], defined as

$$Q = \frac{\langle (\Delta n)^2 \rangle - \langle n \rangle}{\langle n \rangle}.$$

where $\langle n \rangle$ and $\langle (\Delta n)^2 \rangle$ are the mean and variance of the probability distribution. For a displaced-squeezed state these are given by Caves [Caves 81] as

$$\begin{aligned} \langle (\Delta n)^2 \rangle &= \left| \alpha \cosh r - \alpha^* e^{i\phi_s} \sinh r \right|^2 + 2 \cosh^2 r \sinh^2 r, \\ \langle n \rangle &= |\alpha|^2 + \sinh^2 r. \end{aligned}$$

These forms were used to produce the curves given in Fig. 7.5.

7.2.7 Possible Applications

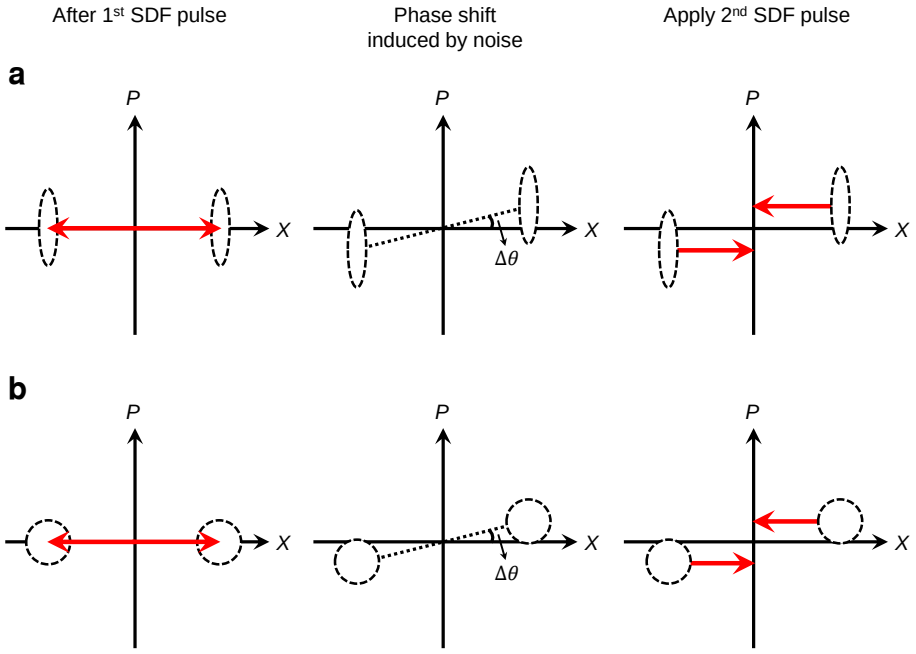

Figure 7.9: **Possible application of using SWESs for interferometry: a**, Use of squeezed state wavepackets. **b**, Use of ground state wavepackets. The first SDF pulse is used to create a spin-motion entangled state. In the middle, a small phase shift $\Delta\theta$ is induced by shot-to-shot fluctuation in the oscillator frequency before the application of the second SDF pulse, which recombines the two distinct oscillator wavepackets.

These novel states present new possibilities both for metrology and for continuous variable quantum information. For the sensitive measurements, an example is illustrated in Fig. 7.9 where we compare an interferometry experiment involving the use of a SWES versus a more standard Schrödinger's cat state based on coherent states. In both cases the superposed states have a separation of $|2\alpha|$ obtained using a SDF. For the SWES this force is aligned along the squeezed quadrature of the state. The interferometer is closed by inverting the initial SDF, resulting in a residual displacement which in the ideal case is zero. One form of noise involves a shot-to-shot fluctuations in the oscillator frequency. On each run of the experiment, this would result in a small phase shift $\Delta\theta$ arising between the two superposed motional states. As a result, after the application of the second SDF pulse the residual displacement would be $\alpha_R = 2i\alpha\sin(\Delta\theta/2)$, which corresponds to the states being separated along the P axis in the rotating-frame phase space. The final state of the system would then be $|\psi(\alpha_R)\rangle$ with a corresponding state overlap given by $X(\alpha_R, \xi)$. Therefore the contrast will be higher for the SWES (Fig. 7.9(a)) than for the coherent Schrödinger's cat state (Fig. 7.9(b)) by a factor

$$\exp\left[-2\left|\alpha_R\right|^2\left(e^{-2r}-1\right)\right].$$

While in our experiments other sources of noise dominate, in other systems such oscillator dephasing may be more significant.

In quantum information with continuous variables, the computational basis states are distinguishable because they are separated in phase space by $|\Delta\alpha|$ and thus do not overlap [Weedbrook 12, Gottesman 01, Bartlett 02]. The decoherence times of such superpositions typically scale as $1/|\Delta\alpha|^2$ [Turchette 00b]. The use of states squeezed along the displacement direction reduces the required displacement for a given overlap by e^r, increasing the resulting coherence time by e^{2r} which is a factor of 9 in our experiments. We therefore expect these states to open up new possibilities for quantum state engineering and control.

Chapter 8

Summary and Outlook

8.1 Summary

This thesis described work towards development of a system for investigations of quantum information science with two species of ion. In close collaboration with Daniel Kienzler and Ben Keitch, the ion trap, optics and computer control systems were set up. A number of theoretical studies and experimental characterizations of beryllium ions were performed. Quantum states of motion such as coherent states, squeezed states, and displaced-squeezed states have been generated by a new method [Kienzler 15a, Kienzler 15b], and also entanglement of the spin and squeezed motion of a single ion have been created [Lo 15]. Both experiments were carried out with a single calcium ion.

The initial step of all the experiments is the design, setup, calibration, and characterization. The major concern of the trapped-ion quantum processor is the scalability. How to increase the number of qubits while maintaining high-fidelity control of them has drawn many research groups' attention. The architecture for a large-scale ion-trap quantum computer [Kielpinski 02, Wineland 98] requires linear ion crystals which are composed of two ion species and moved in segmented trap arrays. Our segmented trap was designed towards this goal, where there are three experimental zones, two zones for splitting/combining/transporting ions, and two zones for loading (Chapter 4). Other new features were added to our trap design, for example the segmented shim electrodes are used in order to compensate the stray fields in different regions of the trap. The imaging system was also designed for monitoring and detecting two ion species simultaneously that increases the flexibility for the complex experiments, for example two ion species gates or quantum simulation of an open quantum system.

We also constructed and characterized all-solid-state continuous-wave laser systems for photoionization loading, cooling and quantum state manipulation of beryllium ions [Lo 14]. The wavelength required for photoionization of

neutral beryllium atoms (235 nm) is created by two stages of second-harmonic generation (SHG) using PPKTP and BBO nonlinear crystals placed inside resonant cavities. In the first stage, we have demonstrated stable generation of 400 mW at 470 nm starting from 560 mW at 940 nm. In the second stage, with 140 mW input to the cavity, an output power of 28 mW at 235 nm is obtained. For quantum control of beryllium ions, three laser wavelengths at 313 nm are produced by sum-frequency generation and subsequent SHG, starting from four infrared fiber lasers. Up to 7.2 W at 626 nm have been generated from 8.5 W at 1051 nm and 8.3 W at 1551 nm. The red light is then frequency-doubled in bowtie cavities using BBO crystals. With an incident power of 3.8 W, we obtain 1.9 W of UV light at 313 nm, which may help in the long-term goal of fault-tolerant quantum computation using stimulated Raman transitions because the difficulties derived from the trade-off between spontaneous scattering and quantum-gate speed can be overcome with high-intensity laser beams.

For the characterization of ions, most of the calcium part have been covered in [Kienzler 15b]. In this thesis, we performed some diagnostic experiments for the beryllium ion. First, the readout error was analyzed by performing the Rabi flops on different qubit states. We found that a high readout fidelity can be achieved with shelving the dark state ion to another "darker" state. Second, the optical pumping efficiency was optimized and compared with the theoretical predictions. Third, with an axial vibrational frequency of 2.7 MHz we found that 98 % ground state preparation ($\langle n \rangle = 0.02$) after optimization of the resolved sideband cooling can be achieved. Fourth, we performed the Ramsey experiment to examine the coherence of the qubit. For the magnetic-field-sensitive qubit, the coherence time is approximately 105 μs without any magnetic field stabilization. A coherence time of ≈ 1.5 s was observed for the field-independent qubit. These results provide a basis for future work with multiple ions.

The main problem we had was the micromotion of the ion. For controlling a mixed-species ion chain, the micromotion compensation is an important task. We use different techniques to minimize the micromotion for both calcium and beryllium ions and to understand its behavior in our trap. Because calcium and beryllium ion have different intrinsic micromotion amplitude, it is not possible to use the same shim voltage setting to minimize their micromotion along the direction of the probe field, which is at 45° with respect to the axial direction. Using the RF tickle method, we could find an optimal shim voltage setting for the calcium ion. Under this situation, the calcium ion should be at the pseudopotential minimum. However, this optimal setting is not for beryllium fluorescence detection due to the projection of intrinsic micromotion on the probe field direction.

The calcium ion has lower intrinsic micromotion, which does not influence

the fluorescence detection too much, so we just need to minimize the excess micromotion by applying additional compensation fields. The main result covered in this thesis is the generation of squeezed Schrödinger's cat states. This novel quantum state is created for the first time. These relied on newly developed techniques, dissipative quantum state preparation. Artificial dissipation for the qubit is introduced to create an efficient irreversible damping channel for the ion's energy. By engineering the spin-oscillator coupling, this results in effective relaxation of the motional state of the ion. This engineered damping processes keep the final state, which is the steady state of the dynamics, protected from other unwanted relaxation mechanisms. Using this technique we were able to prepare the coherent, the squeezed vacuum, and the displaced-squeezed states for an ion's motion. This toolbox for generating and protecting quantum harmonic oscillator states is transferrable to any physical system and may facilitate quantum computation with continuous variables [Gottesman 01].

In the second experiment based on the previous one, we demonstrated superpositions composed of squeezed wavepackets, which we generated by applying an internal-state dependent force to a single trapped ion initialized in a squeezed vacuum state with 9 dB reduction in the quadrature variance. This allowed us to characterize the initial squeezed wavepacket by monitoring the onset of spin-motion entanglement, and to verify the evolution of the number states of the oscillator as a function of the duration of the force. In both cases, we observed clear differences between displacements aligned with the squeezed and anti-squeezed axes. We observed coherent revivals when inverting the state-dependent force after separating the wavepackets by more than 19 times the ground state root-mean-square extent, which corresponds to 56 times the r.m.s. extent of the squeezed wavepacket along the displacement direction. Aside from their fundamental nature, these states may be useful for quantum metrology [Munro 02], quantum state engineering, or quantum information processing [Weedbrook 12, Gottesman 01, Bartlett 02] in a new regime.

8.2 Outlook

Using the system that has been built, there are still plenty of interesting experiments we can do. Here some ongoing and upcoming experiments are listed:

The first one is the transport gate [Leibfried 07]. Typically quantum gate operations are implemented by shining laser pulses to the ions, which are statically in space. The other way around, one can also keep the laser on at certain place and transport the ions through it. For a large-scale trapped-ion quantum processor, a big advantage of the transport gate scheme is that the complexity of the laser systems could be significantly reduced. It may also allow for efficient

use of one and the same laser beam in many parallel operations. Recently, we demonstrated single-qubit gate operations as well as the Ramsey experiment using transported calcium and beryllium ions individually [de Clercq 15]. The two-qubit transport gates will be the next.

The second experiment we will pursue is relevant to quantum simulation of an open quantum system. In the beginning we will start from a small-scale quantum system, consisting of one beryllium ion and one calcium ion. The quantum system is provided by the internal degree of freedom of beryllium ion which we will couple to the motional degree of freedom represent the environment, continuously damped the calcium ion. The motional degree of freedom of beryllium ion is controlled by the calcium ion because the motional states of two ions in the same trap are shared. For quantum simulations, the ability to scatter photons from one "environment" ion (calcium) while preserving internal states of the other "system" ion (beryllium) may allow us to engineer controlled environments consisting of either the shared motional states, or of the internal states of the "environment" ion species.

One possibility is to continuously cool the calcium ion, and simultaneously couple the beryllium to the motion using either a Mølmer-Sørensen type coupling or a Jaynes-Cummings interaction. This should lead to decoherence of a qubit stored in the beryllium ion. The idea here is that we should be able to vary the cooling (damping) rate of the environment and the coupling of the beryllium ion to this environment in order to observe the transition between Markovian and non-Markovian quantum dynamics. This means that one is able to control the information flow between the system and the environment. If the damping rate of the motional mode is made much smaller than the coupling rate, the open quantum system will be in the non-Markovian regime, meaning that the motion remembers the ion coupling to the quantum system. By contrast, if the damping rate of the motional mode is larger than the coupling rate, it induces Markovian processes in which the motion rapidly loses information about the system-environment interaction. Many measures for the degree of non-Markovian behavior of quantum processes in open systems have been proposed [Wolf 08, Breuer 09, Rivas 10]. In our case, we still have to investigate in detail how to measure the degree of non-Markovianity for the beryllium spin.

The same techniques used in this experiment could be applied to an implementation of two-qubit gates using different atomic species [Ballance 15]. Performing an entangling gate on two species of ions is of interest for several reasons. For trapped ion quantum repeaters made up of communication qubits and memory qubits, the entanglement between the communication qubits from two separate registers are created via the photonic channel, and then the quantum information within the communication qubits is coherently mapped to the memory qubits using standard entangling gate operations [Monroe 13].

However, the communication qubits need to be well isolated from the memory qubits because the scattering light from the excitation laser acting on the communication qubits might destroy the information stored in memory qubits. The best solution might be to use two different ion species to avoid the crosstalk. Even for quantum computation which does not necessarily require remote entanglement, the two species quantum gates are still useful in the error correction codes, where we need entanglement between the primary qubit with ancilla qubits, which are then measured by state-dependent fluorescence [Chiaverini 04]. For the same concern, the scattering light or the emitted photons when performing the measurement on the ancilla qubits might disturb the primary qubit. Therefore, using two atomic species can benefit the fidelity of quantum operations.

The third future experiment is to measure the Wigner function of Schrödinger's cat states. So far all experiments on Schrödinger's cat states performed using trapped ions have involved entanglement between the oscillator state and the internal electronic states of the ion. The wavefunction has the form of $|\psi\rangle = \frac{1}{\sqrt{2}}(|+\rangle|\alpha\rangle - |-\rangle|-\alpha\rangle)$, where $|\pm\rangle$ are the eigenstates of $\hat{\sigma}_x$ Pauli matrix, and $|\pm\alpha\rangle$ are the coherent states displaced to different directions. In order to observe interference fringes characteristic of a quantum superposition in the Wigner tomography [Deleglise 08, Vlastakis 13], the wavefunction written in the $\hat{\sigma}_z$ basis is $|\psi\rangle = \frac{1}{2}[|\uparrow\rangle(|\alpha\rangle - |-\alpha\rangle) + |\downarrow\rangle(|\alpha\rangle + |-\alpha\rangle)]$. In principle, we can decouple the motion from the spin by measurement. When we perform a projective measurement on $|\downarrow\rangle$, depending on whether we detect photons or not we know the corresponding cat state. We can post select the events without photon scattering, which means the cat is still alive, and then perform the state tomography to reconstruct the Wigner function for the motional state.

The fourth experiment we plan to perform would be the use of a single beryllium ion "qubit" interacting with an environment of calcium spins, which with appropriate couplings could realize a spin-bath model [Prokofiev 00]. Alternatively, interactions between the beryllium qubit and multiple motional modes may be used to realize spin-boson physics [Porras 08]. Other areas of investigation include the use of engineered environments for quantum state engineering, for example multi-mode squeezed state preparation [Kienzler 15b] and stabilizing Schrödinger's cat states [de Matos Filho 96, Roy 15].

Appendix A

Matrix Elements for the Electric-Quadrupole Interaction

As mentioned in Chapter 2.2, here shows the starting point how to obtain the matrix elements for the electric-quadrupole interaction. The $(\mathbf{I}\cdot\mathbf{J})^2$ term in Eq. (2.4) can be simplified as

$$\begin{aligned}(\mathbf{I}\cdot\mathbf{J})^2 &= (I_zJ_z)^2+\frac{1}{2}(I_zJ_z)(I_+J_-+I_-J_+)+\frac{1}{2}(I_+J_-+I_-J_+)(I_zJ_z)\\ &\quad+\frac{1}{4}(I_+J_-)^2+\frac{1}{4}(I_-J_+)^4+\frac{1}{4}(I_+I_-J_-J_+)+\frac{1}{4}(I_-I_+J_+J_-)\end{aligned}$$

To calculate the matrix elements, one can use the following relations

$$\begin{aligned}J_\pm|J\ m_J\rangle &= \hbar\sqrt{(J\pm m_J+1)(J\mp m_J)}|J\ m_J\pm1\rangle\\ I_\pm|I\ m_I\rangle &= \hbar\sqrt{(I\pm m_I+1)(I\mp m_I)}|I\ m_I\pm1\rangle\end{aligned}$$

Appendix B

Lens Data

Table B.1: The data of the lenses in the imaging system are provided. d is the distance from the current surface to the next one.

Surface number	Radius of curvature (mm)	d 313 nm path (mm)	d 397 nm path (mm)
Object (ion)	Inf	30.918	30.918
1	Inf	5.985	5.985
2	-60.491	9.4	9.4
3	-29.501	0.223	0.223
4	-128.613	3.35	3.35
5	Inf	2.298	2.298
6	-117.496	7.2	7.2
7	-56.446	0.339	0.339
8	-290.973	6.25	6.25
9	-80.576	0.966	0.966
10	311.817	14	14
11	-118.789	0.5	0.5
12	Inf	42.038	42.038
13	Inf	6.35	6.35
14	Inf	650.602	697.495
15	-13.333	3	8.8
16	-19.66	30.398	60.211
17	11.657	6.6	6.6
18	9.934	180.751	98.244
Image (camera or PMT)	Inf		

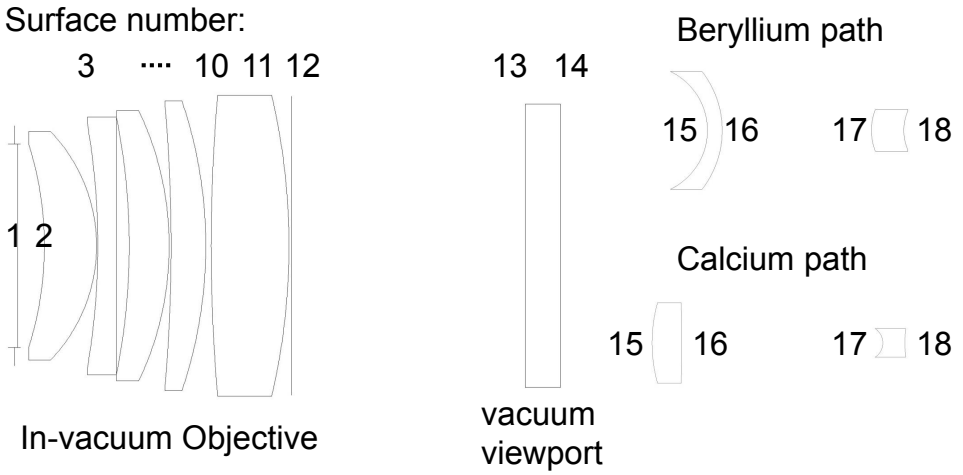

Figure B.1: The lens layouts. The in-vacuum objective is common for beryllium (313 nm) and calcium (397 nm) ions. Outside the vacuum, there is one lens pair in each path.

Appendix C

Second-Harmonic-Generation Efficiency

Here we give the expressions used for the theoretical calculation of the second-harmonic-generation efficiencies plotted in Figs. 5.4, 5.6 and 5.12. The values for the relevant parameters are given in Table C.1.

We start from the original equations from Boyd and Kleinman [Boyd 68] and rearrange them to formulate the conversion efficiency (in SI units [Risk 03]) as

$$\begin{aligned}\Gamma_{\text{eff}} &= \frac{P_{2\omega}}{P_{\omega}^2} \\ &= \frac{16\pi^2 d_{\text{eff}}^2}{\lambda^3 \epsilon_0 c n_\omega n_{2\omega}} l_{\text{c}} e^{-\left(\beta_\omega + \frac{\beta_{2\omega}}{2} l_{\text{c}}\right)} \times h(b, l_{\text{c}}, \beta_\omega, \beta_{2\omega}, \sigma, B) \end{aligned} \quad \text{(C.1)}$$

Here, $P_{2\omega}$ is the SHG power and P_ω the power in the fundamental wavelength at the crystal (the circulating power if a cavity is used); d_{eff} is an effective non-linear coefficient in units of $\text{m} \cdot \text{V}^{-1}$ (related but not identical to parameter d in [Boyd 68]); ϵ_0 and c are the vacuum permittivity and speed of light, respectively; λ is the pump wavelength, l_{c} the crystal length, β_ω ($\beta_{2\omega}$) the absorption coefficient of the fundamental (second harmonic) light in the crystal, and n_ω ($n_{2\omega}$) the refractive index of the crystal sampled by the light in the fundamental (second harmonic) wavelength.

h is a dimensionless function which depends on l_{c}, β_ω, $\beta_{2\omega}$, the confocal parameter $b = 2\pi n_\omega w^2/\lambda$ (where w is the waist radius of the pump beam, assumed to be at the center of the crystal), the wavevector mismatch σ (scaled by b) and the walk-off parameter $B = \rho(\theta, \lambda)\sqrt{\pi l_{\text{c}} n_\omega/(2\lambda)}$ where θ is the phase-matching angle and

$$\rho(\theta, \lambda) = \arctan\left(\frac{1 - \left(\frac{n_{\text{o},2\omega}}{n_{\text{e},2\omega}}\right)^2}{\cot\theta + \left(\frac{n_{\text{o},2\omega}}{n_{\text{e},2\omega}}\right)^2 \tan\theta}\right) \quad \text{(C.2)}$$

$n_{o,2\omega}$ ($n_{e,2\omega}$) is the refractive index for the second-harmonic light along the ordinary (extraordinary) crystal axis.

The explicit expression for h is,

$$\begin{aligned} h &= \frac{1}{4\xi}\int_{-\xi}^{\xi} d\tau' \int_{-\xi}^{\xi} d\tau \frac{1}{(1+i\tau)(1-i\tau')} \times \\ &\quad \exp\left\{ -\frac{b}{2}\left(\beta_\omega - \frac{\beta_{2\omega}}{2}\right)(\tau+\tau') + i\sigma(\tau-\tau') - \frac{B^2}{\xi}(\tau-\tau')^2 \right\} \end{aligned}$$

with $\xi = l_c/b$.

In a cavity the relation between the circulating power P_ω and the fundamental power $P_{\omega,0}$ pumped into it is given by [Targat 05]

$$\frac{P_\omega}{P_{\omega,0}} = \frac{T_1}{\left(1 - \sqrt{(1-T_1)(1-\epsilon)(1-(\Gamma_{\text{eff}}+\Gamma_{\text{abs}})P_\omega)}\right)^2} \tag{C.3}$$

where T_1 is the transmission of the in-coupling mirror, ϵ the round-trip loss in the cavity (excluding frequency conversion) and Γ_{abs} the absorption efficiency of the frequency-doubled light. If this absorption takes place only in the crystal and we consider the limit that frequency conversion occurs exclusively in its center, we can make the approximation

$$\Gamma_{\text{abs}} \approx \Gamma_{\text{eff}}\left(e^{\beta_{2\omega} l_c/2} - 1\right) \tag{C.4}$$

The power ratio given in Figs. 5.4, 5.6 and 5.12 is the ratio between the net power of the second-harmonic light at the output of the doubling cavity $P_{2\omega,\text{out}}$ and the fundamental power at the cavity input:

$$\eta_\lambda \equiv \frac{P_{2\omega,\text{out}}}{P_{\omega,0}} = \frac{P_{2\omega}(1-R_{2\omega})}{P_{\omega,0}} = \frac{P_\omega^2 \Gamma_{\text{eff}}(1-R_{2\omega})}{P_{\omega,0}} \tag{C.5}$$

where $R_{2\omega}$ is the reflection of the second-harmonic light at the output surface of the crystal. For the case of QPM in PPKTP and PPLN the second-harmonic light propagates perpendicularly to the surface, so there is no reflection. However, in the 470→235 nm and 626→313 nm cavities, the incidence is not normal to the (Brewster-cut) surface and the polarization of the second-harmonic light is along the vertical direction, so $R_{2\omega} > 0$ and not all the power generated in the doubled frequency is available at the cavity output. Equation (C.5) can be solved with the expressions above given the cavity-related parameters T_1, ϵ and w; the crystal parameters l_c, d_{eff}, $n_{\omega,2\omega}$, $\beta_{\omega,2\omega}$ and $R_{2\omega}$; the phase-matching parameters σ and θ; and the properties of the light matched into the cavity, λ and $P_{\omega,0}$.

Table C.1: Values used for calculating the expected conversion efficiency from the frequency-doubling cavities. d_{eff} is the effective non-linear coefficient of the crystals (for BBO, see Castech Inc. BBO Product information (2013). http://www.castech.com). Perfect phase matching is assumed in all cases, no absorption inside the BBO crystals and no walk-off inside the PPKTP.

	940→470 nm	470→235 nm	626→313 nm
l_{c}	30 mm	10 mm	10 mm
d_{eff}	9.5 pm/V	1.45 pm/V	2.08 pm/V
$n_\omega/n_{2\omega}$	1.8361/1.9149	1.6810/1.6408	1.6676/1.5888
w	50 µm	17.9 µm	20.7 µm
$\beta_\omega/\beta_{2\omega}$	0.3/14 m^{-1}	0	0
$R_{2\omega}$	0	22 %	20 %
σ	0	0	0
B	0	18.9	16.4
ϵ	2 %	0.7 %	0.9 %
T_1	14.5 %	0.9 %	1.6 %

Bibliography

[Aasi 13] J Aasi, J Abadie, BP Abbott, R Abbott, TD Abbott, MR Abernathy, C Adams, T Adams, P Addesso, RX Adhikari*et al.* *Enhanced sensitivity of the LIGO gravitational wave detector by using squeezed states of light.* Nature Photonics, vol. 7, pages 613–619, 2013.

[Acton 05] M Acton, K-A Brickman, PC Haljan, PJ Lee, L Deslauriers & C Monroe. *Near-perfect simultaneous measurement of a qubit register.* arXiv preprint quant-ph/0511257, 2005.

[Agrawal 07] Govind P Agrawal. Nonlinear fiber optics. Academic Press, 2007.

[Alsing 05] Paul M. Alsing, Jonathan P. Dowling & G. J. Milburn. *Ion Trap Simulations of Quantum Fields in an Expanding Universe.* Phys. Rev. Lett., vol. 94, page 220401, 2005.

[Alt 02] Wolfgang Alt. *An objective lens for efficient fluorescence detection of single atoms.* Optik - International Journal for Light and Electron Optics, vol. 113, pages 142 – 144, 2002.

[Amini 11] J Amini, J Britton, D Leibfried & D. J. Wineland. Micro-fabricated chip traps for ions, pages 395–420. Wiley-VCH Verlag GmbH & Co. KGaA, 2011.

[Ball 13] H. Ball, M. W. Lee, S. D. Gensemer & M. J. Biercuk. *A high-power 626 nm diode laser system for Beryllium ion trapping.* Review of Scientific Instruments, vol. 84, page 063107, 2013.

[Ballance 15] C. J. Ballance, V. M. Schafer, J. P. Home, D. J. Szwer, S. C. Webster, D. T. C. Allcock, N. M. Linke, T. P. Harty, D. P. L. Aude Craik, D. N. Stacey, A. M. Steane & D. M. Lucas. *Hybrid quantum logic and a test of Bell's inequality using two different atomic species.* arXiv:1505.04014, 2015.

[Barenco 95] A. Barenco, C. Bennett, R. Cleve, D. DiVincenzoand, N. Margolus, P. Shor, T. Sleator, J. Smolin & H. Weinfurter. *Elementary gates for quantum computation.* PRA, vol. 52, page 3457, 1995.

[Barreiro 11] Julio T. Barreiro, Markus Müller, Philipp Schindler, Daniel Nigg, Thomas Monz, Michael Chwalla, Markus Hennrich, Christian F. Roos, Peter Zoller & Rainer Blatt. *An open-system quantum simulator with trapped ions.* Nature, vol. 470, pages 486–491, 2011.

[Barrett 04] M. D. Barrett, J. Chiaverini, T. Schaetz, J. Britton, W. M. Itano, J. D. Jost, E. Knill, C. Langer, D. Leibfried, R. Ozeri & D. J. Wineland. *Deterministic quantum teleportation of atomic qubits.* Nature, vol. 429, pages 737–739, 2004.

[Bartlett 02] Stephen D. Bartlett, Hubert de Guise & Barry C. Sanders. *Quantum encodings in spin systems and harmonic oscillators.* Phys. Rev. A, vol. 65, page 052316, 2002.

[Barton 00] P. A. Barton, C. J. S. Donald, D. M. Lucas, D. A. Stevensand A. M. Steane & D. N. Stacey. *Measurement of the lifetime of the* $3d^2D_{5/2}$ *state in* $^{40}Ca^+$. Physical Review A, vol. 62, page 032503, 2000.

[Batchko 98] R.G. Batchko, G.D. Miller, A. Alexandrovski, M.M. Fejer & R.L. Byer. *Limitations of high-power visible wavelength periodically poled lithium niobate devices due to green-induced infrared absorption and thermal lensing.* In Lasers and Electro-Optics, 1998. CLEO 98. Technical Digest. Summaries of papers presented at the Conference on, pages 75–76, 1998.

[Benhelm 08a] J. Benhelm, G. Kirchmair, C. F. Roos & R. Blatt. *Towards fault-tolerant quantum computing with trapped ions.* Nature Physics, vol. 4, pages 463 – 466, 2008.

[Benhelm 08b] Jan Benhelm. *Precision spectroscopy and quantum information processing with trapped calcium ions.* PhD thesis, University of Innsbruck, 2008.

[Berkeland 98] D. J. Berkeland, J. D. Miller, J. C. Bergquist & W. M. Itanoand D. J. Wineland. *Laser cooled mercury ion frequency standard.* Phys. Rev. Lett., vol. 80, page 2089, 1998.

[Bermudez 09] A. Bermudez, D. Porras & M. A. Martin-Delgado. *Competing many-body interactions in systems of trapped ions.* Phys. Rev. A, vol. 79, page 060303, 2009.

[Bermudez 10] A Bermudez, MA Martin-Delgado & D Porras. *The localization of phonons in ion traps with controlled quantum disorder.* New Journal of Physics, vol. 12, page 123016, 2010.

[Berry 07] Dominic W Berry, Graeme Ahokas, Richard Cleve & Barry C Sanders. *Efficient quantum algorithms for simulating sparse Hamiltonians.* Communications in Mathematical Physics, vol. 270, pages 359–371, 2007.

[Blakestad 10] R. B. Blakestad. *Transport of Trapped-Ion Qubits within a Scalable Quantum Processor.* PhD thesis, University of Colorado, 2010.

[Blatt 08] R. Blatt & D. J. Wineland. *Entangled states of trapped atomic ions.* Nature, vol. 453, pages 1008–1015, 2008.

[Blatt 12] R. Blatt & C. F. Roos. *Quantum simulations with trapped ions.* Nature Physics, vol. 8, pages 277–284, 2012.

[Bollinger 85] J. J. Bollinger, J. S. Wells, D. J. Wineland & Wayne M. Itano. *Hyperfine structure of the* $2p^2P_{\frac{1}{2}}$ *state in* $^9Be^+$. Phys. Rev. A, vol. 31, pages 2711–2714, 1985.

[Boyd 68] G. D. Boyd & D. A. Kleinman. *Parametric interaction of focused Gaussian light beams.* Journal of Applied Physics, vol. 39, page 3597, 1968.

[Breitenbach 97] G. Breitenbach, S. Schiller & J. Mlynek. *Measurement of the quantum states of squeezed light.* Nature, vol. 387, pages 471–475, 1997.

[Breuer 09] H-P. Breuer, E-M-Laine & J. Piilo. *Measure for the Degree of Non-Markovian Behaviour of Quantum Processes in Open Systems.* Phys. Rev. Lett., vol. 103, page 210401, 2009.

[Britton 12] J. W. Britton, B. C. Sawyer, C.-C. J. Wang A. C. Keith, J. K. Freericks, H. Uys, M. J. Biercuk & J. J. Bollinger. *Engineered two-dimensional Ising interactions in a trapped-ion quantum simulator with hundreds of spins.* Nature, vol. 484, pages 489–492, 2012.

[Brown 11] K. R. Brown, A. C. Wilson, Y. Colombe, C. Ospelkaus, A. M. Meier, E. Knill, D. Leibfried & D. J. Wineland. *Single-qubit-gate error below* 10^{-4} *in a trapped ion.* Phys. Rev. A, vol. 84, page 030303, 2011.

[Buluta 09] Iulia Buluta & Franco Nori. *Quantum Simulators.* Science, vol. 326, pages 108–111, 2009.

[Carvalho 01] A. R. R. Carvalho, P. Milman, R. L. de Matos Filho & L. Davidovich. *Decoherence and Pointer Engineering and Quantum State Protection.* Phys. Rev. Lett., vol. 86, pages 4988–4991, 2001.

[Casanova 10] J. Casanova, J. J. García-Ripoll, R. Gerritsma, C. F. Roos & E. Solano. *Klein tunneling and Dirac potentials in trapped ions.* Phys. Rev. A, vol. 82, page 020101, 2010.

[Casanova 11] J. Casanova, C. Sabín, J. León, I. L. Egusquiza, R. Gerritsma, C. F. Roos, J. J. García-Ripoll & E. Solano. *Quantum Simulation of the Majorana Equation and Unphysical Operations.* Phys. Rev. X, vol. 1, page 021018, 2011.

[Casanova 12] J. Casanova, C. E. López, J. J. García-Ripoll, C. F. Roos & E. Solano. *Quantum tomography in position and momentum space.* Eur. Phys. J. D, vol. 66, pages 1–5, 2012.

[Caves 81] Carlton M. Caves. *Quantum-mechanical noise in an interferometer.* Phys. Rev. D, vol. 23, pages 1693–1708, 1981.

[Chiaverini 04] J. Chiaverini, D. Leibfried, T. Schaetz, M.D. Barrett, R.B. Blakestad, J. Britton, W.M. Itano, J.D. Jost,

E. Knill, C. Langer, R. Ozeri & D.J. Wineland. *Realization of quantum error correction.* Nature, vol. 432, pages 602–605, 2004.

[Chou 10] C. W. Chou, D. B. Hume, J. C. J. Koelemeij, D. J. Wineland & T. Rosenband. *Frequency Comparison of Two High-Accuracy Al^+ Optical Clocks.* Phys. Rev. Lett., vol. 104, page 070802, 2010.

[Cirac 93a] J. I. Cirac, R. Blatt, A. S. Parkins & P. Zoller. *Preparation of Fock States by Observation of Quantum Jumps in an Ion Trap.* Phys. Rev. Lett., vol. 70, page 6, 1993.

[Cirac 93b] J. I. Cirac, A. S. Parkins, R. Blatt & P. Zoller. *"Dark" squeezed states of the motion of a trapped ion.* Phys. Rev. Lett., vol. 70, pages 556–559, 1993.

[Cirac 95] J. I. Cirac & P. Zoller. *Quantum computations with cold trapped ions.* Phys. Rev. Lett., vol. 74, no. 20, pages 4091–4094, 1995.

[Cohen-Tannoudji 77] Claude Cohen-Tannoudji. *Atoms in strong resonant fields.* In Haroche S. Balian R. & Liberman S., editeurs, Les Houches Session XXVII, 1977.

[Cohen-Tannoudji 92] Claude Cohen-Tannoudji, Jacques Dupont-Roc, Gilbert Grynberg & Patricia Thickstun. Atom-photon interactions: basic processes and applications. Wiley Online Library, 1992.

[Collaboration 11] LIGO Scientific Collaboration*et al.* *A gravitational wave observatory operating beyond the quantum shot-noise limit.* Nature Physics, vol. 7, pages 962–965, 2011.

[de Clercq 15] Ludwig de Clercq. PhD thesis, ETH Zurich, 2015.

[de Matos Filho 96] R. L. de Matos Filho & W. Vogel. *Even and Odd Coherent States of the Motion of a Trapped Ion.* Phys. Rev. Lett., vol. 76, pages 608–611, 1996.

[Dehmelt 68] H. G. Dehmelt. *Radiofrequency Spectroscopy of Stored Ions I: Storage.* Advances in Atomic and Molecular Physics, vol. 3, pages 53 – 72, 1968.

[Dehmelt 75] H Dehmelt. *PROPOSED 1O NU GREATER THAN NU LASER FLUORESCENCE SPECTROSCOPY ON T1+ MONO-ION OSCILLATOR II.* In Bulletin of the American Physical Society, volume 20, pages 60–60. AMER INST PHYSICS CIRCULATION FULFILLMENT DIV, 500 SUNNYSIDE BLVD, WOODBURY, NY 11797-2999, 1975.

[Deleglise 08] Samuel Deleglise, Igor Dotsenko, Clement Sayrin, Julien Bernu, Michel Brune, Jean-Michel Raimond & Serge Haroche. *Reconstruction of non-classical cavity field states with snapshots of their decoherence.* Nature, vol. 455, no. 7212, pages 510–514, 2008.

[Demtroeder 82] W. Demtroeder. Laser spectroscopy and basic concepts and instrumentation. Springer-Verlag, 1982.

[Deng 05] X.-L. Deng, D. Porras & J. I. Cirac. *Effective spin quantum phases in systems of trapped ions.* Phys. Rev. A, vol. 72, page 063407, 2005.

[Deng 08] X-L Deng, D. Porras & J. I. Cirac. *Quantum phases of interacting phonons in ion trap.* Phys. Rev. A, vol. 77, page 033403, 2008.

[Deutsch 85] David Deutsch. *Quantum theory and the Church-Turing principle and the universal quantum computer.* Proceedings of the Royal Society of London A: Mathematical, Physical and Engineering Sciences, vol. 400, pages 97–117, 1985.

[Deutsch 89] David Deutsch. *Quantum computational networks.* Proceedings of the Royal Society of London A: Mathematical, Physical and Engineering Sciences, vol. 425, pages 73–90, 1989.

[Di Fidio 00] C. Di Fidio & W. Vogel. *Damped Rabi oscillations of a cold trapped ion.* Phys. Rev. A, vol. 62, page 031802, 2000.

[DiVincenzo 00] D. P. DiVincenzo. *The physical implementation of quantum computation.* Fortschritte der Physik, vol. 48, pages 771–783, 2000.

[Drever 83] R.W.P. Drever, J.L. Hall, F.V. Kowalski, J. Hough, G.M. Ford, A.J. Munley & H. Ward. *Laser phase and*

frequency stabilization using an optical resonator. Applied Physics B, vol. 31, no. 2, pages 97–105, 1983.

[Duan 10] L.-M. Duan & C. Monroe. *Colloquium : Quantum networks with trapped ions.* Rev. Mod. Phys., vol. 82, pages 1209–1224, 2010.

[Edwards 10] E. E. Edwards, S. Korenblit, K. Kim, R. Islam, M.-S. Chang, J. K. Freericks, G.-D. Lin, L.-M. Duan & C. Monroe. *Quantum simulation and phase diagram of the transverse-field Ising model with three atomic spins.* Phys. Rev. B, vol. 82, page 060412, 2010.

[Feynman 82] R. P. Feynman. *Simulating physics with computers.* International Journal of Theoretical Physics, vol. 21, page 467, 1982.

[Foot 04] Christopher J Foot. Atomic physics. OUP Oxford, 2004.

[Freegarde 01] Tim Freegarde & Claus Zimmermann. *On the design of enhancement cavities for second harmonic generation.* Optics Communications, vol. 199, pages 435 – 446, 2001.

[Friedenauer 08] A. Friedenauer, H. Schmitz, J. T. Glueckert, D. Porras & T. Schaetz. *Simulating a quantum magnet with trapped ions.* Nature Physics, vol. 4, pages 757 – 761, 2008.

[Gaebler 12] J. P. Gaebler, A. M. Meier, T. R. Tan, R. Bowler, Y. Lin, D. Hanneke, J. D. Jost, J. P. Home, E. Knill, D. Leibfried & D. J. Wineland. *Randomized Benchmarking of Multiqubit Gates.* Phys. Rev. Lett., vol. 108, page 260503, 2012.

[Georgescu 14] I. M. Georgescu, S. Ashhab & Franco Nori. *Quantum simulation.* Rev. Mod. Phys., vol. 86, pages 153–185, 2014.

[Gerritsma 10] R. Gerritsma, G. Kirchmair, F. Zähringer, E. Solano, R. Blatt & C. F. Roos. *Quantum simulation of the Dirac equation.* Nature, vol. 463, pages 68–71, 2010.

[Gerritsma 11] R. Gerritsma, B. P. Lanyon, G. Kirchmair, F. Zähringer, C. Hempel, J. Casanova, J. J. García-Ripoll, E. Solano, R. Blatt & C. F. Roos. *Quantum*

Simulation of the Klein Paradox with Trapped Ions. Phys. Rev. Lett., vol. 106, page 060503, 2011.

[Gerry 05] C. Gerry & P. Knight. Introductory quantum optics. Cambridge University Press, 2005.

[Gerstenkorn 78] Simon Gerstenkorn & Paul Luc. Atlas du spectre d'absorption de la molecule d'iode. Paris: Editions du Centre National de la Recherche Scientifique (CNRS), 1978.

[Gibson 98] G.M. Gibson, G.A. Turnbull, M. Ebrahimzadeh, M.H. Dunn, H. Karlsson, G. Arvidsson & F. Laurell. *Temperature-tuned difference-frequency mixing in periodically poled KTiOPO4.* Applied Physics B, vol. 67, no. 5, pages 675–677, 1998.

[Giorgi 10] Gian Luca Giorgi, Simone Paganelli & Fernando Galve. *Ion-trap simulation of the quantum phase transition in an exactly solvable model of spins coupled to bosons.* Phys. Rev. A, vol. 81, page 052118, 2010.

[Gottesman 01] Daniel Gottesman, Alexei Kitaev & John Preskill. *Encoding a qubit in an oscillator.* Phys. Rev. A, vol. 64, page 012310, 2001.

[Gulde 01] S. Gulde, D. Rotter, P. Barton, F. Schmidt-Kaler, R. Blatt & W. Hogervorst. *Simple and efficient photoionization loading of ions for precision ion-trapping experiments.* Applied Physics B, vol. 73, no. 8, pages 861–863, 2001.

[Häffner 08] H. Häffner, C. F. Roos & R. Blatt. *Quantum computing with trapped ions.* Physics Reports, vol. 469, pages 155 – 203, 2008.

[Haljan 05a] P. C. Haljan, K.-A. Brickman, L. Deslauriers, P. J. Lee & C. Monroe. *Spin-dependent forces on trapped ions for phase-stable quantum gates and motional Schrödinger cat states.* Phys. Rev. Lett., vol. 94, page 153602, 2005.

[Haljan 05b] P. C. Haljan, P. J. Lee, K.-A. Brickman, M. Acton, L. Deslauriers & C. Monroe. *Entanglement of trapped-ion clock states.* Phys. Rev A., vol. 72, page 062316, 2005.

[Hanneke 09] D. Hanneke, J. P. Home, J. D. Jost, J. M. Amini, D. Leibfried & D. J. Wineland. *Realization of a programmable two-qubit quantum processor.* Nature Physics, vol. 6, pages 13–16, 2009.

[Hao-Sheng 05] Zeng Hao-Sheng, Hu Ai-Qin, Liu Qiong & Kuang Le-Man. *Direct Measurement of Squeezing in the Motion of Trapped Ions.* Chinese Phys. Lett., vol. 22, page 798, 2005.

[Haroche 06] S. Haroche & J-M. Raimond. Exploring the quantum: Atoms and cavities and photons. Oxford University Press, 2006.

[Haroche 13] Serge Haroche. *Nobel Lecture: Controlling photons in a box and exploring the quantum to classical boundary.* Rev. Mod. Phys., vol. 85, pages 1083–1102, 2013.

[Harty 14] T. P. Harty, D. T. C. Allcock, C. J. Ballance, L. Guidoni, H. A. Janacek, N. M. Linke, D. N. Stacey & D. M. Lucas. *High-Fidelity Preparation, Gates, Memory, and Readout of a Trapped-Ion Quantum Bit.* Phys. Rev. Lett., vol. 113, page 220501, 2014.

[Hemmerich 90] A. Hemmerich, D. H. McIntyre, C. Zimmermann & T. W. Hänsen. *Second-harmonic generation and optical stabilization of a diode laser in an external ring resonator.* Opt. Lett., vol. 15, pages 372–374, 1990.

[Hempel 13] C. Hempel, B. P. Lanyon, P. Jurcevic, R. Gerritsma, R. Blatt & C. F. Roos. *Entanglement-enhanced detection of single-photon scattering events.* Nature Photonics, vol. 7, pages 630–633, 2013.

[Hijlkema 07] Markus Hijlkema. *Single photons from a single atom trapped in a high-finesse optical cavity.* PhD thesis, Technische Universität München, 2007.

[Home 06a] J. P. Home, M. J. McDonnell, D. M. Lucas, G. Imreh, B. C. Keitch, D. J. Szwer, N. R. Thomas, D. N. Stacey & A. M. Steane. *Deterministic entanglement and tomography of ion–spin qubits.* New J. Phys., vol. 8, page 188, 2006.

[Home 06b] J. P. Home & Andrew M Steane. *Electrode configurations for fast separation of trapped ions.* Quantum

Information and Computation, vol. 6, pages 289–325, 2006.

[Home 06c] Jonathan Home. *Entanglement of Two Trapped-Ion Spin Qubits*. PhD thesis, University of Oxford, 2006.

[Home 09] J. P. Home, D. Hanneke, J. D. Jost, J. M. Amini, D. Leibfried & D. J. Wineland. *Complete Methods Set for Scalable Ion Trap Quantum Information Processing*. Science, vol. 325, page 1227, 2009.

[Home 13] Jonathon P. Home. *Quantum Science and Metrology with Mixed-Species Ion Chains*. Advances in Atomic, Molecular, and Optical Physics, vol. 62, pages 231 – 277, 2013.

[Hu 12] Y. M. Hu, M. Feng & C. Lee. *Adiabatic Mach-Zehnder interferometer via an array of trapped ions*. Phys. Rev. A, vol. 85, page 043604, 2012.

[Ibaraki 11] Y. Ibaraki, U. Tanaka & S. Urabe. *Detection of parametric resonance of trapped ions for micromotion compensation*. Applied Physics B, vol. 105, no. 2, pages 219–223, 2011.

[Islam 11] R. Islam, E. E. Edwards, K. Kim, S. Korenblit, C. Noh, H. Carmichael, G-D. Lin, L.-M. Duan, C.-C. Joseph Wang, J. K. Freericks & C. Monroe. *Onset of a quantum phase transition with a trapped ion quantum simulator*. Nature Communications, vol. 2, page 377, 2011.

[Islam 13] R. Islam, C. Senko, W. C. Campbell, S. Korenblit, J. Smith, A. Lee, E. E. Edwards, C.-C. J. Wang, J. K. Freericks & C. Monroe. *Emergence and Frustration of Magnetic Order with Variable-Range Interactions in a Trapped Ion Quantum Simulator*. Science, vol. 340, page 583, 2013.

[Ivanov 09] P. A. Ivanov, S. S. Ivanov, N. V. Vitanov, A. Mering, M. Fleischhauer & K. Singer. *Simulation of a quantum phase transition of polaritons with trapped ions*. Phys. Rev. A, vol. 80, page 060301, 2009.

[Jané 03] Enric Jané, Guifre Vidal, Wolfgang Dür, Peter Zoller & J Ignacio Cirac. *Simulation of quantum dynamics*

with quantum optical systems. Quantum Information and Computation, vol. 3, pages 15–37, 2003.

[Jin 93] Jian Jin & D. A. Church. *Precision lifetimes for the Ca^+ $4p^2P$ levels: Experiment challenges theory at the 1% level.* Phys. Rev. Lett., vol. 70, pages 3213–3216, 1993.

[Jost 09] J. D. Jost, J. P. Home, J. M. Amini, D. Hanneke, R. Ozeri, C. Langer, J. J. Bollinger, D. Leibfried & D. J. Wineland. *Entangled Mechanical Oscillators.* Nature (London), vol. 459, pages 683–685, 2009.

[Jurcevic 14] P. Jurcevic, B. P. Lanyon, P. Hauke, C. Hempel, P. Zoller, R. Blatt. & C. F. Roos. *Observation of entanglement propagation in a quantum many-body system.* arxiv:1401.5387, 2014.

[Kielpinski 02] D. Kielpinski, C. Monroe & D. Wineland. *Architecture for a large-scale ion-trap quantum computer.* Nature, vol. 417, pages 709–711, 2002.

[Kienzler 15a] D. Kienzler, H.-Y. Lo, B. Keitch, L. de Clercq, F. Leupold, F. Lindenfelser, M. Marinelli, V. Negnevitsky & J. P. Home. *Quantum harmonic oscillator state synthesis by reservoir engineering.* Science, vol. 347, pages 53–56, 2015.

[Kienzler 15b] Daniel Kienzler. *Quantum Harmonic Oscillator State Synthesis by Reservoir Engineering.* PhD thesis, ETH Zurich, 2015.

[Kim 09] K. Kim, M-S. Chang, R. Islam, S. Korenblit, L-M Duan & C. Monroe. *Entanglement and Tunable Spin-Spin Couplings between Trapped Ions Using Multiple Transverse Modes.* Phys. Rev. Lett., vol. 103, page 120502, 2009.

[Kim 10] K. Kim, M-S. Chang, S. Korenblit, R. Islam, E. E. Edwards, J. K. Freericks, G-D Lin, L-M-Duan & C. Monroe. *Quantum simulation of frustrated Ising spins with trapped ions.* Nature, vol. 465, pages 590–593, 2010.

[Kim 11] K Kim, S Korenblit, R Islam, EE Edwards, MS Chang, C Noh, H Carmichael, GD Lin, LM Duan, CC Joseph

Wang*et al. Quantum simulation of the transverse Ising model with trapped ions.* New Journal of Physics, vol. 13, page 105003, 2011.

[King 99] Brian E. King. *Quantum State Engineering and Information Processing with Trapped Ions.* PhD thesis, University of Colorado, 1999.

[King 08] BE King. *Angular Momentum Coupling and Rabi Frequencies for Simple Atomic Transitions.* arXiv:0804.4528, 2008.

[Kjaergaard 00] N. Kjaergaard, L. Hornekaer, A.M. Thommesen, Z. Videsen & M. Drewsen. *Isotope selective loading of an ion trap using resonance-enhanced two-photon ionization.* Applied Physics B, vol. 71, no. 2, pages 207–210, 2000.

[Knill 05] E. Knill. *Quantum Computation with realistically noisy devices.* Nature, vol. 434, pages 39–44, 2005.

[Krauter 11] Hanna Krauter, C.A. Muschik, Kasper Jensen, Wojciech Wasilewski, Jonas Meyer Petersen, J.I Cirac & Eugene Simon Polzik. *Entanglement generated by dissipation and steady state entanglement of two macroscopic objects.* Physical Review Letters, vol. 107, no. 8, page 080503, 2011.

[Ladd 10] T. D. Ladd, F. Jelezko, R. Laflamme, Y. Nakamura, C. Monroe & J. L. O/'Brien. *Quantum computers.* Nature, vol. 464, pages 45–53, 2010.

[Lamata 07] L. Lamata, J. León, T. Schätz & E. Solano. *Dirac Equation and Quantum Relativistic Effects in a Single Trapped Ion.* Phys. Rev. Lett., vol. 98, page 253005, 2007.

[Langer 05] C. Langer, R. Ozeri, J.D. Jost, J. Chiaverini, B.L. DeMarco, A. Ben-Kish, R.B. Blakestad, J. Britton, D. Hume, W.M. Itano, D. Leibfried, R. Reichle, T. Rosenband, T. Schaetz, P.O. Schmidt & D.J. Wineland. *Long-Lived Qubit Memory Using Atomic Ions.* Phys. Rev. Lett., vol. 95, page 060502(4), 2005.

[Langer 06] Christopher E. Langer. *High Fidelity Quantum Information Processing with Trapped Ions.* PhD thesis, University of Colorado, 2006.

[Lanyon 11] B. P. Lanyon, C. Hempel, D. Nigg, M. Müller, R. Gerritsma, F. Zähringer, P. Schindler, J. T. Barreiro, M. Rambach, G. Kirchmair, M. Hennrich, P. Zoller, R. Blatt & C. F. Roos. *Universal Digital Quantum Simulation with Trapped Ions.* Science, vol. 334, pages 57–61, 2011.

[Lau 12] Hoi-Kwan Lau & Daniel F. V. James. *Proposal for a scalable universal bosonic simulator using individually trapped ions.* Phys. Rev. A, vol. 85, page 062329, 2012.

[Lee 05] P. J. Lee, K-A. Brickman, L. Deslauriers, P. C. Haljan, L0M. Duan & C. monroe. *Phase Control of Trap Ion Quantum Gates.* Journal of Optics B, vol. 7, page S371, 2005.

[Leibfried 02] D. Leibfried, B. DeMarco, V. Meyer, M. Rowe, A. Ben-Kish, J. Britton, W. M. Itano, B. Jelenković, C. Langer, T. Rosenband & D. J. Wineland. *Trapped-Ion Quantum Simulator: Experimental Application to Nonlinear Interferometers.* Phys. Rev. Lett., vol. 89, page 247901, 2002.

[Leibfried 03a] D. Leibfried, R. Blatt, C. Monroe & D. Wineland. *Quantum dynamics of single trapped ions.* Rev. Mod. Phys., vol. 75, pages 281–324, 2003.

[Leibfried 03b] D. Leibfried, B. DeMarco, V. Meyer, D. Lucas, M. Barrett, J. Britton, W. M. Itano, B. Jelenkovic, C. Langer, T. Rosenband & D. J. Wineland. *Experimental demonstration of a robust and high-fidelity geometric two ion-qubit phase gate.* Nature, vol. 422, pages 412–415, 2003.

[Leibfried 07] D. Leibfried, E. Knill, C. Ospelkaus & D. J. Wineland. *Transport quantum logic gates for trapped ions.* Phys. Rev. A, vol. 76, page 032324, 2007.

[Lin 13] Y. Lin, J. P. Gaebler, F. Reiter, T. R. Tan, R. Bowler amd A. S. Sørensen, D. Leibfried & D. J. Wineland. *Dissipative production of a maximally entangled steady state of two quantum bits.* Nature, vol. 504, pages 415–418, 2013.

[Lindenfelser 11] Frieder Lindenfelser. Laser stabilisation for quantum information experiments with trapped ions. Master's thesis, ETH Zurich, 2011.

[Lo 14] Hsiang-Yu Lo, Joseba Alonso, Daniel Kienzler, BenjaminC. Keitch, LudwigE. de Clercq, Vlad Negnevitsky & JonathanP. Home. *All-solid-state continuous-wave laser systems for ionization, cooling and quantum state manipulation of beryllium ions.* Applied Physics B, vol. 114, pages 17–25, 2014.

[Lo 15] Hsiang-Yu Lo, Daniel Kienzler, Ludwig de Clercq, Matteo Marinelli, Vlad Negnevitsky, Ben C. Keitch & Jonathan P. Home. *Spin-motion entanglement and state diagnosis with squeezed oscillator wavepackets.* Nature, vol. 521, pages 336–339, 2015.

[Loudon 95] R. Loudon. The quantum theory of light. Oxford University Press, 1995.

[Lucas 04a] D. M. Lucas, A. Ramos, J. P. Home, M. J.McDonnell, S. Nakayama, J.-P. Stacey, S. C. Webster andD. N. Stacey & A. M. Steane. *Isotope-selective photoionisation for calcium ion trapping.* Phys. Rev. A, vol. 69, page 012711, 2004.

[Lucas 04b] D. M. Lucas, A. Ramos, J. P. Home, M. J. McDonnell, S. Nakayama, J.-P. Stacey, S. C. Webster, D. N. Stacey & A. M. Steane. *Isotope-selective photoionization for calcium ion trapping.* Phys. Rev. A, vol. 69, page 012711, 2004.

[Madsen 06] Martin J. Madsen. *Advanced Ion Trap Development and Ultrafast Laser-Ion Interactions.* PhD thesis, University of Michigan, 2006.

[Mandel 79] L. Mandel. *Sub-Poissonian photon statistics in resonance fluorescence.* Opt. Lett., vol. 4, pages 205–207, 1979.

[McDonnell 07] M. J. McDonnell, J. P. Home, D. M. Lucas, G. Imreh, B. C. Keitch, D. J. Szwer, N. R. Thomas, S. C. Webster, D. N. Stacey, & A. M. Steane. *Long-lived mesoscopic entanglement outside the Lamb-Dicke regime.* Phys. Rev. Lett., vol. 98, page 063603, 2007.

[Meekhof 96] D. M. Meekhof, C. Monroe, B. E. King, W. M. Itano & D. J. Wineland. *Generation of nonclassical motional states of a trapped atom.* Phys. Rev. Lett., vol. 76, page 1796, 1996. Phys. Rev. Lett. 77, 2346(E) 1996.

[Menicucci 10] Nicolas C Menicucci, S Jay Olson & Gerard J Milburn. *Simulating quantum effects of cosmological expansion using a static ion trap.* New Journal of Physics, vol. 12, page 095019, 2010.

[Milburn 00] G. J. Milburn, S. Schneider & D. F. James. *Ion trap quantum computing with warm ions.* Fortschr. Physik, vol. 48, pages 801–810, 2000.

[Mølmer 99] K. Mølmer & A. Sørensen. *Multiparticle entanglement of hot trapped ions.* Phys. Rev. Lett., vol. 82, pages 1835–1838, 1999.

[Monroe 95a] C. Monroe, D. M. Meekhof, B. E. King, W. M. Itano & D. J. Wineland. *Demonstration of a fundamental quantum logic gate.* Phys. Rev. Lett., vol. 75, pages 4714–4717, 1995.

[Monroe 95b] C. Monroe, D. M. Meekhof, B. E. King, S. R. Jefferts, W. M. Itano, D. J. Wineland & P. Gould. *Resolved-sideband Raman cooling of a bound atom to the 3D zero-point energy.* Phys. Rev. Lett., vol. 75, no. 22, page 4011, 1995.

[Monroe 96] C. Monroe, D. M. Meekhof, B. E. King & D. J. Wineland. *A Schrödinger cat superposition state of an atom.* Science, vol. 272, page 1131, 1996.

[Monroe 13] C. Monroe & J. Kim. *Scaling the Ion Trap Quantum Processor.* Science, vol. 339, no. 6124, pages 1164–1169, 2013.

[Munro 02] W. J. Munro, K. Nemoto, G. J. Milburn & S. L. Braunstein. *Weak-force detection with superposed coherent states.* Phys. Rev. A, vol. 66, page 023819, 2002.

[Myerson 08] A. H. Myerson, D. J. Szwer, S. C. Webster, D. T. C. Allcock, M. J. Curtis, G. Imreh, J. A. Sherman, D. N. Stacey, A. M. Steane & D. M. Lucas. *High-Fidelity Readout of Trapped-Ion Qubits.* Phys. Rev. Lett., vol. 100, page 200502, 2008.

[Nielsen 00] Michael A. Nielsen & Isaac L. Chuang. Quantum computation and quantum information. Cambridge University Press, Cambridge, 2000.

[Northup 14] T. E. Northup & R. Blatt. *Quantum information transfer using photons.* Nat Photon, vol. 8, no. 5, pages 356–363, 2014.

[Oberst 99] Hilmar Oberst. Resonance fluorescence of single barium ions. Master's thesis, University of Innsbruck, 1999.

[Ospelkaus 11] C. Ospelkaus, U. Warring, Y. Colombe, K. R. Brown, J. M. Amini, D. Leibfried & D. J. Wineland. *Microwave quantum logic gates for trapped ions.* Nature, vol. 476, pages 181–184, 2011.

[Ourjoumtsev 07] A. Ourjoumtsev, H. Jeong, R. Tualle-Brouri & P. Grangier. *Generation of optical 'Schrödinger cats' from photon number states.* Nature, vol. 448, pages 784–786, 2007.

[Ozeri 05] R. Ozeri, C. Langer, J. D. Jost, B. L. DeMarco, A. Ben-kish, B. R. Blakestad, J. Britton, J. Chiaverini, W. M. Itano, D. Hume, D. Leibfried, T. Rosenband, P. Schmidt & D. J. Wineland. *Hyperfine Coherence in the Presence of Spontaneous Photon Scattering.* Phys. Rev. Lett., vol. 95, page 030403, 2005.

[Ozeri 07] R. Ozeri, W. M. Itano, R. B. Blakestad, J. Britton, J. Chiaverini, J. D. Jost, C. Langer, D. Leibfried, R. Reichle, S. Seidelin, J. H. Wesenburg & D. J. Wineland. *Errors in trapped-ion quantum gates due to spontaneous photon scattering.* Phys. Rev A., vol. 75, page 4, 2007.

[Porras 04] D. Porras & J. I. Cirac. *Bose-Einstein Condensation and Strong-Correlation Behaviour of Phonons in Ion Traps.* Phys. Rev. Lett., vol. 93, page 263602, 2004.

[Porras 08] D. Porras, F. Marquardt, J. von Delft & J. I. Cirac. *Mesoscopic spin-boson models of trapped ions.* Phys. Rev. A, vol. 78, page 010101(R), 2008.

[Poulsen 75] O Poulsen, T Andersen & NJ Skouboe. *Fast-beam, zero-field level-crossing measurements of radiative lifetimes, fine and hyperfine structures in excited states of ionic and neutral beryllium.* Journal of Physics B: Atomic and Molecular Physics, vol. 8, no. 9, page 1393, 1975.

[Poyatos 96] J. F. Poyatos, J. I. Cirac & P. Zoller. *Quantum Reservoir Engineering with Laser Cooled Trapped Ions*. Phys. Rev. Lett., vol. 77, page 4728, 1996.

[Prokofiev 00] N. V. Prokofiev & P. C. E. Stamp. *Theory of the Spin Bath*. Rep. Prog. Phys., vol. 63, pages 669–726, 2000.

[Puchalski 09] Mariusz Puchalski & Krzysztof Pachucki. *Fine and hyperfine splitting of the* $2P$ *state in Li and* Be^+. Phys. Rev. A, vol. 79, page 032510, 2009.

[Retzker 08] A. Retzker, R. C. Thompson, D. M. Segal & M. B. Plenio. *Double Well Potentials and Quantum Phase Transitions in Ion Traps*. Phys. Rev. Lett., vol. 101, page 260504, 2008.

[Richerme 14] Philip Richerme, Zhe-Xuan Gong, Aaron Lee, Crystal Senko, Jacob Smith, Michael Foss-Feig, Spyridon Michalakis, Alexey V. Gorshkov & Christopher Monroe. *Non-local propagation of correlations in quantum systems with long-range interactions*. Nature, vol. 511, no. 7508, pages 198–201, 2014.

[Risk 03] William Paul Risk, Timothy R Gosnell & Arto V Nurmikko. Compact blue-green lasers. Cambridge University Press, 2003.

[Rivas 10] Ángel Rivas, Susana F. Huelga & Martin B. Plenio. *Entanglement and Non-Markovianity of Quantum Evolutions*. Phys. Rev. Lett., vol. 105, page 050403, 2010.

[Roos 00a] C. F. Roos, D. Leibfried, A. Mundt, F. Schmidt-Kaler, J. Eschner & R. Blatt. *Experimental Demonstration of Ground State Laser Cooling with Electromagnetically Induced Transparency*. Phys. Rev. Lett., vol. 85, pages 5547–5550, 2000.

[Roos 00b] Christian F. Roos. *Controlling the quantum state of trapped ions*. Ph.D. thesis, Universität Innsbruck, Austria, 2000.

[Roos 08] C. F. Roos. *Ion trap quantum gates with amplitude-modulated laser beams*. New J. Phys., vol. 10, page 013002, 2008.

[Roy 15] Ananda Roy, Zaki Leghtas, A. Douglas Stone, Michel Devoret & Mazyar Mirrahimi. *Continuous generation and stabilization of mesoscopic field superposition states in a quantum circuit.* Phys. Rev. A, vol. 91, page 013810, 2015.

[Sackett 00] C. A. Sackett, D. Kielpinski, B. E. King, C. Langerand V. Meyer, C. J. Myatt, M. Rowe, Q. A. Turchette amd W. M. Itano, D. J. Wineland & C. Monroe. *Experimental entanglement of four particles.* Nature, vol. 404, page 256, 2000.

[Schmidt-Kaler 03] Ferdinand Schmidt-Kaler, Hartmut Häffner, Mark Riebe, Stephan Gulde, Gavin PT Lancaster, Thomas Deuschle, Christoph Becher, Christian F Roos, Jürgen Eschner & Rainer Blatt. *Realization of the Cirac-Zoller controlled-NOT quantum gate.* Nature, vol. 422, pages 408 – 411, 2003.

[Schmidt 05] P. O. Schmidt, T. Rosenband, C. Langer, W. M. Itano, J. C. Bergquist & D. J. Wineland. *Spectroscopy Using Quantum Logic.* Science, vol. 309, pages 749–752, 2005.

[Schneider 12] Ch Schneider, Diego Porras & Tobias Schaetz. *Experimental quantum simulations of many-body physics with trapped ions.* Reports on Progress in Physics, vol. 75, no. 2, page 024401, 2012.

[Schrödinger 35] Erwin Schrödinger. *Die gegenwärtige Situation in der Quantenmechanik.* Naturwissenschaften, vol. 23, pages 823–828, 1935.

[Schuck 10] C. Schuck, M. Almendros, F. Rohde, M. Hennrich & J. Eschner. *Two-color photoionization of calcium using SHG and LED light.* Applied Physics B, vol. 100, no. 4, pages 765–771, 2010.

[Senko 15] C. Senko, P. Richerme, J. Smith, A. Lee, I. Cohen, A. Retzker & C. Monroe. *Realization of a Quantum Integer-Spin Chain with Controllable Interactions.* Phys. Rev. X, vol. 5, page 021026, 2015.

[Sepiol 12] Martin A. Sepiol. Frequency stabilization of a 729 nm diode laser to an external high finesse reference cavity. Master's thesis, ETH Zurich, 2012.

[Shankar 13] S. Shankar, M. Hatridge, Z. Leghtas, K. M. Sliwa, A. Narla, U. Vool, S. M. Girvin, L. Frunzio, M. Mirrahimi & M. H. Devoret. *Autonomously stabilized entanglement between two superconducting quantum bits.* Nature, vol. 504, pages 419–422, 2013.

[Shor 94] P. W. Shor. *Polynomial-time algorithms for prime factorisation and discrete logarithms on a quantum computer.* In Proceedings of the 35th annual symposium on foundations of computer science, pages 124–134. IEEE Computer Society Press, 1994.

[Solano 99] E. Solano, R. L. de Matos Filho & N. Zagury. *Deterministic Bell states and measurement of the motional state of two trapped ions.* Phys. Rev. A, vol. 59, pages R2539–R2543, 1999.

[Sørensen 99] A. Sørensen & K. Mølmer. *Quantum computation with ions in thermal motion.* Phys. Rev. Lett., vol. 82, pages 1971–1974, 1999.

[Steane 03] Andrew M. Steane. *Overhead and noise threshold of fault-tolerant quantum error correction.* Phys. Rev. A, vol. 68, page 042322, 2003.

[Targat 05] R. Le Targat, J.-J. Zondy & P. Lemonde. *75frequency doubler.* Optics Communications, vol. 247, pages 471 – 481, 2005.

[Turchette 00a] Q. A. Turchette, D. Kielpinski, B. E. King, D. Leibfried, D. M. Meekhof, C. J. Myatt, M. A. Rowe, C. A. Sackett, C. S. Wood, W. M. Itano, C. Monroe & D. J. Wineland. *Heating of trapped ions from the quantum ground state.* Phys. Rev. A, vol. 61, page 063418, 2000.

[Turchette 00b] Q. A. Turchette, C. J. Myatt, B. E. King, C. A. Sackett, D. Kielpinski, W. M. Itano, C. Monroe & D. J. Wineland. *Decoherence and decay of motional quantum states of a trapped atom coupled to engineered reservoirs.* Phys. Rev. A, vol. 62, page 053807, 2000.

[Uys 10] H. Uys, M. J. Biercuk, A. P. VanDevender, C. Ospelkaus, D. Meiser, R. Ozeri & J. J. Bollinger. *Decoherence due to Elastic Rayleigh Scattering.* Phys. Rev. Lett., vol. 105, page 200401, 2010.

[Vasilyev 11] S. Vasilyev, A. Nevsky, I. Ernsting, M. Hansen, J. Shen & S. Schiller. *Compact all-solid-state continuous-wave single-frequency UV source with frequency stabilization for laser cooling of Be^+ ions.* Applied Physics B, vol. 103, pages 27–33, 2011.

[Verstraete 09] Frank Verstraete, Michael M. Wolf & J. Ignacio Cirac. *Quantum computation and quantum state engineering and and quantum phase transitions driven by dissipation.* Nature Physics, vol. 5, pages 633–636, 2009.

[Vlastakis 13] B. Vlastakis, G. Kirchmair, Z. Leghtas, S. E. Nigg, L. Frunzio, S. M. Girvin, M. Mirrahimi, M. H. Devoret & R. J. Schoelkopf. *Deterministically Encoding Quantum Information Using 100-Photon Schrödinger's Cat States.* Science, vol. 342, pages 607–610, 2013.

[Walls 94] D. F. Walls & G. J. Milburn. Quantum optics. Springer, Berlin, 1994.

[Weedbrook 12] Christian Weedbrook, Stefano Pirandola, Raúl García-Patrón, Nicolas Cerf, Timothy Ralph, Jeffrey Shapiro & Seth Lloyd. *Gaussian quantum information.* Rev. Mod. Phys., vol. 84, pages 621–669, 2012.

[Wilson 11] A.C. Wilson, C. Ospelkaus, A.P. VanDevender, J.A. Mlynek, K.R. Brown, D. Leibfried & D.J. Wineland. *A 750-mW, continuous-wave, solid-state laser source at 313 nm for cooling and manipulating trapped 9Be+ ions.* Applied Physics B, vol. 105, pages 741–748, 2011.

[Wineland 80] DJ Wineland, JC Bergquist, Wayne M Itano & RE Drullinger. *Double-resonance and optical-pumping experiments on electromagnetically confined, laser-cooled ions.* Optics letters, vol. 5, no. 6, pages 245–247, 1980.

[Wineland 83] DJ Wineland, JJ Bollinger & Wayne M Itano. *Laser-fluorescence mass spectroscopy.* Physical Review Letters, vol. 50, no. 9, page 628, 1983.

[Wineland 98] D. J. Wineland, C. Monroe, W. M. Itano, D. Leibfried, B. E. King & D. M. Meekhof. *Experimental issues in coherent quantum-state manipulation of trapped atomic ions.* J. Res. Natl. Inst. Stand. Technol., vol. 103, pages 259–328, 1998.

[Wineland 03] D. J. Wineland, M. Barrett, J. Britton, J. Chiaverini, B. DeMarcoand W. M. Itano, B. Jelenkovic, C. Langer, D. Leibfried, V. Meyer & T. Rosenbandand T. Schätz. *Quantum information processing with trapped ions.* Phil. Trans. R. Soc. Lond. A, vol. 361, pages 1349–1361, 2003.

[Wineland 13] David J. Wineland. *Nobel Lecture: Superposition, entanglement, and raising Schrödinger's cat.* Rev. Mod. Phys., vol. 85, pages 1103–1114, 2013.

[Wolf 08] M. M. Wolf, J. Eisert, T. S. Cubitt & J. I. Cirac. *Assessing Non-Markovian Quantum Dynamics.* Phys. Rev. Lett., vol. 101, page 150402, 2008.

[Woodgate 80] Gordon Kemble Woodgate. Elementary atomic structure. Oxford: Clarendon Press, 1980.

[Yerokhin 08] V. A. Yerokhin. *Hyperfine structure of Li and* Be^+. Phys. Rev. A, vol. 78, page 012513, 2008.

[Yuen 76] Horace P. Yuen. *Two-photon coherent states of the radiation field.* Phys. Rev. A, vol. 13, pages 2226–2243, 1976.

[Zeng 12] Jun Zeng, Rui-Qin Zhang & Herbert Treutlein. Quantum simulations of materials and biological systems. Springer Netherlands, 2012.